

IPPT Reports on Fundamental Technological Research

1/2012

Marcin Białaś

MECHANICAL MODELLING OF THIN FILMS  
Stress Evolution, Degradation, Characterization

Institute of Fundamental Technological Research  
Polish Academy of Sciences

Warszawa 2012

IPPT Reports on Fundamental Technological Research

ISSN 0208-5058

ISBN 978-83-89687-72-2

Kolegium Redakcyjne:

Wojciech Nasalski (Redaktor Naczelny),  
Paweł Dłużewski, Zbigniew Kotulski, Wiera Oliferuk,  
Jerzy Rojek, Zygmunt Szymański, Yuriy Tasinkevych

Recenzent:

Artur Ganczarski

Praca wpłynęła do redakcji 11 stycznia 2012 roku.

---

Copyright © 2012

Instytut Podstawowych Problemów Techniki Polskiej Akademii Nauk  
Pawińskiego 5b, 02-106 Warszawa

Nakład 100 egz. Ark. wyd. 12  
Oddano do druku w maju 2012 roku

---

Druk i oprawa: EXPOL, P. Rybiński, J. Dąbek, Sp. J., Włocławek, ul. Brzeska 4

## Abstract

The thesis reports the research effort aimed at the mechanical modelling of thin films. It is devoted to four particular aspects: stress development due to mechanical and thermal loadings, coating degradation due to through thickness cracking, coating delamination and, finally, mechanical characterization of thin films using non-invasive methods.

The monograph consists of seven chapters. Chapter 1 is an introductory chapter, where thin films deposition methods are described. Then, failure modes observed in coatings are discussed. Since the developed modelling tools will be applied in particular to thermal barrier coatings and human skin, two final sections of the chapter introduce the reader into mechanical and material properties of TBC systems and human skin.

Mathematical preliminaries is the subject of Chapter 2 of the monograph. Basics of elastic fracture mechanics of interfacial cracks are briefly presented and cohesive zone model is introduced. This model makes a basis for subsequent modelling of various types of cracks within coating systems.

Chapters 3–6 report the novel part of the research and, except for the experiment described in the first part of Chapter 4 (bending tests combined with acoustic emission technique), present an original contribution of the Author.

In Chapter 3 an energy model of segmentation cracking with application to silicon oxide film is presented. Chapter 4 reports finite element simulation of stress development, delamination and through-thickness cracking in TBC systems. In Chapter 5 two dimensional model of frictional slip is presented and semi-analytical procedure providing delamination estimation is described. Chapter 6 presents a conceptual setup of piezoelectric sensors used for mechanical characteristic of human skin. The final Chapter 7 concludes the monograph and recapitulates the main achievements of the reported research.

## Abbreviations

Throughout the monograph, for the brevity of presentation, abbreviations for some expressions are used. For the convenience of the Reader, the complete list of them with their expansions is provided below.

<b>AE</b>	acoustic emission
<b>APS</b>	air plasma spray
<b>BC</b>	bond coat
<b>BFGS</b>	Broyden, Fletcher, Glodfarb and Shanno, (algorithm)
<b>CVD</b>	chemical vapour deposition
<b>EB (PVD)</b>	electron beam (physical vapour deposition)
<b>FE(M)</b>	finite element (method)
<b>FRP</b>	fiber reinforced polymer
<b>FSZ</b>	fully stabilized zirconia
<b>FZJ</b>	Forschungszentrum Jülich, (Research Centre Jülich)
<b>LE (CVD)</b>	laser enhanced (chemical vapour deposition)
<b>LP (CVD)</b>	low pressure (chemical vapour deposition)
<b>MASW</b>	multi-channel analysis of surface waves
<b>MO (CVD)</b>	metal-organic (chemical vapour deposition)
<b>MRI</b>	magnetic resonance imaging
<b>NMR</b>	nuclear magnetic resonance
<b>OCT</b>	optical coherence tomography
<b>PE (CVD)</b>	plasma enhanced (chemical vapour deposition)
<b>PET</b>	polyethylene terephthalate
<b>PSZ</b>	partially stabilized zirconia
<b>PVD</b>	physical vapour deposition
<b>PVDF</b>	polyvinylidene difluoride
<b>SASW</b>	spectral analysis of surface waves
<b>SLD</b>	superluminescence diode
<b>TBC</b>	thermal barrier coating
<b>TGO</b>	thermally grown oxide

## Symbols

Throughout the monograph scalars are in mathematical italics, e.g.  $\alpha$ ,  $E$ ,  $h_f$ . For vectors and tensors boldface roman or Greek symbols are used, e.g.  $\mathbf{n}$ ,  $\boldsymbol{\sigma}$ . Their meaning should be clear from the context. For the convenience of the Reader, the complete list of the symbols is provided below.

$A$  fiber cross-sectional area

$A_{ijkl}$  anisotropy tensor

$C_f$  electric capacitance

$C_n$ ,  $C_t$  interfacial compliance

$D_3$  electric displacement

$D_\tau$ ,  $D_\tau^n$  energy dissipated on the interface by the shear stress

$d$ ,  $d^r$  length of delaminated zone

$d^{\text{ox}}$ ,  $d_0^{\text{ox}}$  oxide thickness

$d_{31}$  piezoelectric constant

$E$ ,  $E_s$ ,  $E_f$ ,  $E_1$ ,  $E_2$ ,  $E_{\langle 100 \rangle}$  Young moduli

$e_{ij}^{\text{creep}}$  deviatoric creep strain

$\mathcal{E}_c$  unit area specific energy

$\mathcal{E}_c^{\text{max}}$ ,  $\mathcal{E}_c^{\text{min}}$  limits put on unit area specific energy

$\mathcal{E}_f$ ,  $\mathcal{E}_f^n$ ,  $\mathcal{E}_f^{\text{max}}$ ,  $\mathcal{E}_s$ ,  $\mathcal{E}_s^n$  elastic energy

$F(\sigma, \tau)$ ,  $F_0(\sigma, \tau)$ ,  $F_1(\sigma, \tau)$  yield function

$G$ ,  $G_I$ ,  $G_{II}$  fracture energy

$G_j^i$ ,  $\mathcal{G}_j^i$  Green's functions for the layered viscoelastic half-space

$\mathcal{G}$ ,  $\mathcal{G}_{\text{debond}}$ ,  $\mathcal{G}_{\text{kink}}$  energy release rate

$H$  hardening modulus

$h$ ,  $h_{\text{BC}}$ ,  $h_f$ ,  $h_s$  thickness

$\text{Im}$  imaginary part of complex number

$J_2$ ,  $J_3$  moments of inertia

$K$  complex stress intensity factor

$K_c$  film fracture toughness

$\mathbf{K}$ ,  $K_n$ ,  $K_t$  interfacial stiffness

$K_s$  bulk modulus

$K_1, K_2$  real and imaginary parts of  $K$ , respectively  
 $k_p$  oxidation rate constant  
 $L$  length  
 $l, l_0$  characteristic dimension  
 $l_{\text{seg}}$  crack spacing  
 $m$  failure sliding mode influence parameter  
 $\mathbf{n}$  unit normal vector  
 $P$  point force  
 $Q$  charge density  
 $\mathbf{q}$  fiber-substrate line load  
 $R_a$  technical measure of surface roughness  
 $\mathcal{R}e$  real part of complex number  
 $\{R, \Phi\}, \{r, \varphi\}$  polar space parametrization  
 $s, s_A, s_B$  reference length for mode angle measuring  
 $s_{ij}, s_{ij}^{\text{eff}}$  deviatoric stress  
 $t$  time  
 $\mathbf{t}_1, \mathbf{t}_2$  orthogonal unit tangential vectors  
 $\mathbf{u}, u_f, u_i^f, u_s, u_s^n, u_i^{\text{sub}}, \{u_1, u_2\}$  displacements  
 $\hat{\mathbf{u}}$  half-space free displacement field  
 $\tilde{\mathbf{u}}^j, \tilde{u}$  displacements Green's function  
 $V, V^{(n)}, V_{\text{obs}}^{(n)}$  voltage  
 $v_c$  speed of sound  
 $v_f$  fiber's static absolute permittivity  
 $w$  width  
 $X, x, \{x_1, x_2\}$  cartesian space parametrization  
 $x_{\text{source}}$  AE source location  
 $Z$  softening modulus  
 $\alpha$  thermal expansion coefficient  
 $\Gamma$  film fracture energy  
 $\Delta t_{\text{rt}}$  run-time difference  
 $\boldsymbol{\delta}, \{\delta_1, \delta_2\}, \{\delta_n, \delta_t\}, \{\delta_n, \delta_{t_1}, \delta_{t_2}\}$  crack flank relative displacements

$\delta^e$  elastic part of  $\delta$   
 $\delta^p$  plastic part of  $\delta$   
 $\delta_{eq}$  equivalent crack flank relative displacement  
 $\varepsilon_{ij}$ ,  $\varepsilon_{ij}^{elastic}$ ,  $\varepsilon_{ij}^{creep}$ ,  $\varepsilon_{ij}^{in}$ ,  $\varepsilon_{TGO}^{oxidation}$  strain  
 $\dot{\varepsilon}^{ox}$  one dimensional oxidation strain rate  
 $\dot{\varepsilon}_{creep}^{BC}$ ,  $\dot{\varepsilon}_{creep}^{TBC}$ ,  $\dot{\varepsilon}_{creep}^{TGO}$  one dimensional BC, TBC and TGO creep rates  
 $\varepsilon_{eq}^{creep}$  equivalent creep strain  
 $\varepsilon_f$ ,  $\varepsilon_f^r$ ,  $\varepsilon_{int}$ ,  $\varepsilon_s$ ,  $\varepsilon_s^r$  elongation strain  
 $\eta_j^{(s)}$  set of parameters quantifying the variation of  $\mu_s^*$  with frequency  
 $\theta$  angle describing the direction of tangential traction  
 $\Lambda$  multiplier  
 $\mu$  friction coefficient  
 $\mu_s$ ,  $\mu_s^*$  shear moduli  
 $\nu$ ,  $\nu_1$ ,  $\nu_2$  Poisson's ratios  
 $\xi$ ,  $\xi^{min}$  dimensionless length of delaminated zone  
 $\Pi_\sigma$ ,  $\Pi_\sigma^n$  potential of external forces  
 $\rho$  shape of delaminated zone  
 $\rho_f$ ,  $\rho_s$  mass density  
 $\sigma$ ,  $\sigma_{ij}$ ,  $\sigma_{ij}^b$ ,  $\sigma_{ij}^{eff}$ ,  $\sigma_{ij}^i$ ,  $\sigma_{ij}^p$  stress  
 $\{\sigma, \tau\}$ ,  $\{\sigma, \tau^f\}$ ,  $\{\sigma, \tau_1, \tau_2\}$ ,  $\{\sigma, \tau_1^f, \tau_2^f\}$  normal and tangential traction  
 $\sigma_c$  film fracture stress  
 $\sigma_c(\delta_{eq})$  softening function in tension  
 $\sigma_c^0$  interface critical stress in tension  
 $\sigma_{eq}$  equivalent stress  
 $\sigma_f$ ,  $\sigma_f^r$ ,  $\sigma_s$ ,  $\sigma_s^r$  normal stress  
 $\sigma_0$  external loading  
 $\tilde{\sigma}^j$ ,  $\tilde{\sigma}$  stress Green's function  
 $\tau_c(\delta_{eq})$  softening function in shear  
 $\tau_c^0$  interface critical stress in shear  
 $v$  crack density  
 $\chi$ ,  $\chi_A$ ,  $\chi_B$  mode angle  
 $\psi(\sigma, \tau)$  plastic potential  
 $\omega$  frequency



# Contents

<b>1. Introduction</b>	<b>13</b>
1.1. Thin films — an overview . . . . .	13
1.2. The aim and scope of the monograph . . . . .	16
1.3. Thin films deposition methods . . . . .	19
1.3.1. Physical vapour deposition . . . . .	19
1.3.2. Chemical vapour deposition . . . . .	20
1.3.3. Thermal spray deposition . . . . .	21
1.4. Failure modes in thin films . . . . .	22
1.5. Thermal barrier coating system . . . . .	25
1.5.1. Substrate alloy . . . . .	27
1.5.2. Bond coat . . . . .	28
1.5.3. Thermal barrier coatings . . . . .	30
1.5.4. Degradation of APS TBC systems . . . . .	33
1.5.5. Modelling of TBC systems . . . . .	35
1.6. Human skin . . . . .	38
1.6.1. Structure of human skin . . . . .	38
1.6.2. Mechanical properties of human skin . . . . .	39
1.6.3. Skin imaging . . . . .	41
<b>2. Preliminaries</b>	<b>45</b>
2.1. Fracture mechanics of interface cracks . . . . .	45
2.1.1. General case $\epsilon \neq 0$ . . . . .	47
2.1.2. Special case $\epsilon = 0$ . . . . .	49
2.1.3. Energy release rate . . . . .	50
2.2. Cohesive zone model . . . . .	51
2.2.1. General formulation . . . . .	52
2.2.2. Specification to a slip response . . . . .	56

<b>3. An energy model of segmentation cracking of thin films</b>	<b>59</b>
3.1. Introduction	59
3.2. Problem formulation	60
3.3. Residual stresses	63
3.4. External loading	65
3.4.1. Stage I	67
3.4.2. Stage II	69
3.5. Energy model	71
3.5.1. Failure model based on the total system energy	72
3.5.2. Failure model based on the film/interface sub-system energy	79
3.6. Specification of the fracture energy of a silicon oxide thin coating	80
3.7. The energy model and stress redistribution models	88
3.8. Conclusions	90
<b>4. Modelling of thermal barrier coatings</b>	<b>93</b>
4.1. Introduction	93
4.2. Through-thickness cracking	94
4.2.1. Experimental setup	94
4.2.2. Experimental results	96
4.2.3. Finite element model	99
4.2.4. Mesh dependence	105
4.2.5. Comparison with experimental results	106
4.2.6. Effect of TBC critical energy release rate $G_I$ on segmentation cracking	108
4.3. Delamination	109
4.3.1. The numerical model	110
4.3.2. The time dependent behaviour of CMSX-4	115
4.3.3. Modelling of crack development	116
4.3.4. Stress distribution without microcracks in the unit cell	117
4.3.4.1. The influence of the time-dependent behaviour of CMSX-4	117
4.3.4.2. The effect of cyclic loading	120
4.3.5. Crack development at the TGO/BC interface	126
4.4. Conclusions	131
<b>5. Frictional delamination</b>	<b>135</b>
5.1. Introduction	135
5.2. Problem formulation	136
5.3. Dimensional analysis	140
5.4. Observations - one dimensional slip model	142
5.5. Superposition of solution	145
5.6. Moving boundary $\partial\Omega$	148
5.7. Approximate solution	151
5.8. Results	154
5.8.1. Special case: $\nu = -1$	154

5.8.2. Loading force $P$ versus parameter $l_0$ . . . . .	156
5.8.3. Stress field . . . . .	158
5.8.4. Comparison with finite element results . . . . .	158
5.9. Conclusions . . . . .	161
<b>6. Characterization of thin tissues via surface-wave sensing</b>	<b>165</b>
6.1. Introduction . . . . .	165
6.2. Conceptual sensor setup . . . . .	166
6.3. Point versus integral motion sensing . . . . .	168
6.4. Forward analysis . . . . .	169
6.4.1. Layered tissue model . . . . .	169
6.4.2. Sensing array . . . . .	170
6.4.3. Response of the substrate . . . . .	170
6.4.4. Response of the fiber . . . . .	172
6.4.5. Fiber-substrate interaction . . . . .	174
6.4.6. Solution method . . . . .	174
6.4.7. Computation of output voltages . . . . .	176
6.4.8. Comparison with finite element simulations . . . . .	177
6.4.9. Dominant modes of sensors' deformation . . . . .	177
6.5. Back-analysis . . . . .	182
6.5.1. Observations . . . . .	182
6.5.2. Minimization . . . . .	183
6.6. Numerical results . . . . .	184
6.6.1. Effect of number of sensors . . . . .	185
6.6.2. Effect of frequency sweep . . . . .	185
6.6.3. Experimental noise . . . . .	188
6.7. Conclusions . . . . .	191
<b>7. Summary</b>	<b>193</b>
<b>A. Green's function for a one dimensional elastic strip</b>	<b>199</b>
<b>B. Green's functions for an infinite plate loaded by an in-plane point force</b>	<b>201</b>
<b>C. Parameters used in equations (6.4)</b>	<b>209</b>
<b>Bibliography</b>	<b>211</b>
<b>Extended summary in Polish</b>	<b>229</b>



# Introduction

## 1.1. Thin films — an overview

Thin solid films are used in many types of engineering systems and fulfill a wide variety of functions. For example, in miniature, highly integrated electronic circuits, confinement of electric charge relies largely on interfaces between thin materials with differing electronic properties (Freund and Suresh [69], Lu et al. [128]). The use of surface coatings to protect structural materials in high temperature environments is another thin film technology of enormous commercial significance. In gas turbine engines, for example, thin surface films of materials chosen for their chemical inertness, stability at elevated temperatures and low thermal conductivity are used to increase engine efficiency and to extend significantly the useful lifetimes of the structural materials that they protect (Evans et al. [62, 63]). Multilayered or continuously graded coatings offer the potential for further progress in this effort (Pindera et al. [161, 162]). In the field of biomechanics the mostly encountered thin film is simply the human skin with its highly stratified nature. Mechanical research in that area can be of much help in cancer cells delineation or in production of artificial skin (Białas and Guzina [26], Wagner et al. [209]).

The useful lifetimes of components subjected to friction and wear due to contact can be extended substantially through the use of surface coatings or surface treatments. Among the technologies that rely on the use of thin films in this way are internal combustion engines, artificial hip and knee implants, and computer hard disks for magnetic data storage.

Thin films are integral parts of many micro-electro-mechanical systems designed to serve as sensors or actuators. For example, a piezoelectric thin film deposited on a silicon membrane can be used to detect electronically a deflection of the membrane in response to a pressure applied on its surface or by an acceleration of its supports (Lee et al. [121]). Devices based on thin film technology are used as microphones in hearing aids (Ko et al. [112], Lee and Lee [123]),

monitors of blood pressure during exercise (Kärki et al. [104]), electronically positioned thin films mirrors on flexible supports in optical display systems, and probes for detecting the degree of ripeness of fruits (Taniwaki et al. [189]).

Numerous other technologies rely on thin film behaviour: fiber reinforced polymer sheets are used in structural strengthening techniques (Cottone and Giambanco [50]) or in laminated glass, where two or more glass plies are bonded together by a polymeric interlayer through treatment at high temperature and pressure in autoclave (Ivanov [101], Muralidhar et al. [143]). An immediate observation that follows from the foregoing list is that the principal function of the thin film components in these applications is often not structural. Consequently, load carrying capacity may not be a principal consideration for design or material selection. However, fabrication of thin film configurations typically results in internal stress in the film of a magnitude sufficient to induce mechanical deformation, damage or failure. A tendency for stress-driven failure of a thin film structure can be a disabling barrier to incorporation of that film into a system, even when load carrying capacity is of secondary importance as a functional characteristic. The presence of an internal stress in a thin film structure may also influence the electrical or magnetic properties in functional devices.

A structure of an extent that is small in one direction compared to its extent in the other two directions is termed a thin film. In structural mechanics, such configurations are identified as plates or shells. The difference, though, is that when considering thin films we can not forget the underlying material and its influence upon film's mechanical behaviour. In many situations it is even impossible to perform mechanical experiments on the coating itself, which is a result of its very small thickness. The influence of the substrate in many cases is introduced by the concept of an interface, that is a surface between the film and the substrate with mechanical properties specific to the nature of the two bonded materials. With model of the interface at hand, the next step is to describe the response of thin material in the adequate way. Depending on its behaviour, it can be treated in full fashion as a three dimensional continuum or, as already mentioned, as a two dimensional shell or plate. When loading conditions permit, one dimensional models can also be adopted. In this case one can assume that the film behaves as a beam or, with bending modes excluded, as a stretched or compressed fiber. Apart from the specific mechanical relation for the interface, the film and the substrate can be modelled using any approaches available in mechanics with appropriate choice of constitutive laws for the coating and the substrate.

The qualifier "small", used when describing film thickness, means that the

largest film dimensions are at least twenty times greater than the small dimension. In many cases they are hundreds of times greater. In particular, we talk about a mechanically thin film when the film material either has no intrinsic structural length scales, as in the case of an amorphous film, or the film thickness is much larger than all the characteristic microstructural length scales such as the grain size, dislocation cell size, precipitate or particle spacing, diameter of the dislocation loops, mean free path for dislocation motion, or the magnetic domain wall size. Such structures, typically tens or hundreds of micrometres in thickness, are deposited onto substrates by plasma spray or physical vapour deposition, or layers bonded to substrates through welding, diffusion bonding, explosion cladding, sintering or self-propagating high temperature combustion synthesis. The continuum mechanics approach to be presented for the analysis of stress and fracture in such mechanically thin films applies to a broad range of practical situations.

When the small dimension of the material structure is comparable to the characteristic microstructural size scale, the film is considered to be a microstructurally thin film. Most metallic thin films used in microelectronic devices and magnetic storage media are examples of microstructurally thin films, where the film thickness is substantially greater than atomic or molecular dimensions. Although the film thickness normally includes only a few microstructural units in these cases, the plane of the film has dimensions significantly larger than the characteristic microstructural size scale. The mechanical properties of these films are more strongly influenced by such factors as average grain size, grain shape, grain size distribution, and crystallographic texture than in the case of mechanically thin films. Grain to grain variations in crystallographic orientation as well as crystalline anisotropy of thermal, electrical, magnetic and mechanical properties also have a more pronounced effect on the overall mechanical response of microstructurally thin films. In this case micromechanics is one of the tools allowing for a proper description of system's response.

Atomically thin films constitute layers whose thicknesses are comparable to one or a few atomic layers. An adsorbed monolayer of gas or impurity atoms on a surface is an example of an atomically thin layer. Here the mechanical response of the thin layer is likely to be more influenced by interatomic potentials and surface energy than by macroscopic mechanical properties or by micromechanisms of deformation.

Film stresses can be usually divided into two broad categories. One category is growth stresses, which are those stress distributions present in films following growth on substrates or on adjacent layers. Growth stresses are strongly dependent on the materials involved, as well as on the temperature deposition.

A second category of film stresses represents those arising from changes in the physical environment of the film following its growth. Such externally induced stresses are called extrinsic stresses. In many cases, they arise only when the film is bonded to a substrate, and the clear distinction between the two categories of stresses can at times be difficult to perform.

## 1.2. The aim and scope of the monograph

The subject of the monograph are mechanically thin films, where the qualifier "mechanically thin" should be understood in the sense of the specification presented in the last part of the proceeding Section. It means that neither intrinsic structural length scales will be addressed nor grain or dislocation cell size, precipitate or particle spacing will be taken into account. In all situations the continuum mechanics approach will be applied.

The monograph is devoted to four aspects of mechanics of thin films. Firstly, it concerns the problem of coating degradation due to through thickness cracking. Two specific issues of that phenomenon are addressed, namely a situation when a saturation stage is reached and no more cracks appear in response to substrate stretching. To that end, an energy model is formulated and subsequently validated in case of silicon oxide thin films. Numerical simulation of through thickness cracking of thermal barrier coating (TBC) concerns another aspect of the phenomenon without focus on saturation stage, though. The adopted approach relies on the former works of Camacho and Ortiz [39], Pandolfi et al. [156] and Zhou and Molinari [231, 232]. These authors inserted cohesive elements between typical solid finite elements in order to model cracks propagation in a material. An attempt to predict development of multiple through-thickness cracks following this methodology is presented. Results are compared with experimental data by Majerus [132].

Secondly, the monograph concerns the problem of stress development within thin film structures due to mechanical and thermal loadings. This aspect is particularly important in the case of thermal barrier coatings serving as an insulation layer in gas turbines. Due to severe working conditions (high temperature up to  $1200^{\circ}\text{C}$ , chemical oxidation) the stress state in TBC system is very complex as resulting from creep and relaxation combined with growth of oxide layer. Mechanical modelling adopted in the monograph relies on micro-modelling, where phenomena occurring in a unit cell of TBC system are assumed to be generalized for a whole coating. With the stress state within a TBC unit cell at hand, mechanisms leading to coating spallation and degradation can

be better understood, allowing for formulation of hypothetical failure scenario describing that complex process.

Thin film delamination is a third phenomena addressed in the monograph. An aspect of frictional slip between a coating and a substrate is carefully analysed providing a semi-analytical and, in a particular case, an analytical estimation. In that part of the monograph an attempt is made to depart from the one dimensional strip models (e.g. Białas and Mróz [29, 30], Schreyer and Pfeffer [174], Timm et al. [198]) toward more complex situation of a coating treated as a two dimensional continuum. In this way, effect of material contraction due to Poisson's ratio can be captured.

Fourthly, the monograph aims at mechanical characterization of thin films using non-invasive methods. This is an important subject in itself, since because of the production processes and small thickness of many coatings, it is often almost impossible to experimentally examine stand-alone samples of thin films. Surface wave sensing method combined with usage of piezoelectric sensors can be utilized to estimate complex elastic moduli of stratified thin film structure. A conceptual design of such an array of piezoelectric sensors is a part of the monograph. In order to validate the method, elastic moduli of human skin will be identified.

The novel aspects of the reported research are:

- application of energy model of segmentation cracking to description of saturation stage of multiple cracks within silicon oxide coating on polymer substrates;
- description of the effect of residual stresses during segmentation cracking;
- quantitative analysis of thin coating through-thickness cracking, providing theoretical explanation to the every day engineering experience that multiple cracking in the film can reduce the magnitude of energy release rate for the interface between the coating and the substrate (in other words: through-thickness cracking can be beneficial for film's life-time);
- analysis of the significance of loading step during finite element modelling of multiple through-thickness cracking, practical suggestions allowing to overcome convergence problems during similar analyses;
- analysis of key aspects governing stress development within thermal barrier coatings and subsequent description of mechanisms leading to coating spallation and delamination;
- formulation of semi-analytical methodology allowing for description of two dimensional frictional slip at coating/substrate interface (in contrast to the already known in literature one dimensional strip models);

- derivation of simple analytical formulas describing process of delamination of a rigid film from a rigid substrate;
- formulation of conceptual piezoelectric sensor setup for measurements of complex elastic moduli of stratified thin film structure during non-destructive in vivo experiments;
- suggestions for the effective applications of the sensors array.

The monograph consists of seven chapters. At the beginning of the introductory Chapter 1 thin films deposition methods are described. Subsequently, failure modes observed in coatings are analysed. Since the developed modelling tools will be applied in particular to thermal barrier coatings and human skin, two final sections of the chapter introduce the reader into mechanical and material properties of both TBC systems and human skin.

Mathematical preliminaries is a subject of Chapter 2 of the monograph. Basics of elastic fracture mechanics of interfacial cracks are briefly presented and cohesive zone model previously formulated by Mróz and Białas [142] and Białas and Mróz [28] is introduced. This model is a basis for subsequent modelling of various types of cracks within coating systems.

Chapters 3–6 report the novel part of the research and, except for the experiment described in the first part of Chapter 4 (bending tests combined with acoustic emission technique, Majerus [132]), present an original contribution of the Author.

In Chapter 3 an energy model of segmentation cracking with application to silicon oxide film is presented. Chapter 4 reports finite element simulation of stress development, delamination and through-thickness cracking in TBC systems. In Chapter 5 two dimensional model of frictional slip is discussed, together with semi-analytical procedure providing delamination estimation. Chapter 6 presents a conceptual setup of piezoelectric sensors used for mechanical characterization of human skin. The final Chapter 7 concludes the monograph and recapitulates the main achievements of the reported research.

Both unpublished and published results of the Author are presented in the monograph. Chapter 3, concerned with modelling of segmentation cracking, is an outcome of joint work with Professor Zenon Mróz and has been partially reported by Białas and Mróz [31]. The analysis of through thickness cracking in TBC system was possible due to cooperation with Patric Majerus and Roland Herzog [27]. Development of conceptual piezoelectric sensor array was a joint work with Professor Bojan B. Guzina [26]. Some crucial aspects of description of thermal barrier coating delamination and thin film frictional slip were in brief presented in Białas [24] and Białas [25], respectively.

The research related to thermal barrier coatings was a part of two projects in which the Author was involved (TBC MODELLING and TBC FAILURE). They both included cooperation with Research Center Jülich (FZJ) in Germany and were financed by the European Commission. The research related to mechanical characterization of human skin was performed at the University of Minnesota in USA. Author would like to gratefully acknowledge the possibility to work and exchange ideas with Professor Florian Schubert and Professor Tilmann Beck from Research Center Jülich and with Professor Bojan B. Guzina from University of Minnesota.

### 1.3. Thin films deposition methods

Physical vapour deposition (PVD) and chemical vapour deposition (CVD) are the most common methods for transferring material atom by atom from one or more sources to the growth surface of a film being deposited onto a substrate. Vapour deposition describes any process in which a solid immersed in a vapour becomes larger in mass due to transfer of material from the vapour onto the solid surface. The deposition is normally carried out in a vacuum chamber to enable control of the vapour composition. If the vapour is created by physical means without a chemical reaction, the process is classified as PVD. If the material deposited is the product of a chemical reaction, the process is classified as CVD.

Another general method of film deposition is thermal spray process, referring broadly to a range of deposition conditions wherein a stream of molten particles impinges onto a growth surface.

Many variations of these basic deposition methods have been developed in efforts to balance advantages and disadvantages of various strategies based on the requirements of film purity, structural quality, the rate of growth, temperature constraints and other factors.

#### 1.3.1. Physical vapour deposition

Physical vapour deposition is a technique whereby physical processes, such as evaporation, sublimation or ionic impingement on a target, facilitate the transfer of atoms from a solid or a molten source onto a substrate. Evaporation and sputtering are the two most widely used PVD methods for depositing films (Mahan [130], Ohring [149]).

Figure 1.1 illustrates the basic features of the deposition. In the process, thermal energy is supplied to a source from which atoms are evaporated for de-

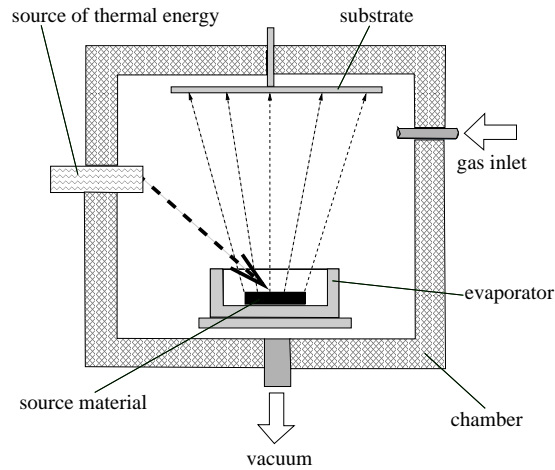


Figure 1.1. Physical vapour deposition.

position onto a substrate. The vapour source configuration is intended to concentrate heat near the source material and to avoid heating the surroundings. Heating of the source material can be accomplished by several methods. The simplest is resistance heating of a wire or stripe of refractory metal, to which the material to be evaporated is attached. Larger volumes of source material can be heated in crucibles of refractory metals, oxides or carbon by resistance heating, high frequency induction heating, or electron beam evaporation (EB PVD). The evaporated atoms travel through reduced background pressure in the evaporation chamber and condense on the growth surface.

### 1.3.2. Chemical vapour deposition

Chemical vapour deposition is a versatile deposition technique that provides a means of growing thin films of elemental and compound semiconductors, metal alloys and amorphous or crystalline compounds of different stoichiometry. The basic principle underlying this method is a chemical reaction between a volatile compound of the material, from which the film is to be made, with other suitable gases in order to facilitate the atomic deposition of a nonvolatile solid film on a substrate (Dobkin and Zuraw [56]).

In CVD, as in PVD, vapour supersaturation affects the nucleation rate of the film, whereas substrate temperature influences the rate of film growth. These two factors together influence the extent of epitaxy, grain size, grain shape and texture. Low gas supersaturation and high substrate temperatures promote

the growth of single crystal films on substrates. High gas supersaturation and low substrate temperatures result in the growth of less coherent, and possibly amorphous, films. Low pressure CVD (LP CVD), plasma enhanced CVD (PE CVD), laser enhanced CVD (LE CVD) and metal-organic CVD (MO CVD) are all variants of the CVD process used in many situations to achieve particular objectives (Dobkin and Zuraw [56]).

### 1.3.3. Thermal spray deposition

The thermal spray process of thin film fabrication refers broadly to a range of deposition conditions wherein a stream of molten particles impinges onto a growth surface. In this process, illustrated schematically in Figure 1.2, a thermal plasma arc or a combustion flame is used to melt and accelerate particles of metals, ceramics, polymers or their composites to high velocities in a stream directed toward the substrate (Herman et al. [91]). The sudden deceleration of a particle upon impact at the growth surface leads to lateral spreading and rapid solidification of the particle, forming a splat in a very short time. The characteristics of the splat are determined by its size, chemistry, velocity, degree of melting and angle of impact of the impinging droplets, and by the temperature, composition and roughness of the substrate surface. Successive impingement of the droplets leads to the formation of a lamellar structure in the deposit. The oxidation of particles during thermal spray of metals also results in pores and contaminants along the splat boundaries. Quench stresses and thermal mismatch stresses in the deposit are partially relieved by the formation of microcracks or pores along the inter-splat boundaries and by plastic yielding or creep of the deposited material.

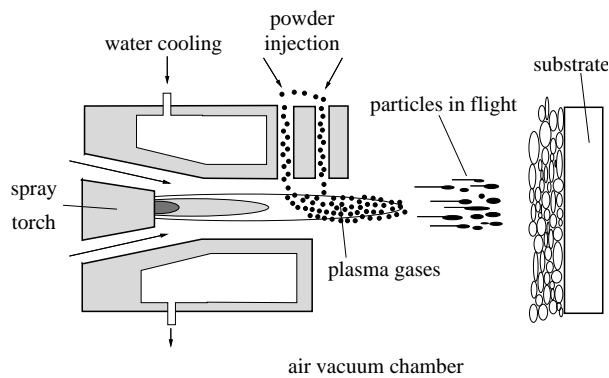


Figure 1.2. Illustration of thermal spraying process.

Among several types of thermal spray processes the air plasma spray (APS) technique offers a straightforward and cost-effective means to deposit metals or ceramics, which are tens to hundreds of micrometres in thickness, onto a variety of substrates in applications involving thermal-barrier or insulator coatings (Beck et al. [21]). Typical plasma-spray deposits are porous, with only 85–90 % of theoretical density. For applications requiring higher density coatings with a strong adhesion to the substrate, low-pressure plasma spray is employed, where spraying is done in an inert-gas container operating at a reduced pressure. Vacuum plasma spray is another thermal spray process which is used to improve purity of the deposited material and to reduce porosity and defect content, albeit at a higher cost than air plasma spray.

#### 1.4. Failure modes in thin films

Hutchinson and Suo [100] gave a concise overview of various fracture patterns in pre-tensioned coatings, together with a discussion of fracture governing parameters. All typical failure modes are depicted in Figure 1.3. One failure type is surface cracking. In this case cracks can nucleate from a flaw but the loading is not high enough to cause a channelling through the film and a subsequent merging of single cracks. Thus, as a result, unconnected slits remain stable and can be tolerable for many applications. For higher stresses within the coating one observes a channelling process with a network of cracks surrounding islands of the intact film (Parker, [159]). This is an unstable situation, where a coating crack is arrested only when reaching an edge or another crack.

Both terms "isolated surface crack" and "channels" refer to cracks qualified with respect to their length measured along film's outer surface. When we need to discuss their extent along film's thickness, one encounters two distinct situations. Firstly, cracks can have their depth substantially smaller than film's thickness, forming a shallow scratch. More often observed is the situation when fracture continues to the film/substrate interface and we say of through-thickness cracking in this case.

Upon reaching coating/substrate interface several failure mechanisms can follow. Cracks can remain arrested at the film/substrate interface, meaning they cease to propagate. Another scenario is that cracks enter the substrate material and stabilize at a certain depth (Chi and Chung [46], Chung and Pon [47], Zhang and Zhao [229]). They can also deviate and propagate along the coating/substrate interface, resulting in a subsequent delamination of the protective film (Erdem Alaca et al. [7], Kokini and Takeuchi [113]). Substrate

spalling is another intriguing phenomenon: the crack enters the substrate and selects a path at a certain depth parallel to the interface. This type of failure is common for brittle substrates (Thouless et al. [194], Thouless and Evans[193]).

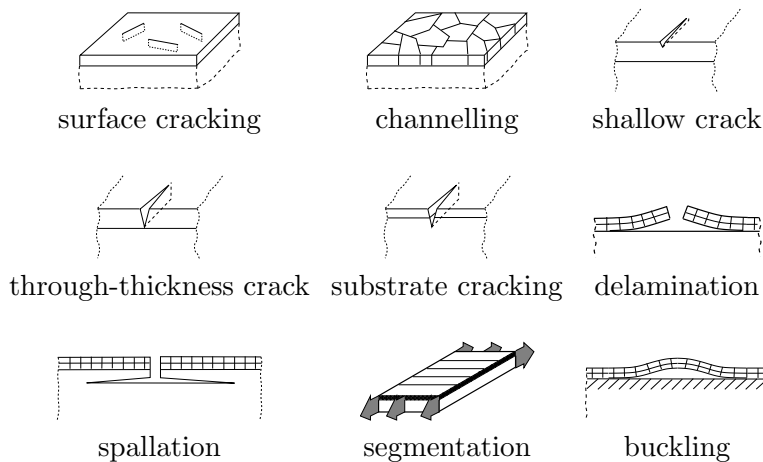


Figure 1.3. Commonly observed failure patterns in thin films.

The situation when a crack develops along the interface between the film and the substrate is particularly interesting. Due to the production process in most situations the interface is the weakest region of the whole film/substrate structure, having mechanical properties different from those of the bonded constituents. Thus, the problem of delamination is so crucial for layered materials.

In many practical applications cracks remain arrested upon reaching coating/substrate interface. It has been observed that uniformly spaced longitudinal cracks form perpendicularly to the direction of applied axial strain (Agrawal and Raj [4, 5], Kim and Nairn [109, 110], Schulze and Erdogan [177]). In such a case new cracks may appear during the course of loading. Crack density initially increases and then stabilizes at a constant value, unaffected by the further loading. This phenomenon is known as a segmentation or multiple cracking of thin films. Many authors analysed the segmentation fracture of thin coatings using energy methods (Hsueh [93], Hsueh and Yanaka [96], Kim and Nairn [109], Nairn and Sung-Ryong [145], Thouless [192], Thouless et al. [195], Yanaka et al. [224, 223], Zhang and Zhao [229]) and considered linear elastic systems without taking into account nonlinear effects at the film/substrate interface and subsequent decohesion of the coating. In brief, the next coating crack was assumed to form when the total energy released by the coating crack exceeded a critical value denoted as the in situ fracture toughness of the coating. Kim and Nairn

[109], Nairn [144] and Nairn and Sung-Ryong [145] derived the energy release rate in a close form using variational mechanics and minimization of complementary energy. Zhang and Zhao [229] analysed depth and spacing of cracks in a residually stressed thin film bonded to a brittle substrate, using the minimum energy theorem on the basis, that the film has the same mechanical properties as the substrate. Yanaka et al. [224, 223] modified a shear lag analysis considering residual strains. They used both stress and energy criteria to analyse crack spacing.

Nonlinear effects at the interface between the coating and the substrate were taken into account by Hu and Evans [97]. They assumed a constant value of shear stress at the interface and performed fracture mechanics analysis of segmentation cracking. Similar elasto-perfectly plastic model for the interface was used by Timm et al. [198], who predicted thermal crack spacing within asphalt pavements. They proposed also a calibration method for the interfacial modulus of elasticity using a benchmark model of an elastic half-space loaded by shear tractions following a bi-linear distribution. Białas and Mróz [29, 30] analysed segmentation cracking of an elastic plate subjected to a temperature loading, assuming softening and friction constitutive relations for the cohesive zone at the interface. In order to measure the ultimate interfacial shear strength Agrawal and Raj [4, 5], Chen et al. [44] and Shieu et al. [184] assumed different stress distributions at the interface. Thus, without assuming a priori any constitutive relation for this region, they were able to capture elastic deformation, plastic yielding and a softening behaviour associated with segmentation cracking and with subsequent decohesion of the film.

In many film-substrate systems, the film is in a state of biaxial compression. Residual compression has been observed in thin films that have been sputtered or vapour deposited and it can arise from thermal expansion misfit. The failure entails the film first buckling away from the substrate in some small regions where adhesion is poor. Buckling then loads the edge of the interface crack between the film and the substrate, causing it to spread. The failure phenomenon couples buckling and interfacial crack propagation. Thin films can buckle into intriguing periodic mode patterns (see for example Breid and Crosby [33], Bowden et al. [32] or Huck et al. [98]), creating one dimensional, square checkerboard, hexagonal, triangular and herringbone modes. In the range of moderate to large overstress, Chen and Hutchinson [45] showed that among one-dimensional (straight-sided), square checkerboard and herringbone modes, the herringbone mode has the lowest energy in the buckled state, while the one-dimensional mode has the greatest. Audoly and Boudaoud [12] examined further details of the post-buckling behaviour of these modes, includ-

ing the range, in which the one-dimensional mode is stable and its transition to the herringbone mode, under stress states which are not equi-biaxial. They also considered the hexagonal mode and showed that the square mode has the lowest energy in the range of small overstress. In companion papers, Audoly and Boudaoud [13, 14] used asymptotic methods to explore aspects of behaviour expected in the range of very large overstress, with emphasis on the herringbone mode.

Despite their practical significance, pre-buckling processes are difficult to quantify. Here are some examples: a contaminated substrate may lead to large unbonded areas after a film is grown; non-planar interfaces can promote buckling (Hutchinson et al. [99]); interface voids are sometimes observed, leading to buckling; and a compressed elastic film can buckle while still bonded to the substrate, provided the substrate has very low elastic stiffness (Huck et al. [98]) or creeps (Sridhar et al. [185]). A thermally grown oxide on a plastically deformable substrate can buckle, when cyclic temperature changes and continued oxidation inside the film repeatedly bring the substrate into the yield condition (He et al. [87]).

Several post-buckling behaviours have been studied (Gioia and Ortiz [75]). Unlike a debond crack initiated from a film edge, a debond crack initiated from a buckled film does have an opening component at the crack front. However, when the crack enlarges, the opening component reduces, the crack approaches the pure sliding mode, and the situation becomes indistinguishable from a debond crack initiated from the film edge. Consequently, a debond buckle under the plane-strain conditions will arrest by friction. Similarly, a circular (or any equiaxed) debond buckle cannot grow indefinitely (Hutchinson and Suo [100]).

## 1.5. Thermal barrier coating system

For the last three decades the use of corrosion protective and thermally insulating coatings on structural materials for combustion chambers and front stage blading (blades and vanes) has been the pre-condition for increasing combustion temperatures in gas turbines. It allows for an improved thermal efficiency and, thus, makes a primary contribution to the conservation of energy resources and to the limitation of CO<sub>2</sub> and other greenhouse gas emissions. Mostly for this reason, the use of thermal barrier coated Ni-based super-alloys for the thermally loaded components helps improve the gas turbine efficiency.

The potential of new generation single crystal super-alloys used for blade production is basically given by their superior creep and fatigue resistance up

to 1000°C (Fleury and Schubert [66], Schubert et al. [175]). The increase of fuel gas temperature in recent years has led to temperatures at the material surface reaching the values up to 1250°C and a further temperature increase is envisaged. These thermal loading conditions can only be handled by a combination of modern cooling methods and protective coatings on top of the blades. In film cooling, the cooling air bled from the compressor is discharged through holes in the turbine blade wall or the end wall. The coolant injected from holes forms a thin thermal insulation layer on the blade surface to protect the blade from being overheated by the hot gas flow from the combustor. Typically, the holes are in diameter not bigger than 0.5 mm and are either normal to the surface or inclined at an angle of 15–30° (Mio and Wu [138], Thoe et al. [191], Voisey and Clyne [207]).

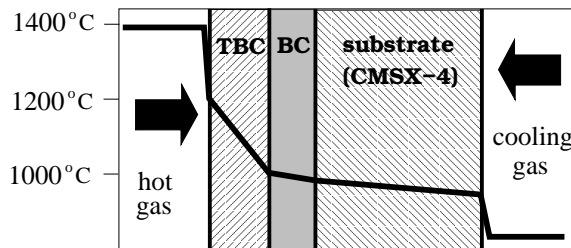


Figure 1.4. Qualitative temperature distribution across the TBC system.

Another technology allowing for an increase in turbines efficiency are high temperature protective coatings. Current protective coatings are two-layer systems, with a metallic, corrosion protective bond coat (BC, e.g. MCrAlY or PtAl) on the super-alloy, and a ceramic thermal barrier coating (TBC, mostly Yttria stabilized ZrO<sub>2</sub>) on top and in contact with the hot gas (Majerus [132]). Ceramic thermal barrier coatings are used on combustors, vanes and blades. The thermal barrier coating having typical thickness ranging from 50 to 300 μm, provides a temperature drop of up to 200°C due to its low thermal conductivity, which is enhanced further by the intentionally porous microstructure. Figure 1.4 demonstrates the reduction of temperature achieved by thermal isolation through TBC and inner cooling. The potential for a temperature reduction by TBC application, however, has not been fully exploited so far because, in the case of failure, the internal and external cooling air must be sufficient to keep the temperature in the structural material below the point at which failure occurs. To use the high potential of TBCs, the different aspects of exposure conditions and failure mechanisms must be understood and integrated

into degradation modelling and lifetime prediction.

A major weakness of TBC systems is the interface between the metallic bond coat and the ceramic TBC. At this interface an in-service degradation is observed, often leading to a macroscopic spallation of the ceramic layer (Miller and Lowell [140]). The interface regions undergo high stresses due to the mismatch of thermal expansion between BC and TBC. Additionally, growth stresses due to the development of thermally grown oxide (TGO) at the interface between TGO and BC, and stresses due to interface roughness, are superimposed. Stress relaxation leads generally to reduced stress levels at high temperature, but can give rise to enhanced stress accumulation after thermal cycling, resulting in early crack initiation at the bond coat/alumina interface and spallation failure afterwards (Bednarz [22], Evans et al. [63]).

### 1.5.1. Substrate alloy

In order to better understand the relevant failure mechanisms and to establish reliable models predicting the lifetime of the coated layers, the choice of the substrate material is certainly the least crucial. This does not mean, however, that the substrate influence can be neglected. Especially thermal expansion, Young's modulus and thermal conductivity have to be considered when simulating life cycles. Apart from that, time dependant deformation, fatigue and fracture mechanical behaviour may in some cases affect the damage evolution of the coatings. With a focus on TBC coated turbine blades, most of the running investigations use a single crystal cast super-alloy as the substrate material.

Table 1.1. Chemical composition of CMSX-4 in wt. % (after Majerus [132]).

Ni	Co	Cr	Al	Ti	Mo	Hf	W	Ta	Re	C
60	9.7	6.5	5.6	1.04	0.60	0.11	6.4	6.5	2.9	0.001

CMSX-4 is a promising single crystal Ni-base candidate for the highly stressed blades and vanes of a heavy stationary gas turbine. The excellent creep properties of this super-alloy are derived directly from its microstructure, which consists of high volume fraction of coherent, cuboidal  $\gamma'$ -precipitates in a  $\gamma$ -matrix. Table 1.1 presents chemical composition of CMSX-4. In the initial state CMSX-4 contains a high volume fraction of approximately 70–75 % regular cubic  $\gamma'$  particles oriented along the crystallographic  $\langle 001 \rangle$  direction. Optical microscopy confirms the regular distribution with approximately 5 cubic  $\gamma'$  precipitates per square micro metre. The particle mean size is about 0.5  $\mu\text{m}$  and the channels are approximately of 50 nm in width, see Figure 1.5.

It has been reported that Ni, Al, Ti and Ta are to be mainly found in  $\gamma'$ , whereas Co and Cr are observed in the  $\gamma$  phase. Element W is approximately equally distributed (Majerus [132]).

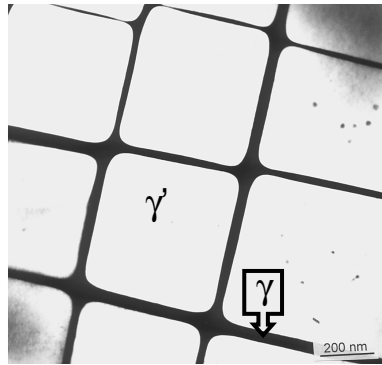


Figure 1.5. Super-alloy CMSX-4 in the initial state,  $\langle 100 \rangle$  plane. After Majerus [131].

Time dependant deformation at high temperature (above  $850^{\circ}\text{C}$ ) is accompanied with a change in morphology of the  $\gamma'$  particles. They coalesce to rafts and the visco-plastic response of the super-alloy is continuously modified. To describe the phenomena, Schubert et al. [175] apply a microstructure dependant, orthotropic Hill potential, whose anisotropy coefficients are connected to the edge length of the of  $\gamma'$  particles.

### 1.5.2. Bond coat

The bond coat (BC) plays a significant role in providing a good adhesion between thermal barrier coatings and the substrate, compensation of the thermal expansion misfit between the materials and a protection for the substrate alloy from oxidation and hot corrosion. The presently applied bond coats have a typical composition MCrAlY, where M is either Ni or Co. The main element contents are in the range of 8–12 wt. % for Al, 15–22 wt. % for Cr, 45–50 wt. % for Ni and 10–30 wt. % for Co, whereas Y concentration is in the order of 0.2–0.5 wt. %.

Bond coats are frequently produced using vacuum or low pressure plasma spraying, which allows more dense and more oxide free coatings than air plasma spraying. The thickness of bond coat layers is typically between 50 and 300  $\mu\text{m}$ . The production process of MCrAlY bond coats provides a rough surface for mechanical bonding of the ceramic top coat and for minimizing the effect of thermal expansion mismatch between the substrate and the coating. The thermal

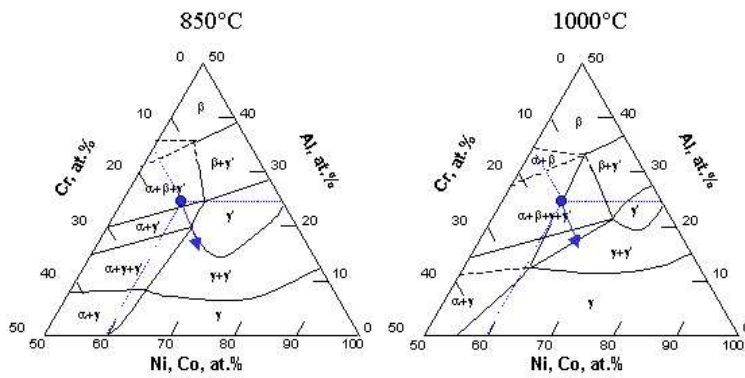


Figure 1.6. Ni-Cr-Al tertiary phase diagrams for 850<sup>0</sup> C and 1000<sup>0</sup> C. After Majerus [131].

expansion coefficient for bond coat is typically in the range of  $14\text{--}16 \times 10^{-6}/^{\circ}\text{C}$  (Trunova et al. [201]), similar to the superalloy. A typical surface roughness in technical measure is  $R_a=6\text{--}7 \mu\text{m}$  (Bialas et al. [27]).

The microstructure and phase composition of NiCoCrAlY bond coats depend strongly on temperature, as shown in Figure 1.6. According to the ternary phase diagram of Ni-Cr-Al at 850<sup>0</sup>C, three phases may occur (Gudmundsson and Jacobson [79]):

- the body-centred  $\alpha$ -Cr phase;
- the ordered face-centred cubic  $\beta$ -NiAl phase;
- the face-centred cubic  $\gamma$ -Ni phase.

Additionally, at 1000<sup>0</sup>C, the intermetallic  $\gamma'$ -Ni<sub>3</sub>Al phase may be present. Figure 1.7 presents a typical microstructure of the bond coat in the as received state.

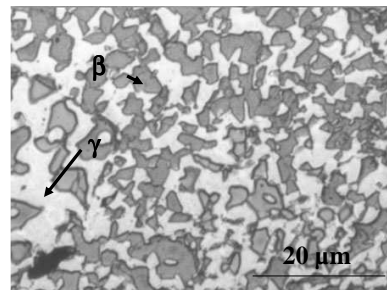


Figure 1.7. Microstructure of the bond coat, as received state. After Majerus [131].

The creep behaviour for MCrAlY coatings is observed in a temperature

range between 600°C and 1050°C. It increases sharply with temperature increase. The high creep rates up to  $10^{-3} \text{ s}^{-1}$  are observed already at 850°C for stress level less than 100 MPa, which can lead to fast relaxation (Brindley and Whittenberger [34]).

Under typical conditions in gas turbines (temperatures around 1200°C, exposure to exhaust gases containing reactive elements) the microstructure of the MCrAlY bond coat does not remain stable. Favoured by facile oxygen diffusion through the porous TBC, a continuous, slow growing oxide scale is formed at the bond coat/TBC interface. The main component of this thermally grown oxide (TGO) is  $\text{Al}_2\text{O}_3$ . The aluminium oxide has several different crystal structures, including  $\gamma$ -,  $\delta$ -,  $\sigma$ - and  $\alpha$ - $\text{Al}_2\text{O}_3$ . It should be mentioned that not only one  $\text{Al}_2\text{O}_3$  modification grows, but we have simultaneous nucleation and transformation sequences, leading to local expansion and shrinkage phenomena.

During the formation of alumina scales, the aluminium and oxygen diffusion through the scale determines the oxide growth. As a result, gradients in metal activity and oxygen partial pressure are established across the scale. The scale thickness is generally roughly proportional to the square root of exposure time  $d^{\text{ox}} = k_p \sqrt{t}$  (Wagner [208]), where  $d^{\text{ox}}$  is the thickness,  $t$  time and  $k_p$  parabolic rate constant. The oxidation kinetics of MCrAlY alloys is significantly affected by the presence of minor additions such as Y, Zr, or trace elements like Si, Ti. They improve scale adherence, decrease growth rate, and enhance selective oxidation in the yttria-containing alloys (Quadakkers et al. [165]). The mechanisms responsible for the beneficial effects of Re are not clear and there are still controversial ideas on the proposed explanations. It has been also reported that the amount and distribution of Re has a significant effect on the performance of MCrAlY coatings (Anton [11], Clemens et al. [48]).

### 1.5.3. Thermal barrier coatings

With regard to the described application, a material used for thermal barrier coating should possess:

- low thermal conductivity;
- high temperature resistance;
- high melting point;
- adapted thermal expansion coefficient;
- chemical stability;
- corrosion and oxidation resistance;
- wear resistance;

- high thermal shock resistance.

Up to now the most promising candidate seems to be zirconia ( $\text{ZrO}_2$ ). The thermal conductivity of dense sintered  $\text{ZrO}_2$  is approximately  $2 \text{ W/mK}$  and can be reduced below  $0.5 \text{ W/mK}$  with increasing the internal porosity. The melting point at normal pressure is  $2680^\circ\text{C}$ . Zirconia's thermal expansion coefficient having values  $9\text{--}11 \times 10^{-6}/\text{K}$  (Guo et al. [80], Schwingel et al. [178]) is close to that of the used substrate alloy. Furthermore, it is chemical stable and corrosion and oxidation resistant, as are most of oxide ceramics.

Pure  $\text{ZrO}_2$  undergoes three reversible phase transformations after solidification and cooling down to room temperature. The cubic phase transforms at  $2370^\circ\text{C}$  into a tetragonal crystallographic structure, which changes into monoclinic at  $1170^\circ\text{C}$ . The tetragonal to monoclinic phase transformation, occurring at typical service temperature for TBC's, is accompanied by a 4 % volume expansion. To avoid this transformation, supplementary oxides are added to extend the area of cubic or tetragonal phase of  $\text{ZrO}_2$  and to suppress the tetragonal to monoclinic phase transformation partially (we obtain Partially Stabilized Zirconia, PSZ) or completely (Fully Stabilized Zirconia, FSZ).

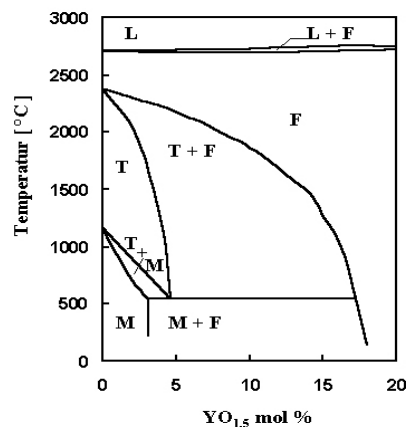


Figure 1.8. Phase diagram of the  $\text{ZrO}_2\text{-Y}_2\text{O}_3$  system (L – liquid; F – cubic phase; T – tetragonal phase; M – monoclinic phase). After Majerus [131].

$\text{ZrO}_2\text{-Y}_2\text{O}_3$  systems are typically used as TBC's for gas turbine applications. At room temperature the microstructure consists of mainly cubic and tetragonal phases with small amounts of monoclinic phase, see Figure 1.8. Although the use of FSZ to avoid the monoclinic to tetragonal phase transformation seems to be advantageous, it has been shown that PSZ exhibits a higher thermal shock resistance. As a good compromise between phase stability and thermal shock

resistance  $\text{ZrO}_2$  with 6–8-wt. %  $\text{Y}_2\text{O}_3$  proved to successfully fulfil the mentioned requirements.

Generally, two processes are used to apply thermal barrier coatings: air plasma spraying (APS) and electron beam physical vapour deposition (EB PVD). The typical respective microstructures are shown in Figure 1.9. The plasma-sprayed ceramic coating is built up by the successive impacts of semi-molten powder particles (splats) on a substrate. The structure and porosity of the resulting TBC depends mostly on particle velocity and temperature, which are controlled by spray parameters such as spraying distance and plasma power. For crack network formation, substrate and coating temperatures during TBC deposition are of the great importance. During EB PVD processing, a high-energy electron beam melts and evaporates a ceramic source ingot in a vacuum chamber. The deposition conditions are designed to create a columnar grain structure with multiscale porosity that provides a good strain tolerance. The microstructure is mainly affected by such deposition parameters as substrate temperature, surface roughness, rotation rate of the component, and vapour flux from the evaporator (Rigney et al. [171]).

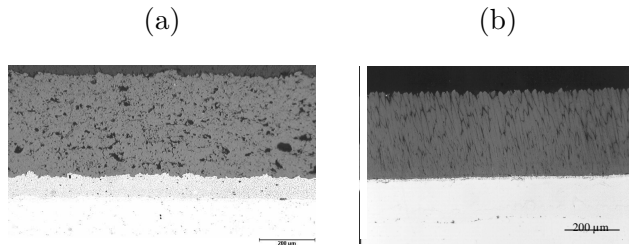


Figure 1.9. Typical microstructure of the TBC: (a) APS, (b) EB PVD. After Majerus [131].

Beside a high strain tolerance, the aerodynamically favourable smooth surface and a higher wear resistance makes the EB PVD coating more advantages than APS. On the other hand, however, high investment costs and the low deposition rates, both increasing the total production costs of the coating, are disadvantageous. The higher thermal conductivity of EB PVD coatings results from the different texture of the porosity. For EB PVD the value of thermal conductivity reaches 1.65 W/mK, whereas for APS we have 0.75 W/mK. The thermal conductivity is almost constant over temperature range up to 1500°C, as it depends mainly on the texture of porosity. Comparing both coating technologies, in modern gas turbines APS coatings are applied at parts of the burning chamber and vanes, while the rotating blades exposed to the highest stresses are mainly coated by EB PVD.

It seems that APS will become more promising in the future, as recent research demonstrated higher lifetimes for APS components under cyclic oxidation experiments (Majerus [131]). This premise leads to an intensive research on APS systems. It was found that the capability to resist failure is based on the quasi visco-plastic deformation behaviour of the APS coating.

#### 1.5.4. Degradation of APS TBC systems

The degradation processes in APS TBCs under service conditions depend strongly on the material constituents, as well as on the particular loading profile. The major difference between laboratory loading profile of TBCs and that observed in stationary gas turbines is the thermal cycle characteristic — thermal cycles of stationary gas turbines last from several hours for peak-load operation up to times of the order of a year in base-load operation. In addition to the high temperatures, the blades are also subjected to mechanical strains. Finally, fatigue cycles occur from each turbine start-up and shutdown, as the load changes from zero to maximum and back to zero. Thus, turbine components experience thermo-mechanical loadings, which lead in most cases to the ceramic top coat spallation near the TBC/bond coat interface (Evans et al. [63], Wright and Evans [215], Haynes et al. [86], Tzimas et al. [202]).

The complex process of degradation is affected by (Trunova [200]):

- growth of the TGO and oxidation-related processes at the interface;
- thermal expansion mismatch strains and stresses at the metal/ceramic interface;
- diffusion of elements from the base material and bond coat to the interface;
- cyclic plastic and time dependent deformation, as well as stress relaxation;
- temperature gradient across the TBC;
- transient factors caused by high heating and cooling rate.

In general, laboratory tests with TBC coated specimen are designed to follow two different approaches (Majerus [132], Trunova [200]). They can focus on only one specific load component, including either high temperature exposure, or thermal cycling, or mechanical cycling, or thermal gradient. In this framework, it is attempted to examine only one aspect of failure development. A typical example for this kind of testing is isothermal oxidation of TBC-coated cylindrical specimen. On the other hand, laboratory tests try to mimic as close

as possible the loading conditions of blades in gas turbines and combine the previously mentioned load components. A typical example of this approach is thermo-mechanical fatigue combined with dwell time at high temperature, resulting in the oxidation process.

For isothermal exposure de Masi et al. [52] has reported that the fracture progresses primarily along the TGO/bond coat interface with small branching into the TGO. This behaviour has been described by Miller and Lowell [140] and explained as fracture initiating at defects, such as transient oxides or Re-rich internal oxidation, but then propagating along the interface to release all of the elastic energy stored in the TGO.

Under thermal cycling operation, TBC systems often fail by crack initiation and propagation close to the bond coat/top coat interface. This failure is attributed to stresses arising from TGO formation on the rough bond coat surface as well as thermal expansion mismatch (Trunova [200]). As expected, the actual stress distribution is rather complex due to the fact that many factors contribute to the failure of TBC systems.

Figure 1.10 presents pictures of typical microcracks formed in the vicinity of metal/ceramic interface after cyclic oxidation. In general, it is agreed (Evans et al. [63]) that spallation occurs through the eventual linkage of microcracks rather than the rapid propagation of a single crack. The description of the entire process requires a model of local failure on a microscopic level.

Although delamination and spallation is the main mode of coating failure, process of segmentation cracking of TBC's is also addressed in the literature. The reason is that in laboratory conditions segmentation cracking can be controlled or easily observed and, as a result, it allows to gain more information about the failure process or material parameters associated with thermal barrier coating. Schmit et al. [173] performed creep tests under constant tensile stress on specimens coated with an air plasma sprayed thermal barrier coating. The TBC adapted to the deformation by forming cracks perpendicular to the surface. These cracks started mainly at the BC/TBC interface and grew up to the free surface. The probability of segmentation cracking increased with increasing creep rate, TBC thickness and amount of pores between the sprayed layers. Döpfer et al. [57] performed strain controlled tensile tests on specimens with APS and EB PVD coatings. The EB PVD coatings resisted a strain of 25 %, without showing any delamination. Only a dense network of cracks perpendicular to the tensile direction could be observed. The APS coating split into segments at the strain around 3 %, but no delamination was observed during subsequent stretching (Zhou et al. [233]). During four point bending tests with the APS TBC under tensile loading, it was observed that segmen-

tation cracks formed usually with a constant spacing equal to the doubled value of TBC thickness (Andritschky et al. [10]). Due to increased loading, the cracks deflected at the BC/TBC interface leading to delamination of the protective layer (Zhou et al. [233]). Four point bending tests with the coating under compression revealed delamination cracks at the BC/TBC interface at lower strain values after pre-oxidation, when compared to the non-oxidized specimens (Moriya et al. [141]).

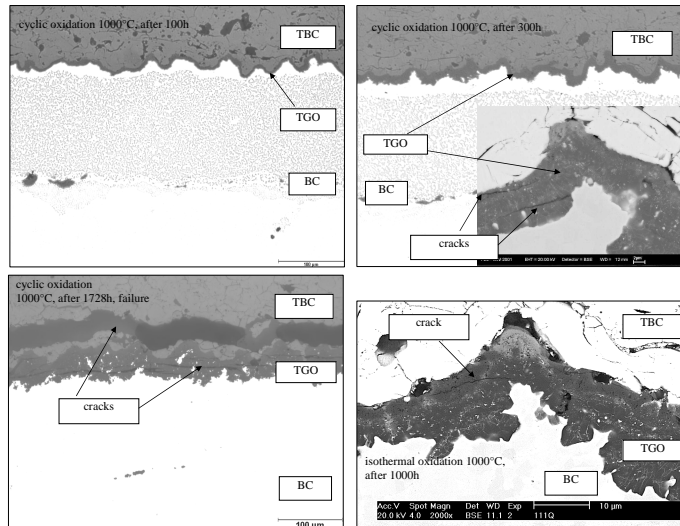


Figure 1.10. Cross section in the vicinity of the metal/ceramic interface after cyclic oxidation. After Majerus [131].

Problematic in all the investigations is the precise detection of a critical strain value at which the TBC starts to undergo a process of damage localization and formation of macroscopic cracks. Indeed, long before appearance of visible cracks, the TBC undergoes a phase of macroscopically homogenous quasi-plastic deformation, occurring mainly due to the growth of microcracks and frictional gliding. These processes are known to be accompanied by acoustic emission (AE) phenomena, see Ma et al. [129]. Monitoring of AE signals should therefore lead to a more precise determination of critical strain values.

### 1.5.5. Modelling of TBC systems

There have been many attempts to numerically investigate stress development in TBC systems due to continuous growth of the TGO layer, creep and mismatch in thermal expansion coefficients of the constituents and the presence

of cracks. In most cases, a unit cell representing a single asperity is used. The stress fluctuation around the asperity is supposed to be representative for the entire interface area. The resulting microcracks could subsequently link and, thus, form a crack crossing a number of asperities at a macro level. In the early work by Chang et al. [43], the effect of thermal expansion mismatch, oxidation and pre-cracking was investigated. The authors did not consider stress relaxation and crack development within the constituents and proposed a failure mechanism induced solely by the oxidation process, which however provided important insights into the thermomechanical behaviour of TBCs. They argued that a combined effect of oxidation and thermal expansion mismatch would result in the growth of tensile zones around the asperity and, thus, promote microcrack nucleation. Freborg et al. [68] performed similar simulations to those of Chang et al. [43]. The main difference was to include the creep effect. It turned out that their results supported the failure mechanism proposed by Chang et al. [43] — early cracking at bond coat peaks and subsequent increasing growth of the microcracks when TGO reaches a critical thickness. This mechanism for TBC delamination is primarily based on the stress component normal to the TBC/BC interface. Finite element simulations (Chang et al. [43], Freborg et al. [68]) have showed that this stress component provides an adequate indication of the stress state component most likely to promote delamination and cracking. It is also consistent with the experimentally observed coating failure by spallation and with the orientation of splats within APS TBCs, placed parallel to the TBC/BC interface and allowing for a microcrack to propagate at their boundaries.

Since oxidation seems to be the most important factor leading to TBC failure, its proper modelling is one of the major tasks in FEM simulations of stress development in the TBCs. There are following approaches reported in the literature:

- oxide growth can be represented by the artificially large thermal expansion coefficient (Chang et al. [43], Freborg et al. [68], Karlsson and Evans [105], Xie and Tong [219]);
- TGO growth can be modelled explicitly by relating the thickness of TGO with time (Bednarz [22], Caliez [37], Sfar et al. [182]);
- incorporation of diffusion models (Caliez et al. [38], Martena et al. [136]);
- TGO is subjected to an elongation strain associated with new oxide formation on the internal grain boundaries (He et al. [87], Karlsson et al. [106], Xu et al. [220]);
- switch from bond coat elements to alumina elements and the subsequent

volumetric increase that takes place during the alumina growth (Jinnes-trand and Sjöström [103]).

Busso et al. [35, 36] considered a sintering effect that manifests itself as a densification and stiffness increase of TBC layer. Their life prediction model was based on damage mechanics, with the assumption that APS TBC failure emerges by cleavage-type damage, and fatigue phenomenon is related to the evolution of microscopic damage parameter  $D$ , ranging from zero to one. The use of damage law with FE-unit cell approach led to calculation of maximal radial tensile stress as a function of cycle number. This type of modelling was restricted only to cyclic thermal loading and not being able to consider continuous isothermal oxidation.

As already discussed, Chang et al. [43] and Freborg et al. [68] explain in qualitative manner the failure mechanism leading to TBC spallation. In order to gain a quantitative information allowing for practical applications, a development of microcracks and their subsequent linking should be included into the FE analysis. The cohesive zone approach allows for a proper modelling of damage development at material interfaces and, in this context, it can be used to simulate crack development at the TGO/BC interface (Caliez et al. [37], Yuan and Chen [225]) or to model the effect of segmentation cracking in the TBC layer (Białas et al. [27], Rangaraj and Kokini [169]). Michlik and Berndt [139] used the extended finite element method to directly model the real microstructure of TBC and analysed the stress intensity factor of through-thickness cracks. It seems that the extended finite element method should be applied for simulation of cracks development and coalescence, since it allows for crack propagation along arbitrary paths.

Another subject is the use of finite elements method to model segmentation cracking. Since it is not so important as delamination failure, the phenomena has not received so much attention yet. However, some papers should be mentioned at this point. Rangaraj and Kokini [167, 168] analysed the influence of segmentation cracks on stress distribution and fracture resistance of functionally graded thermal barrier coatings. The cracks were a priori introduced into finite element mesh and assumed to remain stationary during temperature loading process. Kokini and Takeuchi [113] examined the effect of multiple cracking within graded TBC on the value of critical energy release rate for an interface crack between the coating and the substrate. They found out that multiple segmentation cracks can reduce the magnitude of critical energy release rate for the interface and thus, be beneficial for the life of the coating. In the paper [169] Rangaraj and Kokini used two dimensional finite element model with a cohe-

sive zone to study quasi-static crack growth due to heating-cooling cycle. Xie and Tong [219] incorporated a cohesive interface model into two dimensional analysis of cracking and delamination of thin  $\text{Al}_2\text{O}_3$  film on a ductile substrate.

Due to the complexity of mechanical behaviour, the analytical approaches to TBC modelling are rather few. Convex and concave asperities, modelled as three concentric circles representing three different materials being TBC, BC and TGO, allowed for formulation of analytical models presented by Hsueh and Fuller [94, 95]. Residual thermal stresses at the TGO/BC and TGO/TBC interfaces were functions of TGO thickness. It was shown that for a convex asperity the residual stresses at the TGO/BC interface are tensile and increase as TGO thickness increases. An analytical formula for radial stress as a function of geometrical parameters was obtained by Ahrens et al. [6].

## 1.6. Human skin

The skin is the largest organ of the human body and it has several functions. The most important is to protect the body against external influences. The mechanical behaviour of skin is an important consideration in a number of cosmetic and clinical implications. For example, knowledge of its mechanical behaviour can help to quantify effectiveness of cosmetic products such as creams, to enhance new developments in electrical personal care products such as shavers, and to study skin ageing. Also improvements in cosmetic surgery can be gained with prediction of surgery results by using numerical models of the skin. Finally, changes in mechanical properties of the skin due to skin diseases may play a role in a better understanding and treatment of these diseases.

### 1.6.1. Structure of human skin

The skin is a highly organized structure consisting of three main layers, called the epidermis, the dermis and the hypodermis, see Figure 1.11. The superficial layer, the epidermis, is approximately 75–150  $\mu\text{m}$  in thickness (Odland [148]) and consists largely of outward moving cells, the keratinocytes, that are formed by division of cells in the basal layer of the epidermis. The second layer is the dermis which is a dense fibroelastic connective tissue layer of 1–4 mm thickness (Odland [148]). It mainly consists of collagen fibres, ground substance and elastin fibres and it forms the major mass of the skin. The third layer, the hypodermis (or subcutaneous fat) is composed of loose, fatty connective tissue. Its thickness varies considerably over the surface of the body. For each of the presented layers, several sub-layers can be distinguished, but for the

sensor setup presented in Section 6 it is enough to focus only on the epidermis, the dermis and the hypodermis.

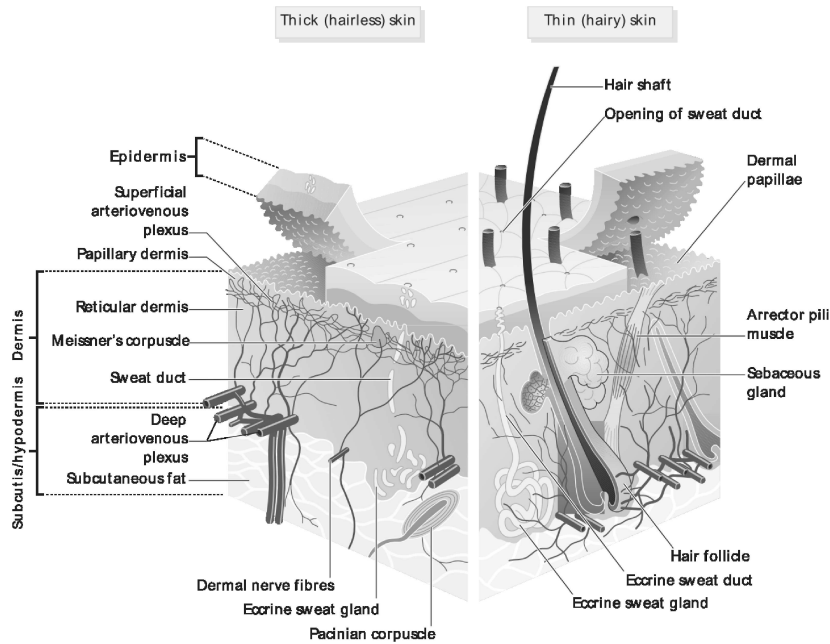


Figure 1.11. Schematic representation of different skin layers (Wikipedia).

### 1.6.2. Mechanical properties of human skin

Mechanical behaviour of the human skin has been studied for a long time. One of the first investigators was Langer in 1861, who punctured skin of human cadavers with a round instrument to study anisotropy (Langer [119]). In the seventies and early eighties of the past century a lot of studies were performed to learn more about skin mechanics (Cook et al. [49], Wan Abas and Barbanel [210], Alexander and Cook [8], Grahame [77], Barbanel et al. [17], Vlasblom [206]). They found that human skin is a non-homogeneous, anisotropic, non-linear viscoelastic material. Its properties vary with age, from site to site and per person. This leads to difficulties in obtaining quantitative descriptions of mechanical properties of the skin.

To enhance the fidelity of mechanical tissue characterization, growing number of studies have employed linear viscoelasticity to approximate the constitutive behaviour of soft tissues (Kruse et al. [117]). While they are clearly non-

linear at high strains and may exhibit complex features related to poromechanics (Thimus et al. [190]), anisotropy (Ventre et al. [204]) and mechanical adaptation (Lokshin and Lanir [127]), studies have shown that linear viscoelastic models provide reasonable approximation of soft tissue's mechanical response in situations involving small strains and fast excitation, with frequencies over 50 Hz in case of dynamic loading (Xydeas et al. [221]).

In most experiments performed *in vivo*, the measured behaviour is ascribed to the dermis. However, as intimate connections exist between the various skin layers, it is hard to isolate the contribution of the dermis to the mechanical behaviour from that of the epidermis and the subcutaneous tissues. Therefore, most tests performed *in vivo* are, in part, also tests of epidermal, stratum corneum and hypodermal properties.

In tensile testing (Manschot [135]) the skin is mainly loaded parallel to its surface. This type of mechanical testing is widely used. Two tabs are attached to the skin and pulled apart. The attachment of the tabs to the skin may significantly influence the results, as many of the double-sided adhesive tapes exhibit creep deformation.

In torsion tests (Agache et al. [2]) a guard ring and an intermediary disc are attached to the skin. A constant torque or rotation is applied by the disc. According to Escoffier et al. [61] this method has two advantages: hypodermis and underlying tissues do not effect the measurements, and the anisotropic character of the skin is minimized.

The principle of the suction method (Barel et al. [18], Diridollu [55], Gniadecka and Serup [76]) is the measurement of skin elevation caused by application of a partial vacuum (usually in the range of 5–50 kPa) via a circular aperture in a measuring probe. The deformation is measured with an optical or ultrasound system.

In indentation experiments a rigid indenter is used to apply a known force or deformation to the skin. Bader and Bowker [16] used a plane-ended indenter to study mechanical behaviour of skin and underlying tissue. Tissue thickness was measured with a skin fold caliper.

In most situations that entail the non-invasive use of elastic waves toward three dimensional reconstruction and characterization of subsurface heterogeneities, studies have largely focused on either one dimensional testing of excised tissues (Catheline et al. [42], Wu et al. [216]), or indentation testing (Suzuki and Nakayama [188], Dhar and Zu [54]) that relies on the premise of local tissue homogeneity. More recently, Liu and Ebbini [126] and Guzina et al. [83] proposed a dynamic testing methodology for the viscoelastic characterization of homogeneous, millimetre-thin tissue constructs on rigid sub-

strates, that utilizes high-intensity ultrasound beam, modulated at frequencies on the order of 102–103 Hz, as the source of mechanical vibrations. A non-invasive surface wave method for skin testing was developed by Zhang et al. [230] and Kirkpatrick et al. [111], who utilized Rayleigh surface waves as a means to expose the tissue’s viscoelastic properties. The latter two works nonetheless model the skin as a homogeneous viscoelastic half-space, a hypothesis that is inconsistent with the stratified nature of skin, that includes mechanically dissimilar epidermis and dermis layers, resting on a subcutaneous tissue (James et al. [102]).

### 1.6.3. Skin imaging

To image the skin without taking biological biopsies, various non-invasive in vivo skin imaging techniques have been developed. Regardless of the approach, however, the experimental setup required for tissue characterization is by rule associated with high cost due to used sophisticated hardware.

Ultrasound is an acoustic technique, which can be used to image the skin perpendicular to its surface. By varying frequency either high resolution (up to 11  $\mu\text{m}$  for high frequencies) or large penetration depth (up to 6 cm for low frequency) can be achieved (Serup et al. [181]).

The physical principle of an ultrasound scanner is the emission of high frequency acoustic waves, caused by electrical signals in a piezoelectric ultrasound transducer. An alternating electric field causes thickness variations in the piezoelectric material. The thickness variations cause pressure waves in the surrounding coupling agent (mostly water) — the ultrasound. At each interface between different tissues in the skin, a change in the acoustic impedance of the tissue causes some of the sound to be reflected back to the transducer, while the rest of the energy continues to the next interface. The amount of sound being reflected depends on the difference in acoustic impedance of the materials, with large reflections for increasing differences. The sound emission is pulsed, which means that the equipment switches automatically and very rapidly between emission of sound and the registration of sound coming back to the same transducer from the object being studied. The result is a train of pulses returning to the transducer. The time lag between emitted and reflected sound waves is a measure for the travelled distance. It depends on the physical distance between the interfaces and on the tissue material, and can be converted into a distance, once the speed of the sound is known.

The used ultrasound frequency is a compromise between desired resolution and penetration depth. Axial resolution is defined by the ratio of sound ve-

locity and the ultrasound frequency. Tissue penetration improves with lower frequencies, whereas higher frequencies lead to a better resolution. Ultrasound waves of 10 MHz penetrate deep enough to visualize the subcutaneous fat, while ultrasound waves of 50 MHz allow a more detailed study of the epidermis. Frequencies from 15 to 20 MHz are mostly used for the skin, as they provide a good compromise between resolution and viewing depth to visualize the entire skin. Generally, 20 MHz scanners have an axial resolution of 0.07 mm and a lateral resolution of 0.15–0.35 mm. The viewing field of depth is typically 15–25 mm (Agner [3], Serup et al. [181]). At this frequency, differentiation between epidermis and dermis by ultrasound is difficult because the thickness of the epidermis is close to that of the system's resolution.

Confocal microscopy is a very high resolution optical technique, that can be used to image the epidermis parallel to the skin surface. Figure 1.12 shows a schematic representation of a backscatter confocal microscope. Excitatory light from a point source is reflected by a dichroic mirror and focused by the microscope objective lens to illuminate a point on the focal plane inside the skin. The illuminated spot is then imaged onto a detector through a pinhole or a point aperture. This aperture acts as a spatial filter, rejecting light that is reflected from out-of-focus portions of the object (dashed line) to fall outside of the focal spot. Only emissions from the focal plane (solid line) are able to pass the aperture, resulting in an image with the high contrast of a thin-section image. By moving the light beam, the desired plane in the specimen can be scanned. In this way a two dimensional image is obtained. Varying the depth of the focal plane and combining the obtained images computationally, leads to a three dimensional image (Sheppard and Shotton [183]).

Signal contrast in confocal reflectance imaging stems from variations in the refractive index of the cell structure. This causes differences in reflection, resulting in varying gray scales. Because of the high scattering coefficient of the skin, the maximum penetration depth in skin is in the order of 250–300  $\mu\text{m}$  and a vertical resolution up to 2  $\mu\text{m}$  can be obtained. The performance of the confocal system is mainly determined by the aperture size and the illumination wavelength. Increasing the wavelength leads to deeper penetration and a decreasing lateral and axial resolution, thus increasing section thickness (Rajadhyaksha and Zavislan [166]).

Optical coherence tomography (OCT) is an interferometric method which supplies information about optical inhomogeneities of the tissue. Both lateral and axial resolution are in the order of 10–20  $\mu\text{m}$ , whereas the penetration depth is in the order of 1–2 mm (Pan et al. [155]). OCT images are represented as two dimensional cross-sectional images, which can be compared with high frequency

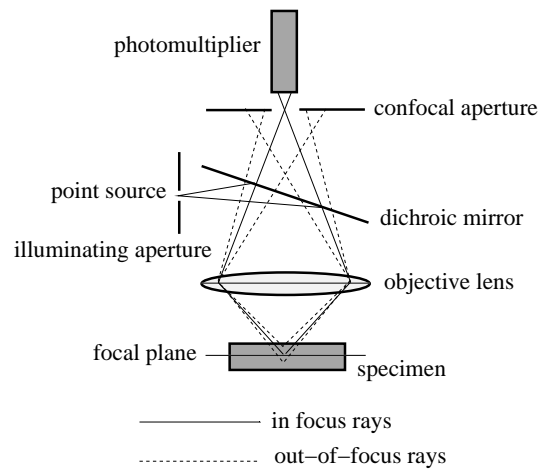


Figure 1.12. Schematic diagram of a backscatter confocal microscope. Adopted from Sheppard and Shotton [183].

ultrasound scans. The OCT system is based on the principle of the Michelson interferometer. An example of a system setup is given in Figure 1.13. Usually the light source is a superluminescence diode (SLD) with a wavelength in the near infrared (approximately 1300 nm) and with a short coherence of about 15  $\mu\text{m}$ . The light is coupled into a single-mode fiberoptic interferometer. Within the first interferometer arm, the reference arm, the light is collimated and directed through a scanning mirror system to a reference mirror mounted on a stepper motor. The position of the reference mirror determines the scan position. The light in the sample arm, the second interferometer arm, is focused onto the spot of interest at the tissue sample. The backscattered light from the tissue sample is collected through the same optics and recombined with reflected light from the scanning reference mirror system at two detectors. Coherent interference signal occurs only when the path length between those arms are matched to within the coherence length of the light source. Due to multiple light scattering and a coherence length longer than most cell diameters, OCT can provide less microstructural details than light microscopy. However, it can show structures which correlate well with ultrasound to a depth of about 600  $\mu\text{m}$ .

Nuclear magnetic resonance (NMR) or magnetic resonance imaging (MRI), a form of NMR, can also be used to image the skin. Disadvantages of NMR are high cost, special building requirements, importability, and its low speed of obtaining images (Zemtsov [227]). However, MRI provides better resolution, which can also be obtained by high-resolution ultrasound (but with smaller penetra-

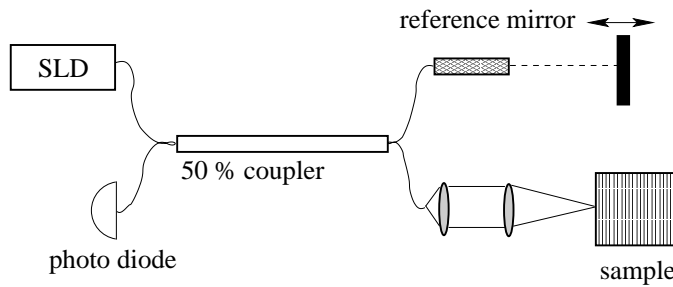


Figure 1.13. Schematic diagram of the OCT system. Adopted from Welzel [211].

tion depths). Other advantages of MRI are the ability to visualize structures in fat and the fact that no coupling liquid is needed.

Over the past decade, studies have demonstrated that quantitative medical imaging (targeting e.g. the spatial distribution of tissue's shear modulus) has a potential of identifying cancerous lesions in tissues that are otherwise visible but indiscernible by anatomical imaging techniques such as those previously mentioned. In particular, results indicate (Ophir et al. [150], Plewes et al. [163]) that the apparent shear modulus of certain types of cancer can be between 5 to 10 times higher than that of the surrounding healthy tissue. Notwithstanding such critical advantage, at present there are no viable in vivo testing procedures nor analyses capable of quantitatively resolving the effective mechanical characteristics of multi-layered, small-scale tissue structures such as skin.

# Preliminaries

In the late 1980s applications involving thin films and composites motivated Evans, Hutchinson, Rice and others to develop interfacial fracture mechanics. Today this field of mechanics is practiced routinely in industries. The emphasis of this chapter is to summarize the basic concepts of this research, focusing on isotropic materials, as this is the subject of the monograph. Extensions to anisotropic materials can be found in Suo [187].

The singular stress field around a tip of the interfacial crack between two linear elastic, dissimilar materials will be discussed first, as this result presented by Williams [212] is of special importance, when considering delamination failure of a thin film bonded to an underlying substrate. The concepts of fracture energy and energy release rate will be discussed next. This all gives ground for the introduction of cohesive zone ahead of crack tip, allowing to add nonlinear effects taking place during failure process. It also allows to get rid of unrealistic singular and oscillatory stresses, stemming from the assumption of linear elasticity and negligence of contact in Williams' solution [212]. A general model of a cohesive zone presented by Mróz and Białaś [142] and Białaś and Mróz [28] will be introduced and discussed with a specification to slip response, describing frictional or yielding interaction between the film and the substrate.

## 2.1. Fracture mechanics of interface cracks

When discussing a thin film bonded to a substrate we consider two materials with different mechanical properties. Let us assume that the failure mode associated with the described setup is the crack propagation along the interface between the two materials. Others, as presented in Figure 1.3, can be describe by the classical fracture mechanics approach, where a crack within a bulk material is considered, see for example the monograph by Anderson [9].

Figure 2.1 presents two isotropic solids joined along the  $x_1$  axis with material 1 above the interface and materials 2 below. Let  $\mu_i$ ,  $E_i$  and  $\nu_i$ ,  $i = 1, 2$  be the

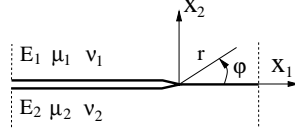


Figure 2.1. Tip of a bimaterial crack.

shear modulus, Young's modulus and Poisson's ratio of the respective materials and let  $\kappa_i = 3 - 4\nu_i$  for plane strain and  $\kappa_i = (3 - \nu_i)/(1 + \nu_i)$  for plane stress. Dundurs [59] observed that wide class of plane problems of elasticity for bimaterials depends on two non-dimensional combination of elastic parameters. They are

$$\alpha_1 = \frac{\mu_1(\kappa_2 + 1) - \mu_2(\kappa_1 + 1)}{\mu_1(\kappa_2 + 1) + \mu_2(\kappa_1 + 1)}, \quad \alpha_2 = \frac{\mu_1(\kappa_2 - 1) - \mu_2(\kappa_1 - 1)}{\mu_1(\kappa_2 + 1) + \mu_2(\kappa_1 + 1)}. \quad (2.1)$$

By solving an eigenvalue problem, Williams [212] discovered that the singular field around the tip of the interfacial crack is not square-root singular, as in elastic bulk material, but takes a new form. At a distance  $r$  ahead the tip of the crack, dominant stress singularity on the interface is given by

$$\sigma_{22} + i\sigma_{12} = \frac{K r^{i\epsilon}}{\sqrt{2\pi r}}, \quad (2.2)$$

where  $i = \sqrt{-1}$  and

$$\epsilon = \frac{1}{2\pi} \ln \left( \frac{1 - \alpha_2}{1 + \alpha_2} \right).$$

When the two materials have identical elastic constants  $\mu_1 = \mu_2$  and  $\nu_1 = \nu_2$ , the constant  $\epsilon$  vanishes and the singular field around the tip of the crack on the interface is similar to that around the tip of a crack in a homogeneous material. The complex interface stress intensity factor  $K = K_1 + iK_2$  has real and imaginary parts  $K_1$  and  $K_2$ , respectively, which play a role similar to conventional mode I and mode II intensity factors. The associated crack flank displacements at a distance  $r$  behind the tip  $\delta_i = u_i(r, \varphi = \pi) - u_i(r, \varphi = -\pi)$  are given by

$$\delta_2 + i\delta_1 = \frac{8}{(1 + 2i\epsilon) \cosh(\pi\epsilon)} \frac{(K_1 + iK_2)}{E_*} \left( \frac{r}{2\pi} \right)^{1/2} r^{i\epsilon}, \quad (2.3)$$

where

$$\frac{1}{E_*} = \frac{1}{2} \left( \frac{1}{E_1} + \frac{1}{E_2} \right)$$

with  $\bar{E}_i = E_i/(1 - \nu_i^2)$  in plane strain and  $\bar{E}_i = E_i$  in plane stress.

The term  $r^{i\epsilon} = \cos(\epsilon \ln r) + i \sin(\epsilon \ln r)$  introduces a so-called oscillatory singularity, which brings in some complications that are not present in the elastic fracture mechanics of homogenous solids. First of all, the Williams' field implies that for certain values of  $r$  the faces of the crack interpenetrate, which makes the solution inconsistent with the assumption that crack faces are traction free, meaning that crack closure is not considered. In other words: in a homogeneous material, the faces of a crack come into contact when the remote load is compressive; by contrast, the faces of an interface crack may come into contact even when the remote load has a tensile component. Interpenetration clearly is a wrong prediction but, under some circumstances, the obtained Williams' field can be very useful. Assuming that the distance of the contact region is small compared to the zone of nonlinear deformation, the pathology of oscillatory singularity becomes insignificant. To use the Williams field for an interfacial crack, all we really need to do is to ensure that the wrong part of the field occurs in a small zone around the tip of the crack, a zone excluded by the  $K$ -annulus. Rice [170] examined the condition for small-scale contact, proving that in many situations, the contact zone is small compared to the overall dimension.

### 2.1.1. General case $\epsilon \neq 0$

It also should be noted that in general  $K_1$  and  $K_2$  do not directly represent normal and shear intensities. An inspection of the stress field (2.2) also shows that  $K$  is of dimension  $[\text{stress}][\text{length}]^{1/2-i\epsilon}$  and the dimension of the magnitude of the stress intensity factor is  $[\text{stress}][\text{length}]^{1/2}$ . Thus, the relative proportion of critical combination of  $(K_1, K_2)$  changes when units are changed. This all means that the notion of a mode I or a mode II crack tip field must be defined precisely. Rice [170] proposed a generalized interpretation of the mode measure. In the following it will be summarized shortly.

Let  $s$  be an arbitrary length. We shall define a quantity called mode angle as

$$\chi = \text{arc tg} \frac{\mathcal{I}m(K s^{i\epsilon})}{\mathcal{R}e(K s^{i\epsilon})}, \quad (2.4)$$

where  $K = K_1 + iK_2$  is the complex stress intensity factor. When  $\epsilon \neq 0$  a mode I crack has zero shear stress traction on the interface a distance  $l$  ahead of the tip, and a mode II crack has zero normal traction at this point. Thus, the measure of proportion of mode II to mode I in the vicinity of the crack tip requires the specification of some length quantity. By using the definition (2.4)

we can write

$$K = |K| s^{-i\epsilon} \exp(i\chi). \quad (2.5)$$

Let us examine the consequences of different choices of the length, say  $s_A$  and  $s_B$ . We want the choice of an arbitrary  $s$  not to affect  $K$  and  $|K|$ . In order to do that, we need to associate one mode angle  $\chi_A$  with one choice of the length  $s_A$  and associate a different mode angle  $\chi_B$  with the other choice of the length  $s_B$ . To keep  $K$  and  $|K|$  unchanged by the different choices of the length, we require that

$$s_A^{-i\epsilon} \exp(i\chi_A) = s_B^{-i\epsilon} \exp(i\chi_B).$$

Rearranging, we obtain

$$\chi_B - \chi_A = \epsilon \ln \frac{s_B}{s_A}. \quad (2.6)$$

As we see, it is a simple matter to transform from one choice to the other. In particular, toughness data can readily be transformed. As an example let  $\epsilon = 0.1$ ,  $s_A = 1$  nm and  $s_B = 1$   $\mu$ m. This change in the length shifts the mode angle by  $\chi_B - \chi_A \approx 40^\circ$ .

To see the significance of the mode angle, let us insert  $K = |K| s^{-i\epsilon} \exp(i\chi)$  into (2.2). After separating real and imaginary parts, we obtain

$$\sigma_{22} = \frac{|K|}{\sqrt{2\pi r}} \cos\left(\chi + \epsilon \ln \frac{r}{s}\right), \quad (2.7)$$

$$\sigma_{12} = \frac{|K|}{\sqrt{2\pi r}} \sin\left(\chi + \epsilon \ln \frac{r}{s}\right). \quad (2.8)$$

The ratio of the shear stress to the tensile stress is

$$\frac{\sigma_{12}}{\sigma_{22}} = \text{tg}\left(\chi + \epsilon \ln \frac{r}{s}\right). \quad (2.9)$$

When  $\epsilon \neq 0$ , the ratio  $\sigma_{12}/\sigma_{22}$  varies with distance  $r$ . The variation is not rapid when  $\epsilon$  is small, due to the fact that logarithm is a slowly varying function. Note that  $\sigma_{12}/\sigma_{22} = \text{tg}\chi$  for  $r = s$ . Thus,  $\text{tg}\chi$  approximates the ratio  $\sigma_{12}/\sigma_{22}$  as long as  $r$  is not too far from  $s$ .

It was mentioned that the choice of the reference length  $s$  was arbitrary. We see now that it is useful to pick up  $s$  based on the material length scale, such as a fracture process zone or plastic zone at fracture. For a brittle interface, for example, a natural choice is  $s = 1$  nm, representative of the bond breaking zone size. With this choice, the mode angle  $\chi$  represents the relative proportion of shear to tension at the size scale of 1 nm.

When a crack extends on an interface between two materials, mixed-mode conditions prevail. Due to elastic mismatch in the two materials, one should specify the length  $s$  in defining the mode angle  $\chi$ . The energy needed to advance the crack is called fracture energy. It is a function of the mode angle,  $G(\chi)$ . The fracture energy tends to increase as the mode angle approaches  $\pm\pi/2$ . The energy cost for debond varies with the relative proportion of opening and shearing of the two faces of the crack. For example, a large amount of shearing may promote more inelastic deformation in the constituent materials, or promote near tip sliding against roughness, provided the interface is not perfectly flat. The  $G(\chi)$  does not need be symmetric with respect to  $\chi = 0$ , because the two materials on either side of the interface are dissimilar. By (2.6), change in one choice of length in the definition of  $\chi$  to another only involves a shift of the  $\chi$ -origin on  $G$  according to

$$G(\chi_B) = G\left(\chi_A + \epsilon \ln \frac{s_B}{s_A}\right). \quad (2.10)$$

This procedure is depicted in Figure 2.2. When  $\epsilon$  is small, the shift will generally be negligible even for changes of  $s$  of several orders of magnitude.

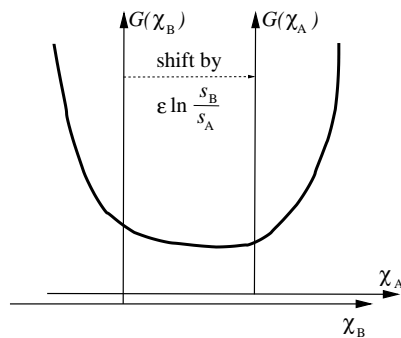


Figure 2.2. Shifting the toughness function from one choice of reference length to the other.

### 2.1.2. Special case $\epsilon = 0$

On the virtue of taking  $\epsilon = 0$ , the stress field becomes the well-known square root singular

$$\sigma_{22} = \frac{K_1}{\sqrt{2\pi r}}, \quad \sigma_{12} = \frac{K_2}{\sqrt{2\pi r}} \quad (2.11)$$

and the two parameters  $K_1$  and  $K_2$  measure the amplitudes of two fields. Consequently, we can treat a crack on an interface the same way as we treat a crack in a homogeneous material under mixed-mode loading. The measure of the relative amount of mode II to mode I at the crack tip becomes

$$\chi = \arctg \frac{K_2}{K_1}. \quad (2.12)$$

Even when we set  $\epsilon = 0$ , however, there is a significant difference between a crack on an interface and a crack in a homogeneous material. When a mixed-mode crack in a homogeneous material reaches a critical condition, the crack kinks out of its plane. By contrast, when a mixed-mode crack on an interface reaches a critical condition, the crack often extends along the interface, provided the interface is sufficiently weak compared to either material.

### 2.1.3. Energy release rate

For the crack extending on the interface, the energy release rate  $\mathcal{G}$  is still defined as the reduction in the potential energy associated with the crack advancing a unit area. All the familiar methods of determining the energy release rate still apply. For example, the energy release rate can be determined by measuring the load-displacement curves for bodies containing cracks of different sizes. As another example, the energy release rate can be calculated by using the  $J$  integral.

The energy release rate for crack advance in the interface was obtained by Malyshev and Sagalnik [134] and takes the form

$$\mathcal{G} = \frac{1 - \alpha_2^2}{E_*} (K_1^2 + K_2^2). \quad (2.13)$$

The criterion for initiation of crack advance in the interface, when the crack tip is loaded in mixed mode characterized by  $\chi$  is  $\mathcal{G} = G(\chi)$ . This condition is assumed for quasi-static crack advance, when crack growth resistance effects can be disregarded.

When the load increases to a critical level, the crack can also kink out of the interface. This phenomenon has been analysed by He and Hutchinson [88]. The condition for the crack to extend on the interface is that the energy release rate of the extension attains the fracture energy of the interface, namely,  $\mathcal{G}_{\text{debond}} = \mathcal{G} = G(\chi)$ . The condition of the crack to kink into one of the bonded materials is that the energy release of the kink attains the fracture energy of the corresponding bulk material, namely,  $\mathcal{G}_{\text{kink}} = G_{\text{bulk}}$ . Debonding and kinking are

competing processes. The outcome depends on which of the above two critical conditions is first attained as the load ramps up. In many cases, however, the interface is substantially weaker compared to either material and the cohesive zone model presented in the following section can be applied to describe the process of interfacial separation.

## 2.2. Cohesive zone model

Up to this moment we have described the process of deformation of a body, focusing on linear elasticity theory. By contrast, the process of separation involving nonlinear effects has not been addressed yet. One of the most common approaches to deal with the problem is to make use of cohesive zone models. The basis of these models stems from early works in fracture mechanics, in which it was postulated that a zone of stress bridging advances ahead of crack tip (Barenblatt [19], Dugdale [58]). In general, it can be understood as an array of nonlinear springs joining two parts of a body, as presented in Figure 2.3. The separation is modelled by the traction-separation curve having the general trend: it should go up and then go down. The deformation in the body can be modelled by any field theory.

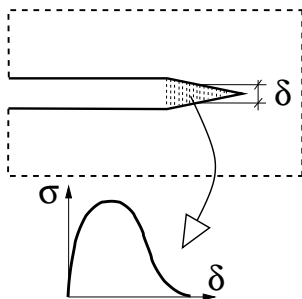


Figure 2.3. Cohesive zone and traction-separation curve.

The obvious advantages of the cohesive zone models are:

- they do not introduce any unrealistic singularities or oscillations in the stress field;
- both the interface deformation and separation processes can be described;
- cohesive zone can easily capture microcracks formation, plastic deformation and all other inelastic processes taking place at the crack tip.

Because of the particular importance of the film/substrate interfaces encountered in mechanics of thin films, cohesive zone approach comes as an obvious choice for their appropriate modelling. In this case the interface constitutes a priori defined plane of weakness, where failure development is likely to occur. A constitutive law for this region can be postulated totally independently from those of the materials in contact and, thus, features specific, for example, to its production process, may be captured. On top of that, it simultaneously allows for the description of its deformation and failure. Mróz and Białaś [142] and Białaś and Mróz [28] introduced a cohesive zone model using theory of plasticity formalism and used it further to analyse instability points associated with decohesion process. It will be also used in this monograph to describe delamination and segmentation of thin films. Its details are presented in the following paragraphs.

### 2.2.1. General formulation

Let us consider an interface  $S$  between two bodies, as presented in Figure 2.4. We neglect the in-plane stress components and express the deformation response in terms of traction  $\boldsymbol{\sigma} = \{\sigma, \tau_1, \tau_2\}^T$ , where

$$\boldsymbol{\sigma} = \mathbf{n} \cdot \boldsymbol{\sigma} \cdot \mathbf{n}, \quad \tau_1 = \mathbf{t}_1 \cdot \boldsymbol{\sigma} \cdot \mathbf{n}, \quad \tau_2 = \mathbf{t}_2 \cdot \boldsymbol{\sigma} \cdot \mathbf{n} \quad (2.14)$$

and  $\mathbf{n}$  is the unit normal vector to  $S$ ,  $\mathbf{t}_1$  and  $\mathbf{t}_2$  are the unit vectors within  $S$ , forming the orthonormal basis. The displacement discontinuity vector  $\boldsymbol{\delta}$  on  $S$  can be decomposed into normal relative displacement, denoted by  $\delta_n$ , and two components of tangential relative displacement, namely  $\delta_{t_1}$  and  $\delta_{t_2}$ . Following the theory of plasticity approach, the total displacement discontinuity and its rate are decomposed into elastic and plastic (slip) components, thus

$$\boldsymbol{\delta} = \boldsymbol{\delta}^e + \boldsymbol{\delta}^p, \quad \dot{\boldsymbol{\delta}} = \dot{\boldsymbol{\delta}}^e + \dot{\boldsymbol{\delta}}^p, \quad (2.15)$$

where dot indicates derivative with respect to time. The constitutive equations relating the interface traction and the reversible part of displacement discontinuity are of the form

$$\dot{\sigma} = K_n \dot{\delta}_n^e, \quad \dot{\tau}_1 = K_t \dot{\delta}_{t_1}^e, \quad \dot{\tau}_2 = K_t \dot{\delta}_{t_2}^e, \quad (2.16)$$

where  $K_n$  and  $K_t$  is an interfacial stiffness respectively in tension (compression) and shear. Upon inversion above relations become

$$\dot{\delta}_n^e = C_n \dot{\sigma}, \quad \dot{\delta}_t^e = C_t \dot{\tau}, \quad (2.17)$$

where

$$\tau = \sqrt{\tau_1^2 + \tau_2^2}, \quad \delta_t^e = \sqrt{(\delta_{t_1}^e)^2 + (\delta_{t_2}^e)^2}$$

and  $C_n = 1/K_n$  and  $C_t = 1/K_t$  are compliance modules respectively for tension (compression) and shear.

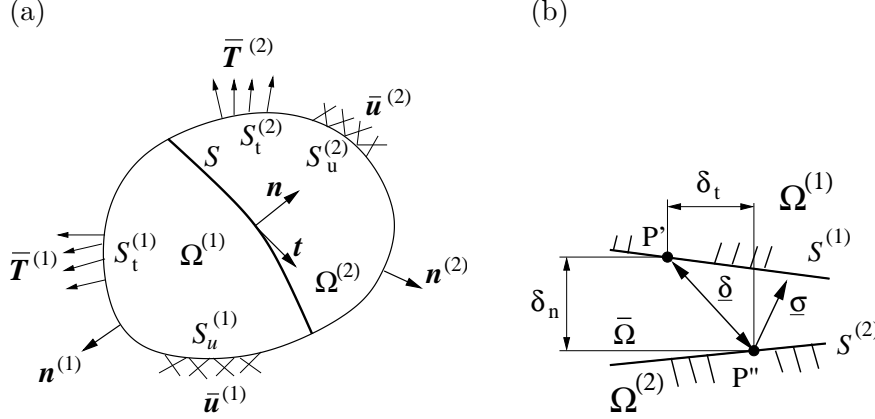


Figure 2.4. (a) Two bodies connected by an interface. (b) The relative displacements and stresses at the interface.

The interface failure criterion is given in terms of normal and shear stresses, satisfying the equality  $F = 0$ . The proposed yield function  $F$  has the form

$$F(\sigma, \tau) = \begin{cases} \sqrt{\sigma^2 + \left(\frac{\sigma_c^0}{\tau_c^0}\right)^2 \tau^2} - \sigma_c(\delta_{eq}), & \sigma \geq 0 \\ \tau + \mu\sigma - \frac{\tau_c^0}{\sigma_c^0} \sigma_c(\delta_{eq}), & \sigma < 0 \end{cases}, \quad (2.18)$$

where  $\mu$  is a friction coefficient and  $\sigma_c^0$  and  $\tau_c^0$  are interface critical stresses respectively for pure tension and shear. A clear distinction has been made between compression and tension modes. In the former, the yield function becomes Coulomb's friction law, whereas in the latter we have an elliptical failure condition. The parameter  $\delta_{eq}$  is defined by the following formula

$$\delta_{eq} = \int_0^t \sqrt{(\dot{\delta}_n^p)^2 + m^2(\dot{\delta}_t^p)^2} d\bar{t}, \quad \dot{\delta}_t^p = \sqrt{(\dot{\delta}_{t_1}^p)^2 + (\dot{\delta}_{t_2}^p)^2}, \quad (2.19)$$

where  $m$  is a material constant expressing the influence of the sliding mode on failure evolution. The constitutive equations for the plastic part of interface relative displacements are

$$\dot{\delta}_n^p = \dot{\lambda} \frac{\partial \psi}{\partial \sigma}, \quad \dot{\delta}_t^p = \dot{\lambda} \frac{\partial \psi}{\partial \tau}, \quad (2.20)$$

where  $\psi$  is a plastic potential and  $\Lambda$  denotes the plastic multiplier. Additionally, the following formulas should be satisfied

$$\dot{\Lambda} \geq 0, \quad F \leq 0, \quad F\dot{\Lambda} = 0, \quad (2.21)$$

leading to the consistency condition  $\dot{F} = 0$ .

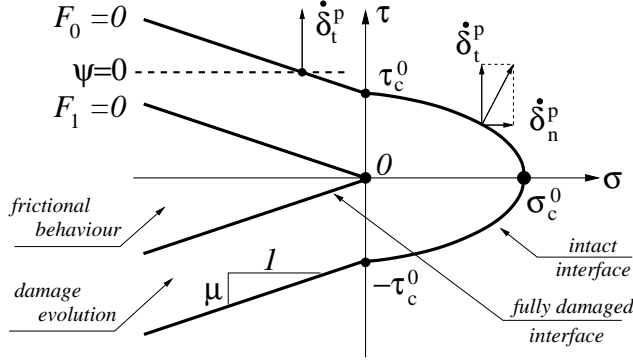


Figure 2.5. Yield function  $F$  and plastic potential  $\psi$ .

The plastic potential  $\psi$  is given by

$$\psi(\sigma, \tau) = \begin{cases} \sqrt{\sigma^2 + \left(\frac{\sigma_c^0}{\tau_c^0}\right)^2 \tau^2} - \sigma_c(\delta_{\text{eq}}), & \sigma \geq 0 \\ \tau - \frac{\tau_c^0}{\sigma_c^0} \sigma_c(\delta_{\text{eq}}), & \sigma < 0 \end{cases}. \quad (2.22)$$

It is clearly seen that for an interface subjected to tension we have an associated flow rule, whereas non-associated rule is assumed for compression mode, leading to vanishing value of normal plastic displacement  $\dot{\delta}_n^p = 0$  in this particular case. Thus, dilatancy effects at the interface are not accounted for. One should note that the assumed plastic potential  $\psi$  is a convex function and satisfies all the requirements needed to fulfill the dissipation inequality (Ottosen and Ristinmaa [151]). From the thermodynamic point of view the present approach is therefore correct. Even introduction of rather untypical concave yield function  $F$  does not lead to any contradiction with general laws of physics. It merely excludes the formulation from application to plastic collapse theory, but by any means can be used as one of models of failure development at an interface. It should be noted that the slip rule (2.20) remains continuous and smooth, when the normal stress  $\sigma$  changes sign, though the damage function  $F$  has a slope discontinuity for  $\sigma = 0$ .

Figure 2.5 presents the yield function  $F$  and the plastic potential  $\psi$  as functions of  $\sigma$  and  $\tau$ . Yield function  $F = 0$  is plotted for two distinct states of interfacial response. The plot of  $F_0$  refers to an intact interface able to sustain stresses up to the values of  $\sigma_c^0$  and  $\tau_c^0$ , respectively in tension and shear. The plot of  $F_1$  is drawn for fully damaged interface, sustaining only compressive and shear loadings in accordance with Coulomb's law of friction. The crack development is described by the evolution of function  $F = 0$  from  $F_0 = 0$  to  $F_1 = 0$ . In order to model this process, the following softening function  $\sigma_c(\delta_e)$  can be proposed

$$\sigma_c(\delta_{\text{eq}}) = \begin{cases} \sigma_c^0 - Z\delta_{\text{eq}}, & \delta_{\text{eq}} \leq \frac{\sigma_c^0}{Z}, \\ 0, & \delta_{\text{eq}} > \frac{\sigma_c^0}{Z}, \end{cases} \quad (2.23)$$

with  $Z$  being a softening modulus. The proposed relation assumes linearly decreasing interface stresses combined with increasing interface relative displacement. For  $\delta_{\text{eq}} > \sigma_c^0/Z$  the ultimate damage stage has been reached with complete interface failure.

To get an interpretation of model parameters  $Z$  and  $m$  let us consider an interface subjected either to pure tension loading or pure shear mode. In the case of pure tension we have  $\tau = 0$ ,  $\sigma \geq 0$ ,  $\delta_{\text{eq}} = \delta_n^p$ . The yield function  $F$  takes the form

$$F(\sigma, \tau) = \sigma - \sigma_c(\delta_{\text{eq}}) \quad (2.24)$$

and the relation between  $\sigma_c$  and  $\delta_{\text{eq}}$  is given by equation (2.23) as presented in Figure 2.6(a). The surface area below the softening function is given by  $G_I = (\sigma_c^0)^2/(2Z)$  and equals the energy needed for creation of an unit area of a fully damaged interface, namely the critical energy release rate. It is clearly seen that the parameter  $Z$  scales the  $G_I$  value.

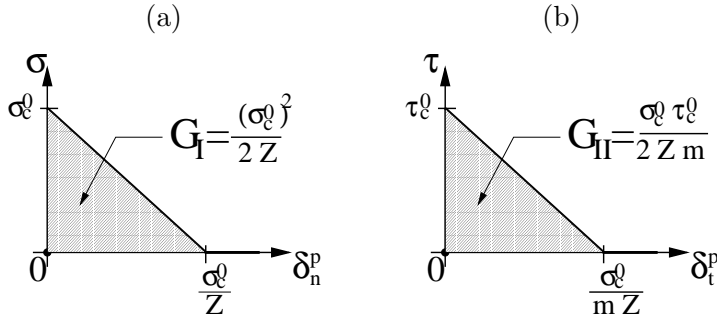


Figure 2.6. Interface softening responses: (a) in pure tension; (b) in pure shear.

In the case of pure shear we obtain  $\sigma = 0$ ,  $\delta_{\text{eq}} = m\delta_t^{\text{P}}$ ,  $F = |\tau| - \tau_c(\delta_{\text{eq}})$ . The function  $\tau(\delta_t)$  is given by the following equation

$$\tau(\delta_t) = \begin{cases} \tau_c^0 - \frac{\tau_c^0}{\sigma_c^0} Z m \delta_t, & \delta_t \leq \frac{\sigma_c^0}{Z m} \\ 0, & \delta_t > \frac{\sigma_c^0}{Z m} \end{cases} \quad (2.25)$$

and presented in Figure 2.6(b). The value  $G_{\text{II}} = \tau_c^0 \sigma_c^0 / (2mZ)$  is the energy needed for creation of a unit surface area of fully damaged interface subjected to shear. Thus, parameter  $m$  scales the critical energy release rate  $G_{\text{II}}$ .

The presented model is characterized by the following eight material parameters:  $C_n$  and  $C_t$  being elastic compliances respectively for normal and tangential opening modes,  $\sigma_c^0$  – critical normal stress,  $\tau_c^0$  – critical shear stress,  $G_I$  – critical energy release rate for opening mode,  $m$  and  $Z$  – critical energies scaling factors,  $\mu$  – friction coefficient.

By putting the compliances  $C_n$  and  $C_t$  in equation (2.17) equal zero we obtain rigid-softening interface, where no relative slip between contacting surfaces is allowed, unless failure criterion  $F = 0$  is reached. This situation can be adopted to model not only interfacial failure development, but also crack extension in bulk material along a priori assumed direction. This can be done, for example, for a symmetric set up of a notched three-point bending specimen, where crack is expected to develop along a symmetry line under the loading force. In such a situation rigid and zero thickness interface do not contribute to the energy balance. When a certain stress threshold is reached, it allows for fractural dissipation. With the crack path not known in advance, one can use the approach suggested by Camacho and Ortiz [39] and introduce surface-like cohesive elements at interfaces between standard volume elements. Crack branching and coalescence can be naturally handled this way.

### 2.2.2. Specification to a slip response

By putting  $\sigma_c^0 = 0$  in equation (2.23) we neglect the decreasing of traction at the interface and obtain elastic-friction response. The yield function  $F$  becomes  $F_1$  (see Figure 2.5) and does not evolve during the loading history. In this case allowed interfacial stress states are bounded by the cone  $\tau + \mu\sigma \leq 0$ , meaning that interface can sustain only compressional loading. With  $C_n = C_t = 0$  in equation (2.23) we have a rigid-frictional interface, where two bodies stick together, unless criterion  $F = \tau + \mu\sigma = 0$  is satisfied.

For thin coatings the normal stress between the coating and the substrate is negligible in many situations. For such a case the failure criterion can be

reformulated  $F = \tau - \tau_c = 0$ , where  $\tau_c$  is a material parameter being a threshold value for the interfacial shear stress. In particular, it can be treated as a plastic shear yield stress of either the coating or the substrate material. In this context, a general slip mechanism, not necessarily related with frictional response, can be handled.



# An energy model of segmentation cracking of thin films

## 3.1. Introduction

Progress in thin film and polymer technology has made it possible to deposit ceramic films of thickness in the range of 10–100 nm on flexible polymer substrates. The total thickness of these composites varies from 10 to 100  $\mu\text{m}$ . Industrial applications are  $\text{SiO}_x$  ( $x \approx 1.65$ ) films deposited by chemical or physical vapour deposition processes on polyethylene terephthalate (PET) substrates. Thanks to the deposition of the  $\text{SiO}_x$  films they are capable of preventing oxygen and water vapour gases from penetrating through the films. Moreover, the small thickness of the  $\text{SiO}_x$  films makes the PET foil transparent. As such they found a considerable interest for packaging purposes, specifically in the pharmaceutical and food industries (Futatsugi et al. [70], Hsueh [93], Hsueh and Yanaka [96], Leterrier et al. [124, 125], McGuigan et al. [137], Yanaka et al. [222, 223, 224]). In such applications, the coating integrity should be assured during the whole life-time of a package. A shortcoming of such materials, though, is that they suffer mechanical damage such as through-thickness cracking and shear-type delamination, when the PET is stretched or bent during manufacturing and service. In order to characterize the fracture strength of the film, a quantitative method of estimating the resistance to tensile loadings should be established. Methods, where coatings are detached from the substrates and subjected to a tensile or a bending test, cannot be used because the ceramic films are simply too thin. The technique of segmentation cracking has been used instead (Futatsugi et al. [70], Hsueh [93], Hsueh and Yanaka [96], Leterrier et al. [124, 125], McGuigan et al. [137], Yanaka et al. [222, 223, 224]), where the relation between the measured mean crack spacing and the applied strain was used to characterize the film strength or fracture energy.

This chapter provides an analysis of delamination of a thin brittle film de-

posited on a stretched substrate. Residual stresses within the system are considered and a constant shear stress at the fully damaged film/substrate interface assumed. On the basis of this analysis an energy model of film segmentation cracking is next formulated. A transition condition states that the potential and dissipated energy of the cracked film cannot be greater than the energy of the intact structure and gives rise to a topological transformation of the coating. Thus, the crack density at the saturation stage can be obtained. Similar approach with application to thermal loading, without taking into account residual stresses, was considered before by Białaś [23]. In order to validate the model, the fracture energy of  $\text{SiO}_x$  film deposited on PET substrate is calculated, assuming the crack spacing and other mechanical and geometrical parameters of the system as given. At the end a comparison of the predicted results with experimental data found in the literature is performed.

### 3.2. Problem formulation

Let us consider a composite plate consisting of a substrate of width  $w$  and length  $L$  with a deposited thin film as presented in Figure 3.1. The substrate material is subjected to external loading  $\sigma_0$  causing its elongation. In the course of loading the film can delaminate and segmentation cracking takes place within the coating perpendicular to the direction of the applied loading. In a general case the external loading can be applied by controlled displacements of the composite ends directly to the substrate and to the film, see Figure 3.1(a). However, as the segmentation cracks within the film appear, the normal stresses at the crack faces become zero and the situation reduces to the considered problem, where the stresses  $\sigma_0$  are subjected only to the substrate material, as presented in Figure 3.1(b). In order to treat the problem analytically we shall consider a simple one dimensional strip model, where the interaction between the substrate and the film is realised by an interface of zero thickness, see Figure 3.1(c). The main stress components are normal stresses  $\sigma_f$  and  $\sigma_s$ , respectively within the film and the substrate. The interaction between the composite constituents is executed by the shear stress  $\tau$  at the film/substrate interface. We assume the relation between the stress  $\tau$  and the relative displacement at the interface presented in Figure 3.2 — a constant shear stress  $\tau_c$  remains independent of the actual value of the relative displacement. The equilibrium equations for the film and the substrate have the forms

$$\frac{d\sigma_f}{dx} - \frac{\tau}{h_f} = 0, \quad (3.1)$$

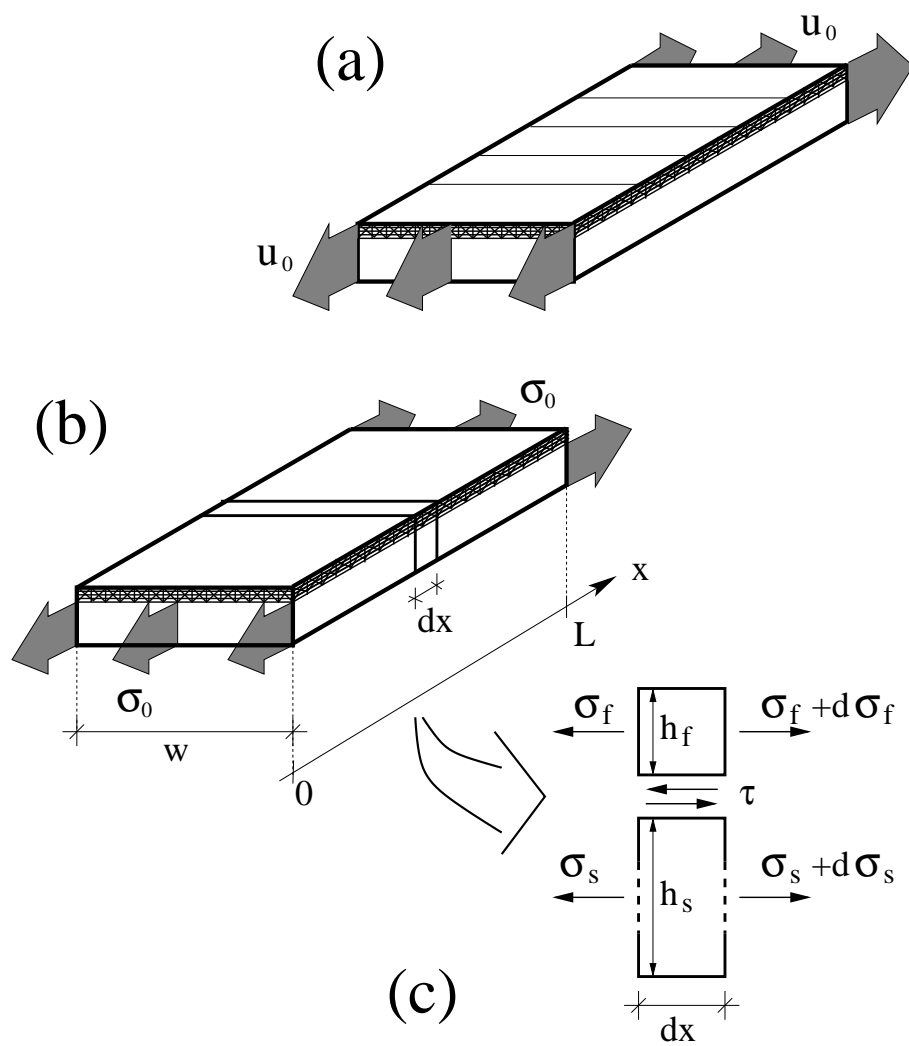


Figure 3.1. (a) Thin film deposited on a stretched substrate. (b) Considered problem with external loading  $\sigma_0$  applied to the substrate. (c) One dimensional strip model. Stresses acting on an infinitesimal composite element.

$$\frac{d\sigma_s}{dx} + \frac{\tau}{h_s} = 0. \quad (3.2)$$

Equations (3.1) and (3.2) can be obtained by considering an equilibrium state of an infinitesimal fragment of the composite as presented in Figure 3.1(c). The heights of the film and the substrate are denoted respectively by  $h_f$  and  $h_s$ .

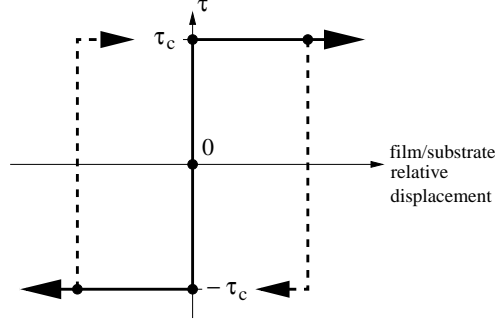


Figure 3.2. Interface constitutive law.

Both the film and the substrate are elastic, so we can write

$$\epsilon_f = \frac{\sigma_f - \sigma_f^r}{E_f}, \quad (3.3)$$

$$\epsilon_s = \frac{\sigma_s - \sigma_s^r}{E_s}, \quad (3.4)$$

where  $\sigma_f^r$  and  $\sigma_s^r$  are residual stresses present in the system, respectively in the film and the substrate, before the external loading  $\sigma_0$  is applied to the structure. Young moduli are denoted by  $E_f$  and  $E_s$ , elongations by  $\epsilon_f$ ,  $\epsilon_s$  with respect to the film and to the substrate. The residual stresses are associated with the residual strains  $\epsilon_f^r$ ,  $\epsilon_s^r$ , so we have

$$\sigma_f^r = E_f \epsilon_f^r, \quad (3.5)$$

$$\sigma_s^r = E_s \epsilon_s^r \quad (3.6)$$

with the residual strains expressed as

$$\epsilon_f^r = \frac{\sigma_f}{E_f} - \epsilon_f, \quad (3.7)$$

$$\epsilon_s^r = \frac{\sigma_s}{E_s} - \epsilon_s. \quad (3.8)$$

To fully formulate the governing equations we write the formulas relating strain  $\epsilon_f$  and  $\epsilon_s$  with the displacement fields  $u_f$  and  $u_s$  along the  $x$  axis, respectively for the film and the substrate. They take the form

$$\frac{du_f}{dx} = \epsilon_f, \quad (3.9)$$

$$\frac{du_s}{dx} = \epsilon_s. \quad (3.10)$$

Equations (3.1)–(3.10) together with the interface constitutive law

$$\dot{u}_f - \dot{u}_s = \dot{\Lambda} \operatorname{sign}(\tau), \quad \dot{\Lambda} \geq 0, \quad |\tau| - \tau_c \leq 0, \quad \dot{\Lambda}(|\tau| - \tau_c) = 0 \quad (3.11)$$

provide slip conditions and will serve as a basis for an energy model of segmentation cracking within the film. Equations (3.11) can be obtained when the cohesive zone model presented in Section 3.2 is specified to a rigid-slip response, with a constant value of threshold shear stress.

### 3.3. Residual stresses

Either because of the mismatch in the thermal expansion coefficients between the film and the substrate or due to a production process, there are residual stresses in the composite system before it is subjected to the external loading. As a result of this residual state two interfacial delamination zones develop from both ends of the plate, where the shear stress at the film/substrate interface reaches the critical value  $\tau_c$ . The interface remains intact in the middle of the system and no relative displacement between the film and the substrate in this particular area takes place. Figure 3.3(a) presents the distribution of shear stresses at the interface. Białas and Mróz [29, 30] considered a similar problem, analysing also a softening response of the interface.

By integrating the equilibrium equations (3.1) and (3.2) we obtain the normal stresses  $\sigma_f$  and  $\sigma_s$  acting respectively on the film and on the substrate. With respect to the coordinate system indicated in Figure 3.1(a), the functions  $\sigma_f(x)$  and  $\sigma_s(x)$  take the form

$$\sigma_f(x) = -\frac{\tau_c}{h_f} x, \quad (3.12)$$

$$\sigma_s(x) = \frac{\tau_c}{h_s} x \quad (3.13)$$

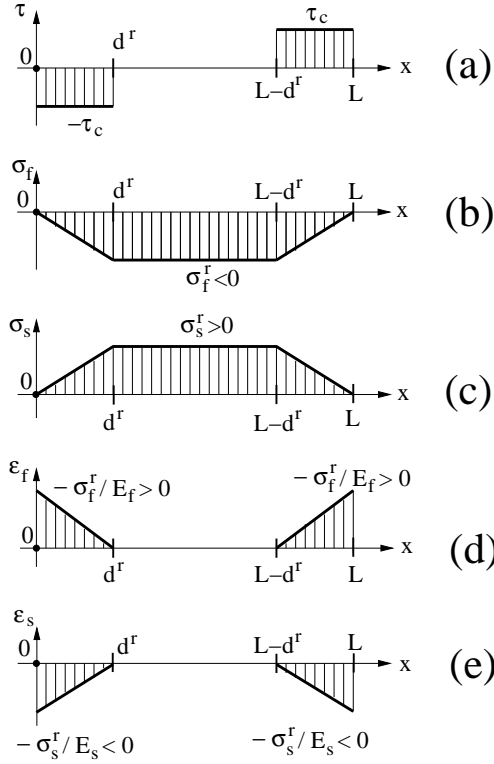


Figure 3.3. The residual stresses: (a) shear stress at the interface; (b) normal stress in the film; (c) normal stress in the substrate; (d) film strain; (e) substrate strain.

for  $x \in \langle 0, d^r \rangle$ , where  $d^r$  is the length of a single delamination zone developed due to the existence of residual stresses. The boundary conditions  $\sigma_s(0) = \sigma_f(0) = 0$  were imposed to obtain equations (3.12) and (3.13). The stress distribution at the other end of the system, that is for  $x \in \langle L - d^r, L \rangle$  has to be symmetric with respect to the symmetry axis of the composite and is schematically presented in Figure 3.3(b,c).

In the middle section of the composite, for  $x \in \langle d^r, L - d^r \rangle$ , the interface remains intact. The values of normal stresses in the substrate and in the film in this area are constant and equal the residual stresses

$$\sigma_f(x) = \sigma_f^r, \quad \sigma_s(x) = \sigma_s^r, \quad x \in \langle d^r, L - d^r \rangle. \quad (3.14)$$

Thus, the presence of the delaminated zones and slip at the film/substrate interface at both ends of the composite is the system response and adaptation to the residual stress state.

The length  $d^r$  of a single damage zone can be obtained from equations (3.12) and (3.13). We obtain respectively

$$d^r = -\frac{h_f}{\tau_c} \sigma_f^r, \quad (3.15)$$

$$d^r = \frac{h_s}{\tau_c} \sigma_s^r, \quad (3.16)$$

where the fact that  $\sigma_f(d^r) = \sigma_f^r$  and  $\sigma_s(d^r) = \sigma_s^r$  was used. It is seen that the values of residual stresses  $\sigma_f^r$  and  $\sigma_s^r$  cannot be independent. They have to satisfy the equality

$$h_s \sigma_s^r + h_f \sigma_f^r = 0, \quad (3.17)$$

resulting directly from equations (3.15) and (3.16). In fact, this is an equilibrium equation of a composite fragment defined by the coordinates  $(0, x)$  where  $x \in \langle 0, L - d^r \rangle$ .

The strain fields in the film and in the substrate can be obtained from equations (3.3), (3.4), (3.12) and (3.13). They take the form

$$\epsilon_f(x) = \begin{cases} -\frac{\tau_c}{h_f E_f} x - \frac{\sigma_f^r}{E_f}, & x \in \langle 0, d^r \rangle \\ 0, & x \in \langle d^r, L - d^r \rangle \end{cases}, \quad (3.18)$$

$$\epsilon_s(x) = \begin{cases} \frac{\tau_c}{h_s E_s} x - \frac{\sigma_s^r}{E_s}, & x \in \langle 0, d^r \rangle \\ 0, & x \in \langle d^r, L - d^r \rangle \end{cases}. \quad (3.19)$$

The fields have to be symmetric for  $x \in \langle L - d^r, L \rangle$ , as schematically presented in Figure 3.3(d,e).

### 3.4. External loading

Let us consider now the system response due to the subsequent external loading in the form of a tensile traction  $\sigma_0$  subjected to the substrate and causing an elongation of the whole composite. There are two stages to be considered. During the first stage the length of a single delamination zone does not increase and remains the same as during the residual state. This is related to the fact that in the residual state the film is pre-compressed, as a result of initial shear stresses at the interface reaching the critical value  $\tau_c$  for  $x \in \langle 0, d^r \rangle$  and  $x \in \langle L - d^r, L \rangle$ , see Figure 3.3.

The external loading is subjected to the substrate and causes the elongation of the whole system. The tensional stresses are transmitted to the film from the

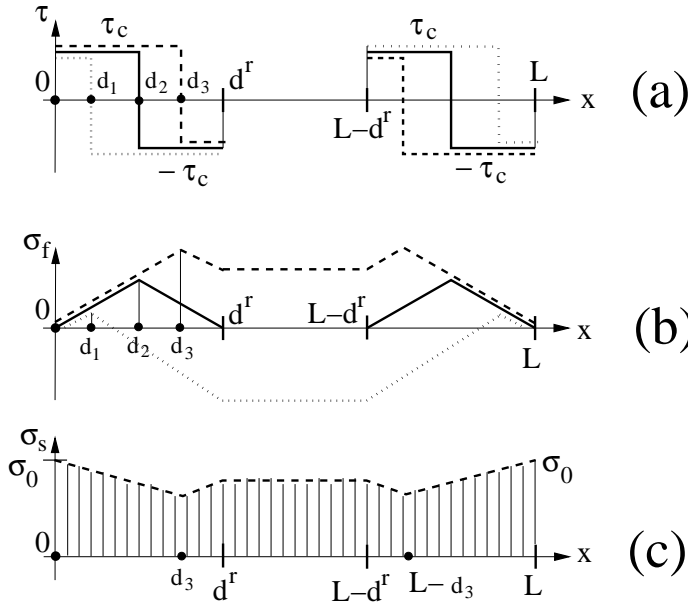


Figure 3.4. Stage I of film delamination: (a) shear stress at the interface; (b) film normal stress; (c) substrate normal stress; the line styles refer to three different lengths of a single reverse slip zone:  $d_3 > d_2 = \frac{d^r}{2} > d_1$  ( $d_3, d_2, d_1 < d^r$ ).

substrate through the interfacial shear stresses, resulting from film/substrate relative slip. In the residual state they caused the compressional stresses within the film; during the subsequent external loading the interfacial stresses should result in film tension. The transformation from film compression to tension is a continuous process, in which the sign of interfacial shear stresses changes continuously together with relative displacement between the film and the substrate. This takes place during the first stage of the loading, when the increase of the external loading results in a formation of reverse slip regions within the already damaged interface, without an increase of the length of a single delamination zone. Due to the initial rigidity of the interface the reverse slip cannot extend over the entire interface. This scenario is schematically presented in Figure 3.4. The length of a single reverse slip zone is denoted by  $d$  and increases from zero, due to an increasing value of the external loading  $\sigma_0$ . During the second stage of the loading, the traction  $\sigma_0$  is high enough to change the sign of interfacial reverse slip along the whole area of the already damaged bond and to cause a further development of the failure process at the film/substrate interface. The length of a single reverse slip zone becomes bigger than the length of a damaged zone resulting from the residual stresses. The configuration of shear and normal



$$\epsilon_f(x) = \begin{cases} \frac{\tau_c}{h_f E_f} (x + d^r), & x \in \langle 0, d \rangle \\ \frac{\tau_c}{h_f E_f} (d^r + 2d - x), & x \in \langle d, d^r \rangle \\ 2 \frac{\tau_c d}{h_f E_f}, & x \in \langle d^r, L - d^r \rangle \end{cases}. \quad (3.22)$$

Fields  $\sigma_f(x)$  and  $\epsilon_f(x)$  for  $x \in \langle L - d^r, L \rangle$  have to be symmetric with respect to the symmetry axis of the structure. The distribution of  $\sigma_f(x)$  is schematically presented in Figure 3.4(b).

By imposing the boundary and continuity conditions

$$\sigma_s(0) = \sigma_0, \quad [\sigma_s(d)] = [\sigma_s(d^r)] = 0 \quad (3.23)$$

and using equation (3.16) we obtain the stress and strain fields in the substrate

$$\sigma_s(x) = \begin{cases} \sigma_0 - \frac{\tau_c}{h_s} x, & x \in \langle 0, d \rangle \\ \sigma_0 + \frac{\tau_c}{h_s} (x - 2d), & x \in \langle d, d^r \rangle \\ \sigma_0 + \frac{\tau_c}{h_s} (d^r - 2d), & x \in \langle d^r, L - d^r \rangle \end{cases}, \quad (3.24)$$

$$\epsilon_s(x) = \begin{cases} \frac{\sigma_0}{E_s} - \frac{\tau_c}{h_s E_s} (x + d^r), & x \in \langle 0, d \rangle \\ \frac{\sigma_0}{E_s} + \frac{\tau_c}{h_s E_s} (x - 2d - d^r), & x \in \langle d, d^r \rangle \\ \frac{\sigma_0}{E_s} - 2 \frac{\tau_c}{h_s E_s} d, & x \in \langle d^r, L - d^r \rangle \end{cases}. \quad (3.25)$$

The fields  $\sigma_s(x)$  and  $\epsilon_s(x)$  for  $x \in \langle L - d^r, L \rangle$  have to be symmetric with respect to the symmetry axis of the composite. The distribution of  $\sigma_s(x)$  is schematically presented in Figure 3.4(c).

The relation between  $d$  and  $\sigma_0$  in equations (3.21)–(3.25), that is between the length of a single reverse slip zone and the loading traction, still remains to be unknown and shall be derived now. In order to do that we shall consider the film/substrate interfacial region for  $x \in \langle d, L - d \rangle$ . As mentioned before, the relative displacement between the film and the substrate in this particular area should remain the same as in the residual state, unchanged by the progressive external loading — this is due to the rigid-slip model of the interface, where the reverse slip zone cannot extend along the entire interfacial region. We have

$$u_s(x) - u_f(x) = \tilde{u}_s(x) - \tilde{u}_f(x), \quad x \in \langle d, L - d \rangle \quad (3.26)$$

and subsequently we can write

$$\epsilon_s(x) - \epsilon_f(x) = \tilde{\epsilon}_s(x) - \tilde{\epsilon}_f(x), \quad x \in \langle d, L - d \rangle. \quad (3.27)$$

The dashed symbols refer to the quantities in the residual state. By substituting equations (3.18), (3.19), (3.22) and (3.25) into equation (3.27) we obtain the following relation between  $\sigma_0$  and  $d$

$$\sigma_0 = \frac{2\tau_c(E_s h_s + E_f h_f)}{E_f h_f h_s} d. \quad (3.28)$$

For  $d = d^r$  the residual damage zone is erased by the developing reverse slip zone and the second stage of the delamination begins.

### 3.4.2. Stage II

During the second stage of the loading the traction  $\sigma_0$  is high enough for the reverse slip zone to totally erase the residual damage zone and to cause a further development of delamination process between the film and the substrate. The configuration of shear stresses at this stage is presented in Figure 3.5. The resulting film and substrate stress and strains can be obtained from equations (3.1), (3.2), (3.3), (3.4) and (3.11). In the film they are described by the functions

$$\sigma_f(x) = \begin{cases} \frac{\tau_c}{h_f} x, & x \in \langle 0, d \rangle \\ \frac{\tau_c}{h_f} d, & x \in \langle d, L - d \rangle \end{cases}, \quad (3.29)$$

$$\epsilon_f(x) = \begin{cases} \frac{\tau_c}{h_f E_f} (x + d^r), & x \in \langle 0, d \rangle \\ \frac{\tau_c}{h_f E_f} (d^r + d), & x \in \langle d, L - d \rangle \end{cases}. \quad (3.30)$$

Equation (3.15) and the boundary and continuity conditions

$$\sigma_f(0) = [\sigma_f(d)] = 0 \quad (3.31)$$

have been imposed to obtain (3.29) and (3.30). The fields  $\sigma_f(x)$  and  $\epsilon_f(x)$  for  $x \in \langle L - d, L \rangle$  have to be symmetric with respect to the symmetry axis of the structure. The distribution of  $\sigma_f(x)$  is schematically presented in Figure 3.5(b).

By imposing the boundary and continuity conditions

$$\sigma_s(0) = \sigma_0, \quad [\sigma_s(d)] = 0 \quad (3.32)$$

and using equation (3.16) we obtain the stress  $\sigma_s$  and the strain  $\epsilon_s$  in the substrate

$$\sigma_s(x) = \begin{cases} \sigma_0 - \frac{\tau_c}{h_s} x, & x \in \langle 0, d \rangle \\ \sigma_0 - \frac{\tau_c}{h_s} d, & x \in \langle d, L - d \rangle \end{cases}, \quad (3.33)$$

$$\epsilon_s(x) = \begin{cases} \frac{\sigma_0}{E_s} - \frac{\tau_c}{h_s E_s} (x + d^r), & x \in \langle 0, d \rangle \\ \frac{\sigma_0}{E_s} - \frac{\tau_c}{h_s E_s} (d^r + d), & x \in \langle d, L - d \rangle \end{cases}. \quad (3.34)$$

Fields  $\sigma_s(x)$  and  $\epsilon_s(x)$  for  $x \in \langle L - d, L \rangle$  have to be symmetric with respect to the symmetry axis of the composite. The distribution of  $\sigma_s(x)$  is schematically presented in Figure 3.5(c).

In order to obtain the relation between the traction  $\sigma_0$  and the length of a single damage zone we have to impose the condition

$$\epsilon_s = \epsilon_f \quad (3.35)$$

for  $x \in \langle d, L-d \rangle$ , meaning that there is no relative displacement between the film and the substrate in this particular area. By substituting equations (3.30) and (3.34) into (3.35) we obtain

$$\sigma_0 = \frac{\tau_c(E_s h_s + E_f h_f)}{E_f h_f h_s} (d + d^r). \quad (3.36)$$

For  $d = L/2$  the whole interface is damaged. Due to the constant value of the interface stress  $\tau = \tau_c$  any further increase in the loading traction  $\sigma_0$  subjected to the substrate does not influence the stress distribution within the film. The film stress can be obtained from equation (3.29) for  $d = L/2$ .

Let us derive now the formulas for the displacement fields of the substrate and of the film for  $x \in \langle 0, d \rangle$ , that is for the zone where the substrate and the film contact through a damaged interface. They will be used in the subsequent section, where an energy model of film segmentation cracking is formulated.

By integrating function (3.34) for  $x \in \langle 0, d \rangle$  and using formula (3.36) one obtains the displacement field of the substrate within the region  $x \in \langle 0, d \rangle$

$$u_s(x) = u_s(0) + \frac{x[4d(E_f h_f + E_s h_s) - E_f h_f(2d^r + x)]\tau_c}{2E_f E_s h_f h_s}, \quad (3.37)$$

where  $u_s(0)$  is the integration constant being the value of  $u_s(x)$  for  $x = 0$ . Assuming that the substrate is constrained for  $x = 0$ ,  $u_s(0) = 0$  we obtain from equation (3.37) the displacement of the substrate material for  $x = L$  in the form:

$$u_s(L) = \frac{[d^2 E_f h_f + (d + d^r) E_s h_s L]\tau_c}{E_f E_s h_f h_s}. \quad (3.38)$$

Integration of function (3.30) for  $x \in \langle 0, d \rangle$  with the continuity condition

$$u_f(d) = u_s(d)$$

provides the displacement field of the film within the region  $x \in \langle 0, d \rangle$

$$u_f(x) = u_s(0) + \frac{[d^2(E_f h_f + E_s h_s) + E_s h_s x(2d^r + x)]\tau_c}{2E_f E_s h_f h_s}. \quad (3.39)$$

Here again equation (3.36) has been used.

The system response to the subjected tensile loading has been fully described. The assumed one dimensional strip model allowed for analytical expressions of all physical quantities at the residual state and at the subsequent two delamination stages. Now we can proceed to the description of segmentation cracking within the film.

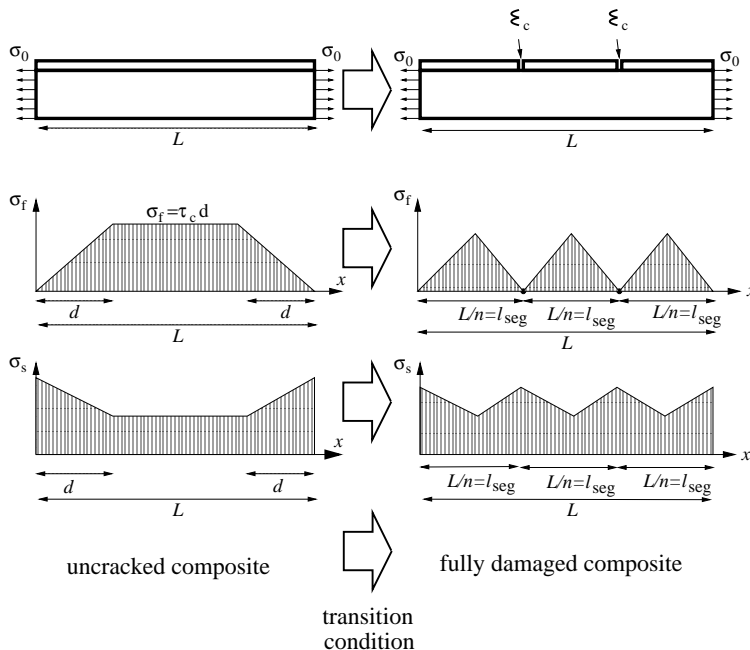


Figure 3.6. Topological transformation from an uncracked to a fully damaged structure.

### 3.5. Energy model

As presented in Figure 3.5(b) a plateau of a constant normal stress is present in the middle section of the structure. Because of that, the formation of cracks within the film is strongly dependent upon a stochastic distribution of micro defects within the material. These issues have been considered in the papers by Handge et al. [84, 85]. Białas and Mróz [29, 30] analysed mechanisms governing multiple cracking within a thin film assuming the film to be perfectly brittle and using a critical stress criterion. They assumed that the cracks form exactly in the middle of the plateau, corresponding to the realistic assumption that interface material cannot be perfectly rigid. As opposed to the critical stress approach, we

shall introduce a topological transformation of the film leading to occurrence of cracks. The present approach does not account for a loading history and focuses only on energy levels of both the intact and the fragmented composite, see Figure 3.6. In Section 3.5.1. we shall consider the energy for the whole composite, being the film, the substrate and the interface. In Section 3.5.2. we shall focus on a sub-system of the structure, being the film and the interface and formulate an energy failure condition only for this special case. It shall be showed that the energy failure condition for the whole structure reduces to the failure condition for the film-interface subsystem when the substrate is thick in comparison to the film  $h_f \ll h_s$  and their stiffnesses  $E_f$  and  $E_s$  are in the same range. Similar energetic approach to segmentation cracking, but for a case of thermal loading and without residual stresses, was presented by Białas [23].

### 3.5.1. Failure model based on the total system energy

The energy of an uncracked composite is expressed by the formula

$$\Pi = \mathcal{E}_s + \mathcal{E}_f + D_\tau - \Pi_\sigma, \quad (3.40)$$

where

$$\mathcal{E}_f = 2 \left( \frac{1}{2} w h_f \int_0^d \frac{\sigma_f(x)^2}{E_f} dx \right) + \frac{1}{2} w h_f \frac{\sigma_f^2}{E_f} (L - 2d) \quad (3.41)$$

is the elastic energy stored in the film,

$$\mathcal{E}_s = 2 \left( \frac{1}{2} w h_s \int_0^d \frac{\sigma_s(x)^2}{E_s} dx \right) + \frac{1}{2} w h_s \frac{\sigma_s^2}{E_s} (L - 2d) \quad (3.42)$$

is the elastic energy stored in the substrate,

$$D_\tau = -2w\tau_c \int_0^d (u_s(x) - u_f(x)) dx \quad (3.43)$$

is the energy dissipated on the film/substrate interface by the shear stress, and

$$\Pi_\sigma = \sigma_0 h_s w u_s(L) \quad (3.44)$$

is the potential of external forces acting on the substrate. Thus, the energy  $\Pi$  should be understood as the potential energy of the structure plus the energy dissipated at the film/substrate interface.

The first terms in equations (3.41) and (3.42) refer to the elastic energy stored within the film and the substrate contacting through two delaminated

zones and  $\sigma_f(x)$  and  $\sigma_s(x)$  are provided by equations (3.29) and (3.33), respectively. The second terms in (3.41) and (3.42) refer to the elastic energy stored within the film and the substrate perfectly bonded with each other and, according to equations (3.29) and (3.33), we have  $\sigma_f = \tau_c d/h_f$ ,  $\sigma_s = \sigma_0 - \tau_c d/h_s$ .

By substituting (3.29), (3.33), (3.36) (3.37), (3.38) and (3.39) into (3.40) we obtain

$$\Pi = \frac{[2d^3 E_f h_f + E_s h_s L d(3d + 6d^f) + 3d^{f^2}(E_s h_s - E_f h_f)L](E_f h_f + E_s h_s)w\tau_c^2}{-6E_f^2 E_s h_f^2 h_s}. \quad (3.45)$$

Let us consider now a composite consisting of  $n$  film fragments contacting with the substrate through a fully damaged interface as presented in Figure 3.6. The system energy for this particular case can be expressed by the formula

$$\Pi^n = \mathcal{E}_s^n + \mathcal{E}_f^n + D_\tau^n - \Pi_\sigma^n + (n-1)wh_f \mathcal{E}_c, \quad (3.46)$$

where

$$\mathcal{E}_f^n = 2 \left( \frac{1}{2} nwh_f \int_0^{L/(2n)} \frac{\sigma_f(x)^2}{E_f} dx \right) \quad (3.47)$$

is the elastic energy stored in  $n$  film fragments,

$$\mathcal{E}_s^n = 2 \left( \frac{1}{2} nwh_s \int_0^{L/(2n)} \frac{\sigma_s(x)^2}{E_s} dx \right) \quad (3.48)$$

is the elastic energy stored in the substrate,

$$D_\tau^n = -2nw\tau_c \int_0^{L/(2n)} (u_s(x) - u_f(x)) dx \quad (3.49)$$

is the energy dissipated at the fully damaged interface by  $n$  film fragments contacting with the substrate, and

$$\Pi_\sigma^n = \sigma_0 h_s w u_s^n(L) \quad (3.50)$$

is the potential of external forces acting on the substrate. The last term in equation (3.46) refers to  $n-1$  cracks formed, with  $\mathcal{E}_c$  being the specific energy of a unit area. The term  $(n-1)wh_f \mathcal{E}_c$  is the energy dissipated to form  $n-1$  segmentation cracks. Similar to the previous case, the energy  $\Pi^n$  is the potential energy of the composite plus the dissipated energy. In the present case, however, the dissipated energy is the energy dissipated at the film/substrate interface and the energy dissipated to create segmentation cracks.

According to equations (3.29) and (3.33) we have

$$\sigma_f(x) = \frac{\tau_c}{h_f} x \quad (3.51)$$

and

$$\sigma_s(x) = \sigma_0 - \frac{\tau_c}{h_s} x \quad (3.52)$$

in equations (3.47) and (3.48). The displacements  $u_s(x)$  and  $u_f(x)$  in (3.49) can be specified for the present case by setting  $d = L/(2n)$  in equations (3.37) and (3.39). We obtain

$$u_s(x) = u_s(0) + \frac{x[2L(E_f h_f + E_s h_s)/n - E_f h_f(2d^f + x)]\tau_c}{2E_f E_s h_f h_s}, \quad (3.53)$$

$$u_f(x) = u_s(0) + \frac{[L^2(E_f h_f + E_s h_s)/(4n^2) + E_s h_s x(2d^f + x)]\tau_c}{2E_f E_s h_f h_s}. \quad (3.54)$$

The substrate displacement  $u_s^n(L)$  in equation (3.50) can be expressed by

$$u_s^n(L) = n 2 \int_0^{L/(2n)} \epsilon_s(x) dx \quad (3.55)$$

with

$$\epsilon_s(x) = \frac{\sigma_0}{E_s} - \frac{\tau_c}{h_s E_s} (x + d^f), \quad (3.56)$$

according to equation 3.34(a).

For the fragmentation process to occur we postulate the following transition condition

$$\Pi \geq \Pi^n \quad (3.57)$$

stating, that the energy  $\Pi^n$  of a damaged system cannot be greater than the energy  $\Pi$  of the intact structure. This should be satisfied for the value of external loading  $\sigma_0$  identical for the uncracked and the fully damaged composite, as presented in Figure 3.6. Inequality (3.57) gives a physical meaning to a transformation changing the topology of the intact film into a system of  $n$  segments forming a maximally damaged structure. This approach does not account for a loading history and considers only energy levels of the intact and the fully fragmented system. The condition (3.57) states that the cracks will occur when the energy  $\Pi$  of an intact composite happens to be greater than the energy  $\Pi^n$  of a cracked structure consisting of  $n$  fragments. Bearing in mind that the energy  $\Pi$  is an increasing function of  $d$ , that is the length of a friction zone, we can formulate what follows. The cracks will occur when for increasing  $d$

the inequality (3.57) happens to be true. The consequent number of strip fragments  $n$  is a function of the smallest possible length  $d$  satisfying the transition condition (3.57) and, as an unknown parameter, can be derived from (3.57).

By substituting (3.36), (3.51), (3.52), (3.53), (3.54) and (3.55) into (3.46) we obtain

$$\begin{aligned} \Pi^n = & \frac{E_f h_f L^2 - 6(d + d^r)[(d - d^r)E_f h_f + (d + d^r)E_s h_s]n^2}{12E_f^2 E_s h_f^2 h_s n^2} \times \\ & \times (E_f h_f + E_s h_s)Lw\tau_c^2 + (n - 1)wh_f \mathcal{E}_c. \end{aligned} \quad (3.58)$$

Using equations (3.45) and (3.58) the inequality (3.57) can be rewritten now in the following form

$$\frac{(\lambda + 1)[\xi^2(3 - \xi)n^2 - 2]}{(n - 1)n^2} \geq \beta, \quad (3.59)$$

where the dimensionless parameters have been introduced

$$\xi = \frac{d}{L/2} \geq \frac{d^r}{L/2}, \quad \lambda = \frac{E_f h_f}{E_s h_s}, \quad \beta = \frac{24h_f^2 E_f}{L^3 \tau_c^2} \mathcal{E}_c. \quad (3.60)$$

Thus,  $\xi$  is a dimensionless length of a single damaged zone,  $0 \leq \xi \leq 1$ . When the film is very thin in comparison to the substrate,  $h_f \ll h_s$ , and the stiffnesses of the film and the substrate are in the same range we can assume  $\lambda \approx 0$ . To understand the meaning of parameter  $\beta$  let us calculate the value of elastic energy stored in the uncracked film, when the whole interface is damaged. From equation (3.41) for  $d = L/2$  we obtain

$$\mathcal{E}_f^{\max} = \frac{\tau_c^2 L^3}{24E_f h_f^2}. \quad (3.61)$$

Thus, the parameter  $\beta$  is the ratio between the specific energy  $\mathcal{E}_c$  of film unit area and the maximum value of elastic energy stored in the intact film

$$\beta = \frac{\mathcal{E}_c}{\mathcal{E}_f^{\max}}. \quad (3.62)$$

By introducing

$$\beta_n(\xi) = \frac{(\lambda + 1)[\xi^2(3 - \xi)n^2 - 2]}{(n - 1)n^2} \quad (3.63)$$

we can write

$$\beta_n(\xi) \geq \beta. \quad (3.64)$$

According to what has been stated above, condition (3.64) has to be satisfied for the smallest possible length of friction zone, that is for the smallest possible  $\xi$ . Condition (3.64) states that the elastic energy of the intact structure is big enough when compared to the specific surface energy of cracks. Thus, the cracks will occur when the increasing elastic energy is high enough to be used as a driving force for the fragmentation process.

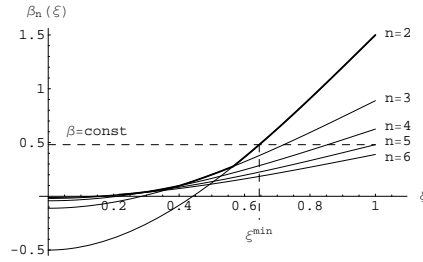


Figure 3.7. The plots of functions  $\beta_n(\xi)$  for  $\lambda = 0$ .

Formula (3.63) provides a whole family of functions  $\beta_n(\xi)$ . They are presented in Figure 3.7 for  $\lambda = 0$  and for several values of  $n$ .

Let us have an equality in the condition (3.64)

$$\beta = \beta_n(\xi) \quad (3.65)$$

and assume that  $\beta$  is a given value defined by the mechanical and geometrical parameters of the system. The smallest possible  $\xi^{\min}$  that satisfies equation (3.65) for the whole family of functions  $\beta_n$  is the actual length of a single delamination zone leading to the segmentation process. The parameter  $n$  for which

$$\beta = \beta_n(\xi^{\min}) = \text{const}$$

happens to be true, is the actual number of strip fragments occurring for a system characterized by the dimensionless parameter  $\beta$ . The parameters  $\xi^{\min}$  and  $n$  can be obtained from Figure 3.7 by considering an intersection of line  $\beta = \text{const}$  with an appropriate  $\beta_n(\xi)$  function. The thick line in Figure 3.7 consists of respective  $\beta_n(\xi)$  functions, providing the smallest possible value of  $\xi$  for any  $\beta$ . The line is presented separately in Figure 3.8 and allows for specification of respective values of  $\xi^{\min}$  and  $n$  for a given  $\beta$ . Thus, the present energy model provides a unique solution in the number of fragments and the length of friction

zone within the intact structure leading to cracks occurrence. It is clearly seen in Figure 3.8 that smaller the specific surface energy, that is the parameter  $\beta$ , the more cracks will occur. For the specific surface energy  $\mathcal{E}_c$  kept constant, it can be concluded that a longer strip breaks into more pieces, since it can store a bigger value of elastic energy. Table 3.1 presents examples of the values of  $\beta_n^{\max}$  and  $\beta_n^{\min}$  being respectively the upper and the lower limits for  $\beta$  for a given number of strip fragments  $n$ , as exemplified in Figure 3.8 for  $n = 5$  and  $n = 6$ . These data can serve as a starting point for an identification of material parameters of the system.

Table 3.1. Upper  $\beta_n^{\max}$  and lower  $\beta_n^{\min}$  limits on the value of  $\beta$  for a given number of fragments  $n$  and for  $\lambda = 0$ .

$n$	$\beta_n^{\max}$	$\beta_n^{\min}$
2	1.5	0.277778
3	0.277778	0.0972222
4	0.0972222	0.045
5	0.045	0.0244444
10	0.00469136	0.00347107
20	0.000540166	0.000464853
30	0.000155899	0.000141057
100	4.06081E-6	3.94079E-6

Let us measure the value of specific surface energy  $\mathcal{E}_c$  for a given crack line spacing  $l_{\text{seg}}$  observed during a saturation stage, when further loading of the substrate does not induce additional cracking within the coating. The configuration is schematically presented in Figure 3.6, where a film of initial length  $L$  has segmented into  $n$  fragments. The following equality holds

$$L = n l_{\text{seg}}. \quad (3.66)$$

By knowing the number  $n$  of strip fragments and by using the data in Table 3.1, we can put an upper and a lower limit on the non-dimensional parameter  $\beta$ , being a function of mechanical and geometrical parameters of the system. By substituting equation (3.66) into the definition of  $\beta$ , equation 3.60(c), we have

$$\beta_n^{\min} < \frac{24h_f^2 E_f}{(n l_{\text{seg}})^3 \tau_c^2} \mathcal{E}_c < \beta_n^{\max}, \quad (3.67)$$

where  $\beta_n^{\min}$  and  $\beta_n^{\max}$  are given for any number of strip fragments. Thus, inequalities (3.67) put an upper and a lower limit on the value of one material

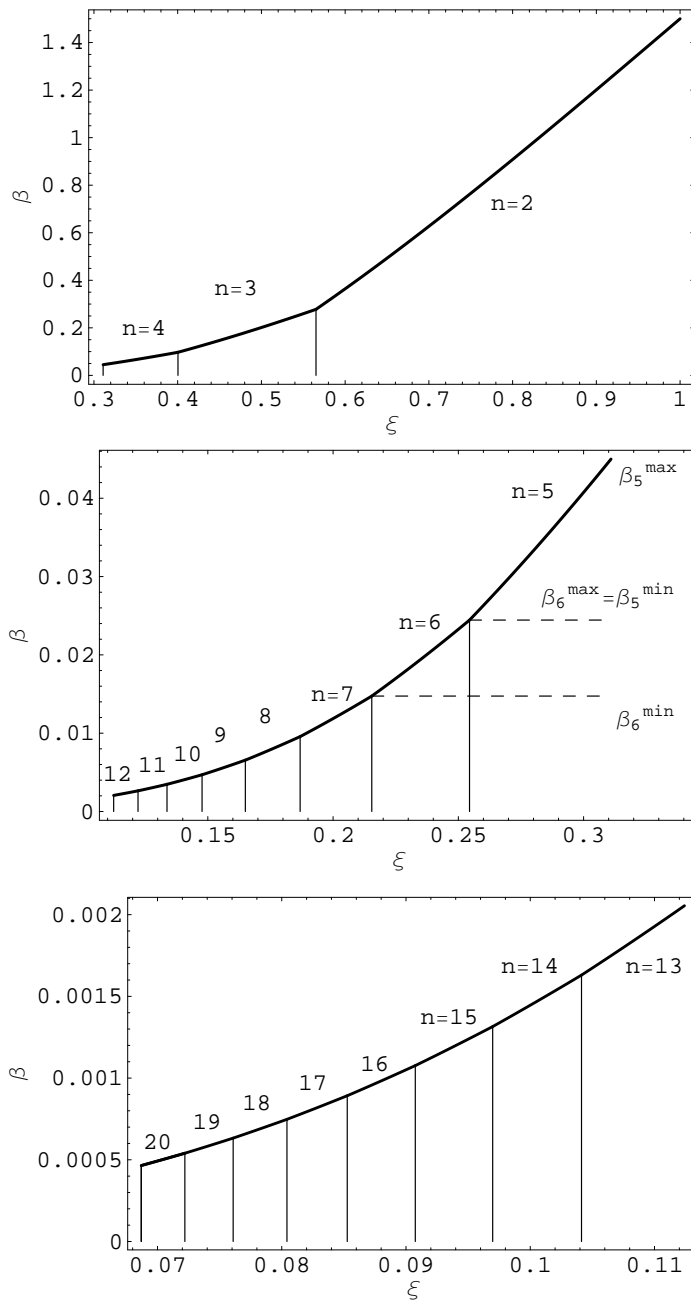


Figure 3.8. Value of  $\beta$  versus the length of friction zone  $\xi$  and the number of strip fragments  $n$  for  $\lambda = 0$ .

parameter (e.g.  $\mathcal{E}_c$ ), when the crack spacing  $l_{\text{seg}}$  at the saturation stage as well as other mechanical and geometrical data (e.g.  $\tau_c$ ,  $E_f$ ,  $h_f$ ) are known. In Section 3.6. we shall use the presented theoretical approach to specify the fracture energy of a silicon oxide thin coatings on polymer substrates.

### 3.5.2. Failure model based on the film/interface sub-system energy

It is very interesting to analyse the influence of energy stored in the substrate on the transition condition (3.57). Let us consider now only the elastic energy stored in the film and the energy dissipated at the interface by the shear forces, and neglect the influence of substrate upon the transition condition (3.57). The formulas for  $\Pi$  and  $\Pi^n$  take the form

$$\Pi_{\text{fi}} = \mathcal{E}_f + D_\tau, \quad (3.68)$$

$$\Pi_{\text{fi}}^n = \mathcal{E}_f^n + D_\tau^n + (n-1)wh_f\mathcal{E}_c, \quad (3.69)$$

where  $\mathcal{E}_f$ ,  $D_\tau$ ,  $\mathcal{E}_f^n$ ,  $D_\tau^n$  are given by equations (3.41), (3.43), (3.47) and (3.49). The energies  $\Pi_{\text{fi}}$  and  $\Pi_{\text{fi}}^n$  account for the potential and dissipated energies in the considered sub-system. All previous remarks apply.

By formulating a transition condition

$$\Pi_{\text{fi}} \geq \Pi_{\text{fi}}^n \quad (3.70)$$

we focus only on a sub-system of the total structure consisting of the film and the film/substrate interface. It is only the energy in this sub-system which governs the topological transformation from the uncracked to the fully damaged state. By substituting (3.68) and (3.69) into (3.70), the transition condition can be rewritten in the following form

$$\frac{\xi^2[3 + (\lambda - 1)\xi]n^2 - 2 - \lambda}{(n - 1)n^2} \geq \beta. \quad (3.71)$$

The dimensionless parameters  $\xi$ ,  $\lambda$  and  $\beta$  have been already introduced by equation (3.60).

It is very interesting to note that the transition condition (3.59) based on the energy for the total system and the transition condition (3.71) for the film/interface sub-system reduce to the same inequality

$$\frac{\xi^2(3 - \xi)n^2 - 2}{(n - 1)n^2} \geq \beta \quad (3.72)$$

for  $\lambda$  approaching zero. This is true, for example, when the film is thin in comparison to the substrate  $h_f \ll h_s$  and their stiffnesses  $E_f$  and  $E_s$  are in the same range. In such a case, one can simplify the problem and focus only upon the energies of the film and the interface and neglect the substrate effect. The obtained results shall be the same as if the energy for the whole composite was considered. This is so, because the topological transformation from an uncracked to a fully damaged state does not influence much the value of substrate potential energy, when the substrate is much thicker than the film.

### 3.6. Specification of the fracture energy of a silicon oxide thin coating

A crucial point in the present study is the distribution of the interfacial shear stress when the segmentation cracking within the film has been saturated. Agrawal and Raj [4] used a sinusoidal shear stress distribution with half a sine wave, Shieu et al. [184] modelled the stress field using one quarter of a sine wave. Cox [51] analysed a fiber embedded within a matrix and assumed interface shear stress to be proportional to the relative displacement between the fiber and the matrix. Some researches (Aveston and Kelly [15], Kelly and Tyson [108], Kelly [107]) investigated fracture mechanisms of fiber-reinforced composites assuming a constant value of a shear stress at fiber/matrix interface. This approach was also applicable to brittle coating/ductile substrate adhesion studies (Hu and Evans [97]) and particularly to silicon oxide thin coatings  $\text{SiO}_x$  on poly(ethylene terephthalate) (PET) substrates (Futatsugi et al. [70], Hsueh [93], Hsueh and Yanaka [96], Leterrier et al. [124, 125], McGuigan et al. [137], Yanaka et al. [222, 223, 224]).

In this case the interfacial shearing responsible for debonding is a result of slip deformation mechanisms observed for PET at high strains in small-angle x-ray spectrometry measurements (Stockfleth et al. [186]). In the papers by Leterrier et al. [124, 125] the substrate shear stress at saturation is compared with the interfacial shear strength, proving that up to 120°C both are equivalent within the experimental scatter. Moreover, the adhesive strength was found to be independent of coating's thickness. Yanaka et al. [224] observed that the crack spacing within  $\text{SiO}_x$  film on PET substrate was proportional to the film thickness. They argued that such a behaviour is expected for a constant shear stress at the film/substrate interface.

Depending upon the properties of the interface two types of the shear lag model have been reported in the literature. In the first one the interfacial shear

stress is governed by a constant yield strength of the substrate (Hu and Evans [97], Shieu et al. [184]). In this case the stress distribution in the system can be related to the yield strength. The second type of models assumes the interface to be elastic. In this case the shear stress is assumed to be proportional to the relative displacement between the film and the substrate (Laws and Dvorak [120], Yanaka et al. [224]). The present treatment can be classified to the first type of shear lag models, where the constant interfacial stress is a result of slip deformation mechanisms observed for PET (Stockfleth et al. [186]). In this context the presented model is applicable to the description of segmentation of  $\text{SiO}_x$  films on PET substrates. Table 3.2 summarizes the values of interfacial shear  $\tau_c$  at the saturation reported in the literature. The data is valid for room temperature. Leterrier et al. [125] presented also the variation of  $\tau_c$  as a function of temperature in the range 20–175°C. In the following the value of  $\tau_c = 70$  MPa will be used for further calculations.

Table 3.2. Interfacial strength  $\tau_c$ , Young modulus  $E_f$  of the  $\text{SiO}_x$  film and Young modulus  $E_s$  of PET substrates.

Reference	$\tau_c$ [MPa]	$E_f$ [GPa]	$E_s$ [GPa]
Leterrier et al. [125]	80	79.5	3.92
Leterrier et al. [124]	60–85	—	—
Yanaka et al. [224]	—	43	4.7
Yanaka et al. [222]	—	73	—
Yanaka et al. [223]	28–42	73	5.92–6.28
McGuigan et al. [137]	63	70	—
Hsueh and Yanaka [96]	—	73	4.84

Table 3.3. Experimental mean crack spacings  $l_{\text{seg}}$  at saturation in  $\text{SiO}_x$  films with different thicknesses  $h_f$  deposited on PET substrates; the absolute values of film residual stresses  $|\sigma_f^r|$  (after Yanaka et al. [224]).

$h_f$ [nm]	$v$ [ $\mu\text{m}^{-1}$ ]	$ \sigma_f^r $ [MPa]
75	0.5	412.8
123	0.299	249.4
215	0.2	176.3
660	0.074	68.8

Linear elasticity is considered in the present analytical modelling. While the yield strain of the PET substrate is about 2.2 % (Yanaka et al. [224]) it was reported by Leterrier et al. [125] that the permanent strain of the  $\text{SiO}_x$ /PET

system upon unloading is negligible for an applied strain up to 4 %. Using this information Hsueh [93] showed that for loading strain greater than 4 % the decreasing rate in the relation between mean crack spacing and the loading strain is very small. Realistically including plasticity in the analysis, the decreasing rate would become even smaller. It can therefore be argued that plastic response of the substrate in the SiO<sub>x</sub>/PET system has a small effect upon the saturation of segmentation cracks within the film. The presented energy model, where the elastic substrate has been assumed, should be therefore applicable.

The other material parameters to be used in the calculations are the Young moduli of the film and the substrate. The data reported in the literature is also presented in Table 3.2 and further calculations will be carried on with the values  $E_f = 73$  GPa,  $E_s = 4.7$  GPa. In the following we shall consider the failure model based on the total system energy, since it is clearly seen that the film and substrate moduli  $E_f$  and  $E_s$  are not in the same range and the parameter  $\lambda$  is not close to zero. Thus, the formulation of Section 3.5.1. shall be used instead of the simplified analysis presented in Section 3.5.2.. Experimental mean crack spacings  $l_{\text{seg}}$  or crack densities at saturation in SiO<sub>x</sub> films with different thicknesses deposited on PET substrates are given in Table 3.3, Table 3.4 and Table 3.5. The data were obtained by Hsueh and Yanaka [96], Leterrier et al. [124] and Yanaka et al. [224], and will serve as an input for measuring the value of fracture energy by means of inequalities (3.67). In all cases the thickness of the PET substrate was 12  $\mu\text{m}$ . The relation between the mean crack spacing  $l_{\text{seg}}$  and the crack density  $v$  has the form

$$l_{\text{seg}} = \frac{1}{v}. \quad (3.73)$$

Table 3.4. Experimental crack density  $\rho$  at saturation in SiO<sub>x</sub> films with different thicknesses  $h_f$  deposited on PET substrates (after Leterrier et al. [124]).

$h_f$ [nm]	$v$ [ $\mu\text{m}^{-1}$ ]
30	$0.725 \pm 0.087$
53	$0.5 \pm 0.022$
96	$0.336 \pm 0.015$
103	$0.389 \pm 0.021$
145	$0.377 \pm 0.027$
156	$0.362 \pm 0.013$

The energy model of segmentation cracking was formulated for the second stage of delamination, that is when the reverse slip zone erases the residual

Table 3.5. Experimental crack density  $\rho$  at saturation in  $\text{SiO}_x$  films with different thicknesses  $h_f$  deposited on PET substrates (after Hsueh and Yanaka [96]).

$h_f$ [nm]	$\nu$ [ $\mu\text{m}^{-1}$ ]
43	0.56
67	0.51
90	0.36
120	0.32
320	0.16

damage zone and the maximal stresses in the film form a plateau in the middle section of the structure. In order to validate the model using the experimental data reported by Hsueh and Yanaka [96], Leterrier et al. [124] and Yanaka et al. [224] we must prove that the fracture stress of the film  $\sigma_c$  is higher than the maximal stress attained in the film at the beginning of the second stage of delamination. By using equation (3.29) for  $x \in \langle d, L - d \rangle$  and considering the beginning of the second stage of delamination, that is setting  $d = d^r$ , we obtain the value of the maximal normal stress within the film for this particular loading moment

$$\sigma_f(x) = \frac{\tau_c}{h_f} d^r, \quad x \in \langle d^r, L - d^r \rangle. \quad (3.74)$$

Equation (3.15) provides immediately

$$\sigma_f(x) = -\sigma_f^r, \quad x \in \langle d^r, L - d^r \rangle. \quad (3.75)$$

Thus, the normal stress within the film at the beginning of the second stage of delamination equals the absolute value of the film residual stress.

It follows that the proposed energy model is applicable when  $\sigma_c \geq -\sigma_f^r$ . In this case the segmentation cracking indeed takes place during the second stage of film delamination. From the researches reporting the experimental data summarised in Table 3.3, Table 3.4 and Table 3.5 only Yanaka et al. [224] provided values of residual strains within the film. The residual stresses have been obtained using equation (3.5) and are also presented in Table 3.3. The value of the film fracture stress  $\sigma_c$  is a function of film thickness  $h_f$ . Figure 3.9 presents the dependence between  $\sigma_c$  and  $h_f$  following the data reported in the literature. Indicated in Figure 3.9 are also the absolute values of film residual stresses  $|\sigma_f^r|$  obtained from Yanaka et al. [224] and presented in Table 3.3. It is seen that the condition  $\sigma_c \geq |\sigma_f^r|$  can be assumed for every  $h_f$  and the film segmentation process takes place during the second delamination stage indeed.

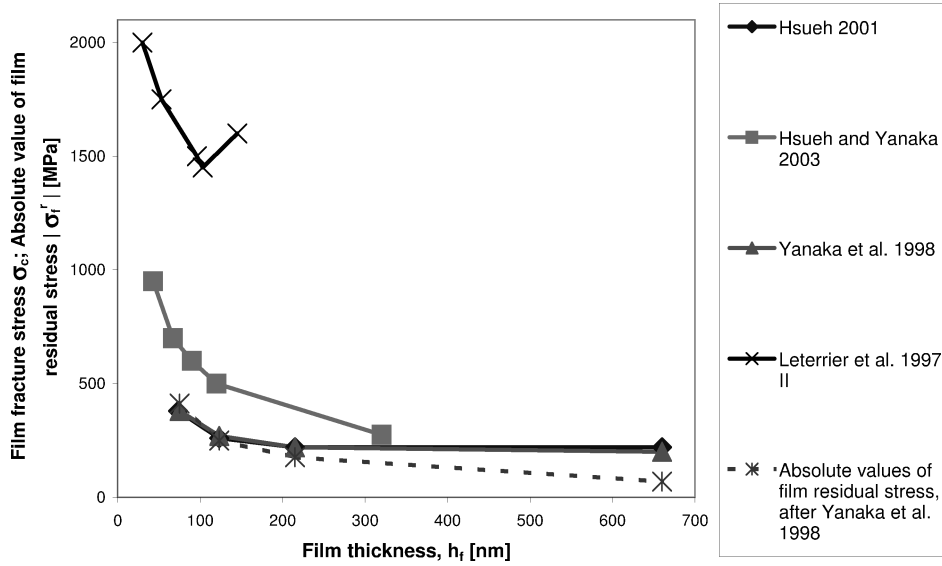


Figure 3.9. Film fracture stress  $\sigma_c$  as a function of film thickness (continuous line); absolute value of film residual stress as a function of film thickness (dashed line).

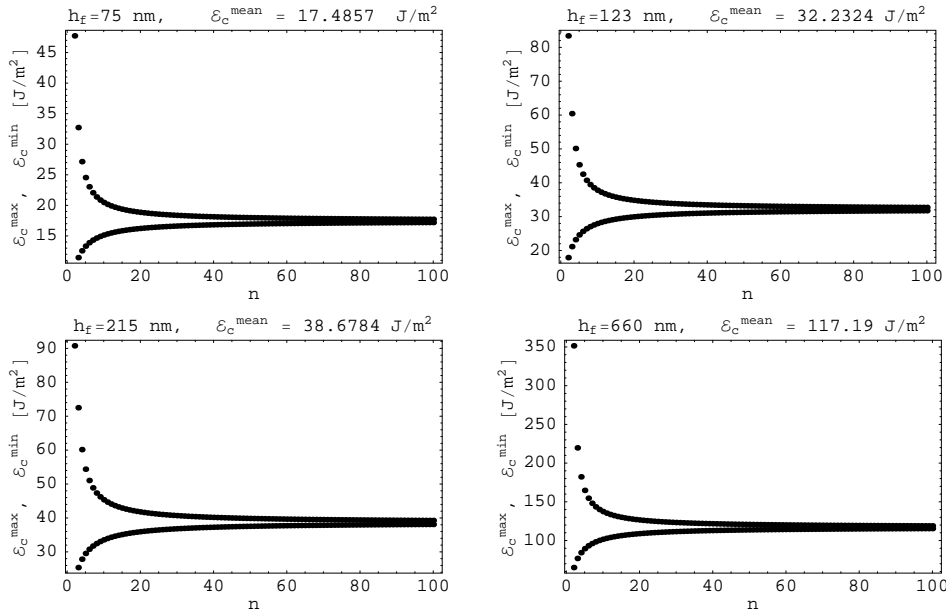


Figure 3.10. Upper and lower limits put on  $\mathcal{E}_c$  for various film thicknesses  $h_f$  as a function of  $n$  (using the experimental data in Table 3.3);  $\mathcal{E}_c^{\text{mean}} = 0.5(\mathcal{E}_c^{\text{max}} + \mathcal{E}_c^{\text{min}})$  – mean value of  $\mathcal{E}_c$  obtained for  $n = 100$ .

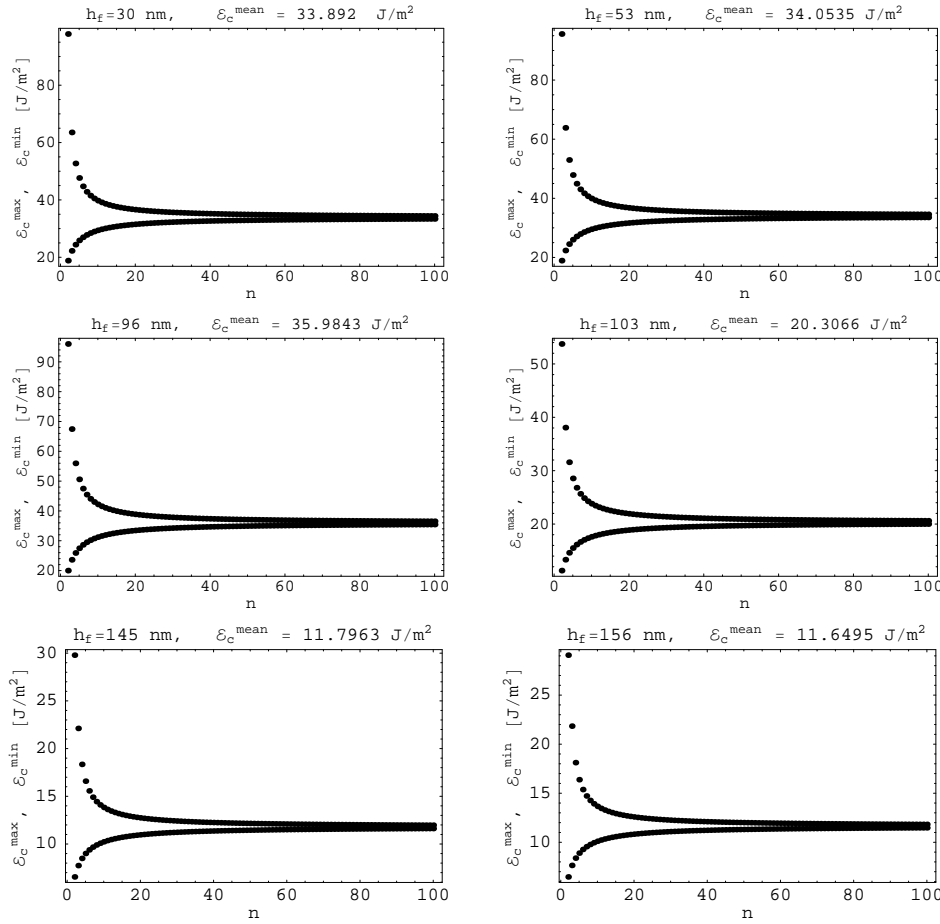


Figure 3.11. Upper and lower limits put on  $\mathcal{E}_c$  for various film thicknesses  $h_f$  as a function of  $n$  (using the experimental data in Table 3.4);  $\mathcal{E}_c^{\text{mean}} = 0.5(\mathcal{E}_c^{\text{max}} + \mathcal{E}_c^{\text{min}})$  – mean value of  $\mathcal{E}_c$  obtained for  $n = 100$ .

Residual stresses are usually of biaxial nature. The aim of this study is a one dimensional model and it cannot cover the full spectrum of aspects related with residual stresses. In order to do that a three dimensional analysis should be performed. However, the evolution of the residual stresses in the system is based on the experimental data obtained by considering an initial curl of a thin film/substrate strip, where the biaxial nature of initial stress was also not taken into account (Yanaka et al. [224]). Therefore, the model is consistent with the data serving as its input parameters.

Figures 3.10–3.12 present the upper  $\mathcal{E}_c^{\text{max}}$  and the lower  $\mathcal{E}_c^{\text{min}}$  limits put

on  $\mathcal{E}_c$  and obtained using inequalities (3.67) and the experimental data in Tables 3.3–3.5. It is seen that the values of  $\mathcal{E}_c^{\max}$  create a decreasing sequel, whereas the values of  $\mathcal{E}_c^{\min}$  create an increasing sequel. Thus, the bound specified for  $n$  fragments falls within the range defined by  $\mathcal{E}_c^{\max}$  and  $\mathcal{E}_c^{\min}$  for  $n - 1$  fragments. Although the differences between  $\mathcal{E}_c^{\max}$  and  $\mathcal{E}_c^{\min}$  for small values of  $n$  ( $n \leq 5$ ) are considerable, they disappear quickly as  $n$  increases. For example, for film thickness  $h_f = 75$  nm (Figure 3.10) we have  $\mathcal{E}_c^{\max} = 47.73$  J/m<sup>2</sup>,  $\mathcal{E}_c^{\min} = 9.27$  J/m<sup>2</sup> for  $n = 2$  and  $\mathcal{E}_c^{\max} = 16.94$  J/m<sup>2</sup>,  $\mathcal{E}_c^{\min} = 16.44$  J/m<sup>2</sup> for  $n = 100$ . As seen in Figures 3.10–3.12, already for  $n = 50$  the bounds set up by  $\mathcal{E}_c^{\max}$  and  $\mathcal{E}_c^{\min}$  allow to identify the energy  $\mathcal{E}_c$  with a good precision. The mean values of  $\mathcal{E}_c^{\text{mean}}$  defined by  $\mathcal{E}_c^{\text{mean}} = 0.5(\mathcal{E}_c^{\max} + \mathcal{E}_c^{\min})$  can be related to the film fracture energy  $\Gamma$  by the following equality

$$\mathcal{E}_c^{\text{mean}} = 2\Gamma \quad (3.76)$$

where 2 indicates that two new surfaces are created for each segmentation crack. Mode I fracture energy is relevant in our case due to the character of external loading imposed on the structure, and value of  $\Gamma$  used here should be understood as  $G_I$  representing crack resistance for mode I, in accordance with the nomenclature introduced in Section 2.

Figure 3.13 presents  $\Gamma$  as a function of film thickness obtained from Equation (3.76) for  $\mathcal{E}_c^{\text{mean}}$  calculated for  $n = 100$ . The results are obtained for experimental data sets presented in Tables 3.3–3.5 and compared with data found in the literature. Yanaka et al. [223] assumed a shear deformation either in the substrate or in the film in the shear lag model. Resulting film fracture energies  $\Gamma$  as functions of film thickness are indicated in Figure 3.13 by (a) and (b), respectively. Using fracture toughness  $K_c = 0.794$  MPa $\sqrt{\text{m}}$  (Leterrier et al. [124]) for the glass film, the corresponding fracture energy becomes  $\Gamma = K_c^2/2E_f = 4.32$  J/m<sup>2</sup> which is in the range of  $\Gamma$  in Figure 3.13. It is premature to discuss the variation of  $\Gamma$  with the film thickness without knowing the accuracy of data in Tables 3.3–3.5 used for the calculations of  $\Gamma$ . However, it should be stated that both the present model and the values of  $\Gamma$  found in the literature and presented in Figure 3.13 are reasonably close in the range 4–18 J/m<sup>2</sup>. Only Yanaka et al. [223] predict  $\Gamma$  to be in the range either 11–35 J/m<sup>2</sup> or equal approximately 0.5 J/m<sup>2</sup>, depending on the assumption of shear deformation in the shear lag model (substrate or film, respectively). The experimental data provided by Yanaka et al. [224] (Table 3.3) and used as an input for the present model suggests that  $\Gamma$  increases from 8 J/m<sup>2</sup> up to 60 J/m<sup>2</sup> when the film thickness increases from 75 nm up to 660 nm. This is in opposition to the other results, where such a distinctly increasing relation is

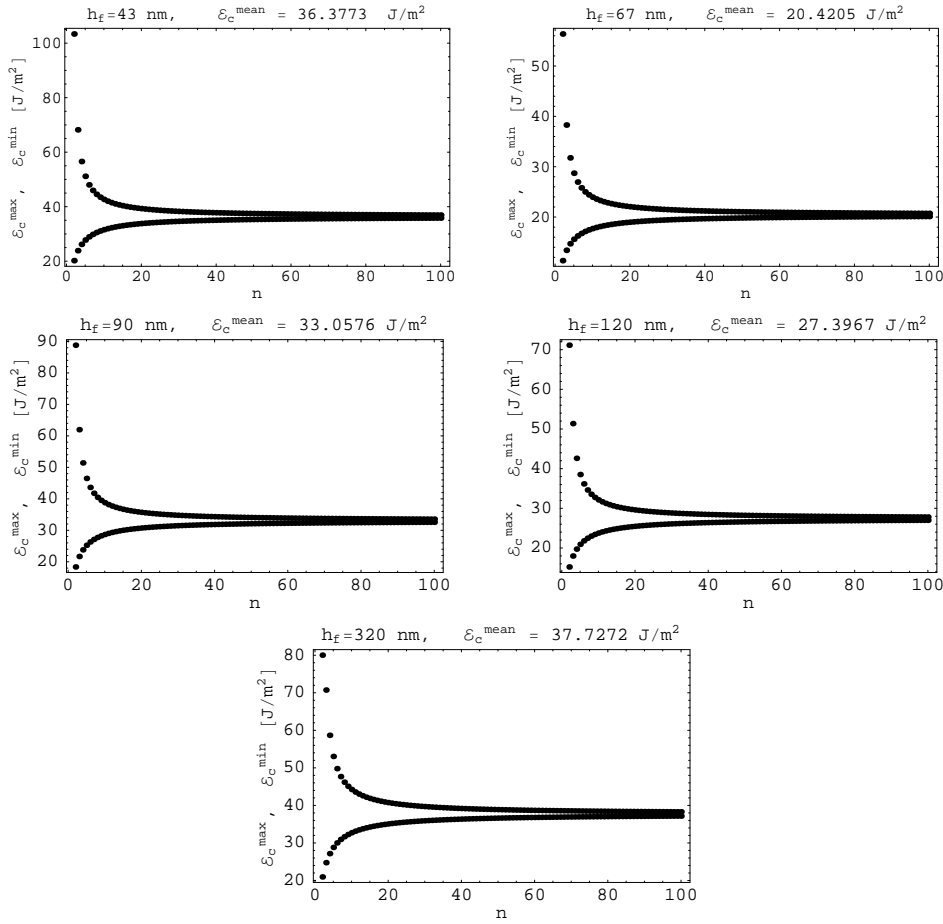


Figure 3.12. Upper and lower limits put on  $\mathcal{E}_c$  for various film thicknesses  $h_f$  as a function of  $n$  (using the experimental data in Table 3.5);  $\mathcal{E}_c^{\text{mean}} = 0.5(\mathcal{E}_c^{\max} + \mathcal{E}_c^{\min})$  – mean value of  $\mathcal{E}_c$  obtained for  $n = 100$ .

not observed.

In their paper [96], Hsueh and Yanaka presented results of calculations performed in order to obtain values of  $\Gamma$  for following film thicknesses  $h_f = 43$  nm, 67 nm, 90 nm, 120 nm and 320 nm. They are visualized in in Figure 3.13. The recorded crack densities for these films are given in Table 3.5. These data serve as input parameters for the present model. Thus, we can compare  $\Gamma$  for films of thicknesses  $h_f = 43$  nm, 67 nm, 90 nm, 120 nm and 320 nm obtained by Hsueh and Yanaka [96] with those provided by the present model. It can be seen in Figure 3.13 that the results are very close and in the range 10–19 J/m<sup>2</sup>

depending on film thickness. This observation validates the proposed model with respect to its ability to render accurate values of unknown in question. In particular, it confirms that the transition condition, based on comparison of potential energies between uncracked and fully damaged composites, can be used in practical applications.

### 3.7. The energy model and stress redistribution models

There is a number of segmentation cracking models, where fracture criterion is based on stress redistribution (Białas and Mróz [29, 30], Hsueh [93], Yanaka et al. [223, 224]). Hsueh [93] showed, that in the case of  $\text{SiO}_x$  films on PET substrates, the film fracture stress decreases initially with increasing film thickness and then becomes insensitive to film thickness, when the film thickness is greater than 200 nm. In the present model it is the fracture energy  $\Gamma$  which plays the same role as film fracture stress in stress criterion models. It should be stated that, according to the present model, the value of  $\Gamma$  has a tendency to decrease as the film thickness increases (except for experimental data obtained by Yanaka et al. [224], see Figure 3.13), but there is always an oscillation around this trend. In particular, within the range of the considered film thicknesses, one cannot see any stabilization of  $\Gamma$  at a constant value, which is expected as film thickness becomes higher.

The main assumption of the energy model is equal spacing between segmentation cracks in the saturation stage. Experimental results show a variation of crack spacing around a mean value. Using a stress redistribution model Agrawal and Raj [4] showed that the maximum and minimum crack spacing should differ by a factor of two. This effect cannot be captured by the present approach.

There is another phenomena that is also not included in the present analysis. Since we use a topological transformation from an uncracked to a fully damaged state of the system, we do not consider the loading history. In the framework of this energy approach it is not possible to model a relation between applied load and crack density. This effect can be easily captured by stress redistribution models (see, for instance, Białas and Mróz [29]).

The energy model was formulated for the second stage of loading. With that in mind it should be stated that the residual stresses do not have any effect upon segmentation cracking, since the residual damage zones are erased by reverse slip zones during the second stage of loading. This result is in a clear contrast to the analysis presented by Yanaka et al. [223, 224] who considered residual stresses using critical stress models of segmentation cracking. According to the

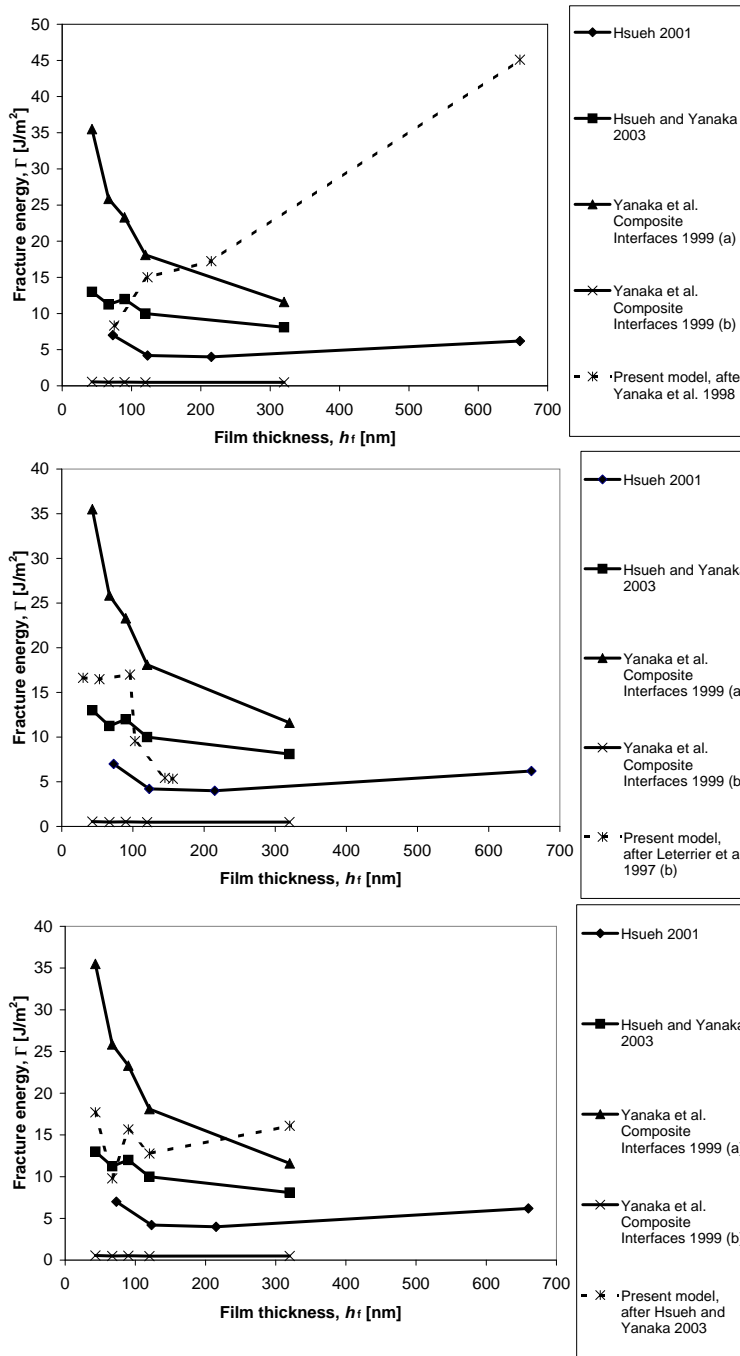


Figure 3.13. Fracture energy  $\Gamma$  as a function of film thickness  $h_f$ .

present approach the residual stresses would have effect upon the results when segmentation cracking took place during the first loading stage.

### 3.8. Conclusions

In this chapter an energy model of segmentation cracking of a thin film deposited on a stretched substrate was derived. The model was based on an analytical analysis of film delamination, where a constant shear stress at the film/substrate interface and a presence of residual forces was assumed. The residual stresses can be a result either of a mismatch in thermal expansion coefficients between the film and the substrate or a result of the production process. The system response to the residual loading is a development of delaminated zones at the film/substrate interface at both ends of the composite. Another consequence of the residual stresses is a two stage delamination process, when the substrate is subsequently stretched. During the first stage the length of a single delamination zone does not increase and remains the same as during the residual state. The increase of the external loading results in a formation of reverse slip regions within the already damaged interface. During the second stage of loading a further development of the failure process at the interface takes place. Characteristic is an existence of a plateau of a constant normal stress acting on the film. Because of that, the formation of cracks within the film is strongly dependent upon random distribution of micro defects within the material and difficult to model by conventional critical stress approach. Instead of using a critical stress approach we introduce a transition condition stating, that the segmentation occurs when the energy of the cracked system is lower than the energy of the intact system. By the energy of the system we understand its potential energy and the energy dissipated to create the segmentation cracks and to damage the film/substrate interface. This approach does not account for a loading history and assumes a transformation of the film topology. Crack density at the saturation stage can be uniquely identified in this way.

It has been shown that the analysis can be simplified when the film is much thinner than the substrate and their stiffnesses are in the same range. In such a case, one can focus only upon the energies of the film and the interface and neglect the substrate effect. The obtained results shall be the same as if the whole composite was considered.

The model was validated to measure the value of fracture energy of a silicon oxide thin film deposited on a poly(ethylene terephthalate) (PET) substrate,

where constant plastic stresses at the film/substrate interface are present. The values of the film fracture energy  $\Gamma$  found in literature and obtained from the model are reasonably close in the range 4–19 J/m<sup>2</sup>.



# Modelling of thermal barrier coatings

## 4.1. Introduction

The current chapter presents the results of experiments and of numerical simulation of stress distribution and failure development within thermal barrier coatings. A particular attention is given to two types of cracks, namely through-thickness cracking and delamination cracking. In the first case, acoustic emission and simultaneous optical inspection of the interface area during bending tests are used as in-situ diagnostics. This allows to examine the correlation between continuously increasing strain and the process of macroscopic crack formation and propagation. The critical strain values leading to crack initiation are thus identified. The results of APS TBC through-thickness cracking during three point bending test are further compared to numerical simulations of the experiment. Simulations also enables to check the influence of the energy release rate of TBC layer on crack patterns during bending. Modelling of stresses and failure development around a typical asperity at TBC/BC interface constitutes the second part of the chapter. The results allow for a description of the process of micro crack formation within a unit cell that can eventually lead to TBC spallation.

In both cases the concept of a cohesive zone ahead of a crack tip, stemming from works by Barenblatt [19] and Dugdale [58], is used to simulate crack nucleation and propagation. Whereas in most cases this approach is used to model crack development at material interfaces, it has also been adopted for cracks in bulk material. Camacho and Ortiz [39] used a cohesive law fracture model to simulate propagation of cracks along arbitrary paths. Surface-like cohesive elements were introduced at the interfaces between standard volume elements. Simulation of dynamic crack propagation have been presented in the papers by Pandolfi et al. [156] and Zhou and Molinari [231, 232] in three dimensional problems. Tijssens et al. [197] used the damaging cohesive surfaces to study concrete fracture. Following this approach, the cohesive zone model presented

in Section 2.2. will be used not only to model interfacial cracking for the delamination phenomena, but also through-thickness cracking during three point bending.

## 4.2. Through-thickness cracking cracking

### 4.2.1. Experimental setup

Standardized three point bending tests (EN 843-1) at room temperature were performed on TBC coated samples before and after annealing for 300 hours at 1050°C. Set up of the three point bending tests performed with the TBC subjected to tensional in-plane stresses is presented in Figure 4.1. The Ni-base single crystal alloy samples (CMSX-4) had a length of 50 mm, a width of 3.5 mm and an average thickness of 2.5 mm. On the top surface an MCrAlY-type bond coat (BC) was applied by vacuum plasma spraying with an average thickness of 150  $\mu\text{m}$ . Two different methods, air plasma spraying (APS) and electron beam-physical vapour deposition (EB PVD) were used for producing 250  $\mu\text{m}$  (EB PVD) and 300  $\mu\text{m}$  (APS) thick TBC. The TBC consisted of a partially stabilized (6–8 wt. %  $\text{Y}_2\text{O}_3$ ) zirconia. The TBC/BC interface roughness was in the order of  $R_a=6\text{--}7\ \mu\text{m}$  (technical measure). Prior to applying the EB PVD coating, the BC surface had been smoothed and the interface roughness did not exceed the value of  $R_a = 1\ \mu\text{m}$ .

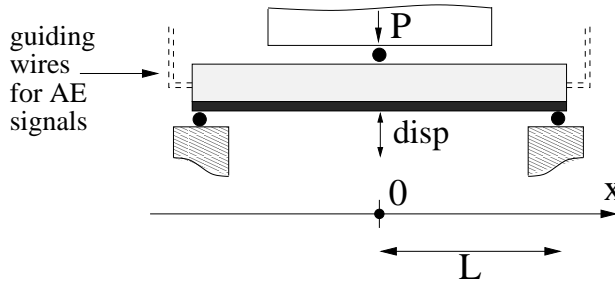


Figure 4.1. Scheme of the bending tests.

The tests were performed on a universal testing facility (Instron, type 1362). Displacement of the points laying on samples symmetry axis were measured inductively using a scanning stick. They were further used to calculate the strain  $\epsilon_{\text{int}}$  at the TBC/BC interface by using formula

$$\epsilon_{\text{int}} = \frac{3(h_s + h_{\text{BC}})w}{8L^2}. \quad (4.1)$$

In the above  $h_s + h_{BC}$  is a sum of substrate and bond coat thicknesses,  $w$  is the measured displacement and  $L$  is the distance between two loading points, see Figure 4.1. The calculations have been verified during several tests using optical methods and a good correlation between calculated and measured strain was found up to a displacement of 1 mm. Above this value the measured strain at the TBC/BC interface becomes significantly higher, see Majerus [132].

Three point bending was chosen to induce in-plane tensile loads within the coatings. During these tests the strain distribution over the sample length is inhomogeneous with a local maxima at the central loading position. This has advantages for camera observation as the position of first crack appearance is most likely known in advance.

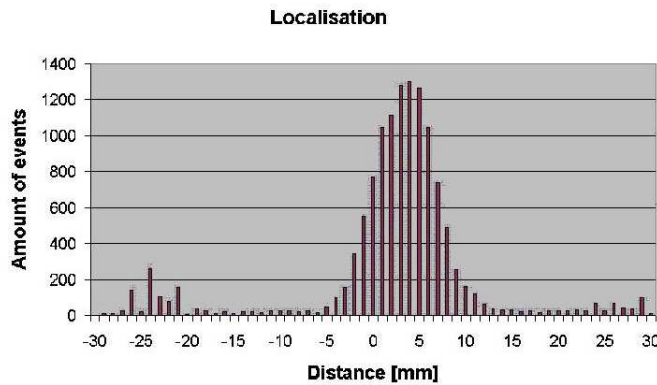


Figure 4.2. Illustrative AE localization results during one of the bending tests. All accumulated acoustic events are plotted versus the axial coordinate of the specimen (after Białas et al. [27]).

Acoustic emission (AE) was monitored with an AMSY4 system by Vallen with three individual channels and wide band (300–2000 kHz) sensors (VS2M-P). This acquisition system is efficient in the fact that it digitizes true, multiple frequency waveform. The system consisted of a built in Pentium PC with a 32 bit, 10 MHz acquisition. The preamplifier gain was set at 34 dB. The signals were recorded via acoustic conductor wires of equal length being spot welded at both ends of the specimen.

In order to localize the sources of AE signals a standard localization technique depending on run-time differences of AE signals collected by both acoustic sensors was applied. The relatively high length to thickness ratio of the specimens (50 mm/3.5 mm) allowed to apply a linear method for localization. A source location  $x_{\text{source}}$  with respect to the specimen's symmetry axis (see Fig-

ure 4.1) is given by the formula:

$$x_{\text{source}} = \Delta t_{\text{rt}} v_c, \quad (4.2)$$

where  $\Delta t_{\text{rt}}$  is the run-time difference between two signals recorded each by a single sensor,  $v_c$  is the speed of sound within the investigated material. A source of two signals was said to be located in the centre of the specimen, when their run-time difference  $\Delta t_{\text{rt}}$  was equal to zero. Two signals coming from the same source within the specimen and recorded each by a single sensor were called an acoustic event. The accuracy of event localization was within the range of  $\pm 2$  mm. Figure 4.2 displays illustrative results of events localization during one of the bending tests. The events localized at the distances of around  $\pm 25$  mm from the symmetry axis were produced by the friction at the contact area between the specimen and the bearings.

Furthermore, the formation and growth of cracks was observed optically in-situ using a telescope system (Questar, QM 100) and a charged-coupled device (CCD) camera (Adimec, MX12). An observation area of one over one millimetre was sufficient. The magnification factor of 300 was used for displaying the camera pictures. The minimum crack length observable under these conditions equalled  $40 \mu\text{m}$ .

#### 4.2.2. Experimental results

During the tests most signals were localized in the centre of the samples within a region of approximately 12 mm. The stress concentration in the vicinity of loading points led to a significant increase of unwanted acoustic events. As a consequence a localization filter was applied to eliminate these events. The measured force-displacement curve and the monitored acoustic events were compared with pictures taken by the camera. Figure 4.3 shows results of a typical three point bending test with APS coating. The graph shows the relation between the bending moment and the strain at the BC/TBC interface at the centre of the sample. The accumulated acoustic events are represented by the grey surface. Slightly above 0.5 % of TBC strain a massive increase of events took place. At this stage no well defined crack was observed by the camera. At the TBC strain of approximately 0.9 % a clear through-thickness crack becomes visible. Subsequent loading at around 1.2 % strain value coincided with two cracking events. Firstly, through-thickness cracks were deflected parallel to the TBC/BC interface and led to debonding of macroscopic parts of TBC. Secondly, cracks penetrated into the bond coat and were stopped at the

BC/CMSX-4 interface. The occurrence of delamination cracks and bond coat cracking began at nearly the same strain value.

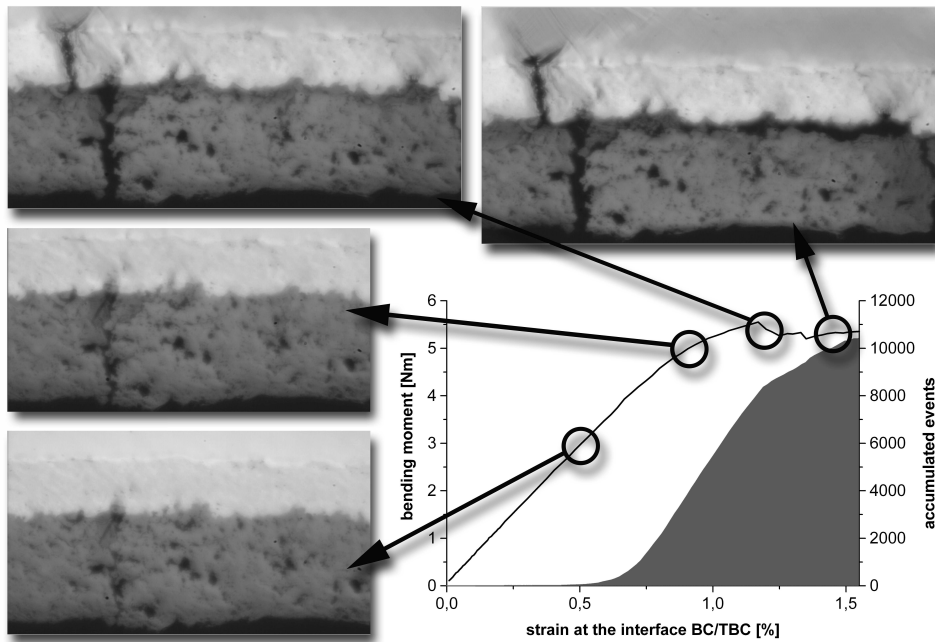


Figure 4.3. Typical correlation between the observations made by optical camera and the monitored accumulated acoustic emission events with respect to the strain at the BC/TBC interface (after Białas et al. [27]). The strain rate was  $3.2 \times 10^{-5}$  1/s with the APS TBC under tension.

Visual observation revealed that crack propagation in the TBC is a relatively slow process when compared to the cracking of bond coat. Crack extension from the free surface of the TBC to the TBC/BC interface was correlated with the strain value of 0.8 %. Cracking of the bond coat appeared nearly instantaneously. The formation of bond coat cracks can be recognized also by small load dips of the bending moment versus strain curve for strain values higher than 1.2 %, as presented in Figure 4.3.

A similar comparative procedure between acoustic emissions and camera observations was systematically performed on all samples. It was observed that the acoustic signals coming from both through-thickness and delamination crackings had comparable amplitudes, durations and energies. In contrast, acoustic signals coming from bond coat cracking had higher energies and amplitudes than those produced by TBC cracking. Precise onset of crack initiation was

Table 4.1. Critical strains for crack initiation within TBC, determined by acoustic emission techniques during three point bending tests (after Białaś et al. [27]).

	loading rate [ $\mu\text{m}/\text{min}$ ]	TBC critical strain [%] under tension room temperature	
		APS	EB PVD
		before annealing	20
	2000	0.44	0.5
after annealing 300h/1050°C	2000	0.18	0.14

Table 4.2. Critical strains for delamination of TBC determined by optical observation during three point bending tests (after Białaś et al. [27]).

	loading rate [ $\mu\text{m}/\text{min}$ ]	TBC critical strain [%] under tension room temperature	
		APS	EB PVD
		before annealing	20
	2000	1.51	> 2
after annealing 300h/1050°C	2000	1.68	2

correlated with the first increase of acoustic emission events. The camera pictures allowed to determine strains leading to TBC macroscopic delamination.

The influence of different deformation rates and the effect of atmospheric annealing at 1050°C during 300 hours was also analysed. The obtained critical strain values for crack initiation determined by acoustic emission techniques are shown in Table 4.1. Both coating types revealed a clear influence of the deformation rate on critical strain values, i.e. an increase in the bending rate led to a decrease in the critical strain. After annealing the crack initiation strains were significantly reduced. The APS coatings turned out to be more strain tolerant than the EB PVD coatings.

The first observed macroscopic delaminations of a TBC segment has been correlated with respective strain values. They are presented in Table 4.2. Several

tests did not lead to a failure of the coating as the loading unit reached its limit of 1000 N. For these tests the maximal attained strains are also given in Table 4.2.

The APS coatings failed at strains around 1.4 %. It is not fully clear how the bond coat cracking at strains around 1.25 % influenced the formation of delamination cracks at TBC/BC interface. After annealing the bond coat exhibited a less brittle behaviour without the formation of cracks and, as a result, macroscopic failure of the TBC occurred at significantly higher strains. The EB PVD coatings did not show any macroscopic delamination in the as-received state. Even bond coat cracking around 1.5 % tensile strain did not lead to TBC debonding. Delamination was observed after annealing at 2 % of tensile strain.

Figure 4.4 presents the relation between the loading force and the beam displacement at the loaded point during the experiment. It has been obtained for both APS and EB PVD coatings for room temperature and loading rate of 20  $\mu\text{m}$  per minute. The shaded area presents the region on the curve where the formation of through-thickness cracking took place. It follows with stabilization of the loading force due to the plastic deformation of the beams. Small jumps in the force-displacement relation were caused by cracking of BC layer for both APS and EB PVD coatings and delamination in the case of APS TBC.

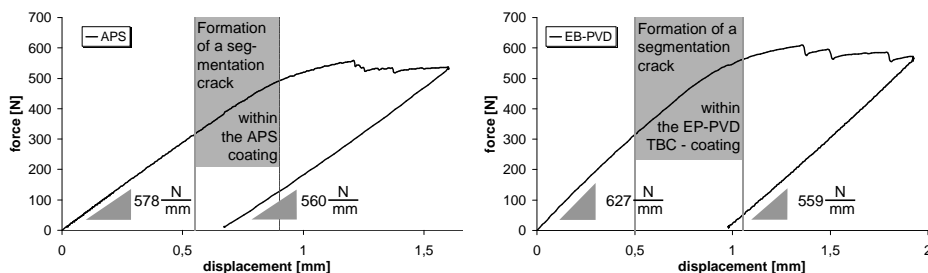


Figure 4.4. The loading force versus beam displacement at the loaded point for APS and EB PVD coatings (after Bialas et al. [27]). Room temperature, loading rate: 20  $\mu\text{m}/\text{min}$ .

### 4.2.3. Finite element model

Numerical simulations have been performed in order to capture the through-thickness cracking within the APS TBC layer at room temperature. Thus, it has not intended to go beyond the shaded area in Figure 4.4. Time dependent effects within the bond coat and TBC layers are not accounted for. It is assumed that both the beam substrate, being CMSX-4 super-alloy, and the bond

coat layer are elastic-plastic materials, whereas TBC proves to be elastic. The irreversible processes within the coatings are captured by means of cohesive zones serving as potential regions for TBC cracking. To capture the through-thickness cracking of the coating, they are placed between the solid elements of the coating and allows a crack to propagate from the free surface and to remain arrested at the TBC/BC interface. Two types of interface elements have been developed: four and three nodes elements as presented in Figure 4.5(a) and Figure 4.5(b), respectively. The elements are composed of two straight lines  $A$  and  $B$ . The integration points located in element nodes result in Lobatto integration scheme. The effects of numerical integration schemes of interface elements on stress prediction were addressed by Schellekens and de Borst [172], who observed better performance of nodal lumping and Newton-Cotes or Lobatto integration schemes than the traditional Gauss scheme. In the case of an intact interface lines  $A$  and  $B$  coincide and simulate full bond between two solid finite elements. Their relative normal  $\delta_n$  and tangential  $\delta_t$  displacements model crack evolution and subsequent material failure. The constitutive relations presented in Section 2.2. are assumed now.

Time discretization provides the following set of equations

$$\delta_{n+1}^e = \delta_{n+1} - \delta_{n+1}^p, \quad (4.3)$$

$$\sigma_{n+1} = \mathbf{K} \delta_{n+1}^e, \quad (4.4)$$

$$\delta_{n+1}^p = \delta_n^p + \Delta \Lambda_{n+1} \frac{\partial \psi(\sigma_{n+1})}{\partial \sigma}, \quad (4.5)$$

$$\delta_{\text{eq}n+1} = \delta_{\text{eq}n} + \sqrt{(\delta_{n+1}^p - \delta_n^p)^2 + m^2 (\delta_{t_{n+1}}^p - \delta_{t_n}^p)^2}, \quad (4.6)$$

$$0 = F(\sigma_{n+1}, \tau_{n+1}) = \begin{cases} \sqrt{\sigma_{n+1}^2 + \left(\frac{\sigma_c^0}{\tau_c^0}\right)^2 \tau_{n+1}^2} - \sigma_{cn+1} & \text{for } \sigma_{n+1} \geq 0 \\ |\tau_{n+1}| + \mu \sigma_{n+1} - \frac{\tau_c^0}{\sigma_c^0} \sigma_{cn+1} & \text{for } \sigma_{n+1} < 0 \end{cases}, \quad (4.7)$$

$$\psi(\sigma_{n+1}, \tau_{n+1}) = \begin{cases} \sqrt{\sigma_{n+1}^2 + \left(\frac{\sigma_c^0}{\tau_c^0}\right)^2 \tau_{n+1}^2} & \text{for } \sigma_{n+1} \geq 0 \\ |\tau_{n+1}| & \text{for } \sigma_{n+1} < 0 \end{cases}, \quad (4.8)$$

where  $(\cdot)_n$  stands for the previous state and  $(\cdot)_{n+1}$  refers to the current, or unknown, state.

With linear degradation of the critical normal stress  $\sigma_c$  as a function of parameter  $\delta_{\text{eq}}$  we have

$$\sigma_{cn+1} = \begin{cases} \sigma_c^0 - Z \delta_{\text{eq}n+1} & \text{for } \delta_{\text{eq}n+1} \leq \frac{\sigma_c^0}{Z} \\ 0 & \text{for } \delta_{\text{eq}n+1} > \frac{\sigma_c^0}{Z} \end{cases}. \quad (4.9)$$

By making use of the fully implicit integration scheme, we seek for a solution satisfying the yield function (4.7) and the flow rule (4.5) at the end of each time step. Since the process is displacement controlled, for a given displacement increment  $\Delta\delta_{n+1} = \delta_{n+1} - \delta_n$  we postulate a trial stress in the form

$$\sigma_{n+1}^{\text{trial}} = \sigma_n + \mathbf{K} \Delta\delta_{n+1}. \quad (4.10)$$

If for the trial stress  $\sigma_{n+1}^{\text{trial}}$  we have  $F < 0$ , then there is no failure evolution associated with the increment  $\Delta\delta_{n+1}$  and the stress  $\sigma$  equals  $\sigma_{n+1}^{\text{trial}}$ . For  $\sigma_{n+1}^{\text{trial}}$  yielding  $F > 0$  we have a failure development and the amount of slip  $\delta_{n+1}^p$  and current values of parameters  $\delta_{\text{eq},n+1}$  and  $\Delta\Lambda_{n+1}$  are obtained simultaneously from equations (4.5), (4.6) and (4.7) by using the Newton-Raphson iteration scheme. The resulting stresses are then calculated from equations (4.3) and (4.4).

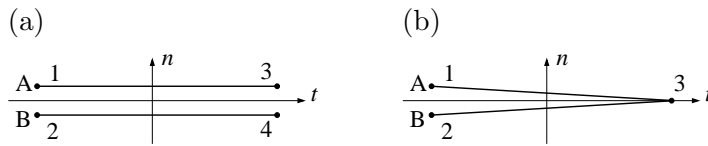


Figure 4.5. Two types of cohesive zone elements: (a) four nodes element; (b) three nodes element.

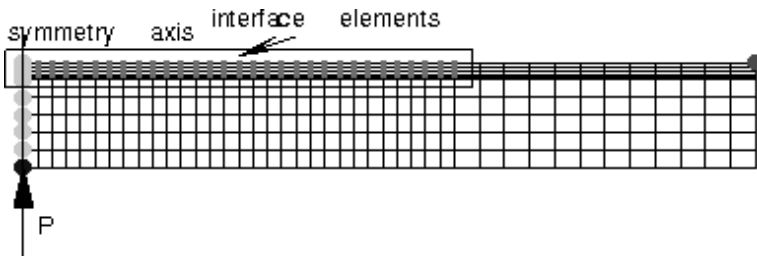


Figure 4.6. Typical mesh for finite elements calculations - one half of the experimental setup. TBC and bond coat layers are on the top of the specimen. Cohesive zone elements inserted vertically between TBC solid elements.

A typical mesh for calculations is presented in Figure 4.6. Due to the symmetry of the experimental setup, only half of the specimen has been modelled and appropriate boundary conditions have been imposed, that is vanishing horizontal displacement of nodes lying on the symmetry axis. In order to simulate TBC segmentation in the middle area of the structure, there are cohesive elements introduced vertically between TBC finite elements in this particular zone.

The three nodes elements presented in Figure 4.5(b) are used to simulate crack arrest upon reaching TBC/BC interface, allowing for relative displacement of nodes 1 and 2 only. The super-alloy CMSX-4 is assumed to be elastic-perfectly plastic and the bond coat is treated as elastic-isotropic hardening material with a linear hardening function, see Majerus [132]. The APS TBC finite elements are taken to be linearly elastic. All material data is summarized in Table 4.3.

Table 4.3. Material properties of CMSX-4, bond coat and thermal barrier coating. The hardening modulus  $H$  for NiCoCrAlY relates the stress with the total strain  $\dot{\sigma} = H\dot{\epsilon}_{\text{total}}$ , where  $\epsilon_{\text{total}} = \epsilon^e + \epsilon^p$ .

	CMSX-4	NiCoCrAlY bond coat	APS TBC
Young modulus [GPa]	122	145	1.8
Poisson ratio	0.36	0.32	0.22
yield stress [MPa]	952	870	—
hardening modulus [GPa]	—	50	—

Table 4.4. Material parameters of TBC cohesive elements.

$C_n$	$C_t$	$\sigma_c^0$ [MPa]	$\tau_c^0$ [MPa]	$G_I$ [J/m <sup>2</sup> ]	$m$	$\mu$
0	0	10	$\sigma_c^0/\sqrt{3} = 5.8$	30–90	1	0

In order to simulate fracture evolution within TBC we set the interface compliances  $C_n$  and  $C_t$  in equation (2.17) to be equal zero. Unless the failure criterion equation (2.18) is met, the interfaces simulate a perfect bond between TBC finite elements. In order to do that, penalty stiffness method is used. When equation (2.18) is satisfied, a vertical crack starts to propagate. Since in the case of three point bending test TBC is subjected only to tension, the interface material data of most importance are  $\sigma_c^0$  and  $G_I$ , that is tensile strength and critical energy release rate for mode one, respectively. It has been assumed that the TBC critical normal stress  $\sigma_c^0$  is equal to 10 MPa, being a stress value for TBC corresponding to the onset of acoustic emission signals. The value of critical energy release rate was taken in the range 30–90 J/m<sup>2</sup> following experimental data reported by Thurn et al. [196]. The material parameters of TBC cohesive zones are presented in Table 4.4.

The constitutive model for interface elements has been implemented within a displacement based formulation. In contrast to papers by Camacho and Ortiz [39], Pandolfi et al. [156] and Zhou and Molinari [231, 232], the present analysis does not consider dynamic fracture, since it is not relevant in this case. It is very important to note, that the finite loading step has to be sufficiently

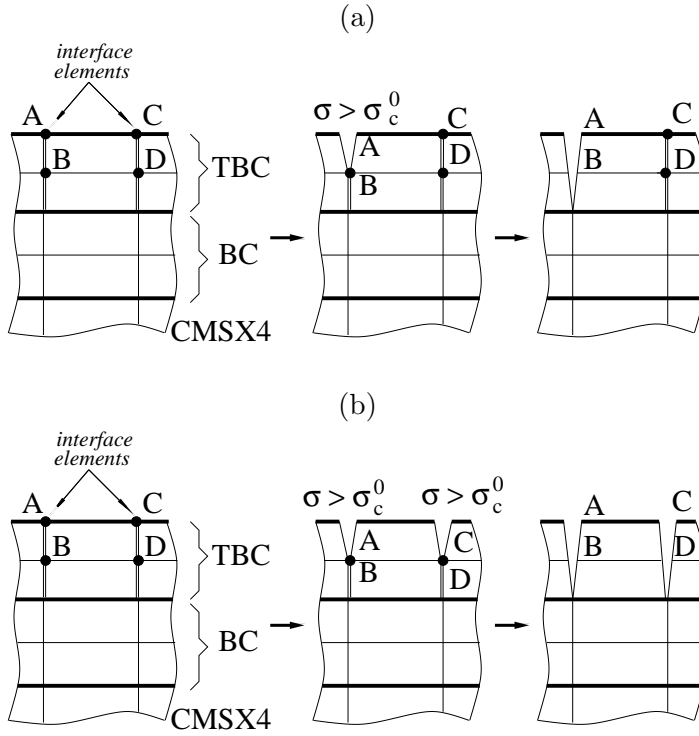


Figure 4.7. (a) Failure localization within one through-thickness crack for a sufficiently small loading step. (b) Unrealistic cracking scenario when the loading step is not small enough.

small for a failure localization to occur. In fact, during the calculations condition

$$0 \leq F(\sigma, \tau) = \begin{cases} \sqrt{\sigma^2 + \left(\frac{\sigma_c^0}{\tau_c^0}\right)^2 \tau^2} - \sigma_c^0, & \sigma \geq 0 \\ |\tau| + \mu\sigma - \tau_c^0, & \sigma < 0 \end{cases} \quad (4.11)$$

is satisfied only in one integration point within all interface elements per loading step. The reason for doing that is schematically clarified in Figure 4.7(a), presenting a section of finite element mesh with cohesive zone elements. Having in mind that the integration points coincide with nodes of interface elements and assuming that the loading step is sufficiently small, we satisfy the failure criteria (4.11) in point A only. The opening mode of interface element in point A follows. During subsequent loading step the failure condition (4.11) is reached in point B, that is in only one integration point within all interface elements. The energy released in the structure during this step can be used to propagate crack from point A to point B and the failure can localize within one

through-thickness crack, in accordance with the non-uniform stress distribution during three point bending. When a single crack reaches the TBC/BC interface it becomes arrested. Subsequent loading with the failure condition (4.11) satisfied in one integration point during the step allows us to find the most loaded cohesive element and enables the failure process to be localized within next through-thickness crack.

In contrast, when the loading step is not small enough, it has been observed that the failure condition (4.11) can be satisfied simultaneously in two integration points  $A$  and  $C$ , as presented in Figure 4.7(b). During subsequent loading step the energy released in the structure is used to propagate simultaneously many through-thickness cracks. Such a static analysis has led to convergence problems resulting from the fact, that the physical state of structural equilibrium with failure localization within a few through-thickness cracks has not any longer been obtained. Instead, an unrealistic cracking scenario is followed with cracks forming within a spacing of a length of a single TBC solid element. In the present formulation, the failure condition (4.11) is monitored at all integration points within interface elements and the loading step is modified whenever criteria (4.11) is reached in more than one integration point.

The software tool has been *Mathematica* [214] enhanced by the finite element package *Computational Templates* developed by Korelc [114, 116]. It allows for an automatic generation of finite element code by simultaneous optimization of expressions. It is also an effective finite element environment allowing for modification or enhancement of the numerical procedure. With this capability it was well suited for global monitoring of all integration points within cohesive zone elements.

The function  $F$  given by equation (4.7) is different from the plastic potential (4.8). This leads to non-associated flow rule for tensional loading mode and, consequently, does not satisfy Drucker's postulate. In the context of integration of constitutive law provided by equations (4.3)–(4.9), generally we obtain unsymmetrical stiffness matrix. The finite element package *Computational Templates* [114, 116] allows to chose a solver for non-symmetric tangent matrices and, thus, can easily deal with related numerical subtleties. As a matter of fact it should be noted that in our bending test the cohesive zone elements are all subjected to tensional loading, resulting in symmetry of elements' stiffness matrices. Consequently, even use of symmetric tangent matrix solver can be appropriate here.

A standard cohesive zone analysis is used mostly to model delamination processes, that is a development of cracks at a material interface, being a well defined plane of weakness. In such a case several integration points can be

simultaneously subjected to progressive damage leading anyway to failure localization on a single plane and enabling to follow a physical equilibrium path. The present static analysis, however, tries to simulate development of a number of segmentation cracks for neither of which a formation place can be defined in advance. A way to find it and to overcome convergence problems is to allow for satisfaction of failure condition (4.11) in only one integration point within a single loading step.

#### 4.2.4. Mesh dependence

As mentioned before, the cohesive zone method is usually used when a certain plain of weakness is known a priori and the aim is to simulate failure development within this given region. This usually means a bond between two dissimilar materials, e.g. a fiber and a matrix. In our case, however, the effort is put on modelling cracks development within a uniform material with no distinct failure zones. Therefore, it seems probable that the numerical results might depend on interface elements density.

The following number of TBC elements pro specimen length was used along specimen's middle section (framed region in Figure 4.6): 32, 64, 128, 512. The elasticity modulus of TBC was 1200 MPa and the critical energy release rate for interface elements equalled  $40 \text{ J/m}^2$ . The remaining material data are given in Table 4.3 and Table 4.4 for bulk material and cohesive zones, respectively. Each simulation resulted in six segmentation cracks. The deformed mesh presented in Figure 4.8(a) has been obtained for 512 elements pro specimen's length. It has been magnified ten times for the sake of clarity. The calculations performed for the mesh with 32 elements along specimen's middle section resulted in a coarse crack patterns which does not resemble the cracking scenarios presented in Figure 4.8(a). Upon mesh refinement though, that is for 64, 128 and 512 elements, the same failure patterns is repeated — we obtain the same number of segmentation cracks within a similar distance from each other. For 64 elements the distance between the cracks is slightly bigger than that obtained from simulations with 128 and 512 elements. Mesh refinement leads to more consistent results. Localization of cracks number 1, 2 and 3 in Figure 4.8(a) for meshes with 128 and 512 TBC elements is identical. There are slight discrepancies in distances between cracks number 3, 4, 5 and 6 but the overall failure trend is preserved and qualitative nature of cracks pattern is repeated reasonably well. It should be noted that the opening displacement within crack number 1, that is within crack lying on the specimen symmetry axis, is very small and fracture occurs mostly within cracks number 2, 3 and 4.

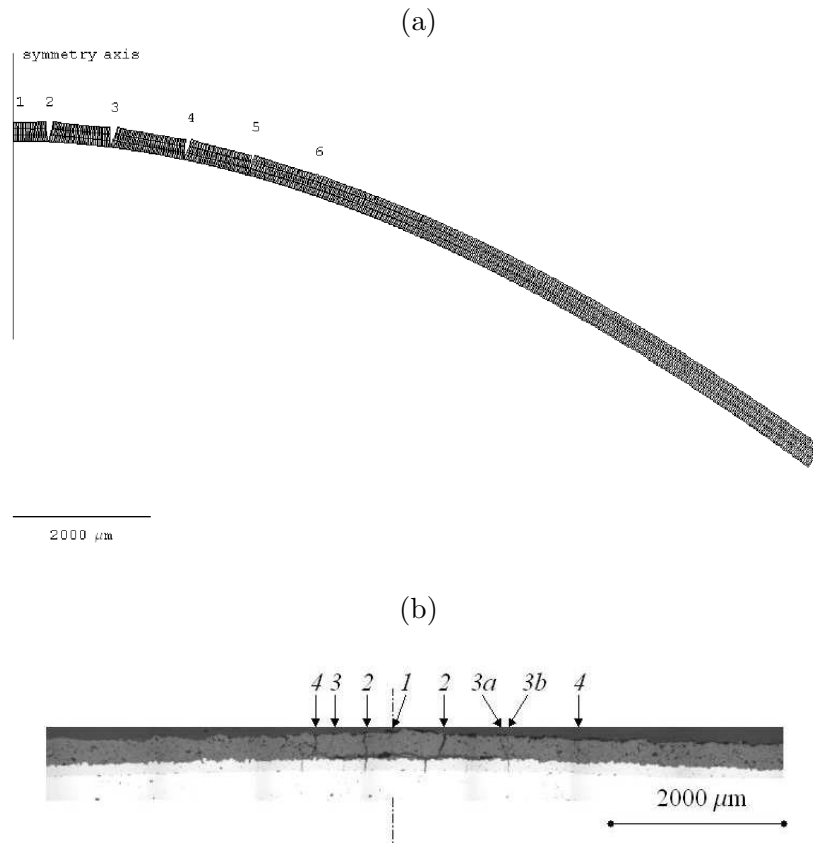


Figure 4.8. Through-thickness cracks pattern for APS coating after three point bending: (a) results of numerical simulation, 512 TBC elements along specimen's middle section (framed region in Figure 4.6); (b) crack patterns obtained during the experiment.

#### 4.2.5. Comparison with experimental results

Figure 4.8(b) presents through-thickness crack patterns for APS coating subjected to tension during three point bending at room temperature with strain rate  $3.2 \times 10^{-4}$  1/s at BC/TBC interface. The picture was taken when the bending experiment was finished and therefore there are delamination and bond coat cracks present. Due to the inhomogeneous structure of APS TBC the through-thickness cracks within the coating are not symmetrically localized with respect to the symmetry axis. It is also probable that bond coat cracking stimulated subsequent TBC degradation, as it may be the case with the crack number 3a in Figure 4.8(b). Results of numerical simulations pre-

sented in Section 4.2.4. accounted only for TBC through-thickness cracking without subsequent delamination and bond coat failure. Though, upon comparison of Figure 4.8(b) with the crack pattern in Figure 4.8(a) the following can be stated. The numerical simulation provides results which resemble the experiment quantitatively. The major cracks 1, 2, 3a, 3b and 4 on the right hand side of Figure 4.8(b) can be compared with cracks number 1, 2, 3 and 4 in Figures 4.8(a) resulting from numerical simulations. The distance between through-thickness cracks observed during the experiment and following FEM calculations is similar and the same trend is preserved: it is more or less the same between cracks 2-3b and 3b-4 in Figure 4.8(b) and equals  $840 \mu\text{m}$ . The distance between cracks 1-2 is approximately a half of this value and equals  $500 \mu\text{m}$ . Similar results are provided by numerical simulation with the value of  $920 \mu\text{m}$  as a distance between cracks 2-3 and 3-4 (see Figure (4.8a)) and  $460 \mu\text{m}$  as a distance between cracks 1-2.

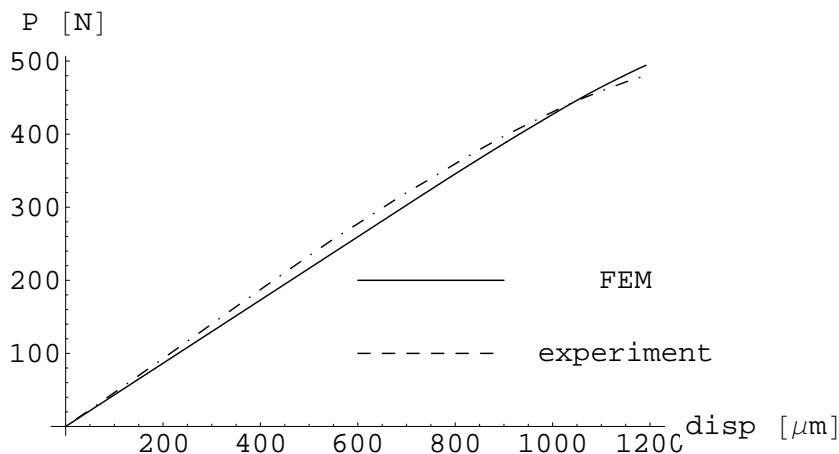


Figure 4.9. The loading force versus beam displacement at the loaded point.

Cracks number 5 and 6 resulting from numerical simulations are not observable in Figure 4.8(b). In comparison to cracks 2, 3 and 4 they are very small and do not propagate through TBC thickness. As such, their presence does not contradict the experimental cracking scenario in Figure 4.8(b).

Figure 4.9 presents the relation between the loading force  $P$  and beam displacement at the loaded point obtained from the experiment and the numerical simulation. The results match each other reasonably well. It does not come as a

surprise though, since the stresses within the APS coating are small in comparison to the stresses within the substrate and the segmentation process within the protective layer does not influence much the overall structural response. Thus, the global behaviour presented in Figure 4.9 reveals a good correlation between the experiment and the numerical simulation. As presented in Figure 4.4, the following stage in the failure of the coating is TBC delamination accompanied by the plastic deformation of the substrate.

#### 4.2.6. Effect of TBC critical energy release rate $G_I$ on segmentation cracking

The most problematic in the finite element calculations was the value of critical energy release rate  $G_I$  for cohesive elements, that is for APS TBC material. This value was reported by Thurn et al. [196] to be in the range 20–200 J/m<sup>2</sup>. Depending on crack length it starts from 20 J/m<sup>2</sup> for crack lengths below 100  $\mu\text{m}$  and reaches values between 50 and 230 J/m<sup>2</sup> at crack lengths between 300 and 400  $\mu\text{m}$ .

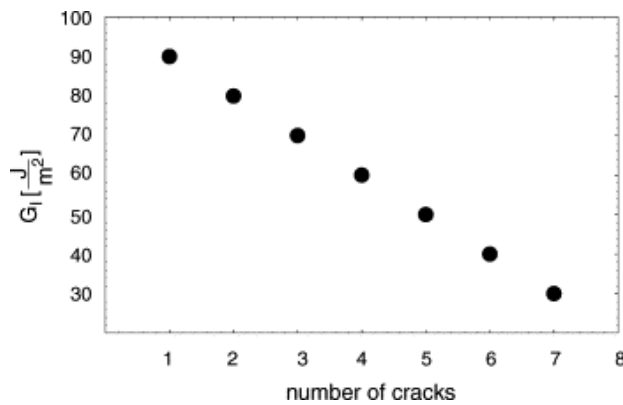


Figure 4.10. The effect of different values of critical energy release rate  $G_I$  for TBC material on resulting number of through-thickness cracks. Results obtained for loading force  $P$  equal 490 N.

Numerical study of effect of  $G_I$  value upon crack patterns was performed. As already presented in Figure 4.8(a) obtained for  $G_I=40$  J/m<sup>2</sup>, the distances between cracks are identical with the exception for cracks 1 and 2, where the cracks distance is the half of the typically observed. The same result was obtained for other values of critical energy release rate. The changes in  $G_I$  affected the number of observed cracks and their location in the coating, though.

Figure 4.10 presents the relation between different values of  $G_I$  and the

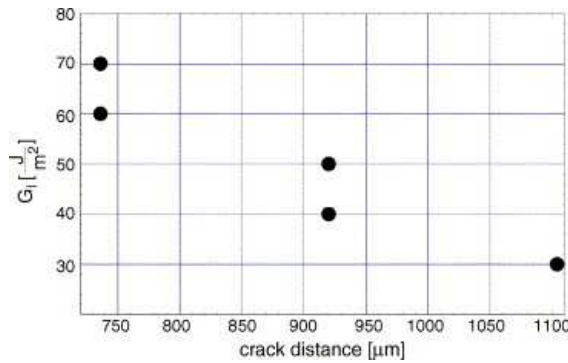


Figure 4.11. The effect of different values of critical energy release rate  $G_I$  for TBC material on crack distances. Results obtained for loading force  $P$  equal 490 N.

resulting number of through-thickness cracks within one half of the structure obtained for maximal loading force  $P$  equal 490 N. It is observed that due to the decreasing value of  $G_I$ , increasing number of cracks within the coating is obtained. Similar observation was reported by Kim and Nairn [109] for a polymeric coating on a steel substrate. In our case, however, the relation between crack density and critical energy release rate can be approximated by a linear function, whereas it was nonlinear in the paper by Kim and Nairn [109].

Figure 4.11 presents the relation between different values of  $G_I$  and the cracks distance obtained for maximal loading force equal 490 N. Upon decreasing the value of critical energy release rate we obtain increasing distances between segmentation cracks.

As examined by Kokini and Takeuchi [113], multiple cracking within a coating can reduce the magnitude of critical energy release rate for the interface between the coating and the substrate, suggesting that the through-thickness cracking can be beneficial for coating life time. Results presented in Figure 4.10 provide a framework allowing to explain better failure resistance of EB PVD coatings, where the critical energy release rate is significantly lower than in the case of APS TBC. Thus, lower value of  $G_I$  can stimulate through-thickness cracking and reduce delamination, as it is widely observed within EB PVD systems.

### 4.3. Delamination

There have been many attempts to numerically investigate stress development in TBC systems, as described in Section 1.5.5. In most cases a two

dimensional unit cell representing a single asperity was used. The stress field around the asperity was supposed to be representative for the entire interface area. The resulting microcracks could subsequently link and thus form a crack crossing a number of asperities at a macro level. Using a unit cell approach we adopt the multi-scale modelling concept in the present analysis.

Of particular interest for the following research is the experimental work on TBCs by Majerus [132], in which CMSX-4 super-alloy hollow cylindrical specimens were tested. The specimens were plasma sprayed with yttria stabilized zirconia (APS TBC) on NiCoCrAlY bond coat. Experimentally determined data for APS TBC, TGO and BC creep (Heckmann et al. [89], Majerus [132], Trunova [201]) serves here as an input for material modelling of the constituents. The time dependent model of CMSX-4 presented by Fleury and Schubert [66] and Shubert [175] has been used. The oxidation process has been simulated by increase of thickness of TGO elements. The development of cracks at the TGO/BC interface has been simulated using cohesive zone elements. The results are next discussed in relation to the failure mechanism presented by Chang et al. [43] and Freborg et al. [68].

#### 4.3.1. The numerical model

Figure 4.12 illustrates the modelling concept. The test cylinder is sufficiently long compared to its diameter for the problem to be approximated by a two-dimensional plane-strain case. It has been assumed that the strain in the axial direction is uniform. As proposed in Figure 4.12, the bond coat topography is idealized by circular segments within a unit cell. Symmetry of the problem allows meshing only one half of the undulation. The assumed boundary conditions put constraints on the displacement field in the cylindrical direction, only radial displacements are allowed to take place along lines OA and OB in Figure 4.12, as schematically indicated on the finite element mesh in Figure 4.13. The cylinder was subjected to cyclic temperature loading with homogenous temperature distribution. A single loading cycle is presented in Figure 4.14.

The bond coat, the thermally grown oxide and the thermal barrier coating are treated as elastic and viscous materials. Their mechanical properties are functions of temperature as listed in Table 4.5 (see Fleury and Schubert [66] for the discussion of anisotropy of mechanical properties of CMSX-4). The value of temperature loading equal to 200°C was chosen for the initial stress free state. It matches approximately with the coating stress free temperature for the air plasma spraying process (Bednarz [22]).

The creep data for TBC and BC were experimentally determined by com-

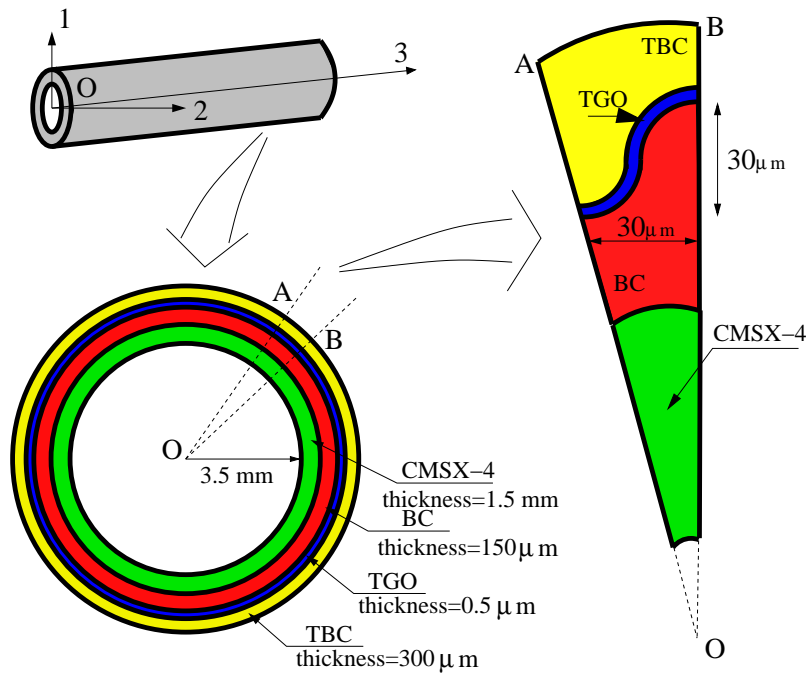


Figure 4.12. The model of the cylindrical test specimen. The proportions of the layers in the figure do not resemble their actual dimensions.

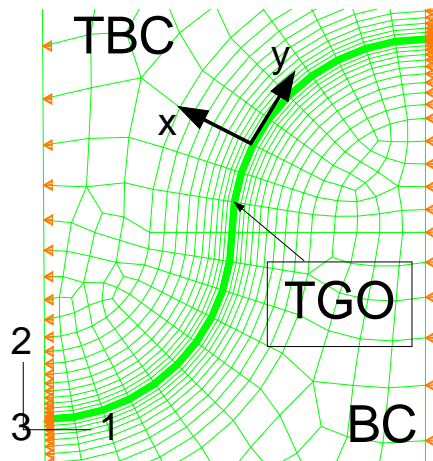


Figure 4.13. Local coordinate system for the oxidation modelling. On the edges of the unit cell boundary conditions are indicated.

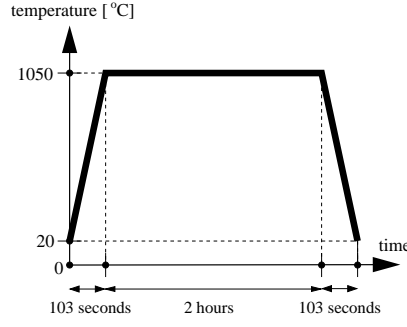


Figure 4.14. Temperature profile during a single loading cycle.

pression creep tests with stand-alone coatings (TBC, BC) and shear deformation experiments on TBC composites (Heckmann et al. [89], Majerus [132], Trunova [201]). The data for one dimensional case were approximated using the following equation

$$\dot{\varepsilon}_{\text{creep}}^{\text{TBC,BC}} = A' \sigma^{n'} e^{-\frac{\varepsilon_{\text{creep}}^{\text{TBC,BC}}}{\varepsilon'}} + A'' \sigma^{n''} e^{-\frac{\varepsilon_{\text{creep}}^{\text{TBC,BC}}}{\varepsilon''}} + A \sigma^n, \quad (4.12)$$

where  $A'$ ,  $n'$ ,  $\varepsilon'$ ,  $A''$ ,  $n''$ ,  $\varepsilon''$ ,  $A$ ,  $n$  are temperature dependent material parameters. They are listed in Table 4.6. The TGO time dependent behaviour is represented by the following formula

$$\dot{\varepsilon}_{\text{creep}}^{\text{TGO}} = A \sigma^n. \quad (4.13)$$

The TGO creep starts at 750°C. The values of material parameters  $A$  and  $n$  in this case are temperature independent and equal 7.3e-4 and 1, respectively (Bednarz [22]).

By using standard approach let us generalize the one dimensional equations (4.12) and (4.13) to a three dimensional case. We start with strain rate decomposition into elastic and creep parts

$$\dot{\varepsilon}_{ij} = \dot{\varepsilon}_{ij}^{\text{elastic}} + \dot{\varepsilon}_{ij}^{\text{creep}}. \quad (4.14)$$

Next, the creep strains are assumed to be incompressible and we write

$$\dot{\varepsilon}_{ij}^{\text{creep}} = \dot{e}_{ij}^{\text{creep}}, \quad (4.15)$$

where  $e_{ij}^{\text{creep}} = \varepsilon_{ij}^{\text{creep}} - \varepsilon_{kk}^{\text{creep}} \delta_{ij}/3$  is a deviatoric part of  $\varepsilon_{ij}^{\text{creep}}$ . In the case of isotropic creep we have proportionality between the deviatoric part of stress tensor  $s_{ij} = \sigma_{ij} - \sigma_{kk} \delta_{ij}/3$  and the deviator of creep strain rate

$$\dot{e}_{ij}^{\text{creep}} = B s_{ij}, \quad (4.16)$$

where  $B$  is a proportionality coefficient. By multiplying (4.16) by itself we obtain

$$\dot{\epsilon}_{ij}^{\text{creep}} \dot{\epsilon}_{ij}^{\text{creep}} = B^2 s_{ij} s_{ij} \quad (4.17)$$

and consequently have

$$B = \frac{3 \dot{\epsilon}_{\text{eq}}^{\text{creep}}}{2 \sigma_{\text{eq}}}. \quad (4.18)$$

In the above we have used equivalent creep strain rate  $\dot{\epsilon}_{\text{eq}}^{\text{creep}} = \sqrt{2\dot{\epsilon}_{ij}^{\text{creep}}\dot{\epsilon}_{ij}^{\text{creep}}/3}$  and equivalent stress  $\sigma_{\text{eq}} = \sqrt{3s_{ij}s_{ij}/2}$ . Now we assume, that formulas (4.12) and (4.13) for a one dimensional case are the same as those relating  $\dot{\epsilon}_{\text{eq}}^{\text{creep}}$  and  $\sigma_{\text{eq}}$ . Creep constitutive relation (4.16) becomes

$$\dot{\epsilon}_{ij}^{\text{creep}} = \frac{3 \dot{\epsilon}_{\text{eq}}^{\text{creep}}}{2 \sigma_{\text{eq}}} s_{ij}, \quad (4.19)$$

where the following relation holds for TBC and BC

$$\dot{\epsilon}_{\text{eq}}^{\text{creep}} = A' (\sigma_{\text{eq}})^{n'} e^{-\frac{\epsilon_{\text{eq}}^{\text{creep}}}{\epsilon'}} + A'' (\sigma_{\text{eq}})^{n''} e^{-\frac{\epsilon_{\text{eq}}^{\text{creep}}}{\epsilon''}} + A (\sigma_{\text{eq}})^n \quad (4.20)$$

and

$$\dot{\epsilon}_{\text{eq}}^{\text{creep}} = A (\sigma_{\text{eq}})^n \quad (4.21)$$

holds for TGO.

Growing of the alumina scale at high temperature at the BC/TBC interface is simulated using the swelling option in ABAQUS [53], see for example Bednarz [22] or Sfar et al [182]. The oxidation process is considered in the temperature range 950–1050°C. It is modelled as an orthotropic swelling strain of the TGO layer. Its initial thickness was assumed to be equal to 0.5  $\mu\text{m}$ . The relation between the thickness of oxide layer and time was experimentally determined for three different temperatures (Echsler [60]) and approximated by the following equation

$$d^{\text{ox}}(t) = \left( A^0 e^{-\frac{E_a}{RT} t} \right)^n, \quad (4.22)$$

with  $T$  being temperature and  $t$  time. The values of coefficients  $A^0$ ,  $n$ ,  $E_a$  and  $R$  are listed in Table 4.7. The one dimensional oxidation strain is defined as

$$\epsilon^{\text{ox}} = \ln \frac{d^{\text{ox}}}{d_0^{\text{ox}}}, \quad (4.23)$$

Table 4.5. The temperature dependance of Young modulus  $E_{\langle 100 \rangle}$  in direction  $\langle 100 \rangle$ , Poisson ratio  $\nu$  and thermal expansion coefficient  $\alpha$  for CMSX-4, TGO, BC and TBC (after Bednarz [22]).

T [°C]	$E_{\langle 100 \rangle}$ [MPa]	$\nu$	$\alpha$ [1/°C]	$E$ [MPa]	$\nu$	$\alpha$ [1/°C]
CMSX-4				TGO		
20	123286	0.359632	1.20023e-05	380365	0.27	5.07939e-06
220	115546	0.365476	1.2105e-05	369060	0.27	5.90395e-06
420	107806	0.370447	1.25212e-05	361225	0.27	6.72851e-06
620	100066	0.374547	1.34314e-05	351876	0.27	7.55307e-06
820	92326	0.377774	1.46843e-05	336032	0.27	8.37763e-06
1020	84586	0.380129	1.57968e-05	308708	0.27	9.2022e-06
BC				TBC		
20	151857	0.31886	1.23579e-05	17500	0.2	9.68e-06
220	150746	0.32701	1.30407e-05	16340.9	0.2	9.67479e-06
420	145253	0.33434	1.39115e-05	15181.8	0.2	9.70578e-06
620	132337	0.34086	1.49703e-05	14022.7	0.2	9.80975e-06
820	108921	0.34656	1.62171e-05	12863.6	0.2	1.00235e-05
1020	71890	0.35145	1.76519e-05	11704.5	0.2	1.03837e-05

Table 4.6. Creep data for BC and TBC (after Bednarz [22]).

T [°C]	$A$	$n$	$A'$	$n'$	$\epsilon'$	$A''$	$n''$	$\epsilon''$
BC								
750	1.25e-14	4.5	1.25e-9	4.5	0.09	1.25e-12	4.5	0.24
850	1.4e-11	3.8	1.4e-6	3.8	0.08	1.4e-9	3.8	0.23
950	2.3e-9	3.1	2.3e-4	3.1	0.07	2.3e-7	3.1	0.22
1050	9.5e-8	2.55	9.5e-3	2.55	0.06	9.5e-6	2.55	0.21
TBC								
750	2.e-22	4.5	1.e-10	4.5	0.01	2.2e-18	4.5	0.05
850	2.e-20	4.32	1.e-10	4.32	0.02	2.e-16	4.32	0.08
950	3.e-18	4.15	3.e-10	4.15	0.03	9.e-15	4.15	0.12
1050	3.77e-16	3.98	3.77e-11	3.98	0.04	3.02e-13	3.98	0.18
1150	4.8e-14	3.8	1.44e-10	3.8	0.05	4.8e-12	3.8	0.25

where  $d_0^{\text{ox}}$  is the initial thickness of TGO layer,  $d_0^{\text{ox}} = 0.5 \mu\text{m}$ . Making use of equation (4.22) the one dimensional oxidation strain rate takes now the form

$$\dot{\varepsilon}^{\text{ox}} = \frac{nA^0 e^{-\frac{E_a}{RT}}}{\sqrt[n]{d_0^{\text{ox}} e^{\frac{\varepsilon^{\text{ox}}}{n}}}}, \quad \varepsilon^{\text{ox}}(0) = 0. \quad (4.24)$$

The oxidation strain rate in tensor notation is provided by the formula

$$\dot{\varepsilon}_{\text{TGO}}^{\text{oxidation}} = \frac{1}{3} \dot{\varepsilon}^{\text{ox}} \mathbf{R}, \quad (4.25)$$

where  $\dot{\varepsilon}^{\text{ox}}$  is given by equation (4.24) and  $\mathbf{R}$  takes the form

$$\mathbf{R} = R_x \mathbf{e}_x \otimes \mathbf{e}_x + R_y \mathbf{e}_y \otimes \mathbf{e}_y + R_z \mathbf{e}_z \otimes \mathbf{e}_z. \quad (4.26)$$

Vectors  $\mathbf{e}_i$ ,  $i = x, y, z$  define a local coordinate system with axis x and y respectively perpendicular and parallel to the initial TGO layer, see Figure 4.13. Thus, equation (4.25) makes a generalization of the one dimensional oxidation law (4.24) to a three dimensional case. By setting  $R_x = 3$ ,  $R_y = R_z = 0$  we describe solely the thickness growth of the TGO layer (direction x in Figure 4.13).

Table 4.7. Parameters for oxidation kinetics (after Bednarz [22]).

T [°C]	$A^0$	$n$	$E_a$	$R$
950	1.57e-15	0.33	180000	8.314
1000	1.57e-15	0.325	180000	8.314
1050	1.57e-15	0.3225	180000	8.314

The preliminary calculations have been made to check the effect of lateral oxidation ( $R_y \neq 0$ ). They showed that with the TGO layer relaxing at high temperature, the deformation arising due to lateral oxidation has only a minor influence on stress distribution. The TGO creep (equation 4.13) is implemented in the present FEM model and the assumption  $R_x = 3$ ,  $R_y = R_z = 0$  is used.

#### 4.3.2. The time dependent behaviour of CMSX-4

The base material CMSX-4 is modelled as an elastic body with plastic and creep effects taking place in the temperature higher than 800°C. Microstructural dependent constitutive equations introduced by Fleury and Schubert [66] and Schubert et al. [175] have been adopted. They aim at the evolution of  $\gamma/\gamma'$  particles in high temperatures, using the orthotropic Hill's potential, whose anisotropy coefficients are related to the edge length of  $\gamma'$  particles. The model

is described in detail by Fleury and Schubert [66]. Here only its main features are shortly summarized.

The inelastic strain rate can be expressed as

$$\dot{\varepsilon}_{ij}^{\text{in}} = \frac{3}{2} K_{\langle 001 \rangle} (\sigma_{\text{V}}^{\text{eff}})^{N-1} A_{ijkl} s_{kl}^{\text{eff}}, \quad (4.27)$$

with  $K_{\langle 001 \rangle}$  and  $N$  being material parameters. The anisotropy tensor  $A_{ijkl}$  depends upon the evolution of dimensions of  $\gamma'$  particles. The  $s_{kl}^{\text{eff}}$  is a deviator of the effective stress. The effective stress  $\sigma_{kl}^{\text{eff}}$  has been introduced in order to estimate the microstructural impact on the global deformation. It is the difference between the applied stress and an internal stress

$$\sigma_{kl}^{\text{eff}} = \sigma_{kl} - \sigma_{kl}^{\text{i}}, \quad (4.28)$$

The internal stress  $\sigma_{kl}^{\text{i}}$  describes the resistance of the microstructure against the deformation due to the applied stress. It is composed as

$$\sigma_{kl}^{\text{i}} = \sigma_{kl}^{\text{b}} + \sigma_{kl}^{\text{p}}, \quad (4.29)$$

where the "back stress"  $\sigma_{kl}^{\text{b}}$  represents the dislocation movement within the  $\gamma'$  channels and the "friction stress"  $\sigma_{kl}^{\text{p}}$  is caused by the dislocation/particle interaction. The formation of both is given in detail by Fleury and Schubert [66].

#### 4.3.3. Modelling of crack development

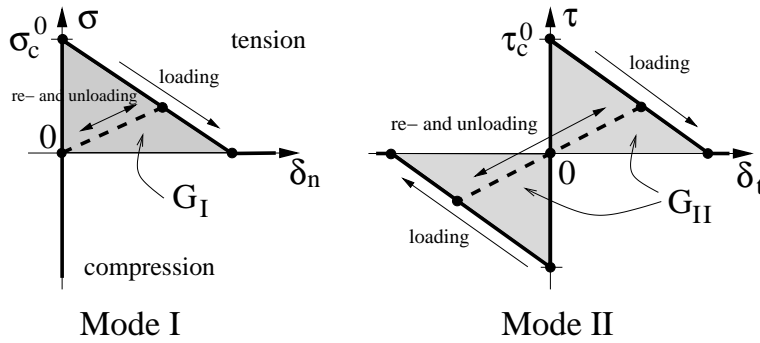


Figure 4.15. Pure mode constitutive equations.

To simulate the damage initiation and propagation cohesive zone elements are located at the TGO/BC interface. The mixed-mode decohesion model of

Camanho and Dávila [40] implemented in ABAQUS [53] is used. The following quadratic nominal stress criterion to model damage initiation is applied

$$\left(\frac{\langle \sigma \rangle}{\sigma_c^0}\right)^2 + \left(\frac{\tau}{\tau_c^0}\right)^2 = 1, \quad (4.30)$$

where  $\sigma_c^0$  and  $\tau_c^0$  are interface critical stresses respectively in opening or sliding modes. The linear damage evolution, as presented in Figure 4.15, is used to model the descending branch of the traction-separation relation. The dependence of the fracture energy on the mode mix has been defined by the following criterion

$$\frac{\mathcal{G}_I}{G_I} + \frac{\mathcal{G}_{II}}{G_{II}} = 1. \quad (4.31)$$

In the expression above  $G_I$  and  $G_{II}$  are the critical energy release rates respectively in mode one and two. It has been assumed that cohesive elements do not undergo damage under pure compression. As reported by Heckmann et al. [89], He et al. [87], Xu et al. [220] the following material data were used for BC/TGO interface:  $G_I=20$  J/m<sup>2</sup>,  $\sigma_c^0=200$  MPa,  $G_{II}=60$  J/m<sup>2</sup>,  $\tau_c^0=100$  MPa.

In reality the cracking in TBC systems is not confined only to the TGO/BC interface. It spreads into TGO and TBC and finally leads to coating spallation. With presence of a temperature gradient throughout the protective layer also TBC chipping can be observed, see Trunova [200]. Therefore, the present analysis should be understood only as a preliminary step of the proper modelling of TBC cracking. Though, it agrees well with the general scenario of TBC delamination process, as will be demonstrated in the following sections.

#### 4.3.4. Stress distribution without microcracks in the unit cell

##### 4.3.4.1. The influence of the time-dependent behaviour of CMSX-4

In the present section a comparison of the results obtained with and without the creep of the base material CMSX-4 will be presented. No crack development at the TGO/BC interface is considered at this stage. Figure 4.16 shows the stresses  $\sigma_{22}$  at the end of each subsequent phase of the 100th loading cycle: heating to 1050°C, hold up at 1050°C, cooling down to 20°C. It is seen that the CMSX-4 creep has no significant effect on the stress distribution close to the asperity. Figure 4.17 (bond coat peak), Figure 4.18 (TGO peak) and Figure 4.19 (BC/CMSX-4 interface) present the development of stress  $\sigma_{22}$  in points A, B and C at the end of the cooling phase (20°C) throughout 100 cycles. It can be seen that at points A and B stresses obtained for the case of CMSX-4 creep are

slightly bigger than those obtained without CMSX-4 creep, and the difference increases with the number of cycles. However, for practical interest it does not seem to be relevant. Only in the region close to the substrate the influence of CMSX-4 creep can be observed — the rheological behaviour of CMSX-4 leads to 30 % increase in the  $\sigma_{22}$  stress after 100 cycles. The rheological and oxidation phenomena result in the interplay of two effects: the relaxation of stresses in every component of the specimen taking place during the dwell time at 1050°C, and their increase due to TGO growth. Consequently, during dwell time, stresses in the entire specimen become more uniform and their perturbation around the asperity is mostly due to TGO growth. The TGO growth leads also to the increase in the maximal values of stresses around the imperfection. Both effects can be clearly seen in Figure 4.16, where the stress variation around the asperity at the temperature of 1050°C can be observed only at the peak and in the valley of the TGO. On the other hand, the absolute maximal and minimal values of  $\sigma_{22}$  have increased during the dwell time, which can be observed by comparing Figure 4.16(a) and Figure 4.16(b). The bigger is components adjustment due to relaxation at high temperature, the higher are mismatch stresses after cooling the specimen down to room temperature due to differences in thermal expansion coefficients of its constituents. This explains the fact that it is the cooling phase being the most crucial for failure of TBC systems. Figure 4.16(c) presents these mismatch stresses after cooling and, as expected, they are slightly bigger in the case of simulation performed with the creep of CMSX-4. The differences around the asperity are in fact very small and can be easily neglected for practical purposes, see Figure 4.17 and Figure 4.18. The influence of CMSX-4 creep on the overall behaviour of the whole specimen is only limited to the bond coat region close to the super-alloy, see Figure 4.19.

Schulz et al. [176] have examined the influence of substrate materials on oxidation behaviour of TBC systems. They showed that the cyclic lifetime of TBCs depends not only on the bond coat but also very much on the substrate alloy. They explain this fact by different adhesion of the TGO on the bond coat, being a result of the chemical composition of the substrate material. This is certainly correlated also with the mechanical behaviour of the substrate, that is also with its creep at high temperatures. Due to the present analysis, however, the influence of creep of CMSX-4 on the coating stress state can be easily neglected, as will be done in the following. The reason for a small impact of CMSX-4 creep on the overall specimen deformation is that only the thermal loading was modelled. Combined thermo-mechanical loading analysis could lead to a stronger impact of creep of CMSX-4 on stress distribution around the asperity. Also a smaller thickness of the super-alloy cylinder would increase the

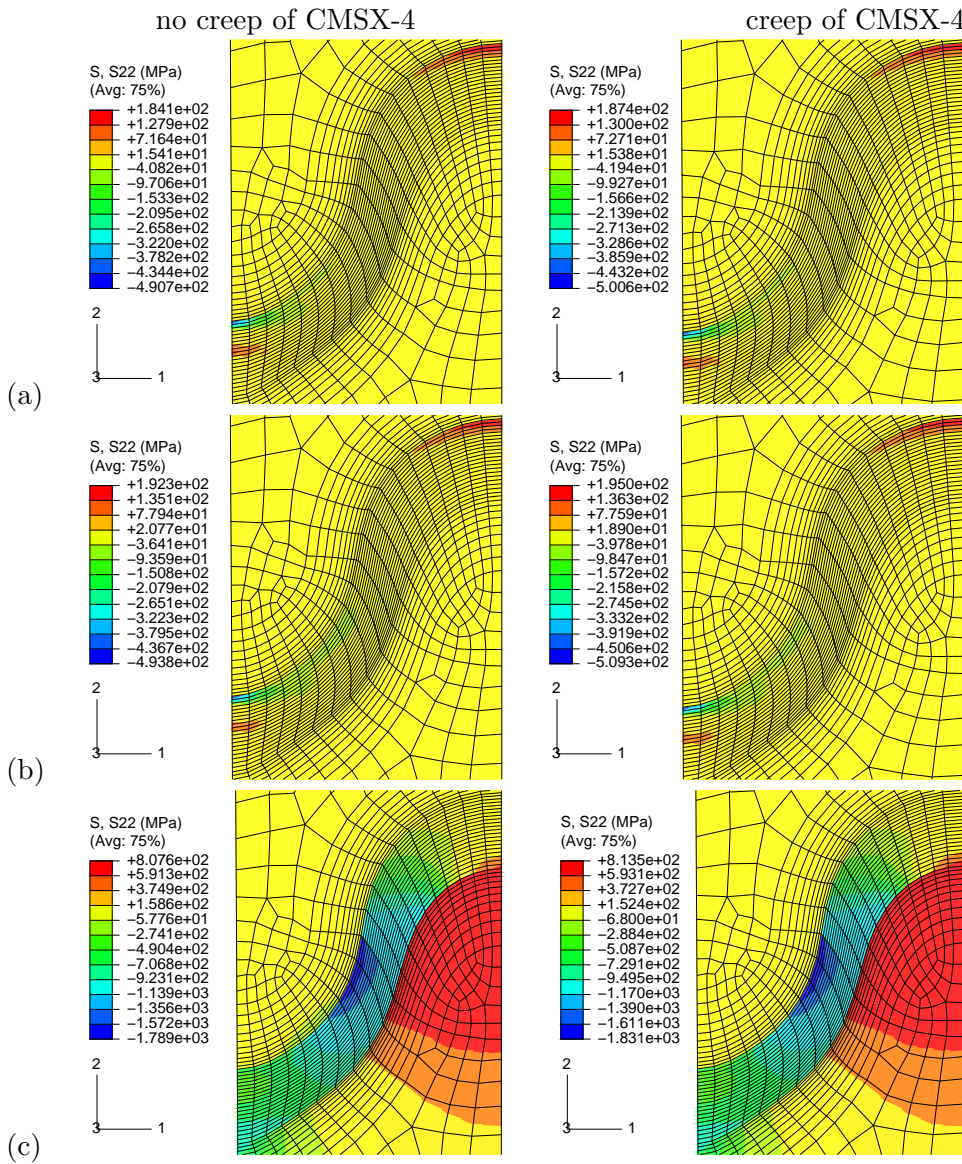


Figure 4.16. The stresses  $\sigma_{22}$  at the end of each subsequent phase of the 100th cycle with and without creep of CMSX-4: (a) heating up to 1050°C; (b) hold up at 1050°C; (c) cooling down to 20°C.

creep-related response of the whole specimen.

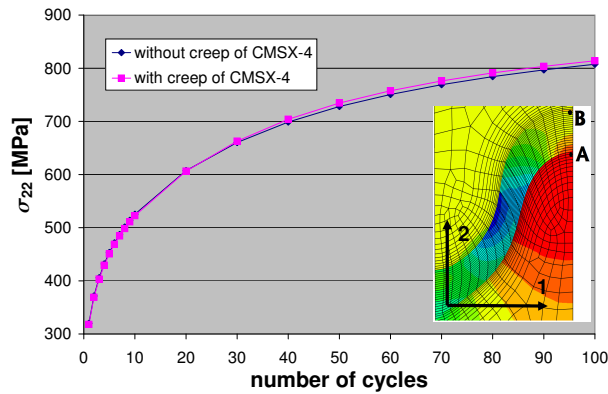


Figure 4.17. Stresses  $\sigma_{22}$  at BC/TGO interface (point A) after cooling down to 20°C versus number of cycles.

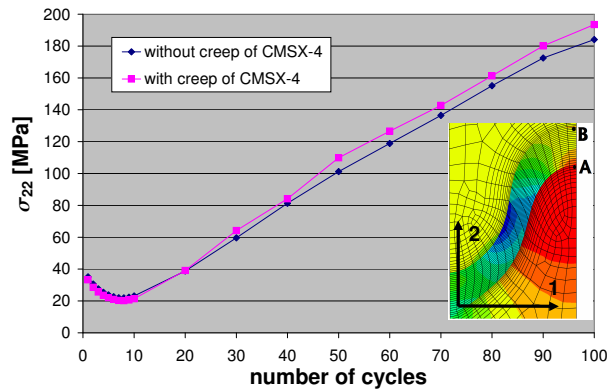


Figure 4.18. Stresses  $\sigma_{22}$  at TGO (point B) after cooling down to 20°C versus number of cycles.

#### 4.3.4.2. The effect of cyclic loading

Karlsson et al. [106] mention five conditions which together are prerequisites for the delamination: (a) the temperature cyclic loading, (b) thermal expansion misfit, (c) bond coat and TGO yielding, (d) bond coat oxidation, (e) geometrical imperfections at the interface. They examined the effect of cyclic loading upon stresses in the TGO for EB PVD TBCs with and without plastic yielding of the bond coat and TGO, and with other constituents being elastic. They

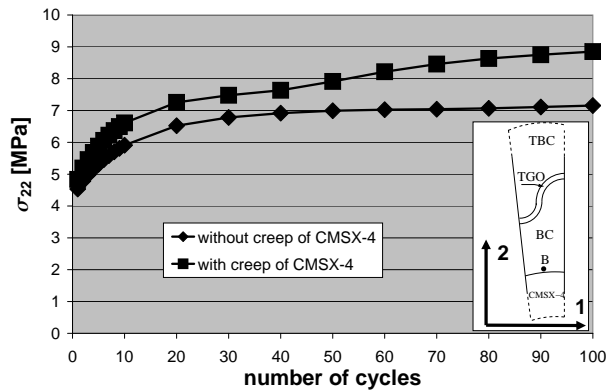


Figure 4.19. Stresses  $\sigma_{22}$  at the bond coat/substrate interface (point C) after cooling down to 20°C versus number of cycles.

showed that the thermal cycling causes substantially larger radial enlargement of the TBC-TGO-BC system when the TGO is allowed to yield at the peak temperature.

The effect of cyclic loading on the stress distribution will be now addressed for the present case of APS TBC, with all constituents modelled as presented in Section 4.3.1. Only CMSX-4 will be treated as an elastic body due to the negligible impact of its creep upon stress distribution around the asperity, the other constituents are considered as elastic with creep. No crack development at the TGO/BC interface is considered at this stage.

Two thermal loading histories will be used to conduct the calculations: (i) a multicycle scenario with a single sub-cycle presented in Figure 4.14 — 10, 20 and 50 multicycles will be considered; (ii) a single thermal cycle with the dwell time at peak temperature being the total for 10, 20 and 50 multicycles of case (i) (20, 40 and 100 hours respectively). Cooling and heating rates are the same for both cases: the temperature difference between ambient (20°C) and peak (1050°C) is achieved during 103 seconds. These two loading histories are contrasted in Figure 4.20.

Figure 4.21 presents  $\sigma_{22}$  stresses after cooling down to room temperature for these two loading histories. It can be seen that for the cases considered, monotonic and cyclic loadings yield almost the same result: the distributions of  $\sigma_{22}$  stresses are almost identical, the differences of minimal and maximal values of  $\sigma_{22}$  stresses are not higher than 2.5 %. Thus, it is seen that for the present analysis cyclic loading has no real effect on stress distribution. This is easily understood for the case without crack development, where only viscous materials are assumed not giving rise to any cyclic loading related effects.

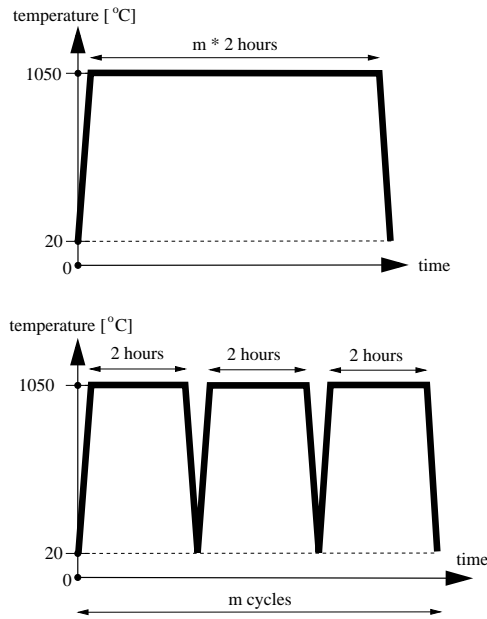


Figure 4.20. A single loading cycle with the dwell time of  $m$  multiple loading cycles.

Evans et al. [62] have presented a simple analytical model allowing for gaining some understanding of the various mechanisms governing stress distribution during thermal exposure of the TBC systems. Although they considered PVD TBCs, the generality of the approach can also be applied to the present case. Using an imperfection having a spherical symmetry and taking into account only elastic behaviour of the constituents, they prescribed the damaged driving forces to two effects, namely: (i) the oxidation process and (ii) the thermal expansion misfit. They claimed that the oxidation process results in tensile hoop stresses in the TBC. The hoop tensions induced in the TBC as the TGO thickens, would allow radial cracks to form within TBC. Subsequent cooling to ambient and the thermal expansion misfit would result in the tensile stresses at the TGO/BC interface and the possible extension of the TBC crack into TGO and its further development along the TBC/TGO interface.

Thus, Evans et al. [62] neglected the creep related phenomena and the effect of cyclic loading. It is interesting to compare the results of the present numerical simulation where the creep of TBC, TGO and BC are taken into account with the simple model of Evans et al. [62]. In the present case there are two distinct phases crucial for the stress development in the system: (i) dwell time at 1050°C and (ii) cooling down to ambient. The hold up phase activates the oxidation

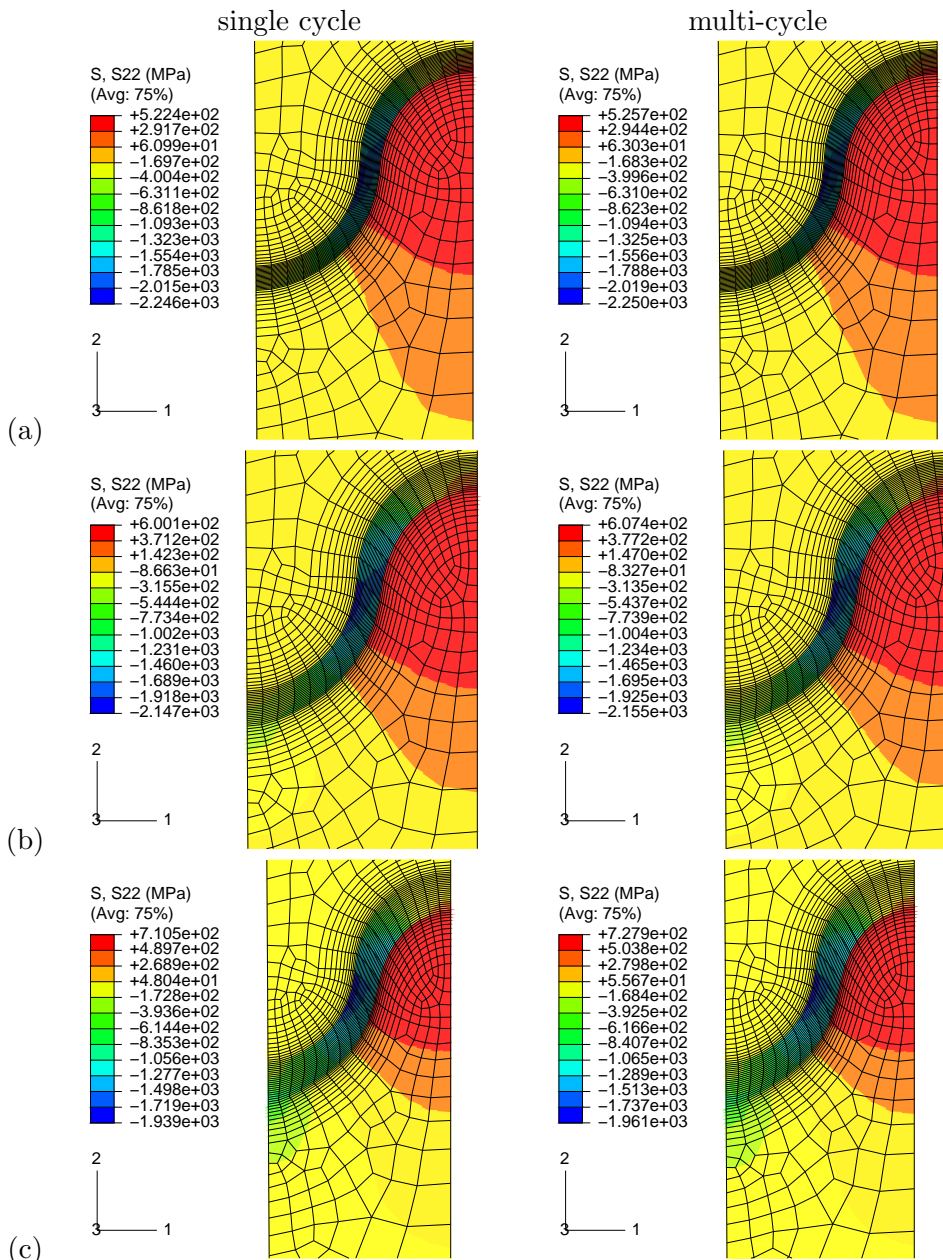


Figure 4.21. The stresses  $\sigma_{22}$  at ambient for a single cycle and a multicycle case: (a) after 20 hours of hold up at the peak temperature; (b) after 40 hours of hold up at peak temperature; (c) after 100 hours hold up at peak temperature.

process and cooling down phase results in thermal expansion misfit stresses. As already presented, cyclic loading has in fact a small impact upon stress distribution around the asperity and a single cycle with a long hold up time presented in Figure 4.20 can be used. Results obtained in this way would refer to those of Evans et al. [62].

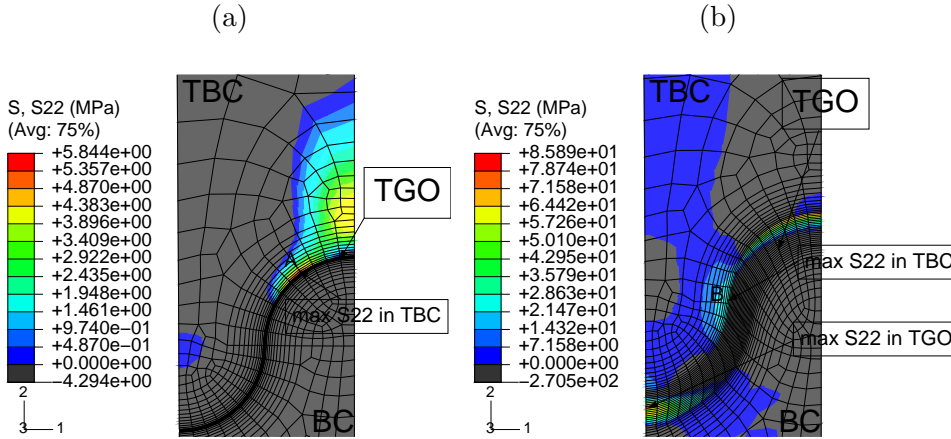


Figure 4.22. The stresses  $\sigma_{22}$  during 100 hours dwell time at peak temperature (equivalent to 50 sub-cycles presented in Figure 4.14): (a) at the beginning of the dwell time; (b) after 100 hours at the end of the dwell time. Compressive zones in grey.

Figure 4.22 presents the tensile  $\sigma_{22}$  stresses within TBC at the beginning and at the end of 100 hours hold up at peak temperature. This result is equivalent to 50 cycles of the shape presented in Figure 4.14. Compressive zones are indicated in grey, since they are irrelevant for crack evolution. In fact, we see that the oxidation process results in the creation of a tensile zone in the middle of the asperity — point B in Figure 4.22(b). The stresses  $\sigma_{22}$  in TBC increase as the TGO thickens during the dwell time, and after 100 hours reach about 35 MPa. The location of the maximal  $\sigma_{22}$  stress at the beginning of the oxidation process is point A in Figure 4.22(a). However, the value of the  $\sigma_{22}$  stress at this point decreases as the TGO thickens, and the value of the  $\sigma_{22}$  stress in point B in Figure 4.22(b) increases. The change of the maximal  $\sigma_{22}$  stress with time is presented in Figure 4.23. After 2 hours dwell time (one typical loading cycle) it reaches 14 MPa. Values of the critical normal stress for TBC reported in the literature vary from 10 to 100 MPa ( Białas et al. [27], Majerus [132]). It is assumed here that there is no crack formation within TBC during the first hold up-phase.

The location of maximal  $\sigma_{22}$  stresses within TGO has also been indicated in

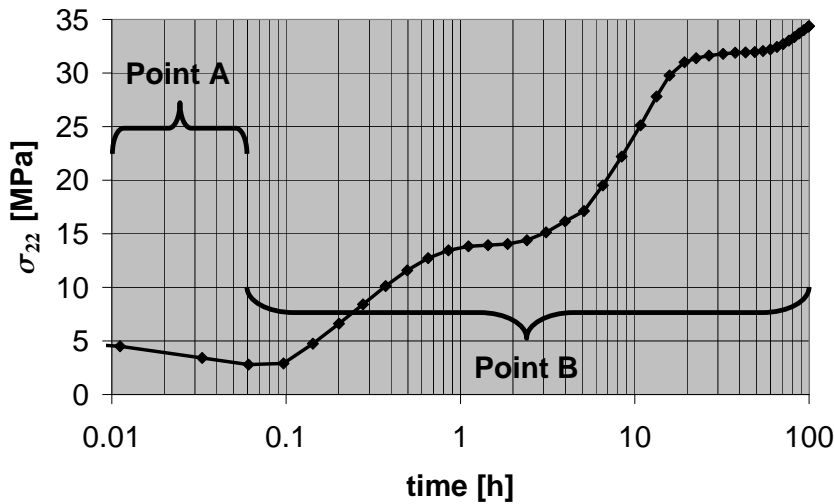


Figure 4.23. The maximal value of stresses  $\sigma_{22}$  within TBC during 100 hours dwell time at peak temperature. Points A and B are depicted in Figure 4.22.

Figure 4.22(b). After 100 hours of dwell time it reaches about 110 MPa being much below the critical stress for TGO equal 1200 MPa (Xie and Tong [219]).

Let us now turn our attention to the effect of thermal expansion mismatch and analyse the stress distribution within the TGO and BC during the cooling phase. The comparison of the results with the predictions of analytical model of Evans et al. [62] will also be made. Figure 4.24 presents the tensile  $\sigma_{22}$  stresses after cooling to ambient after 100 hours hold up at peak temperature. This hold up time is equivalent to 50 sub-cycles presented in Figure 4.14. Compressive zones are indicated in grey, since they are irrelevant for crack evolution. We see big tensile stresses at the peak of the TGO/BC interface appearing due to thermal expansion mismatch. Certainly they are the driving force for a crack running along the interface. This observation is in agreement with the predictions of the analytical model of Evans et al. [62].

Figure 4.17 presents the values of  $\sigma_{22}$  stresses at the peak of the TGO/BC interface at room temperature after different number of cycles. It can be observed, that already after 2 hours dwell time (one loading cycle) big tensional stresses appear at the interface reaching about 300 MPa. With the interfacial strength being 50–80 MPa (Gell et al. [74]), we conclude that the first microcrack would appear at the peak of the TGO/BC interface already during the first cooling down to ambient. The development of this microcrack and its influence on the stress redistribution within the system will be analysed in the next section.

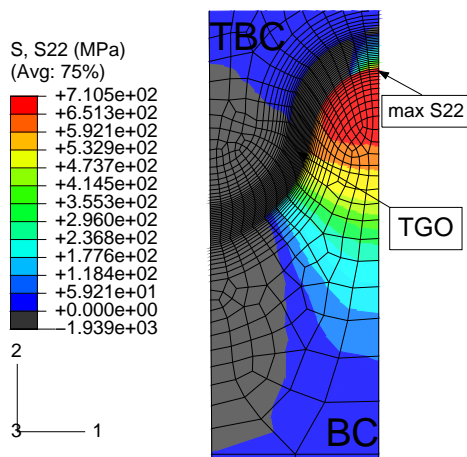


Figure 4.24. The stresses  $\sigma_{22}$  at the end of cooling to ambient after 100 hours hold up at peak temperature (equivalent to 50 sub-cycles presented in Figure 4.14). Compressive zones in grey.

#### 4.3.5. Crack development at the TGO/BC interface

Figure 4.25 shows the stresses  $\sigma_{22}$  at the end of the first cycle (2 hours of dwell time) with and without modelling of the TGO/BC interface crack. We can see that the crack development has a considerable influence on the stress distribution around the asperity. The development of the interfacial crack allows for a creation of a tensile zone within the TBC (region A in Figure 4.25) with the maximal  $\sigma_{22}$  stress reaching 87 MPa already after two hours of dwell time. Due to the relaxation taking place at high temperature, heating and hold-up phases produce stresses much smaller than those observed during the cooling down. Thus, when considering crack development at the interface it is the cooling phase being the most crucial for a further development of damage within the system.

Figure 4.26 shows the influence of cyclic loading upon the stress redistribution around the asperity when the development of the interfacial crack is modelled. It can be seen that even now both monotonic and cyclic loadings (20, 40 and 100 hours dwell time obtained for two loading histories presented in Figure 4.20) result in a similar stress redistribution after cooling down to ambient temperature. Figure 4.27 shows the length of the interfacial crack versus time. It is seen that the crack forms already during the first cooling down to ambient and its length stabilizes already after 3 cycles. For the single cycle case the duration of the high temperature exposure has no effect upon length of the crack after cooling down: it reaches the same length after 4, 20, 40 and

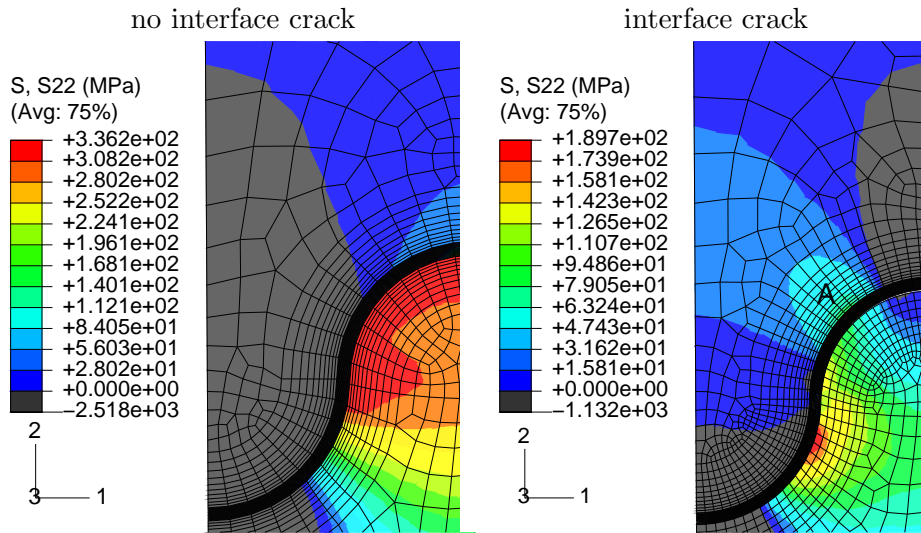


Figure 4.25. The stresses  $\sigma_{22}$  at the end of the first cycle (2 hours dwell time) with and without the TGO/BC interface crack. Compressive zones in grey.

100 hours of exposure at peak temperature. The cyclic loading manifests itself only by a longer crack during the stabilization phase, when compared with that after a single cycle loading. The differences in length are in fact small and one could say that cyclic loading has a negligible effect upon the length of the interfacial crack. Białaś and Mróz [30] and Mróz and Białaś [142] have shown that a cohesive interface subjected to a cyclic shear loading can accumulate damage regardless of loading direction (incremental failure). The cohesive model of Mróz and Białaś [142], however, does not assume unloading to the initial state, as it is the case in the model by Camanho and Dávila [40, 53] used in the present analysis. The minor influence of cyclic thermal loading upon crack development at the TGO/BC interface should therefore be explained by a small amplitude of cyclic loading at the interface itself, where upon unloading the normal and shear stresses decrease without additional damage accumulation. In this context, it is only the dwell time alone that influences the stress distribution around the asperity, and not the way it is realized in practice (cyclic or monotonic loading).

The stabilization of crack length after a few cycles contradicts the experience that failure occurs after a sufficient number of cycles. This result just shows that all the crucial factors for coating delamination are not included yet in the present FE model. One of them could be the cracking within TBC, that will be

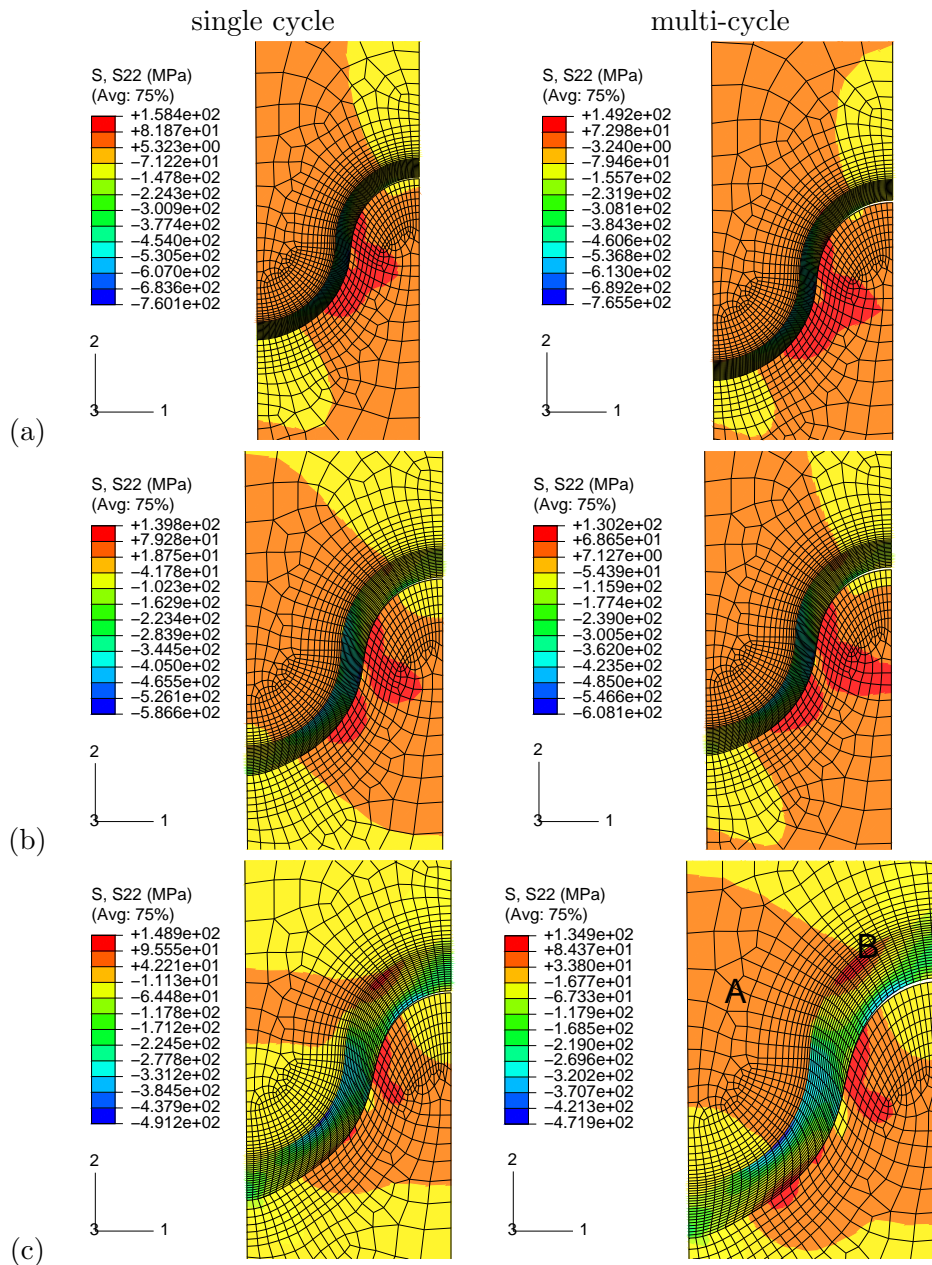


Figure 4.26. The stresses  $\sigma_{22}$  at ambient for a single cycle and a multi-cycle case after cooling to ambient. Modelling of crack development at the TGO/BC interface. (a) after 20 hours hold up at peak temperature; (b) after 40 hours hold up at peak temperature; (c) after 100 hours hold up at peak temperature.

considered in the upcoming research.

There are two crucial aspects related to the stress redistribution within the system due to crack formation at the TGO/BC interface: (i) development of a tensile zone within TBC (region A indicated in Figure 4.25 and in Figure 4.26) and (ii) development of a tensile zone within TGO (region B in Figure 4.26). These zones can be observed only during the cooling phase and the  $\sigma_{22}$  stresses within them reach their biggest values at ambient temperature. These two aspects will be addressed next.

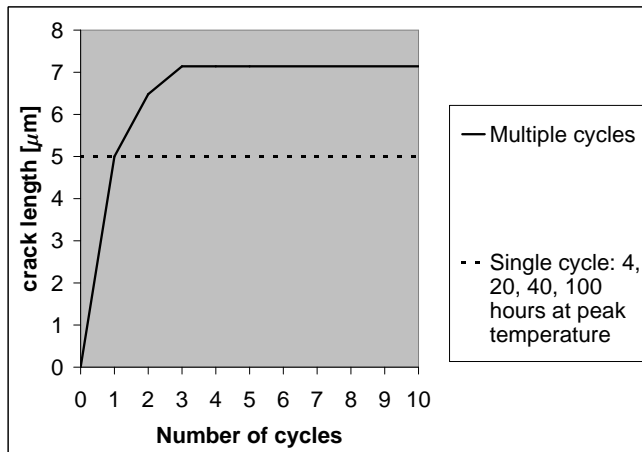


Figure 4.27. Length of the interfacial crack versus time: multiple cycles and a single cycle case.

As already indicated in Figure 4.25, the tensional zone around point A forms in the case of interfacial cracking already during the first cooling down. Subsequent loading results in the extension of this tensile zone over the whole valley of the asperity, see Figure 4.26. However, the point where the stresses reach the maximal values remains the same — it is the point A in Figure 4.25. Figure 4.28 presents the values of stress  $\sigma_{22}$  at this point at room temperature after different dwell time. The biggest value is reached already after 2 hours of dwell time and equals 87 MPa. It decreases for longer dwell times, which is correlated with stress relaxation within TBC taking place at high temperature. However, the rate of decrease is relatively slow and after 100 hours of dwell the stress is still about 60 MPa. With the critical strength of TBC varying from 10 to 100 MPa (Białas et al [27], Majerus [132]) it is very likely, that the first micro-crack within TBC would form independent from dwell time already during first cooling down to ambient. It should be remembered that this is a consequence of crack formation at the TGO/TBC interface.

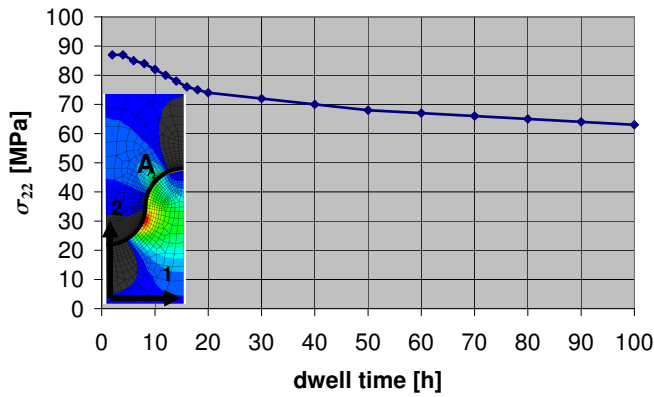


Figure 4.28. The maximal value of stress  $\sigma_{22}$  within TBC (point A) at room temperature after different dwell times. Influence of crack development at the TGO/BC interface.

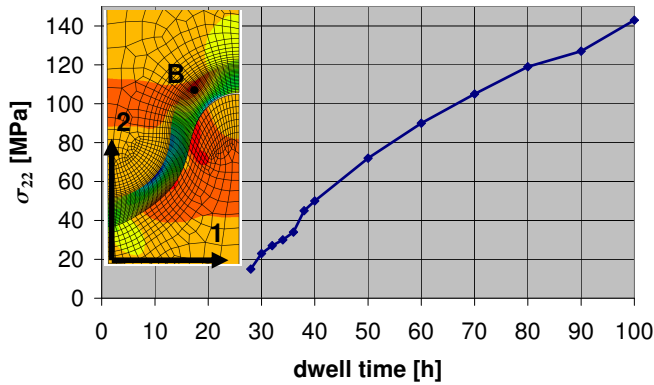


Figure 4.29. The maximal value of stress  $\sigma_{22}$  within TGO (point B) at room temperature after different dwell times. Influence of crack development at the TGO/BC interface.

The development of the tensile zone within TGO (region B in Figure 4.26) can be correlated with the thickness of the oxide film. The zone forms after 28 hours of dwell time (14 typical sub-cycles presented in Figure 4.14) and then the value of maximal stress  $\sigma_{22}$  there increases, as presented in Figure 4.29. The critical stress for TGO reported by Xie and Tong [219] equals 1200 MPa. The result suggests that cracking within TGO will not take place but micro-crack development within the TBC will occur. At this point, however, it is difficult to say to what extent the TBC crack could influence the overall stress redistribution around the asperity and particularly within TGO. As presented in Figure 4.30, the maximal stresses within TGO and TBC are located close to each other but they do not coincide. The next step of this research will be

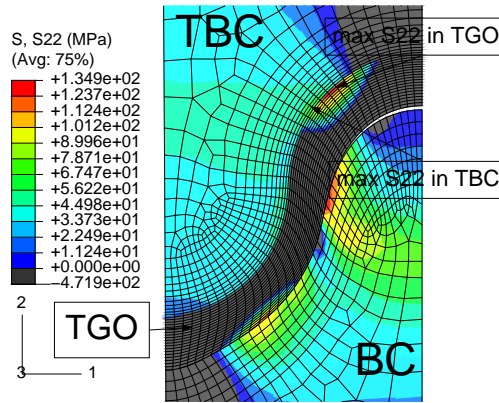


Figure 4.30. The location of maximal  $\sigma_{22}$  stresses within TBC and TGO at ambient temperature after 100 hours of dwell time. Influence of crack development at the TGO/BC interface. Compressive zones in grey.

the modelling of microcrack development within the TBC. It could provide an outlook on possible failure development modes and, particularly, on the linking of the TBC and BC/TGO interface microcracks through zone B indicated in Figure 4.26. The almost coinciding location of maximal stresses within TGO and TBC suggests furthermore the following hypothesis of damage evolution. Already after 2 hours of dwell time, during cooling down to ambient, a microcrack at the TGO/BC interface forms. Its appearance influences the stress redistribution within TBC, allowing for a creation of a tensional zone and a formation of TBC micro-crack. Subsequent TGO thickening (cyclic or monotonic temperature loading) increases the area under tension within TBC and promotes the development of the TBC crack. With TGO being thick enough, a tensional zone develops within TGO, allowing for linking of TBC and the interface crack through TGO.

#### 4.4. Conclusions

It is difficult to experimentally determine consistent material properties of APS TBC, being a porous and highly anisotropic material. In spite of that, by the numerical simulation, the effect of the value of critical energy release rate  $G_I$  for APS TBCs on through-thickness cracking was examined. It revealed that due to decreasing value of  $G_I$  one obtains increasing number of cracks within the coating. Multiple cracking within a coating can reduce the magnitude of critical energy release rate for the interface between the coating and the substrate,

suggesting that segmentation cracking can be beneficial for coating life time, as it is observed within EB PVD. This is the main conclusion of the first part of the chapter, concerning segmentation cracking within TBC layer. Quantitative results of the finite element simulations can be used to tailor coating properties.

In order to obtain crack localization during the numerical computations, the loading step had to be small enough to allow for satisfaction of failure criteria in only one integration point per loading step. Only this procedure led to a realistic failure scenario and helped overcome convergence difficulties. The obtained numerical results resembled the experiment quantitatively — both provide similar number of TBC through-thickness cracks as well as their localization.

In the early work by Chang et al. [43] the effect of thermal expansion mismatch, oxidation and precracking was investigated. The authors proposed a failure mechanism induced solely by the oxidation process, which provided important insights into the thermomechanical behaviour of TBCs. Freborg et al. [68] performed similar simulations to those of Chang et al. [43]. The main difference was to include the creep effect. It turned out that their results supported the failure mechanism proposed by Chang et al. [43]: early cracking at bond coat peaks and subsequent increasing growth of the microcracks when TGO reaches a critical thickness.

The analysis presented in the second part of the chapter took into account a broad spectrum of aspects crucial for thermal loadings of TBC systems, namely creep of all constituents, oxidation process, thermal expansion mismatch, the effect of interfacial asperity and crack development at TGO/BC interface. The main results can be summarized as:

- during thermal loading the creep of CMSX-4 substrate can be neglected, since it does not play almost any role on the stress redistribution around the asperity;
- the cooling stage is the most crucial for micro-crack development within the unit cell;
- for elastic and viscous materials stress distribution after cooling to ambient is basically identical for a single loading cycle with the dwell time of  $m$  multiple loading cycles;
- crack development at the TGO/BC interface leads to a formation of crucial tensile zones within TBC and, provided the TGO layer is sufficiently thick, also within TGO.

Combined development of the interface crack and of the thickening of the TGO leads to an appearance of a tensional zone within TGO besides the roughness peak and the following hypothesis of damage evolution around an asperity

can be formulated. After cooling down to ambient a microcrack at the TGO/BC interface forms. Its appearance influences the stress redistribution within TBC, allowing for a creation of a tensional zone and a formation of TBC microcrack. Subsequent TGO thickening increases the area under tension within TBC and promotes the development of the TBC crack. With TGO being thick enough, a tensional zone develops within TGO, allowing for linking of TBC and the interface crack through TGO.

This hypothesis is in good agreement with the cracking scenario presented by Chang et al. [43] and Freborg et al. [68] and provides additional quantitative information. Further research would require to model crack development within TBC (using for example cohesive zone elements) and to examine its influence upon stress redistribution within TGO. The next step could be modelling of linking of the TBC and the interface cracks.



# Frictional delamination

## 5.1. Introduction

Due to their mathematical simplicity strip models serve as a basis for analytical solutions providing insight into many generally complex problems involving delamination, film cracking or snap-back response, see for example Białaś and Mróz [28] or Schreyer and Pepper [174]. Even though they provide closed-form solutions, they are not able to capture many features intrinsic to two or three dimensional nature of film stiffening or interfacial failure phenomena, like shape of delaminated zone or effect of substrate curvature on failure propagation.

An analytical solution to a two dimensional problem of a thin plate adhesively bonded to a surface of an elastic half-space and loaded by a concentrated Mindlin-type force is presented by Selvadurai and Willner [179]. A problem related to a flexure of a plate-like surface layer bonded to an elastic half-space region is discussed by Selvadurai et al. [180]. The flexure of the coating is induced by a nucleus of thermo-elastic strain acting within the half-space region. In both contributions it is assumed, that the film remains fully bonded to the substrate, with no separation allowed.

The chapter presents a solution to a two dimensional delamination problem of an infinite elastic film resting on a rigid substrate and loaded by a monotonically increasing in-plane point force. A rigid-slip contact is assumed between the film and the substrate, allowing for modelling of interfacial failure in the sliding mode. From a mathematical point of view it is an attempt to go beyond the limits of one dimensional strip models, when describing decohesion and frictional slip. The presented approach can be used to obtain approximate closed-form solutions of similar delamination phenomena. The problem can be encountered in many practical applications, for example, fiber reinforced polymer sheets used in structural strengthening techniques (Cottone and Giambanco [50]), or in laminated glass, where two or more glass plies are bonded together by a polymeric interlayer through treatment at high temperature and pressure in

autoclave (Ivanov [101], Muralidhar et al. [143]).

## 5.2. Problem formulation

Let us consider an infinite elastic film of thickness  $h$  resting on an infinite rigid foundation. The film is subjected to a monotonically increasing point load  $\mathbf{P}$  acting in the plane  $xy$  on its upper surface, as presented in Figure 5.1(a). By assuming rigid-slip interaction between the film and the substrate we have two zones developed at the interface, namely  $\Omega$ , where the film is displaced due to the external loading  $\mathbf{P}$ , and  $\Sigma$ , where the structure remains fully bonded with vanishing film displacements. Let  $\partial\Omega$  denote the delamination front between the regions  $\Omega$  and  $\Sigma$ , as schematically presented in Figure 5.1(b). Assuming the film thickness  $h$  to be small as compared to  $2l$ , being the characteristic length of the delaminated zone  $\Omega$ , the problem can be treated as two dimensional with the film in plane-stress conditions. The interaction between the film and the substrate is reduced to shear traction  $\boldsymbol{\tau}^f$ , treated as in-plane body forces acting on the film. Magnitude of traction  $\boldsymbol{\tau}^f$  reaches the critical value  $|\boldsymbol{\tau}^f| = \tau^f = \text{const}$  within the delaminated zone  $\Omega$ . The equilibrium equations are

$$\sigma_{ij,j} + \frac{\tau_i^f}{h} + \frac{P_i}{h} \delta_0 = 0, \quad (i, j) = 1, 2, \quad 1 \sim x, \quad 2 \sim y, \quad (5.1)$$

where  $\delta_0$  is Dirac distribution. The term  $(P_i/h)\delta_0$  introduces the effect of concentrated force acting at point  $O$ . By assuming that the directions of axis  $x$  and vector  $\mathbf{P}$  coincide we have  $P_1 = P_x = P$ ,  $P_2 = P_y = 0$ . The components of shear traction at the damaged interface have the form

$$\tau_1^f = \tau_x^f = \tau^f \cos \theta, \quad \tau_2^f = \tau_y^f = \tau^f \sin \theta, \quad (5.2)$$

where  $\theta$  is the angle between the vector of interfacial traction and axis  $x$ , see Figure 5.1(b).

The stress-strain relations for an isotropic elastic medium in plane-stress conditions are

$$\begin{aligned} \varepsilon_{ii} &= \frac{\sigma_{ii} - \nu\sigma_{jj}}{E}, \quad (i, j) = x, y, \\ \varepsilon_{xy} &= \frac{1 + \nu}{E} \sigma_{xy}, \\ \varepsilon_{zz} &= -\frac{\nu}{E} (\sigma_{xx} + \sigma_{yy}). \end{aligned} \quad (5.3)$$

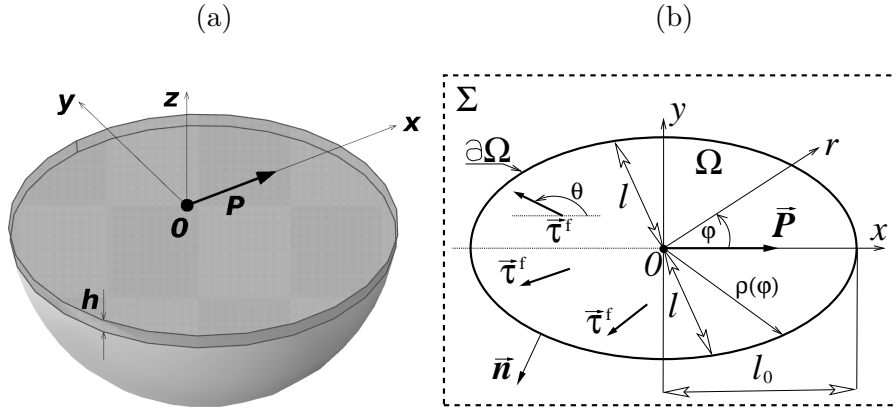


Figure 5.1. (a) Infinite elastic film resting on a rigid substrate. In-plane point loading. (b) Two dimensional model: plane-stress conditions with interfacial traction  $\tau^f$  treated as in-plane body forces.

The strains are defined as

$$\varepsilon_{ij} = \frac{1}{2}(u_{i,j} + u_{j,i}), \quad \varepsilon_{zz} = u_{z,z}, \quad (i, j) = x, y, \quad (5.4)$$

where  $\mathbf{u}$  is the film displacement field.

We assume rigid-slip interface to model the interaction between the film and the foundation. The slip condition is defined in terms of function  $F$

$$F(\tau_x^f, \tau_y^f) = \sqrt{(\tau_x^f)^2 + (\tau_y^f)^2} - \tau^f \quad (5.5)$$

and we have  $F = 0$  for  $|\dot{\mathbf{u}}| > 0$  (zone  $\Omega$  in Figure 5.1b) and  $F \leq 0$  for  $|\dot{\mathbf{u}}| = 0$  (zone  $\Sigma$  in Figure 5.1b). The constitutive law for the slip at the interface takes the form

$$\begin{aligned} \dot{u}_i &= -\dot{\Lambda} \frac{\partial F}{\partial \tau_i^f}, \quad \dot{\Lambda} \geq 0, \quad i = (x, y), \\ F &\leq 0, \quad \dot{\Lambda} F = 0, \end{aligned} \quad (5.6)$$

where  $\Lambda$  is a multiplier. The geometrical representation of slip rule (5.6) is given in 5.2(a). Equations (5.6) can be obtained when the cohesive zone model presented in Section 3.2 is specified to the rigid-slip response, with a constant value of threshold shear stress.

By means of equations (5.5) and (5.6) we can write formulas for the sine and cosine of angle  $\theta$  between the vector of interfacial traction  $\tau^f$  within  $\Omega$  and

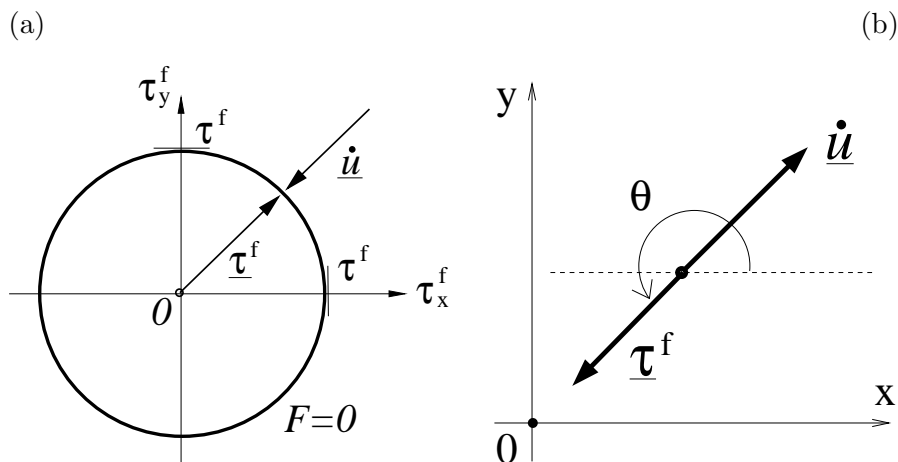


Figure 5.2. (a) Slip function  $F = 0$ . (b) Co-linearity of vectors  $\tau^f$  and  $\dot{u}$ .

$x$  axis

$$\sin \theta = -\frac{\dot{u}_y}{\sqrt{\dot{u}_x^2 + \dot{u}_y^2}}, \quad \cos \theta = -\frac{\dot{u}_x}{\sqrt{\dot{u}_x^2 + \dot{u}_y^2}}. \quad (5.7)$$

Thus, vectors  $\tau^f$  and  $\dot{u}$  are co-linear and point in opposite directions, see Figure 5.2(b).

To fully formulate the problem we have to add boundary conditions to equations (5.1)–(5.7). In order to do so, let us first consider the region  $\Sigma$ , where the structure is fully bonded with vanishing film displacements. Vanishing film displacements result in vanishing strains and consequently in zero stress and we can write

$$\mathbf{u} = \mathbf{0}, \quad \boldsymbol{\sigma} = \mathbf{0} \quad \text{in } \Sigma. \quad (5.8)$$

To fulfil the displacement and stress continuity at the delamination front  $\partial\Omega$  separating the damaged and intact zones we therefore impose

$$\mathbf{u} = \mathbf{0}, \quad \boldsymbol{\sigma} = \mathbf{0} \quad \text{on } \partial\Omega. \quad (5.9)$$

Thus, we have values of both natural and essential boundary conditions prescribed on  $\partial\Omega$ . The unknown to the problem remains  $\partial\Omega$  itself and, as a part of the solution, has to be determined. Our problem belongs to the class of moving boundary problems.

When formulating the problem we need to properly describe the existence of two regions within the film, namely with zero and with non-zero displacement fields. Boundary conditions (5.9) describe the interaction between them. While

within  $\Sigma$  we have  $\mathbf{u} = \mathbf{0}$  by definition, equality  $\mathbf{u} = \mathbf{0}$  holds also on  $\partial\Omega$  due to continuity of displacement field. The condition  $\boldsymbol{\sigma} = \mathbf{0}$  on  $\partial\Omega$  is not so straightforward, however. Vanishing  $\mathbf{u}$  within  $\Sigma$  obviously results in vanishing  $\boldsymbol{\sigma}$  in the bonded portion of the film, but it does not necessarily mean that the stress can be continued analytically on the debonded portion passing through the boundary  $\partial\Omega$ . For example, Gastaldi and Kinderlehrer [72] consider an elastic beam on a rigid table. The precise variational characterization of their problem is not at all trivial and prescribes the formation of a concentrated force at the point between the region where the beam is detached and the region where it is in contact with the substrate. In this context, a rigorous consideration of the character of stress field on  $\partial\Omega$  in our case, would probably require advanced variational arguments, and as such it would go beyond the scope of the present analysis, aimed only at finding the solution to the problem. Keeping all that in mind, one should treat  $\boldsymbol{\sigma} = \mathbf{0}$  as an assumption regarding the interaction between the displaced and bonded portion of the film. The following physical argument can be considered in favour of this assumption. One may infer, albeit tentatively, that any stress concentration might provoke a singularity in the interfacial shear stress, that would certainly overcome the strength of the adhesive bonding, thus producing delamination from the substrate. From this point of view, condition  $\boldsymbol{\sigma} = \mathbf{0}$  on  $\partial\Omega$  becomes the only one that is compatible with the limited strength of adhesives introduced by equations (5.5) and (5.6). Capozucca [41], Grande et al. [78] and Yuan et al. [226] presented experimentally obtained distribution of strain in fiber reinforced polymer (FRP) sheets bonded to concrete or clay prisms. During pull-push shear tests the sheets were subjected to a loading condition similar to that discussed in the present paper. The decohesion between the FRP reinforcement and the underlying prisms was the predominant failure mode. The strain gauges located on polymer sheets revealed gradual development of a slip zone between the FRP and the substrate. Recorded strain decreased to zero outside and on the boundary of the detached area. These experimental results provide some support to the condition  $\boldsymbol{\sigma} = \mathbf{0}$  on  $\partial\Omega$  assumed in the present analysis.

In the above it is assumed that in the detached area the plate is in slip condition. In general, however, one can think of a more complex situation in which there are some non-slip zones within the detached region. It seems that from physical point of view there are no reasons to exclude a priori such a situation. In this context, the solution sought in the following should be understood as belonging to only one family of possible responses. The fact that it might be the only reasonable response comes from engineering intuition backed up with results of finite element method, which can be obtained totally indepen-

dently from the forthcoming considerations. The finite element results will be presented in Section 5.8.4.

### 5.3. Dimensional analysis

The governing parameters, which characterize the considered problem, are:  $E$ ,  $\tau^f$ ,  $\nu$ ,  $h$ ,  $r$ ,  $\varphi$  and  $l$ . As indicated in Figure 5.1(b), parameters  $r$  and  $\varphi$  are the polar coordinates and  $2l$  is a length of the delaminated zone measured along an arbitrary but constant angle. Instead of  $l$  a value of the loading force  $P$  could also be used, since both these parameters describe uniquely the delamination process. Both  $P$  and  $l$  can be prescribed the meaning of time, since only monotonically increasing loading is considered.

By assuming  $l$  and  $\tau^f$  to introduce the independent dimensions we can write

$$\frac{\rho}{l} = f^\rho\left(\varphi, \frac{E}{\tau^f}, \nu\right), \quad (5.10)$$

$$\theta = f^\theta\left(\frac{r}{l}, \varphi, \frac{E}{\tau^f}, \nu\right), \quad (5.11)$$

where  $\rho$  is a function describing the shape of the boundary  $\partial\Omega$  between the intact and damaged interfacial zones. In our analysis the film is assumed to remain elastic during the slip process and to be in plane-stress conditions due to its small thickness, when compared with characteristic length of damaged zone. For fixed loads  $\tau^f$  and  $\mathbf{P}$  smeared uniformly over the film thickness, as done in the equilibrium equation (5.1), we have the strains, stresses and displacements inversely proportional to  $h$  and can write

$$\begin{aligned} \varepsilon_{ij} \frac{h}{l} &= f_{ij}^\varepsilon\left(\frac{r}{l}, \varphi, \frac{E}{\tau^f}, \nu\right), \\ \frac{\sigma_{ij}}{\tau^f} \frac{h}{l} &= f_{ij}^\sigma\left(\frac{r}{l}, \varphi, \frac{E}{\tau^f}, \nu\right), \\ \frac{u_i h}{l^2} &= f_i^u\left(\frac{r}{l}, \varphi, \frac{E}{\tau^f}, \nu\right), \end{aligned} \quad (5.12)$$

$$(i, j) = x, y.$$

Equations (5.10) and (5.11) indicate that the shapes of the moving boundary  $\partial\Omega$ , as well as the spatial distribution of  $\theta$ , vary with  $l$ , while remaining

geometrically similar. In fact, we encounter here a self-similar phenomenon, where any characteristic of the problem can be written as

$$\frac{\mathfrak{F}(r, \varphi, t)}{\bar{\mathfrak{F}}(t)} = \mathbf{f}\left(\frac{r}{\bar{r}(t)}, \varphi\right). \quad (5.13)$$

In other words, there exist time-dependent scales  $\bar{\mathfrak{F}}(t)$  and  $\bar{r}(t)$  such that measured in these scales the characteristic  $\mathfrak{F}$  becomes time-independent (Barenblatt [20]). Since only monotonically increasing loading is considered and the parameter  $l$  has also the meaning of time, we have  $t \sim l = \bar{r}(t)$ .

Let us derive a general relation between the loading force  $P$  and the characteristic length of the delaminated zone  $2l$ . Formula

$$P = -\tau^f \iint_{\Omega} \cos \theta \, d\Omega = -\tau^f \int_0^{2\pi} \int_0^{\rho} \cos \theta(r, \varphi) r \, dr d\varphi \quad (5.14)$$

simply states that the external force has to be equilibrated by the tangential traction at the interface. By normalizing the coordinate  $r$  by  $l$  and by virtue of equations (5.10) and (5.11) we can write

$$P = -l^2 \tau^f \int_0^{2\pi} \int_0^{\rho/l} \cos \theta\left(\frac{r}{l}, \varphi\right) \frac{r}{l} \frac{dr}{l} d\varphi = l^2 \tau^f f^P\left(\frac{E}{\tau^f}, \nu\right), \quad (5.15)$$

where

$$f^P\left(\frac{E}{\tau^f}, \nu\right) = - \int_0^{2\pi} \int_0^{\rho/l} \cos \theta\left(\frac{r}{l}, \varphi\right) \frac{r}{l} \frac{dr}{l} d\varphi. \quad (5.16)$$

Thus, there is a quadratic functional dependance between the loading force  $P$  and the extent of the delaminated zone.

By virtue of equations (5.12) it is easy to show that the strain, stress and displacement fields satisfy the following relations

$$\begin{aligned} \varepsilon_{ij}(x, y, l) &= l \varepsilon_{ij}\left(\frac{x}{l}, \frac{y}{l}, 1\right), \\ \sigma_{ij}(x, y, l) &= l \sigma_{ij}\left(\frac{x}{l}, \frac{y}{l}, 1\right), \\ u_i(x, y, l) &= l^2 u_i\left(\frac{x}{l}, \frac{y}{l}, 1\right), \\ (i, j) &= x, y, \end{aligned} \quad (5.17)$$

where we have changed space parametrization from polar to cartesian. Formulas (5.17) state that functions  $\varepsilon_{ij}$  and  $\sigma_{ij}$  are homogenous of degree one, and functions  $u_i$  are homogenous of degree two.

## 5.4. Observations - one dimensional slip model

Before we proceed with the analysis of our problem, let us focus for a moment on its one dimensional counterpart presented in Figure 5.3. It is simply an elastic strip of height  $h$  and width  $w$ , resting on a rigid substrate and loaded by a point force  $P$ . There is a rigid-sticking and frictional slip between the strip and the substrate, governed by the same interface law as presented in Chapter 3 by equation (3.11). In the present case it can be rewritten as

$$\dot{u} = \dot{\Lambda} \text{sign}(\tau), \quad \dot{\Lambda} \geq 0, \quad |\tau| - \tau^f \leq 0, \quad \dot{\Lambda}(|\tau| - \tau^f) = 0, \quad (5.18)$$

where  $\Lambda$  is a multiplier,  $u$  is the strip displacement and, as in the two dimensional case,  $\tau^f$  is the maximal value of frictional stress at the interface. Force  $P$  is monotonically increasing, creating a slip zone for  $x$  satisfying  $-l \leq x \leq l$ , see Figure 5.3. By assuming that the strip is thin compared with the extent of the slip zone and treating the interfacial traction as body forces, the equilibrium equation can be formulated

$$\frac{d\sigma}{dx} - \frac{\tau^f}{h} = 0. \quad (5.19)$$

Hooke's law  $\sigma = E\varepsilon$ , strain-displacement relation  $du/dx = \varepsilon$  and boundary conditions  $u(\pm l) = \sigma(\pm l) = 0$  provide respectively stress and displacement fields

$$\sigma(x, l) = \begin{cases} \frac{\tau^f}{h} (x - l), & x \in \langle 0, l \rangle \\ \frac{\tau^f}{h} (x + l), & x \in \langle -l, 0 \rangle \end{cases}, \quad (5.20)$$

$$u(x, l) = \begin{cases} \frac{\tau^f}{2Eh} (x - l)^2, & x \in \langle 0, l \rangle \\ \frac{\tau^f}{2Eh} (x + l)^2, & x \in \langle -l, 0 \rangle \end{cases}. \quad (5.21)$$

They are schematically depicted in Figure 5.4. Global equilibrium for the displaced fragment  $P = w \int_{-l}^l \tau^f dx$  results in a relation between the loading force and the extent of the slip zone

$$P = 2\tau^f w l. \quad (5.22)$$

As we see the one dimensional counterpart to our original problem is rather trivial and allows for an analytical solution by solving a set of simple differential equations. Let us think of it in a slightly different manner. The strip is elastic and infinite and, because of that, its stress and displacement fields are resultants of superposition of all forces acting on it. In our case they are the point force  $P$

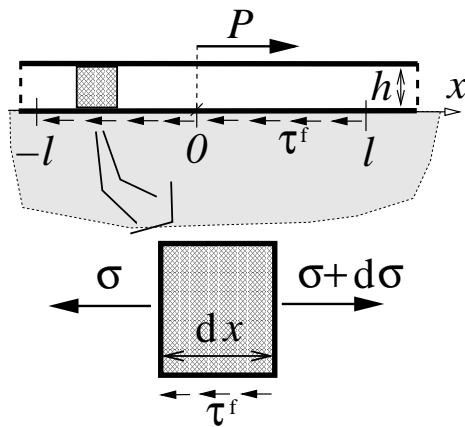


Figure 5.3. Elastic strip on rigid substrate loaded by a point force.

and the continuously distributed frictional traction  $\tau^f$ . We can therefore write

$$\sigma(x) = \sigma^P(x) + \sigma^{\tau^f}(x), \quad (5.23)$$

$$u(x) = u^P(x) + u^{\tau^f}(x), \quad (5.24)$$

where

$$\sigma^P(x) = P \tilde{\sigma}(x, 0), \quad u^P(x) = P \tilde{u}(x, 0),$$

$$\sigma^{\tau^f}(x) = w \int_{-l}^l \tau^f \tilde{\sigma}(x, X) dX, \quad (5.25)$$

$$u^{\tau^f}(x) = w \int_{-l}^l \tau^f \tilde{u}(x, X) dX.$$

In the above formulas,  $\tilde{\sigma}(x, X)$  and  $\tilde{u}(x, X)$  are respectively stress and displacement at point  $x$  resulting from a unit force impose at point  $X$  of an infinite elastic strip of thickness  $h$  and width  $w$ . They are derived in Appendix A and given by equations (A.3) and (A.4).

By substituting stress and displacements Green's functions (A.3) and (A.4) into equations (5.23) and (5.24) and integrating we obtain

$$\sigma(x) = -\frac{P}{2hw} \text{sign } x + \frac{\tau^f}{h} x, \quad (5.26)$$

$$u(x) = \frac{\tau^f}{2hE} [x^2 + l^2 - \mathcal{D}(l)] - \frac{P}{2hwE} [|x| - d(0)], \quad (5.27)$$

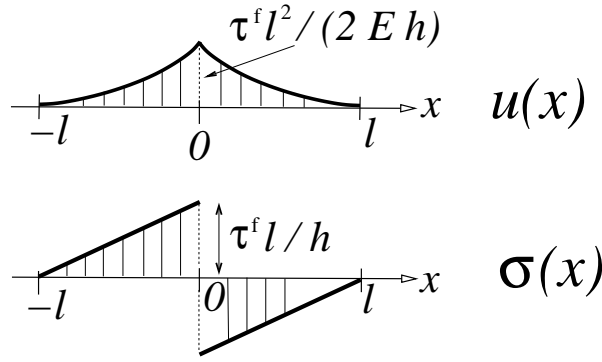


Figure 5.4. Displacement and stress field within an elastic strip loaded by a point force and frictional traction.

where

$$\mathcal{D}(l) = \int_{-l}^l d(X) dX$$

and  $d(0)$  result from integration performed when deriving displacement Green's function (A.4). By making use of the global equilibrium  $P = w \int_{-l}^l \tau^f dx$  and equation (5.22) we have

$$\sigma(x) = -\frac{\tau^f}{h}(x + l \operatorname{sign} x), \quad (5.28)$$

$$u(x) = \frac{\tau^f}{2hE}[x^2 + l^2 - \mathcal{D}(l)] - \frac{\tau^f l}{hE}[|x| - d(0)]. \quad (5.29)$$

The displacement condition  $u(l) = 0$  provides the relation

$$\mathcal{D}(l) = 2l d(0), \quad (5.30)$$

which can be consequently substituted into (5.29). Finally we obtain

$$u(x) = \frac{\tau^f}{2hE}(x^2 + l^2 - 2l|x|) \quad (5.31)$$

and see that in the end  $u(x)$  does not depend on the value of  $d(0)$ .

Note that stress (5.28) and displacement (5.31) are essentially identical to those previously obtained and given by equations (5.20) and (5.21), respectively. It was expected from the mathematical point of view, but some comment is needed here with regard to the mechanical background of the problem. Our one dimensional slip problem is nonlinear and has a moving boundary enclosing

a zone with the stresses and displacements localized around the loading force. Nevertheless, it was possible to solve it by applying a superposition methodology coherent to linear elasticity problems. The formulas (5.23) and (5.24) could be regarded as Somigliana's identities respectively for stresses and displacements. By allowing the Green's function to be valid for an infinite strip, we searched for a situation when the resultant stresses and displacements disappeared on a certain boundary enclosing the concentrated force. In the one dimensional case this boundary reduces to a point, making the situation trivial and allowing for an analytical solution. The result seems to be appealing and provides motivation that the same superposition methodology could be applied to a more complex two dimensional situation.

## 5.5. Superposition of solution

Due to the fact that the film is assumed to remain elastic during the delamination process, the displacements and the stresses within the film are the superposition of respective displacements and stresses induced by both the point load  $P$  and the forces at the interface. There are zero tractions and displacements at the moving boundary  $\partial\Omega$  as imposed by the conditions (5.9) and we can write

$$u_i(\mathbf{x}) = u_i^P(\mathbf{x}) + u_i^{\tau^f}(\mathbf{x}), \quad (5.32)$$

$$\sigma_{ij}(\mathbf{x}) = \sigma_{ij}^P(\mathbf{x}) + \sigma_{ij}^{\tau^f}(\mathbf{x}), \quad (5.33)$$

where

$$u_i^P(\mathbf{x}) = P \tilde{u}_i^x(\mathbf{x}; \mathbf{0}), \quad \sigma_{ij}^P(\mathbf{x}) = P \tilde{\sigma}_{ij}^x(\mathbf{x}; \mathbf{0}),$$

$$u_i^{\tau^f}(\mathbf{x}) = \iint_{\Omega} \left[ \tau_x^f(\mathbf{X}) \tilde{u}_i^x(\mathbf{x}; \mathbf{X}) + \tau_y^f(\mathbf{X}) \tilde{u}_i^y(\mathbf{x}; \mathbf{X}) \right] d\Omega, \quad (5.34)$$

$$\sigma_{ij}^{\tau^f}(\mathbf{x}) = \iint_{\Omega} \left[ \tau_x^f(\mathbf{X}) \tilde{\sigma}_{ij}^x(\mathbf{x}; \mathbf{X}) + \tau_y^f(\mathbf{X}) \tilde{\sigma}_{ij}^y(\mathbf{x}; \mathbf{X}) \right] d\Omega,$$

$$(i, j) = x, y.$$

With  $j$  being either  $x$  or  $y$ , the functions  $\tilde{u}^j(\mathbf{x}; \mathbf{X})$  and  $\tilde{\sigma}^j(\mathbf{x}; \mathbf{X})$  in equations (5.34) are respectively plane-stress displacements and stresses at point  $\mathbf{x}$  resulting from a unit force imposed at point  $\mathbf{X}$  of an infinite plate of given thickness  $h$  and acting in the  $j$  direction. In this context, equations (5.32)

and (5.33) can be treated as particular forms of Somigliana's identities respectively for displacements and stresses, specified for a structure in plane-stress conditions and loaded only by mass forces and a point load, with neither traction nor displacements on the boundary  $\partial\Omega$ . The Green's functions  $\tilde{\mathbf{u}}^j(\mathbf{x}; \mathbf{X})$  and  $\tilde{\boldsymbol{\sigma}}^j(\mathbf{x}; \mathbf{X})$  are derived in Appendix B — equations (B.13), (B.14) and (B.18), (B.19) are respectively stress and displacement Green's function in the cartesian parametrization of space, equations (B.16), (B.17) and (B.20) provide Green's functions written in the polar space parametrization.

Because of the particular choice of Green's functions  $\tilde{\mathbf{u}}^j(\mathbf{x}; \mathbf{X})$  and  $\tilde{\boldsymbol{\sigma}}^j(\mathbf{x}; \mathbf{X})$  valid for an infinite plate, we consider an infinite film while searching for the solution. For a given point force  $\mathbf{P}$  loading the infinite medium we try to find a zone  $\Omega$  around  $\mathbf{P}$  and such a distribution of stresses  $\boldsymbol{\tau}^f$  within  $\Omega$  that, by virtue of superposition, there is no interaction between  $\Omega$  and the surrounding area  $\Sigma$ , see Figure 5.1(b). In order to be so, the condition  $\boldsymbol{\sigma} = \mathbf{0}$  on  $\partial\Omega$  has to be satisfied. When this is the case, the film within the external region  $\Sigma$  is loaded neither by body forces nor on its boundary and, with zero rigid motion, shows no displacements and remains fully bonded to the substrate. Within  $\Omega$ , on the other hand, the solution to our problem can be obtained by virtue of superposition (5.32) and (5.33). Of course, when searching for the distribution of  $\boldsymbol{\tau}^f$  within  $\Omega$ , we should satisfy the slip condition (5.6), where the meaning of time is prescribed to the monotonically increasing force  $\mathbf{P}$ . Having done so, all equations governing the problem would be satisfied.

In short, to effectively make use of equations (5.34) we have to determine two unknowns, namely the distribution of the shear forces at the interface, that is the angle  $\theta$ , and the shape of the delaminated zone  $\Omega$ .

Before we proceed, let us analyse the displacement field provided by Green's functions  $\tilde{\mathbf{u}}^x(\mathbf{x}; \mathbf{0})$ , that is resulting from a unit force acting on an infinite plate in the  $x$  direction and imposed at point  $O$ . It can be specified from equation (B.20) in Appendix for source point coordinates  $R = \Phi = 0$  in the polar parametrization of space

$$\begin{aligned}\tilde{u}_x^x(r, \varphi; \mathbf{0}) &= \frac{1 + \nu}{4\pi Eh} \left[ (3 - \nu) \ln \frac{d}{r} - (1 + \nu) \sin^2 \varphi \right], \\ \tilde{u}_y^x(r, \varphi; \mathbf{0}) &= \frac{(1 + \nu)^2}{8\pi Eh} \sin(2\varphi),\end{aligned}\tag{5.35}$$

where  $(r, \varphi)$  are polar coordinates of an observation point. In the above formulas  $d$  is an integration constant with a physical meaning of a distance from the loading force to a point on the line co-axial with the loading force vector,

where the field  $\tilde{\mathbf{u}}^x(\mathbf{x}; \mathbf{0})$  vanishes. In our case  $d$  can in general depend on the loading parameter  $l$ . A general form of function  $d(l)$  can be deduced by taking into account the homogeneity of the displacement field  $\mathbf{u}$ . Remembering that formula (5.15) states that  $P$  is a quadratic function of  $l$ , we see that in order for  $u_x^P(\mathbf{x})$  to be a homogenous function of degree two,  $d$  in (5.35) has to be a homogenous function of  $l$  of degree one. As such, it can only be a linear function of  $l$  and we can write

$$d = cl, \quad (5.36)$$

where  $c$  is as yet an undefined constant.

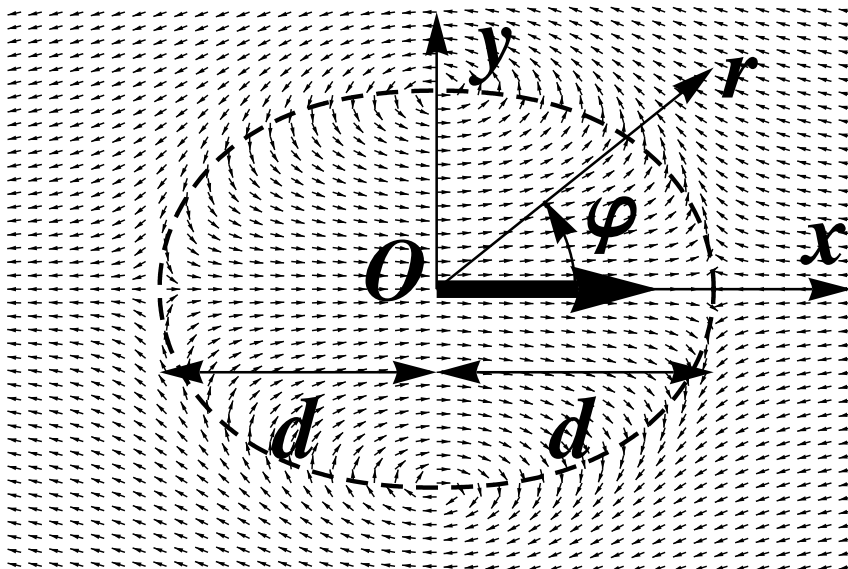


Figure 5.5. Plot of plane-stress vector field  $\tilde{\mathbf{u}}^x(\mathbf{x}; \mathbf{0})$  resulting from a concentrated unit force acting in the  $x$  direction and imposed at point  $O$ . Dashed line encloses the zone where the horizontal components of the displacement field point in the same direction as the loading force.

Vector field  $\tilde{\mathbf{u}}^x(\mathbf{x}; \mathbf{0})$  is presented in Figure 5.5. It has a feature typical for two dimensional fundamental problems — there exists a zone around the loading force where the horizontal components of the displacement vectors point in the same direction as the loading force. The extent of this zone is governed by the value of  $d$ . Outside of this zone the horizontal components of the displacement vectors point in the direction opposite to that of the loading force.

## 5.6. Moving boundary $\partial\Omega$

To derive the formula for the moving boundary  $\partial\Omega$  let us assume for the moment that we use equation (5.33) to calculate the stress field by taking an arbitrary distribution of interfacial traction within the entire space. We also assume the integration area in (5.33) to be totally arbitrary. In other words, let us calculate stresses in equation (5.33) using an arbitrary function  $\theta^*$  and an arbitrary region  $\Omega^*$ . Without loss of generality, we require only the function  $\theta^*$  and the region  $\Omega^*$  to be symmetric with respect to axis  $x$ , and  $\Omega^*$  to enclose point  $O$ , where the concentrated force is imposed. With respect to the concentrated force, we want its cartesian components to be calculated in (5.33) from formula

$$P_x^* = P^* = -\tau^f \iint_{\Omega^*} \cos \theta^* d\Omega^*, \quad P_y^* = -\tau^f \iint_{\Omega^*} \sin \theta^* d\Omega^* = 0, \quad (5.37)$$

where the equality  $P_y^* = 0$  is guaranteed by the symmetry of function  $\theta^*$  and region  $\Omega^*$  with respect to axis  $x$ . It is seen that  $\mathbf{P}^*$  equilibrates the interfacial forces acting within region  $\Omega^*$ .

We stress out that the choice of function  $\theta^*$  and integration region  $\Omega^*$  used for calculation of stresses in (5.33) and  $P_x^*$  in (5.37) is totally arbitrary, except for the minor symmetry considerations and the need of  $\Omega^*$  to include point  $O$ . In addition to that,  $\theta^*$  and  $\Omega^*$  are independent of each other. The situation is presented in Figure 5.6, where an arbitrary interfacial traction  $\boldsymbol{\tau}^{f*}$  as well as two arbitrary regions  $\Omega_{(1)}^*$  and  $\Omega_{(2)}^*$  have been sketched. They are loaded respectively by external forces  $\mathbf{P}_{(1)}^*$  and  $\mathbf{P}_{(2)}^*$ , equilibrating the interfacial traction  $\boldsymbol{\tau}^{f*}$  within the integration areas.

In the following all values corresponding to the arbitrary choice of  $\Omega^*$  and  $\theta^*$  will have superscript  $*$  (for example  $\boldsymbol{\sigma}^*$ ,  $\boldsymbol{\tau}^{f*}$ ), in contrast to fields being the solution to our original slip problem (for example  $\boldsymbol{\sigma}$ ,  $\boldsymbol{\tau}^f$ ).

Due to the arbitrary choice of  $\Omega^*$  and  $\theta^*$ , the stress  $\boldsymbol{\sigma}^*$ , obtained from equation (5.33) and resulting from the superposition of external force  $\mathbf{P}^*$  and interfacial traction  $\boldsymbol{\tau}^{f*}$  acting within  $\Omega^*$ , in general does not have to vanish on  $\partial\Omega^*$ . It would vanish, however, when  $\boldsymbol{\tau}^{f*}$  would be the same as the distribution of interfacial stresses at an arbitrary moment of frictional slip in our original delamination problem, and  $\partial\Omega^*$  would be the corresponding free boundary between detached and undamaged interface.

Since  $\mathbf{P}^*$  equilibrates the interfacial traction within  $\Omega^*$ , forces  $\mathbf{t}^* = \boldsymbol{\sigma}^* \cdot \mathbf{n}^*$  on the boundary  $\partial\Omega^*$  have no input to the global equilibrium of region  $\Omega^*$  and,

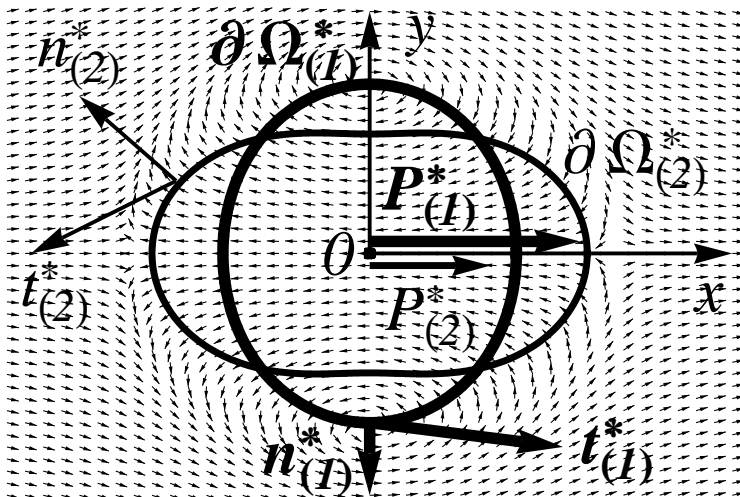


Figure 5.6. Integration within arbitrary symmetric regions  $\Omega^*_{(1)}$  and  $\Omega^*_{(2)}$  and with an arbitrary vector field  $\tau^{f^*}$ . Forces  $P^*_{(1)}$  and  $P^*_{(2)}$  are both applied at point  $O$ .

as a result, the following integral has to be zero for any choice of  $\theta^*$  and  $\Omega^*$

$$\int_{\partial\Omega^*} \sigma^* \cdot n^* d(\partial\Omega^*) = \mathbf{0}, \tag{5.38}$$

where  $n^*$  is a versor normal to  $\partial\Omega^*$ . In the polar parametrization of space we can write equality (5.38) as

$$\int_0^{2\pi} \sigma^* \cdot n^* ds^* = \mathbf{0} \tag{5.39}$$

with integration done along curve  $\rho^*(\varphi)$ .

Let us calculate a variation of equality (5.39) with respect to function  $\rho^*$ . We obtain

$$\int_0^{2\pi} \delta\sigma^* \cdot n^* ds^* + \int_0^{2\pi} \sigma^* \cdot \delta n^* ds^* + \int_0^{2\pi} \sigma^* \cdot n^* \delta(ds^*) = \mathbf{0}. \tag{5.40}$$

Let us analyse the first term in equation (5.40). Writing the multiplication in index notation, using Gauss theorem, commutativity of variation and differen-

tiation and finally equilibrium equation we obtain

$$\begin{aligned} \int_{\partial\Omega^*} \delta\sigma_{ij}^* n_j^* d(\partial\Omega^*) &= \iint_{\Omega^*} (\delta\sigma_{ij}^*)_{,j} d\Omega^* = \iint_{\Omega^*} \delta(\sigma_{ij,j}^*) d\Omega^* = \\ &= -\frac{1}{h} \iint_{\Omega^*} \delta(\tau_i^{f*} + P_i^* \delta_0) d\Omega^* = -\frac{1}{h} \left( \delta P_i^* + \iint_{\Omega^*} \delta\tau_i^{f*} d\Omega^* \right) = 0, \end{aligned} \quad (5.41)$$

$$(i, j) = 1, 2, \quad 1 \sim x, \quad 2 \sim y.$$

It should be noted that  $\delta_0$  in (5.41) is Dirac's distribution at point  $O$ , in contrast to symbol  $\delta$  indicating variation.

Let us analyse equations (5.40) and (5.41). The variations in these equations are made with respect to the boundary of integration area  $\Omega^*$ . Because of that values of  $\delta\boldsymbol{\sigma}^*$  and  $\delta P_x^* = \delta P^*$  in general do not vanish, as  $\boldsymbol{\sigma}^*$  and  $P_x^* = P^*$  depend on the choice of  $\Omega^*$ , see (5.33) and (5.37) respectively. Variations  $\delta\mathbf{n}^*$  and  $\delta(ds^*)$  also do not vanish, since both  $\mathbf{n}^*$  and  $ds^*$  depend on the geometry of  $\partial\Omega^*$ . In the case of  $\delta\boldsymbol{\tau}^{f*}$  the situation is different. As mentioned before, the function  $\theta^*$  was chosen totally arbitrary and independently from the choice of integration area  $\Omega^*$ . With variation  $\delta\boldsymbol{\tau}^{f*}$  done with respect to  $\partial\Omega^*$ , we can therefore write

$$\delta\tau_i^{f*} = 0, \quad (5.42)$$

since in the used reasoning  $\boldsymbol{\tau}^{f*}$  does not depend on the choice of  $\partial\Omega^*$ . Equation (5.40) can then be rewritten as

$$-\frac{1}{h} \delta\mathbf{P}^* + \int_0^{2\pi} \boldsymbol{\sigma}^* \cdot \delta\mathbf{n}^* ds^* + \int_0^{2\pi} \boldsymbol{\sigma}^* \cdot \mathbf{n}^* \delta(ds^*) = \mathbf{0}. \quad (5.43)$$

It is valid for any choice of  $\partial\Omega^*$  and  $\theta^*$  and we remind that the variations  $\delta\mathbf{P}^*$ ,  $\delta\mathbf{n}^*$ ,  $\delta(ds^*)$  are done with respect to the boundary of integration zone  $\partial\Omega^*$ .

Since  $\partial\Omega^*$  and  $\theta^*$  in equation (5.43) are arbitrary we can make the following choice. Let  $\theta^*$  be a distribution of interfacial traction for an arbitrary moment of frictional slip in our original delamination problem. In addition to that, let  $\partial\Omega^*$  be the free boundary between the detached and undamaged interface at the same moment. Then  $\mathbf{P}^*$ ,  $\theta^*$  and  $\partial\Omega^*$  in equation (5.43) become respectively  $\mathbf{P}$ ,  $\theta$  and  $\partial\Omega$  and describe the distribution  $\theta$  of frictional stress within damaged zone  $\Omega$  loaded by a point force of magnitude  $P$ . We recover our original problem and immediately have  $\boldsymbol{\sigma}^* = \boldsymbol{\sigma} = \mathbf{0}$  on the curve  $\rho(\varphi)$ . Remembering that  $P_1 = P_x = P$  and  $P_2 = P_y = 0$ , equality (5.43) reduces to

$$\delta P = 0, \quad (5.44)$$

which states that the variation of force  $\mathbf{P}$  made with respect to the boundary of delamination zone has to vanish.

The global equilibrium (5.37) written in the polar parametrization of space takes the form

$$P^* = -\tau^f \int_0^{2\pi} \int_0^{\rho^*(\varphi)} \cos \theta^*(r, \varphi) r \, dr \, d\varphi. \quad (5.45)$$

To make use of result (5.44) we choose  $\rho^*(\varphi)$  and  $\theta^*$  to describe the boundary  $\rho(\varphi)$  and angle  $\theta$  at an arbitrary moment in our delamination problem. We obtain

$$\delta P = -\tau^f \delta \left( \int_0^{2\pi} \int_0^{\rho(\varphi)} \cos \theta(r, \varphi) r \, dr \, d\varphi \right) = 0, \quad (5.46)$$

or equivalently

$$\delta \int_0^{2\pi} I(\rho, \varphi) \, d\varphi = 0, \quad (5.47)$$

where the function

$$I(\rho, \varphi) = \int_0^{\rho(\varphi)} \cos \theta(r, \varphi) r \, dr$$

has been introduced. Euler's equation for variation (5.47) takes now the form  $\partial I / \partial \rho = 0$ , providing us with the non-trivial solution

$$\cos \theta(\rho, \varphi) = 0. \quad (5.48)$$

Thus, on the boundary  $\partial\Omega$  between the delaminated and intact interface regions, cosine of angle  $\theta$  between vectors of interfacial forces and axis  $x$  has to be zero. It allows for identification of boundary  $\partial\Omega$ , provided the distribution of forces at the interface is known a priori.

## 5.7. Approximate solution

Being self-similar, our problem is also self-similar to the delamination resulting from an infinitesimal loading increasing from 0 to  $dP$ . Let us therefore discuss the mechanism of slip for this particular situation.

For the displacement field resulting from an infinitesimal loading increasing from 0 to  $dP$ , the velocity vectors  $\dot{\mathbf{u}}$  are co-linear with displacement vectors  $\mathbf{u}$ .

For this particular situation we can write

$$\begin{aligned}\sin \theta &= \frac{-\dot{u}_y}{\sqrt{(\dot{u}_x)^2 + (\dot{u}_y)^2}} = \frac{-u_y}{\sqrt{u_x^2 + u_y^2}} = \frac{-(u_y^{\text{P}} + u_y^{\text{f}})}{\sqrt{(u_x^{\text{P}} + u_x^{\text{f}})^2 + (u_y^{\text{P}} + u_y^{\text{f}})^2}}, \\ \cos \theta &= \frac{-\dot{u}_x}{\sqrt{(\dot{u}_x)^2 + (\dot{u}_y)^2}} = \frac{-u_x}{\sqrt{u_x^2 + u_y^2}} = \frac{-(u_x^{\text{P}} + u_x^{\text{f}})}{\sqrt{(u_x^{\text{P}} + u_x^{\text{f}})^2 + (u_y^{\text{P}} + u_y^{\text{f}})^2}},\end{aligned}\quad (5.49)$$

where the superposition (5.32) has been used.

We introduce the following approximation of  $\sin \theta$  and  $\cos \theta$ , providing us with formulas, which can be easily used in further calculations

$$\begin{aligned}\sin \theta &\approx \frac{-u_y^{\text{P}}}{\sqrt{(u_x^{\text{P}})^2 + (u_y^{\text{P}})^2}} = \frac{-\tilde{u}_y^x(\mathbf{x}; \mathbf{0})}{\sqrt{[\tilde{u}_x^x(\mathbf{x}; \mathbf{0})]^2 + [\tilde{u}_y^x(\mathbf{x}; \mathbf{0})]^2}}, \\ \cos \theta &\approx \frac{-u_x^{\text{P}}}{\sqrt{(u_x^{\text{P}})^2 + (u_y^{\text{P}})^2}} = \frac{-\tilde{u}_x^x(\mathbf{x}; \mathbf{0})}{\sqrt{[\tilde{u}_x^x(\mathbf{x}; \mathbf{0})]^2 + [\tilde{u}_y^x(\mathbf{x}; \mathbf{0})]^2}}.\end{aligned}\quad (5.50)$$

Thus, we approximate the exact distribution of interfacial forces for infinitesimal loading  $dP$  by the distribution co-linear with displacement field induced by the concentrated force alone.

Upon substituting (5.35) into equations (5.50) and using  $d = cl$ , we finally obtain

$$\begin{aligned}\sin \theta &\approx \frac{-(1 + \nu) \sin(2\varphi)}{\sqrt{4[(\nu - 3) \ln \frac{r}{cl} - (1 + \nu) \sin^2 \varphi]^2 + (1 + \nu)^2 \sin^2(2\varphi)}}, \\ \cos \theta &\approx \frac{2[(3 - \nu) \ln \frac{r}{cl} + (1 + \nu) \sin^2 \varphi]}{\sqrt{4[(\nu - 3) \ln \frac{r}{cl} - (1 + \nu) \sin^2 \varphi]^2 + (1 + \nu)^2 \sin^2(2\varphi)}}.\end{aligned}\quad (5.51)$$

Conceptually our deduction was performed for an infinitesimal loading  $dP$  increasing from the undamaged state and, as such,  $l$  in (5.51) should be treated as infinitesimal. However, by virtue of problem's self-similarity, we know that in the normalized coordinates  $(r/l, \varphi)$  angle  $\theta$  remains constant and this is true for any value of  $l > 0$ . Equations (5.51) are therefore valid for any positive  $l$  and can be used as approximate formulas for cosine and sine of angle  $\theta$ .

Formula (5.51)<sub>2</sub> for  $\cos \theta$  substituted into condition (5.48) provides us immediately with an approximate function  $\rho(\varphi)$  for the boundary  $\partial\Omega$

$$\rho(\varphi) \approx cl e^{\frac{(1+\nu)\sin^2\varphi}{\nu-3}}.\quad (5.52)$$

Now we can determine the constant  $c$  in equations (5.51) and in the boundary function (5.52). For the sake of convenience we choose  $l$  to be a distance from the point of external loading  $O$  to the boundary  $\partial\Omega$ , measured along the line coinciding with the vector of point force  $\mathbf{P}$ , as presented in Figure 5.1(b). We shall denote this particular  $l$  by  $l_0$ . Our choice of parameter  $l$  implies that function  $\rho(\varphi)$  must equal  $l_0$  for  $\varphi = 0$  resulting in  $c = 1$ . The boundary function (5.52) now takes the form

$$\rho(\varphi) \approx l_0 e^{\frac{(1+\nu)\sin^2\varphi}{\nu-3}}. \quad (5.53)$$

Plots of function  $\rho(\varphi)$  are presented in Figure 5.7 for various values of Poisson's ratio  $\nu$ , governing the shape of the delaminated zone  $\Omega$ . For  $\nu > 1/3$  the delaminated zone is concave, for  $\nu \leq 1/3$  it is convex.

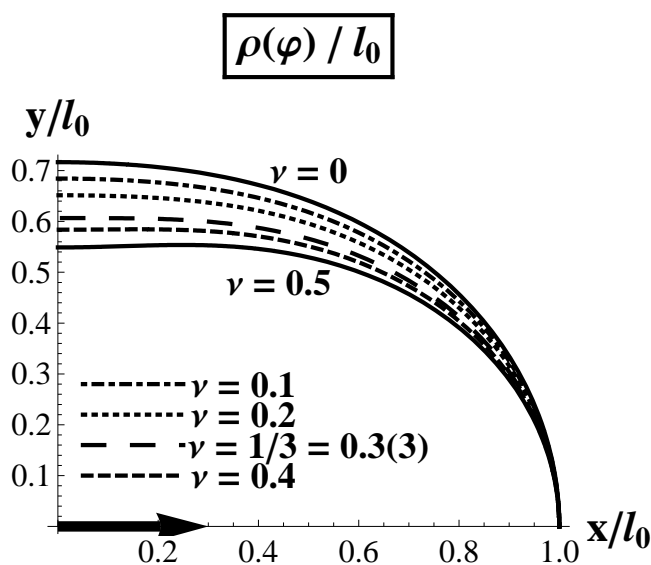


Figure 5.7. Shapes of approximate boundary  $\partial\Omega$  between the delaminated and intact interface for  $x \geq 0$  and  $y \geq 0$  for various values of  $\nu$ . Plots of function  $\rho(\varphi)$  are symmetric with respect to  $x$  and  $y$  axis. Zone  $\Omega$  is convex for  $\nu \leq 1/3$ .

In our approximation the forces at the interface are co-linear with displacement vectors resulting from a concentrated force alone. This analogy allows us to explain a physical meaning of condition  $\delta P = 0$ , or equivalently  $\cos\theta(\rho, \varphi) = 0$ , which has enabled us to obtain the moving boundary  $\partial\Omega$ , by referring to  $\tilde{\mathbf{u}}^x(\mathbf{x}; \mathbf{0})$  vector field. The field  $\tilde{\mathbf{u}}^x(\mathbf{x}; \mathbf{0})$  has this unique feature of

a zone around the loading force, where the horizontal components of the displacement vectors point in the same direction as the loading force. Outside of this zone the horizontal components of the displacement vectors point in the direction opposite to that of the concentrated force. On the boundary between these two zones we have  $\tilde{u}_x^x(\mathbf{x}; \mathbf{0}) = \cos \theta = 0$ . Thus, our approximate free boundary  $\partial\Omega$  defined by the condition  $\cos \theta = 0$  is simply the curve dividing the two regions of  $\tilde{\mathbf{u}}^x(\mathbf{x}; \mathbf{0})$  field. We also see that the internal zone maximizes value of  $P^*$  defined by

$$P^* = -\tau^f \iint_{\Omega^*} \cos \theta \, d\Omega^*$$

and variation  $\delta P^*$  has to be zero for  $\Omega^*$  coinciding with this particular region.

Let us consider consequences of the approximation we made in (5.50). By taking derivative of (5.32) we obtain  $d\mathbf{u} = d\mathbf{u}^P + d\mathbf{u}^{\tau^f}$ , and we see that when calculating  $\cos \theta$  and  $\sin \theta$  we simply use  $d\mathbf{u} \approx d\mathbf{u}^P$ . As the concentrated force induces infinite displacements at the loading point, we expect our approximation to render accurate results within a distance not too far from the force. Closer to the moving boundary, we should expect it to generate some error. It manifests itself in the fact that we do not satisfy the condition  $\boldsymbol{\sigma} = \mathbf{0}$  exactly at every point of the moving boundary (5.53). This condition remains satisfied, however, in the weak sense defined by equation (5.38), because  $\mathbf{P}$  equilibrates the interfacial traction within  $\Omega$ . Accordingly, forces  $\mathbf{t} = \boldsymbol{\sigma} \cdot \mathbf{n}$  on  $\partial\Omega$  have no input to the global equilibrium.

## 5.8. Results

Upon substituting equations (5.51) and (5.53) into formulas (5.33) and performing the integration we can calculate stresses in the plate within the delaminated area. Due to the complexity of the integrands the integration in (5.33) can be done only numerically. For  $\nu = -1$  the integrals in (5.33) simplify and one obtains an analytical solution.

### 5.8.1. Special case: $\nu = -1$

For  $\nu = -1$  we obtain

$$\sin \theta = 0, \quad \cos \theta = -1, \quad \rho(\varphi) = l_0. \quad (5.54)$$

Thus, the delaminated zone becomes a circle and the components of interfacial forces are given by  $\tau_x^f = -\tau^f$ ,  $\tau_y^f = 0$ . The relation between the value of  $P$  and

the radius of the delaminated zone  $l_0$  takes the form

$$P = -\tau^f \int_0^{2\pi} \int_0^{\rho} \cos \theta(r, \varphi) r \, dr \, d\varphi = \pi \tau^f l_0^2. \quad (5.55)$$

In the polar parametrization of space formulas (5.33) for the stresses within the delaminated zone reduce now to

$$\begin{aligned} \sigma_{xx} &= -\frac{\tau^f l_0^2 \cos \varphi}{2hr} + \frac{\tau^f}{2\pi h} \int_0^{2\pi} \int_0^{l_0} \frac{(r \cos \varphi - R \cos \Phi)R}{r^2 + R^2 - 2rR \cos(\Phi - \varphi)} \, dR \, d\Phi = \\ &= \frac{\tau^f (r^2 - l_0^2) \cos \varphi}{2hr}, \\ \sigma_{yy} &= -\sigma_{xx} = \frac{\tau^f l_0^2 \cos \varphi}{2hr} - \frac{\tau^f}{2\pi h} \int_0^{2\pi} \int_0^{l_0} \frac{(r \cos \varphi - R \cos \Phi)R}{r^2 + R^2 - 2rR \cos(\Phi - \varphi)} \, dR \, d\Phi = \\ &= \frac{\tau^f (l_0^2 - r^2) \cos \varphi}{2hr}, \\ \sigma_{xy} &= -\frac{\tau^f l_0^2 \sin \varphi}{2hr} + \frac{\tau^f}{2\pi h} \int_0^{2\pi} \int_0^{l_0} \frac{(r \sin \varphi - R \sin \Phi)R}{r^2 + R^2 - 2rR \cos(\Phi - \varphi)} \, dR \, d\Phi = \\ &= \frac{\tau^f (r^2 - l_0^2) \sin \varphi}{2hr}, \end{aligned} \quad (5.56)$$

where equation (5.55) has been used. Plots of cartesian components of the stress tensor  $\sigma$  are presented in Figure 5.8. They satisfy the boundary condition  $\sigma = \mathbf{0}$  on  $\partial\Omega$ .

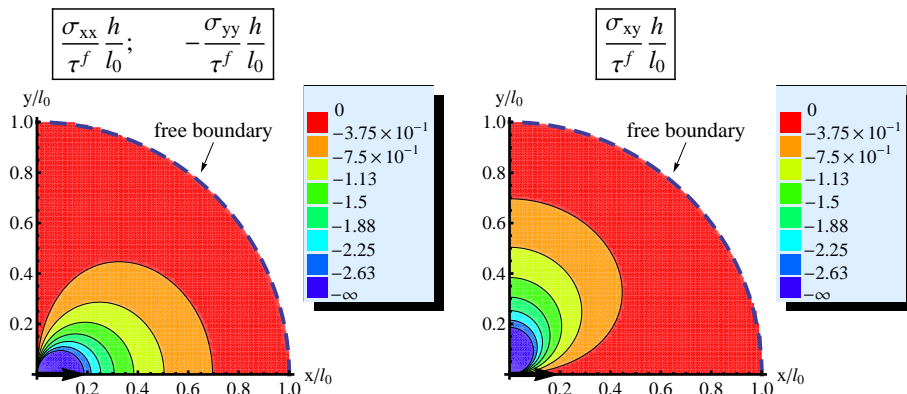
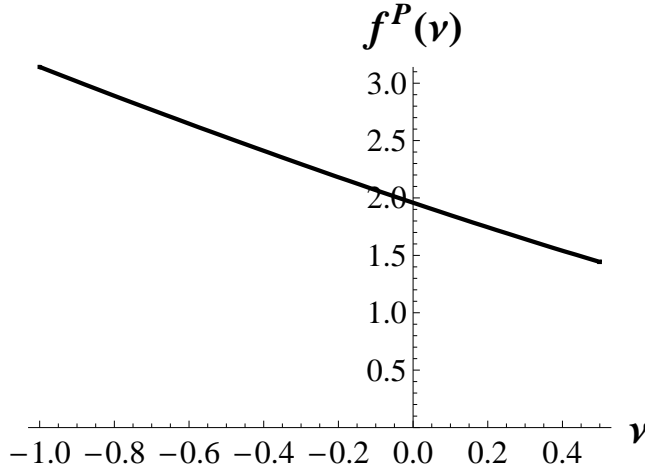


Figure 5.8. Cartesian components of the stress tensor  $\sigma$  within one quadrant of the delaminated zone  $\Omega$  ( $x \geq 0, y \geq 0$ ) obtained for  $\nu = -1$ . Arrow indicates the external point force.

Figure 5.9. Plot of function  $f^P(\nu)$ .

The formulas (5.32) for the displacement field in our special case provide  $\mathbf{u} = \mathbf{0}$ , which in turn yields vanishing strain tensor  $\boldsymbol{\varepsilon} = \mathbf{0}$ . In order to explain it, let us notice that the untypical value of Poisson's ratio  $\nu = -1$  results in infinite shear modulus of the plate  $G = \frac{E}{2(1+\nu)}$ , thus our material is perfectly rigid for every deformation which is not purely volumetric. In fact, what we obtained is a statically and kinematically admissible solution for a problem of an infinite rigid film resting with frictional contact on a rigid substrate, and loaded by an in-plane point force. The approximation (5.50) we had made for the angle  $\theta$  turned out to provide a correct solution for the special case of  $\nu = -1$ . Thus, the formulas (5.54)–(5.56) constitute an exact solution for our problem specified to a rigid film — they satisfy the boundary conditions (5.9) and can be accepted in terms of the slip rule (5.6).

### 5.8.2. Loading force $P$ versus parameter $l_0$

Equation (5.15) provides a relation between the concentrated force  $P$  and the parameter  $l$ , which in our case has been specified to  $l_0$ . Through formulas (5.51) and (5.53) we see that the distribution of forces at the interface given by angle  $\theta$  and the shape of the delaminated zone  $\rho$  do not depend on film's Young's modulus. Thus,  $f^P$  appearing in equation (5.15) is a function of Poisson's ratio  $\nu$  only. Figure 5.9 presents a plot of function  $f^P(\nu)$  obtained by integration (5.16) for our specific choice of parameter  $l = l_0$ . In accordance with result (5.55) it reaches  $\pi \approx 3.14$  for  $\nu = -1$ .

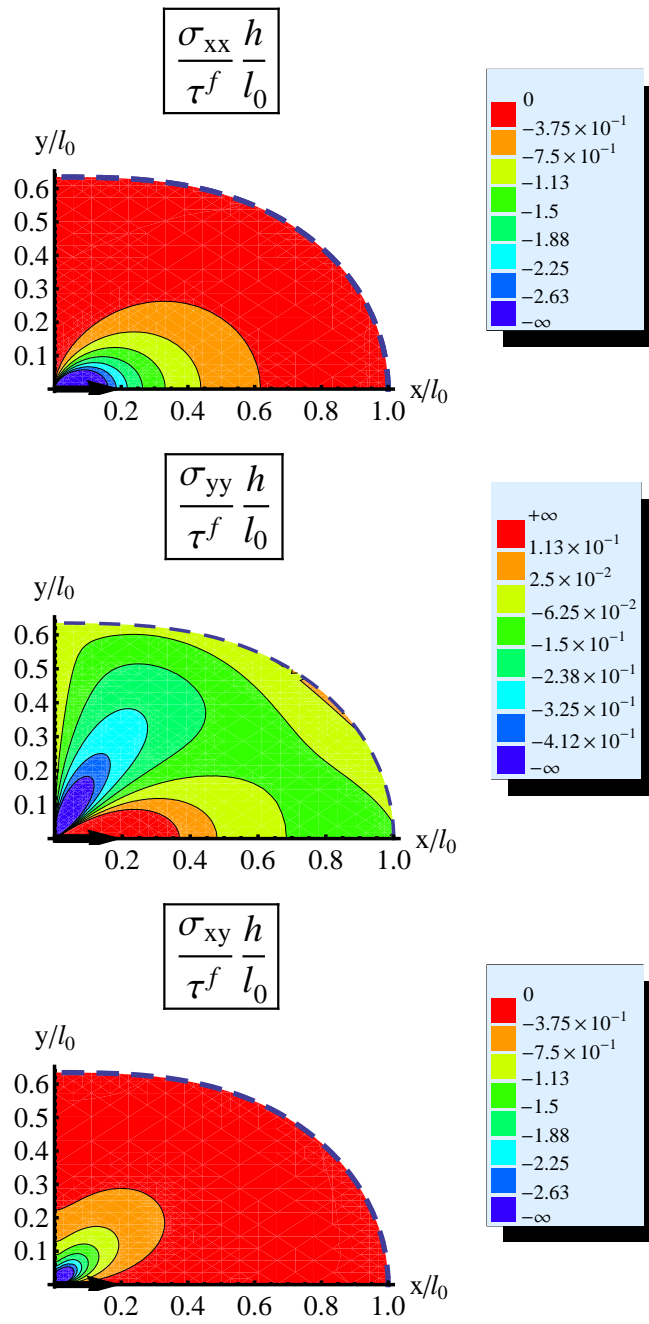


Figure 5.10. Distribution of stresses in the plate within one quadrant of the delaminated zone  $\Omega (x \geq 0, y \geq 0)$  obtained for  $\nu = 0.3$ . Dashed line indicates the free boundary.

### 5.8.3. Stress field

Figure 5.10 presents contour stress fields provided by a numerical integration of equations (5.33) for Poisson’s ratio  $\nu = 0.3$ . The components  $\sigma_{ij}^P$  in (5.33) introduce the singular behaviour of the stress field in the point  $O$ , where the concentrated force is imposed. As mentioned before, the boundary condition  $\sigma = \mathbf{0}$  is not exactly satisfied, which is clearly seen for stress component  $\sigma_{yy}$ .

### 5.8.4. Comparison with finite element results

Two dimensional geometry of finite element model is presented in Figure 5.11(a). It is a rectangular plate consisting of plane-stress elements. The frictional contact between the plate and the rigid substrate is modelled using zero thickness interfacial elements reported by Białaś and Mróz [28]. The interface element is presented in Figure 5.11(b), with nodes 5, 6, 7, 8 constrained to have zero displacements, as they belong to the rigid substrate. Nodes 1, 2, 3, 4 have tangential displacements with components  $u_\xi$  and  $u_\beta$ . They also define the corresponding plane-stress element of the plate.

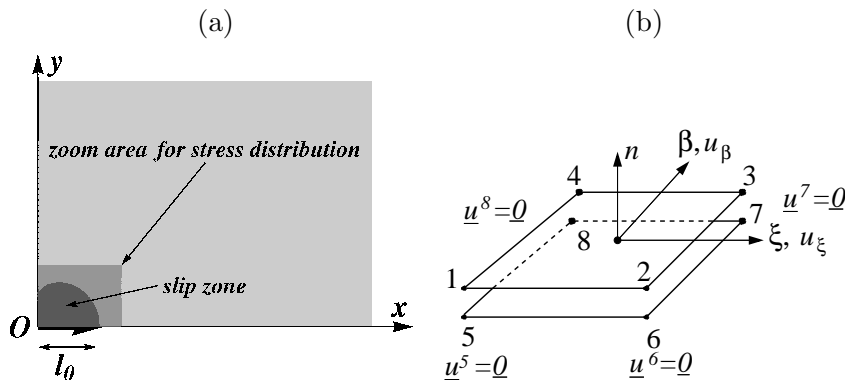


Figure 5.11. (a) Geometry of finite element model. (b) Interface element.

Fully implicit scheme has been used to integrate the interface constitutive law (5.6) with slip condition (5.5). Algorithmic tangent matrices have been calculated for all the elements and penalty stiffness method adopted to enforce the initial rigidity of the interface. Simulations have been performed using *Mathematica* [214] and finite element package *AceFEM* [116] developed by Korelc [115]. It allows for an automatic generation of finite element code by simultaneous optimization of expressions within *Mathematica* [214].

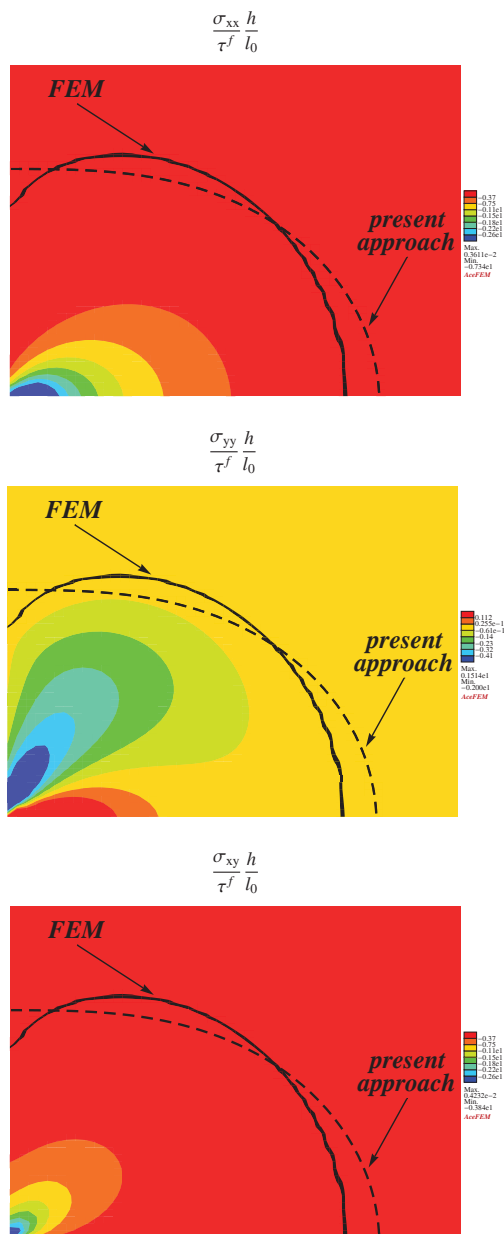


Figure 5.12. Finite element calculations. Distribution of stresses in the zoom area of Figure 5.11(a) for  $\nu = 0.3$ . The dashed curve indicates the moving boundary given by equation (5.53). The continues curve is the moving boundary resulting from FEM.

Due to problem symmetry, plate nodes on lines  $x = 0$  and  $y = 0$  have been constrained to have zero  $u_y$  displacements. The concentrated force has been applied at plate node at point  $O$  in Figure 5.11(a). The plate has been modelled with 40000 rectangular elements, that is with 200 elements in each direction. As long as the loading force is not too big to make the slip zone interact with the plate unconstrained boundaries, the finite element model corresponds adequately to the original infinite plate problem. During the simulations, the maximum value of the loading force was chosen to result in the characteristic length  $l_0$  of slip zone to be roughly one fifth of plate width along  $x$  axis, as presented in Figure 5.11(a). Any numerical difficulties associated with unstable response and plate rigid motion were thus avoided.

Figure 5.12 presents distribution of stresses within the slip zone obtained from finite element calculations for  $\nu = 0.3$ . The values have been normalized in order to be easily compared with results presented in Figure 5.10. Moreover, the moving boundaries resulting from both the analytical expression (5.53) and the FEM are indicated. It is seen that the free boundaries agree with each other qualitatively and the complicated shape of FEM boundary is only approximately captured by equation (5.53). In particular, the FE slip zone is concave, whereas the curve resulting from function (5.53) does not enclose a concave area. The  $\sigma_{yy}$  stress distribution is the most complex and it is seen that the variation of  $\sigma_{yy}$  close to the moving boundary in Figure 5.10 does not resemble the result obtained from FEM. This is due to the fact that the boundary condition  $\sigma_{yy} = 0$  on  $\partial\Omega$  is not satisfied exactly in Figure 5.10. When we move from the free boundary toward the location of the loading force, however, we see that both FEM and semi-analytical results agree reasonably good with each other and become almost identical. This can be seen particularly clear in the variation of  $\sigma_{xx}$  and  $\sigma_{xy}$  stress components, which are rather localized around the loading point. This is in agreement with the previous discussion at the end of Section 5.7., where we noted that our approximation is likely to generate some error in the vicinity of the moving boundary.

Figure 5.13 presents shapes of delaminated zone obtained using finite element method and those provided by the analytical solution (5.53) for various values of  $\nu$ . We see that for all values of Poisson's ratio ranging from 0 to 0.5 the shape of the delaminated zone obtained by finite element method is concave, in contradiction to the analytical result, where it is concave only for  $\nu > 1/3$ . The differences in  $\partial\Omega$  provided by the analytical and the numerical approaches tend to be smaller for lower values of  $\nu$ . The general trend, however, remains qualitatively preserved and, as expected, shapes of  $\partial\Omega$  coincide for  $\nu = -1$ , since we have obtained an exact solution for this case.

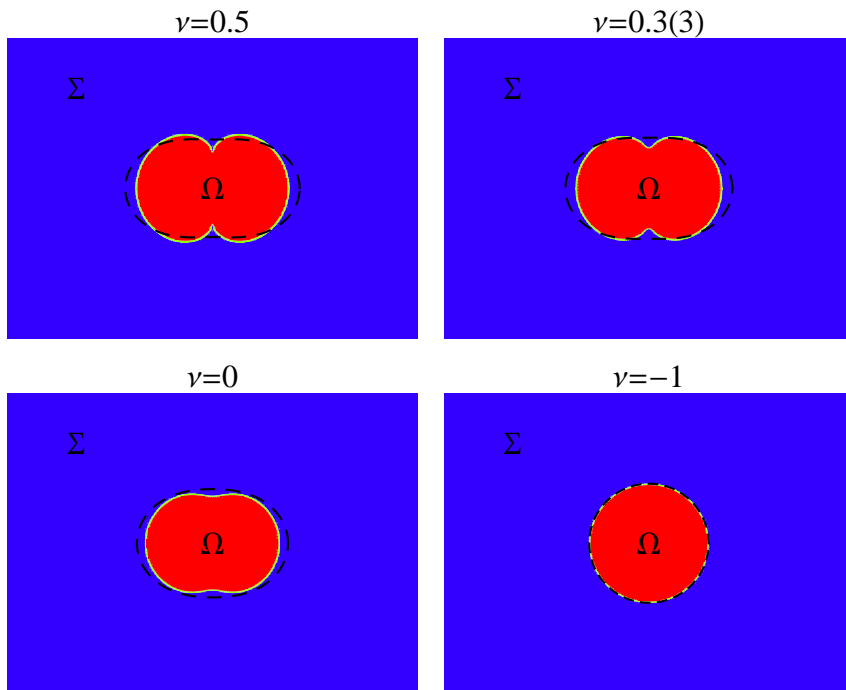


Figure 5.13. Shapes of delaminated zone obtained using finite element method (green line) and provided by the analytical solution (dashed black line).

## 5.9. Conclusions

The chapter presents an approximate solution to a self-similar problem of frictional delamination. The approximate distribution of interfacial traction enabled us to obtain a closed-form solution. The displacement Green's functions of the fundamental two dimensional problem of an infinite elastic space in plane-stress conditions loaded by a point force, provide analytical expressions for the distribution of interfacial traction and the shape of the moving boundary. In context of the approximation, it can be stated that the mechanism of delamination is governed solely by the fundamental solution due to a concentrated force — this solution determines the interfacial stresses and the moving boundary. The delamination area is the same as the region of field  $\tilde{\mathbf{u}}^x(\mathbf{x}; \mathbf{0})$ , where the horizontal components of the displacement vectors point in the same direction as the loading force. A special case for  $\nu = -1$  is a solution of rigid film delamination.

The presented approach can be used to obtain approximate, closed-form

solutions for similar delamination problems, for example when considering a film in the shape of a two dimensional wedge loaded at its vertex by an in-plane point force inducing symmetrical frictional slip, see Figure 5.14(a). The algorithm providing an approximate solution is:

1. obtain a solution for the displacement field  $\{u_x^P, u_y^P\}$  resulting from the point force alone;
2. approximate the distribution of interfacial forces by expressions (5.50);
3. condition  $\delta P = 0$  provides a function representing the moving boundary  $\partial\Omega$ ;
4. use the superposition principle to calculate the stress field.

Skipping the simple mathematics we calculate the slip zone for the problem presented in Figure 5.14(a). It has the form

$$\rho(\varphi) = l_0 e^{-\frac{1+\nu}{2} \sin^2 \varphi}, \tag{5.57}$$

where  $l_0$  is the length of the zone measured from wedge vertex along  $x$  axis. Plots of  $\rho(\varphi)$  for various values of  $\nu$  are presented in Figure 5.14(b). It is seen that the approximate slip zone for this case does not depend on the wedge opening angle  $\alpha$ .

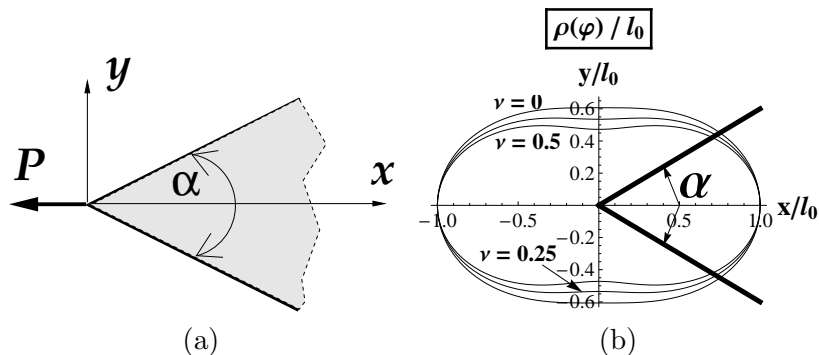


Figure 5.14. (a) Wedge-shaped film loaded at its vertex. (b) Slip zones for various values of  $\nu$ .

With the value of  $\tau^f$  remaining constant during the slip process we make a crude assumption regarding the interface constitutive law. More realistic relation between the shear stress and relative displacement would require the stress first to reach a peak shear strength  $\tau^{\text{peak}}$  and then to decrease to a residual value denoted in our case by  $\tau^f$ , where  $\tau^f < \tau^{\text{peak}}$ . Such an analysis was performed, for example, by Palmer and Rice [154], who considered growth of slip

surfaces in over-consolidated clay. In the present case, however, the assumption of plane-stress conditions is crucial and makes the results applicable to an advanced slip situation only, where the characteristic length  $2l_0$  of the damaged zone is big when compared to film thickness  $h$ . In such a case, the value of the interface shear stress is likely to be higher than  $\tau^f$  only in the vicinity of the moving boundary  $\partial\Omega$  and, with a good approximation, within most of the damaged area  $\Omega$  the ultimate shear stress  $\tau^f$  is reached. It should also be mentioned that simple interface constitutive laws, as that adopted here, are used for film segmentation cracking problems, rendering solutions which can be successfully used in practice when calculating crack densities, see for example Białaś and Mróz [30] or Timm et al. [198].



# Characterization of thin tissues via surface-wave sensing

## 6.1. Introduction

The Multi-channel Analysis of Surface Waves (MASW) technique is an effective engineering tool for the shallow subsurface delineation of geological profiles via seismic surface waves, where the surface ground motion is monitored by a linear array of motion sensors such as geophones or accelerometers, see Figure 6.1 (Park et al. [157, 158]). Empowered by the multitude of sensing locations, this technique makes it possible to deal with the plurality of Rayleigh-wave modes, an item that has traditionally been an issue with the MASW's two-receiver predecessor, known as the Spectral Analysis of Surface Waves (SASW, Heisey et al., [90], Ganji et al. [71]). Notwithstanding such critical advantage, however, the viscoelastic MASW analyses targeting the characterization of dissipative subsurface profiles are rather limited (Xia et al. [217]), in that they commonly revolve around a two-step, uncoupled interpretation procedure. In the technique, the moduli of subsurface layers are first obtained using elastic analysis from the observed dispersion data. Equipped with such approximate information about the subterranean stratigraphy, the damping characteristics of individual layers are then computed from the available dispersion and attenuation (i.e. amplitude decay) measurements. As shown by Lai and Rix [118], however, such uncoupled approach to data interpretation which neglects the effects of material dissipation on the dispersion of surface waves is applicable only to weakly dissipative media, where material damping does not exceed 5 %. This is in sharp contrast to the viscoelastic characteristics of most soft tissues (Kruse et al. [117]), which exhibit significantly higher attenuation characteristics.

Motivated by the above-described developments in engineering geophysics, this chapter aims to develop computational platform for the non-invasive vis-

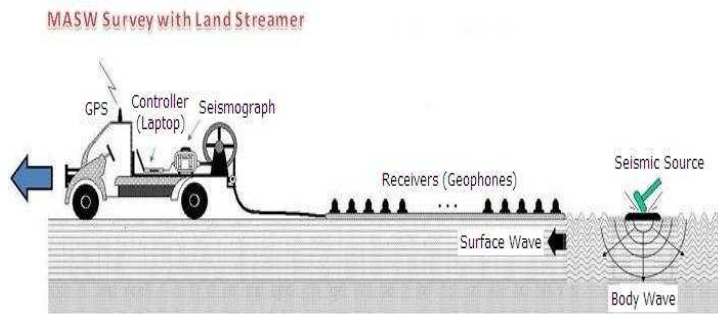


Figure 6.1. Schematic of MASW test ([www.masw.com](http://www.masw.com)).

coelastic characterization of laterally-homogeneous skin and its sublayers via a spectral analysis of Rayleigh surface waves. In such quest, the key issues to be addressed include the possibility of a low-cost, small-scale motion sensing in skin, and that of comprehensive waveform analysis that accounts for the coupling effects of tissue's elasticity and viscosity on induced surface motion. To this end, the developments entail:

- the conceptual design of a miniature, piezoelectric PolyVinylidene DiFluoride (PVDF) motion sensing array that would be attached to the skin via an adhesive tape;
- computationally-effective, coupled viscoelastic model of a PVDF-sensor-on-a-substrate system;
- affiliated full-waveform inverse analysis that relates electric charges generated by the PVDF array to the tissue's viscoelastic profile.

For completeness, the developments are accompanied by a set of numerical results that illustrate the feasibility of the proposed sensing methodology. Beyond aiming at the necessary preparatory step toward three dimensional elastic wave reconstruction of skin lesions, the proposed sensing framework may also be useful in achieving better understanding of skin aging (Vexler et al. [205]) and exposing the effectiveness of various cosmetic treatments (Wissing and Muller [213]), where tissue viscoelasticity appears to be a useful indicator parameter.

## 6.2. Conceptual sensor setup

The envisioned scale reduction of the MASW test involves the development of a "band aid"-like PVDF transducer with dimensions on the order of

1 cm  $\times$  1cm, as shown in Figure 6.2. As shown in the display, the transducer contains an array of string-shaped PVDF sensors oriented in the  $x_1$ -direction of the reference Cartesian coordinate system. A time-harmonic, localized force is applied normal to the tissue in the neighbourhood of the transducer. Under the surface motion induced by an arrival of the generated body and (Rayleigh) surface waves (Ganji et al. [71], Guzina and Lu [81], Guzina and Madyarov [82], Xia et al. [218]), each PVDF sensor i.e. string, in contact with the tissue surface, deforms and generates an electrical signal owing to its favorable piezoelectric properties. To ensure both i) non-slip contact with the surface of the skin and ii) proper alignment of the hair-like PVDF sensors, the PVDF fibers are envisioned to be attached to the top surface of a flexible backing tape whose adhesive bottom is in direct contact with the tissue. The backing tape could be either made thin and compliant and thus neglected during the analysis, or taken into considerations as the top layer with known thickness and viscoelastic properties. In the ensuing analysis we assume the first option, i.e. neglect the presence of the adhesive top layer.

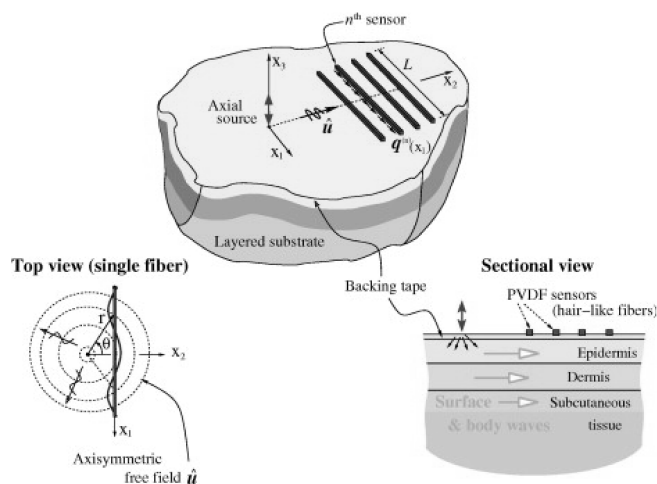


Figure 6.2. Conceptual design and operation of a PVDF transducer array, consisting of  $N$  slender PVDF fibers, for the viscoelastic characterization of skin and subcutaneous tissue (after Biała and Guzina [26]). Each piezoelectric fiber is of length  $L \sim 10$  mm and oriented in the  $x_1$ -direction; the  $n$ th fiber ( $n = 1, 2, \dots, N$ ) is centred at  $(x_2^{(n)}, 0, 0)$  and interacts with the substrate via line-load vector  $\mathbf{q}^{(n)}(x_1)$ . In the top and left panels,  $\hat{\mathbf{u}}$  is the so-called free field, signifying the motion of fiber-free substrate due to prescribed excitation.

To maximize the compliance of the sensor and, thus, its sensitivity to the soft-tissue motion, each strip, i.e. fiber, can be made to have a small rectangular

cross-section of dimensions  $h \times w$ , where  $h$  is the thickness of the fiber and  $w$  is its width,  $w = O(h)$ . Here the hair-like sensors are envisioned to be manufactured (cut) from PVDF films having standard thicknesses of 9, 28, 52 or 100  $\mu\text{m}$ , with ground electrode covering their upper side.

The calculation of charges generated by deformed piezoelectric fibers will follow strictly the approach presented by Lee [122] and Preumont [164]. When used in a sensing mode, piezoelectric fibers are connected to an operational amplifier to form either a current amplifier or a charge amplifier. An operational amplifier is an active electrical circuit working as a linear voltage amplifier with infinite input resistance and zero output resistance. The open loop gain is usually very high, which means that the allowable input voltage is very small. As a result, when the electrodes of the piezoelectric fibers are connected to an operational amplifier, they can be regarded as short-circuited and the electric field through the piezoelectric material can be neglected, see Preumont [164]. The immediate consequence of such configuration is that the mechanical and electrical phenomena are decoupled. This in particular allows for the following solution scheme: first, the mechanical problem can be solved separately by disregarding the piezoelectric effects. Having obtained the strains within the piezoelectric fibers, the electrical charges can then be calculated by integrating the electrical displacement over the area of the electrodes.

### 6.3. Point versus integral motion sensing

In MASW testing (Park et al. [157, 158], Xia et al. [217]) the surface ground motion, generated by a localized vibratory source, is commonly monitored via a coaxial array of point motion sensors such as geophones (velocity sensors) or accelerometers. As a result, the MASW measurements are amenable to notably simplified interpretation in that: (i) the motion sensors, owing to their limited mass, are considered not to affect the free-field ground vibration (i.e. the axisymmetric surface motion that would have existed in the absence of any sensors), and (ii) each motion sensor can be assumed to yield the information about ground motion at a single source-receiver distance  $r$ . In the proposed setup depicted in Figure 6.2, on the other hand, the length of each fiber i.e. sensor is expected to be on the order of the wavelength of the illuminating (surface and body) waves, at least over a portion of the frequency band examined. With reference to the left panel in Figure 6.2, this in particular implies that:

- at a given frequency of excitation  $\omega$ , each piezoelectric sensor will sense the substrate motion over a range of source-receiver distances  $r$ , and

integrate i.e. "compress" the information into a scalar voltage quantity  $V(\omega)$ ;

- each fiber will, due to its own stiffness characteristics, perturb the free-field motion of the substrate.

The ensuing forward analysis aims to account for these two complications in a rigorous and computationally-effective fashion.

## 6.4. Forward analysis

### 6.4.1. Layered tissue model

Experimental investigations on tissues and tissue-mimicking phantoms have revealed that the dynamic tissue response, when excited at frequencies on the order of 100 Hz, can be well approximated as being linear viscoelastic, see Section 1.6.2. Here it is worth noting that soft tissues are nearly (but not fully) incompressible, having the bulk modulus on the order of GPa and the shear modulus on the order of kPa (Nightingale et al. [146]). In terms of the viscosity, it was further found that the attenuation of shear waves is orders of magnitude larger than that of compressional waves (Fatemi and Greenleaf [64]). To account for such material behaviour, it is assumed in this study that the bulk modulus of the tissue is elastic and set to an a priori value of 1.5 GPa.

In the sequel the tissue is treated as a layered half-space consisting of a stack of fully bonded  $S$  layers, each with thickness  $h_s$  ( $h_S = \infty$ ), complex viscoelastic shear modulus  $\mu_s^*$ , elastic bulk modulus  $K_s = 1.5$  GPa, and mass density  $\rho_s$ ,  $s = 1, 2, \dots, S$ . To describe the viscoelastic tissue behaviour in shear, one may for example adopt Zener fractional model, i.e. the standard linear solid (Findley et al. [65]), whose applicability to a variety of manufactured and biological materials has been demonstrated in a number of studies (Ouis [152], Zhang [228], Guzina et al. [83]). More generally, however, the complex shear modulus of the  $s$ th tissue layer can be parameterized as

$$\mu_s^* = \mu_s^*(\omega; \eta_1^{(s)}, \eta_2^{(s)}, \dots, \eta_P^{(s)}), \quad s = 1, 2, \dots, S, \quad (6.1)$$

where  $\eta_j^{(s)}$ , ( $j = 1, 2, \dots, P$ ) is a set of parameters quantifying the variation of  $\mu_s^*$  with frequency. Assuming that the mass density  $\rho_s$  and bulk modulus  $K_s$  of each layer is known beforehand, the purpose of the ensuing analysis is to establish the analytical and computational framework for identifying the vector of material parameters,  $\mathbf{p} = \{\eta_1^{(1)}, \eta_2^{(1)}, \dots, \eta_P^{(1)}, \dots, \eta_1^{(S)}, \eta_2^{(S)}, \dots, \eta_P^{(S)}\}$ , that characterizes the substrate in terms of its viscoelastic shear moduli.

For completeness, it is noted that the featured hypothesis of perfect bonding between viscoelastic layers can be effectively relaxed via the introduction of "ultra thin" soft layers to account for weak interfaces such as that between epidermis and dermis. As shown by Mal [133] this approach to control the interfacial conditions is effective and free from numerical instabilities across a wide range of frequencies.

#### 6.4.2. Sensing array

To quantify the deformation of an array of  $N$  piezoelectric fibers, each of length  $L$ , bonded to the surface of a layered substrate (e.g. skin) due to external vibration caused by time-harmonic point load, a semi-analytical model is developed which considers a set of parallel Euler beams perfectly bonded to a layered viscoelastic half-space as shown in Figure 6.2. For future reference the location of the  $n$ th fiber ( $n=1, 2, \dots, N$ ), oriented parallel to the  $x_1$ -axis of the reference Cartesian system, is denoted by  $x_2^{(n)}$ . With such definition, the interface between the substrate and the  $n$ th fiber can be more precisely specified as

$$\left\{ (x_1, x_2, x_3) : -\frac{L}{2} \leq x_1 \leq \frac{L}{2}, x_2^{(n)} - \frac{w}{2} \leq x_2 \leq x_2^{(n)} + \frac{w}{2}, x_3 = 0 \right\}.$$

On setting for convenience  $x_2^{(1)} = a$ , the external force is applied normally to the substrate at the origin of the Cartesian coordinate system, i.e. at distance  $a$  from the sensing array. By virtue of the earlier hypothesis on fiber geometry whereby the length,  $L$ , of each fiber is roughly three decades larger than the characteristic dimension ( $h$ ) of its cross-section, the analysis of the interaction problem can be simplified by assuming that, for given  $n$ th fiber, all relevant quantities (displacements, tractions at the fiber/substrate interface, etc.) are functions of  $x_1$  only.

#### 6.4.3. Response of the substrate

With reference to Figure 6.2, the effect of the  $m$ th PVDF sensor on tissue deformation can be synthesized via line load  $\mathbf{q}^{(m)}(x_1)$ , distributed along the length of the sensor. By way of superposition, the substrate displacement in the  $j$ th coordinate direction ( $j = 1, 2, 3$ ) along its interface with the  $n$ th fiber can accordingly be computed via integral representation

$$u_j^{\text{sub}(n)}(x_1) = \hat{u}_j^{(n)}(x_1) + \sum_{m=1}^N \sum_{i=1}^3 \int_{-L/2}^{L/2} q_i^{(m)}(\zeta_1) \mathcal{G}_j^i(x_1, x_2^{(n)}, \zeta_1, \zeta_2^{(m)}) d\zeta_1. \quad (6.2)$$

Here  $\hat{u}_j^{(n)}(x_1)$  is the so-called free field, i.e. the response of the substrate along line segment  $(-\frac{L}{2} \leq x_1 \leq \frac{L}{2}, x_2^{(n)}, 0)$  due to external excitation in the absence of any fibers; the summation over  $m$  introduces the effect of each fiber; the summation over  $i$  takes into account the  $i$ th coordinate component,  $q_i$ , of the line load vector  $\mathbf{q}^{(m)}$ , and  $\mathcal{G}_j^i(x_1, x_2^{(n)}, \zeta_1, \zeta_2^{(m)})$  are the Green's functions for the layered viscoelastic half-space, i.e. the displacement response of the (fiber-free) semi-infinite solid at  $(x_1, x_2^{(n)}, 0)$  in the  $j$ th coordinate direction, due to unit-resultant line load acting at position  $\zeta_1$  over the width  $w$  of the  $m$ th fiber, i.e. over line segment  $\{(\zeta_1, \zeta_2, 0): \zeta_2^{(m)} - w/2 \leq \zeta_2 \leq \zeta_2^{(m)} + w/2\}$  in direction  $i$ . It is noted that (6.2) formally applies to both static and dynamic problems. In particular, for situations involving time-harmonic excitation, (6.2) is interpreted as being written in the frequency domain. In this setting functions  $u_j^{\text{sub}(n)}$ ,  $\hat{u}_j^{(n)}$ ,  $q_i^{(m)}$  and  $\mathcal{G}_j^i$  are complex-valued, with their real and imaginary parts signifying respectively the in- and out-of-phase components of the respective quantities.

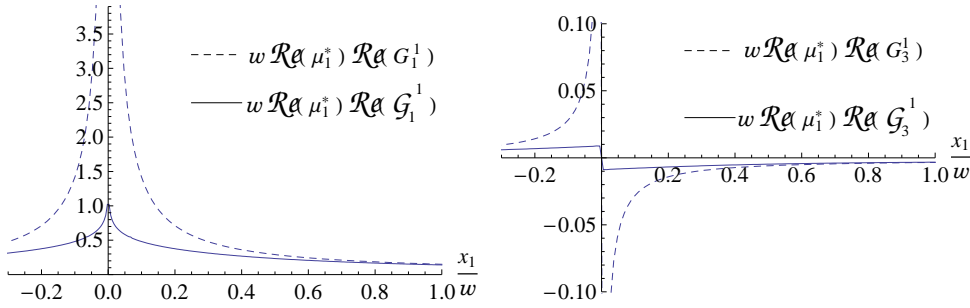


Figure 6.3. Near-source distribution of the dynamic Green's functions  $G_1^1(x_1, 0, 0, 0, 0, 0)$ ,  $G_3^1(x_1, 0, 0, 0, 0, 0)$ ,  $\mathcal{G}_1^1(x_1, x_2^{(m)}, 0, x_2^{(m)})$ , and  $\mathcal{G}_3^1(x_1, x_2^{(m)}, 0, x_2^{(m)})$  assuming  $w = 100 \mu\text{m}$ ,  $\omega = 200 \pi \text{ rad/s}$  and substrate properties as in Table 6.1.

To obtain the substrate Green's functions  $\mathcal{G}_j^i(x_1, x_2^{(n)}, \zeta_1, \zeta_2^{(m)})$  and free-field displacement  $\hat{u}_j^{(n)}(x_1)$ , the point-load solution as reported by Pak and Guzina [153] is employed. Using the method of displacement potentials, Pak and Guzina [153] obtained the displacement response  $G_j^i(x_1, x_2, x_3, \zeta_1, \zeta_2, \zeta_3)$  of a layered viscoelastic half space at  $(x_1, x_2, x_3)$  in the  $j$ th coordinate direction due to time-harmonic point force acting at  $(\zeta_1, \zeta_2, \zeta_3)$  in direction  $i$ . Accordingly, the relationship between  $\mathcal{G}_j^i$  and  $G_j^i$  can be written as

$$\mathcal{G}_j^i(x_1, x_2^{(n)}, \zeta_1, \zeta_2^{(m)}) = \frac{1}{w} \int_{\zeta_2^{(m)} - w/2}^{\zeta_2^{(m)} + w/2} G_j^i(x_1, x_2^{(n)}, 0, \zeta_1, \zeta_2, 0) d\zeta_2 \quad (6.3)$$

where  $w$  is the width of the sensor. Thus, Green's function  $\mathcal{G}_j^i$  is an average of  $G_j^i$  along sensor's width, and as such it implicitly depends on  $w$ .

As an illustration, Figure 6.3 plots the real parts of  $\mathcal{G}_j^i(x_1, x_2^{(n)}, \zeta_1, \zeta_2^{(m)})$  and its generator  $G_j^i(x_1, x_2^{(n)}, 0, \zeta_1, \zeta_2^{(m)}, 0)$  assuming  $w = 100 \mu\text{m}$ ,  $\omega = 100\pi \text{ rad/s}$  and  $x_2^{(m)} = \zeta_2^{(n)}$  in a three-layer viscoelastic half-space whose properties are given in Table 6.1. They visualize the selected displacement components along line  $(x_1, x_2^{(n)}, 0)$ , in the vicinity of a relevant time-harmonic source centred at  $(0, x_2^{(n)}, 0)$ . From the display it is clearly seen that the averaging procedure (6.3) decreases the singularity of function  $\mathcal{G}_j^i$  as we approach the location of the point force, that is  $x_1 \rightarrow \zeta_1$ . In particular, it can be shown that  $G_j^i = O(1/r)$  and  $\mathcal{G}_j^i = O(\log(r))$  as  $r$  tends to zero,  $r \rightarrow 0$ , where  $r$  denotes the relevant source-receiver distance. As a result, all integrals in equation (6.2) are proper and can be evaluated using standard numerical quadrature schemes, with appropriate number of integration points. This makes the evaluation of  $\mathcal{G}_j^i$  effective and straightforward.

Table 6.1. Mechanical properties of skin, dermis, epidermis and subcutaneous tissue — three-layer half-space model ( $K_s = 1.5 \text{ GPa}$ ,  $s = 1, 2, 3$ ).

	$h_s$ [mm]	$\rho_s$ [kg/m <sup>3</sup> ]	$\mathcal{R}e(\mu_s^*)$ [kPa]	$\mathcal{I}m(\mu_s^*)$ [kPa]
epidermis ( $s = 1$ )	0.5	1100	9.4 (Geerligts [73])	3.4 (Geerligts [73])
dermis ( $s = 2$ )	2	1100	7 (Holt et al. [92])	0.3 (Holt et al. [92])
subcutis ( $s = 3$ )	—	1100	1.1 (Patel et al. [160])	0.5 (Patel et al. [160])

#### 6.4.4. Response of the fiber

With the above result in place, the effect of the line load  $\mathbf{q}^n$  on the displacement of the  $n$ th fiber can next be quantified using the concept of fiber's Green's function. With reference to the fiber alignment depicted in Figure 6.2 and symmetry of the problem with respect to the  $x_2 - x_3$  plane, it can specifically be shown assuming time-harmonic excitation at frequency  $\omega$  that displacements of

$n$ th fiber in all directions are given by the following set of functions

$$\begin{aligned}
u_1^{\text{f}(n)}(x_1) &= \frac{1}{2\vartheta_1 EA} \int_{-L/2}^{L/2} q_1^{(n)}(\zeta_1) \mathcal{S}(x_1, a_1(\zeta_1), b_1(\zeta_1); \vartheta_1) d\zeta_1, \\
u_2^{\text{f}(n)}(x_1) &= \frac{1}{4\vartheta_3^3 E J_3} \int_{-L/2}^{L/2} q_2^{(n)}(\zeta_1) \mathcal{B}(x_1, a_2(\zeta_1), b_2(\zeta_1), c_2(\zeta_1), d_2(\zeta_1); \vartheta_3) d\zeta_1 + \\
&\quad + u_2^{\text{f}(n)}(0) \mathcal{B}(x_1, a_3, b_3, c_3, d_3; \vartheta_3), \\
u_3^{\text{f}(n)}(x_1) &= \frac{1}{4\vartheta_2^3 E J_2} \int_{-L/2}^{L/2} q_3^{(n)}(\zeta_1) \mathcal{B}(x_1, a_2(\zeta_1), b_2(\zeta_1), c_2(\zeta_1), d_2(\zeta_1); \vartheta_2) d\zeta_1 + \\
&\quad + u_3^{\text{f}(n)}(0) \mathcal{B}(x_1, a_3, b_3, c_3, d_3; \vartheta_2),
\end{aligned} \tag{6.4}$$

where  $-L/2 \leq x_1 \leq L/2$  and

$$\begin{aligned}
\mathcal{S}(x, a, b; \vartheta) &= a \sin(\vartheta x) + b \cos(\vartheta x), \\
\mathcal{B}(x, a, b, c, d; \vartheta) &= a \sin(\vartheta x) + b \cos(\vartheta x) + c \sinh(\vartheta x) + d \cosh(\vartheta x),
\end{aligned}$$

together with

$$\vartheta_1 = \omega \sqrt{\frac{\rho_f}{E}}, \quad \vartheta_2 = \sqrt{\omega} \sqrt[4]{\frac{\rho_f A}{E J_2}}, \quad \vartheta_3 = \sqrt{\omega} \sqrt[4]{\frac{\rho_f A}{E J_3}}.$$

Here  $E$  denotes the fiber's Young modulus,  $\rho_f$  is its mass density, while  $A$ ,  $J_2$  and  $J_3$  are respectively the fiber's cross-sectional area and moments of inertia with respect to  $x_2$  and  $x_3$  axes, while the expressions for  $a_i$ ,  $b_i$ ,  $i = 1, 2, 3$  and  $c_j$ ,  $d_j$ ,  $j = 2, 3$  are given in Appendix C. Physically, the displacement field  $u_1^{\text{f}(n)}$  develops due to stretching by axial load  $q_1^{(n)}$  (note that  $u_1^{\text{f}(n)}(0) = 0$  due to symmetry of the problem), whereas  $u_k^{\text{f}(n)}$ ,  $k = 2, 3$  are each represented as the sum of two contributions, namely i) the motion of a double-cantilever beam, fixed in the middle, due to bending induced by transverse load  $q_k^{(n)}$ , and ii) that generated by the oscillation of its support,  $u_k^{\text{f}(n)}(0)$ , in the absence of distributed loads. Due to small cross-sectional dimensions of the fiber, the torsional and shear effects induced by traction  $q_2^{(n)}$  and  $q_3^{(n)}$  are not taken into account. Figure 6.4 schematically presents that we consider three modes of sensor deformation: stretching due to traction  $q_1^{(n)}$  and in- and out-of plane bending due to forces  $q_2^{(n)}$  and  $q_3^{(n)}$ , respectively.

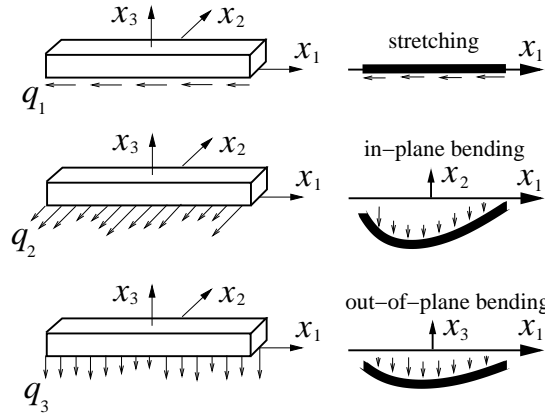


Figure 6.4. Three modes of deformation of PVDF sensors.

#### 6.4.5. Fiber-substrate interaction

When the fibers are bonded to the substrate, one clearly has

$$u_i^{\text{f}(n)}(x_1) = u_i^{\text{sub}(n)}(x_1), \quad -\frac{L}{2} \leq x_1 \leq \frac{L}{2}, \quad i = 1, 2, 3, \quad n = 1, \dots, N. \quad (6.5)$$

By virtue of (6.2) and (6.4), compatibility conditions (6.5) provide  $3N$  equations for the  $3N$  unknown functions  $q_1^{(n)}$ ,  $q_2^{(n)}$  and  $q_3^{(n)}$ ,  $n = 1, \dots, N$ . Here it is noted, however, that formulas (6.4) entail two unknown constants, namely  $u_k^{\text{f}(n)}(0)$ ,  $k=2, 3$  for each  $n$ . To close the system of equations, (6.5) are complemented by enforcing the balance of linear momentum in direction  $x_k$  for each fiber, namely

$$\int_{-L/2}^{L/2} \left\{ q_k^{(n)}(x_1) + \rho_f \omega^2 A u_k^{\text{f}(n)}(x_1) \right\} dx_1 = 0, \quad k = 2, 3, \quad n = 1, \dots, N. \quad (6.6)$$

We have  $3 \times N$  equations (6.5) together with  $2 \times N$  conditions (6.6), enabling us to obtain  $3 \times N$  unknown line loads  $q_i^{(n)}(x_1)$ ,  $i=1, 2, 3$  and  $2 \times N$  values of fiber displacements  $u_2^{\text{f}(n)}(x_1)$ ,  $u_3^{\text{f}(n)}(x_1)$ , where  $n = 1, \dots, N$ .

#### 6.4.6. Solution method

For a generic testing configuration involving layered viscoelastic substrate and multiple sensing fibers, (6.5) and (6.6) can be conveniently solved via the collocation method, equipped by (6.2), (6.4) and numerically-computed Green's functions for the substrate,  $G_j^i$ , following (6.3). We divide each sensor into  $J-1$

elements with nodes at  $x_1^{(0)} = -L/2, x_1^{(1)}, \dots, x_1^{(J)} = L/2$  and approximate the field  $\mathbf{q}^{(n)}$  for  $j$ th element by a linear function

$$\mathbf{q}^{(n)}(x_1) = \mathbf{q}^{(n)}(x_1^{(j)})f_1(x_1) + \mathbf{q}^{(n)}(x_1^{(j+1)})f_2(x_1), \quad (6.7)$$

where

$$f_1(x_1) = \frac{x_1^{(j+1)} - x_1}{x_1^{(j+1)} - x_1^{(j)}},$$

$$f_2(x_1) = \frac{x_1 - x_1^{(j)}}{x_1^{(j+1)} - x_1^{(j)}}$$

and  $\mathbf{q}^{(n)}(x_1^{(j)}) = \{q_1^{(n)}(x_1^{(j)}), q_2^{(n)}(x_1^{(j)}), q_3^{(n)}(x_1^{(j)})\}^T$  is a vector of values of  $\mathbf{q}^{(n)}$  at node  $x_1^{(j)}$ , where  $n$  indicates sensor's number. The situation is presented in Figure 6.5. Upon substituting approximation (6.7) into (6.5) and (6.6) the set of integral equations transforms to a set of linear algebraic equations

$$\mathbf{A}\mathbf{q} = \mathbf{R} \quad (6.8)$$

with unknown vector  $\mathbf{q}$  representing values of  $q_1^{(n)}, q_2^{(n)}, q_3^{(n)}$  calculated at each node.

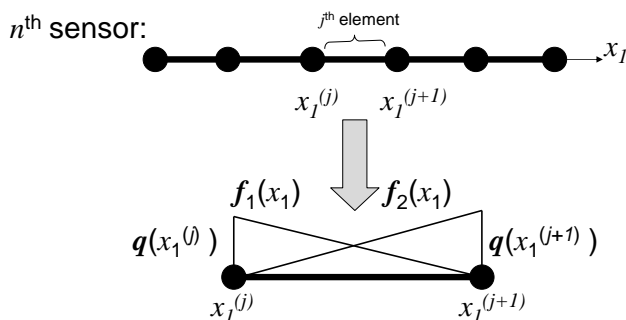


Figure 6.5. Division of sensor into elements.

Solution of (6.8) and approximation (6.7) enable us to obtain the interaction line loads  $q_i^{(n)}(x_1)$ ,  $i = 1, 2, 3$ , which, in turn, are used in equations (6.4), providing the deformation of each fiber.

### 6.4.7. Computation of output voltages

On taking into account the electro-mechanical decoupling discussed in Section 6.2., the charge generated by each PVDF fiber can next be calculated by integrating electric displacement over an electrode area. Assuming that the top and bottom electrode cover respectively the entire top and bottom surfaces of the sensor (as would be the case if the fiber is cut from a PVDF sheet), the charge equation for the  $n$ th fiber can be written, following Lee [122], as

$$\begin{aligned} Q^{(n)} &= w \int_{-L/2}^{L/2} D_3 dx_1 = d_{31} E w \int_{-L/2}^{L/2} \left( \frac{du_1^{f(n)}}{dx_1} - \frac{h}{2} \frac{d^2 u_3^{f(n)}}{dx_1^2} \right) dx_1 \\ &= 2 w d_{31} E u_1^{f(n)} \left( \frac{L}{2} \right) - h w d_{31} E \frac{du_3^{f(n)}}{dx_1} \left( \frac{L}{2} \right), \end{aligned} \quad (6.9)$$

where  $Q^{(n)}$  is the charge generated by the fiber,  $D_3$  is the electric displacement (charge density) in the  $x_3$ -direction, and  $d_{31}$  is a constant quantifying the so-called direct piezoelectric effect of axial strain in the sensor on  $D_3$ . Consistent with the discussion in Lee [122], formula (6.9) reflects the fact that a slender PVDF fiber can sense only stretching and bending modes of deformation, noting in particular that (i) the shear stress in the fiber is, following Euler hypothesis, negligible, and (ii) the lateral bending strain  $d^2 u_2^{f(n)}/dx_1^2$  generates zero net electric displacement due to material homogeneity of the fiber in the  $x_2$ -direction. Within this framework the term in parentheses under the integral sign signifies the net axial strain at the top surface of the  $n$ th fiber, that is solely responsible for generating the electric displacement  $D_3$ . Once (6.9) is computed, the voltage generated by the  $n$ th sensor can be calculated as

$$V^{(n)} = \frac{Q^{(n)}}{C_f}, \quad C_f = \frac{Lw}{h} v_f, \quad (6.10)$$

where  $C_f$  denotes fiber's capacitance, and  $v_f$  is the static absolute permittivity of a PVDF material (Fraden [67]). For completeness, typical values of the material parameters for a PVDF sheet, relevant to the foregoing analysis, are given in Table 6.2.

Table 6.2. Material parameters for PVDF sensors (after Fraden [67] and Ueberschlag [203]).

$E$ [GPa]	$\rho_f$ [ $\frac{\text{kg}}{\text{m}^3}$ ]	$d_{31}$ [ $\frac{\text{pC}}{\text{N}}$ ]	$v_f$ [ $\frac{\text{nF}}{\text{m}}$ ]
1.1	1780	23	0.11

### 6.4.8. Comparison with finite element simulations

To verify the implementation of the semi-analytical model proposed in Section 6.4., finite element (ABAQUS [53]) calculations are performed assuming two fibers ( $N = 2$ ) on a homogeneous, elastic half-space that is statically loaded by a point force  $F = -F_{x_3} = 1$  mN, at the origin of the reference coordinate system (see also Figure 6.2). The fibers are represented by beam elements and, due to problem symmetry with respect to the  $x_2 - x_3$  plane, only one half of the structure is modelled. Note that the comparison is performed at zero frequency to avoid issues associated with non-reflecting (i.e. wave-absorbing) boundaries in the FE solution, and thus to facilitate unbiased examination of the semi-analytical interaction model. As an illustration, a detail of the FE mesh featuring refined discretization in the vicinity of fiber/substrate interfaces is shown in Figure 6.6. Both simulations assume  $w = h = 100 \mu\text{m}$ ,  $x_2^{(1)} = 10$  mm,  $x_2^{(2)} = 11$  mm,  $L = 10$  mm,  $E = 1$  GPa (Young's modulus of the fiber),  $\mu_1^* = 3$  kPa and  $K_1 = 74$  kPa (shear modulus and bulk modulus of an elastic substrate with Poisson's ratio  $\nu = 0.48$ ). Figure 6.7 shows a comparison between the FE result and its companion obtained by solving (6.5) and (6.6) with 100 collocation points equally distributed along the length of each fiber. As can be seen from the display, there is a reasonable agreement between the two solutions, with the maximum discrepancy not exceeding 4 %. In general, this deviation can be attributed to (i) simplifying hypothesis of the semi-analytical model which synthesizes the action of a thin fiber as that of a line load, and (ii) spatial discretization error inherent to the FE solution. In this regard, it is noted that the FE displacements underestimate their semi-analytical counterparts which points to the latter cause of discrepancy, and that the three dimensional finite element simulation is performed with the maximum number of elements permitted by the computer. Noting further that the semi-analytical simulations with 100 and 1000 collocation nodes along the length of each fiber yielded no observable differences in the accuracy of displacement estimates, it is finally mentioned that the FE compute time required to produce results in Figure 6.7 exceeds that of the 100-node semi-analytical model by an excess of a decade.

### 6.4.9. Dominant modes of sensors' deformation

To check the modes of sensors' deformation, we solve equations (6.5) numerically for a static case and for one fiber. Similarly as in the previous section, a homogenous elastic half-space is assumed. Simulations are performed for three sets

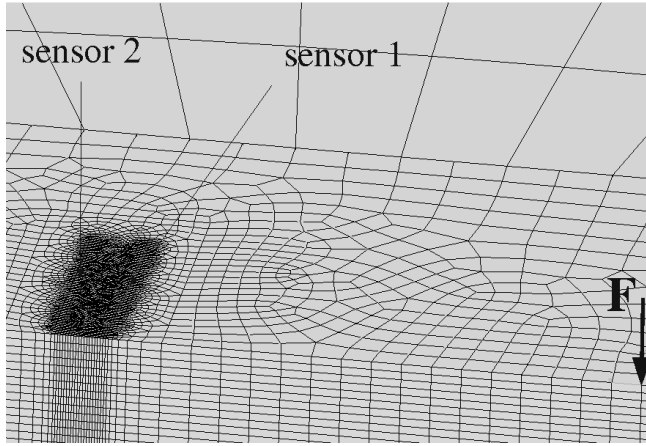


Figure 6.6. Detail of finite element mesh with two fiber sensors.

of sensor's rectangular cross-sections with dimensions  $w = h = 10, 50, 100 \mu\text{m}$ . Young's modulus of the fiber is 1 GPa, its length  $L = 10 \text{ mm}$  and distance from the fiber to the loading force equals also 10 mm. Substrate Poisson's ratio is assumed to be  $\nu = 0.48$ , whereas shear modulus takes following values  $\mu_1^* = 1, 7, 14 \text{ kPa}$ . Dominant modes of fiber's deformation can be captured by considering ratios  $\varepsilon_{\text{out-of-plane-bending}}^{\text{max}}/\varepsilon_{\text{stretching}}$  and  $\varepsilon_{\text{in-plane-bending}}^{\text{max}}/\varepsilon_{\text{stretching}}$ , where the strains are defined as

$$\begin{aligned}\varepsilon_{\text{stretching}}(x_1) &= \frac{du_1^{f(1)}(x_1)}{dx_1}, \\ \varepsilon_{\text{in-plane-bending}}^{\text{max}}(x_1) &= \frac{w}{2} \frac{d^2u_2^{f(1)}(x_1)}{dx_1^2}, \\ \varepsilon_{\text{out-of-plane-bending}}^{\text{max}}(x_1) &= \frac{h}{2} \frac{d^2u_3^{f(1)}(x_1)}{dx_1^2}.\end{aligned}$$

Thus,  $\varepsilon_{\text{stretching}}$  is the strain of fiber due to axial loading  $q_1^{(1)}$ . Remaining strains  $\varepsilon_{\text{in-plane-bending}}^{\text{max}}$  and  $\varepsilon_{\text{out-of-plane-bending}}^{\text{max}}$  are the maximal strains at a cross-section due to in- and out-of-plane bending, respectively.

Results are presented in Figure 6.8 for  $0 \leq x_1 \leq L/2$  due to the symmetry of the problem. The following conclusions can be stated:

- for thick fibers ( $100 \mu\text{m}$ ) the deformation is dominant by out-of-plane bending;

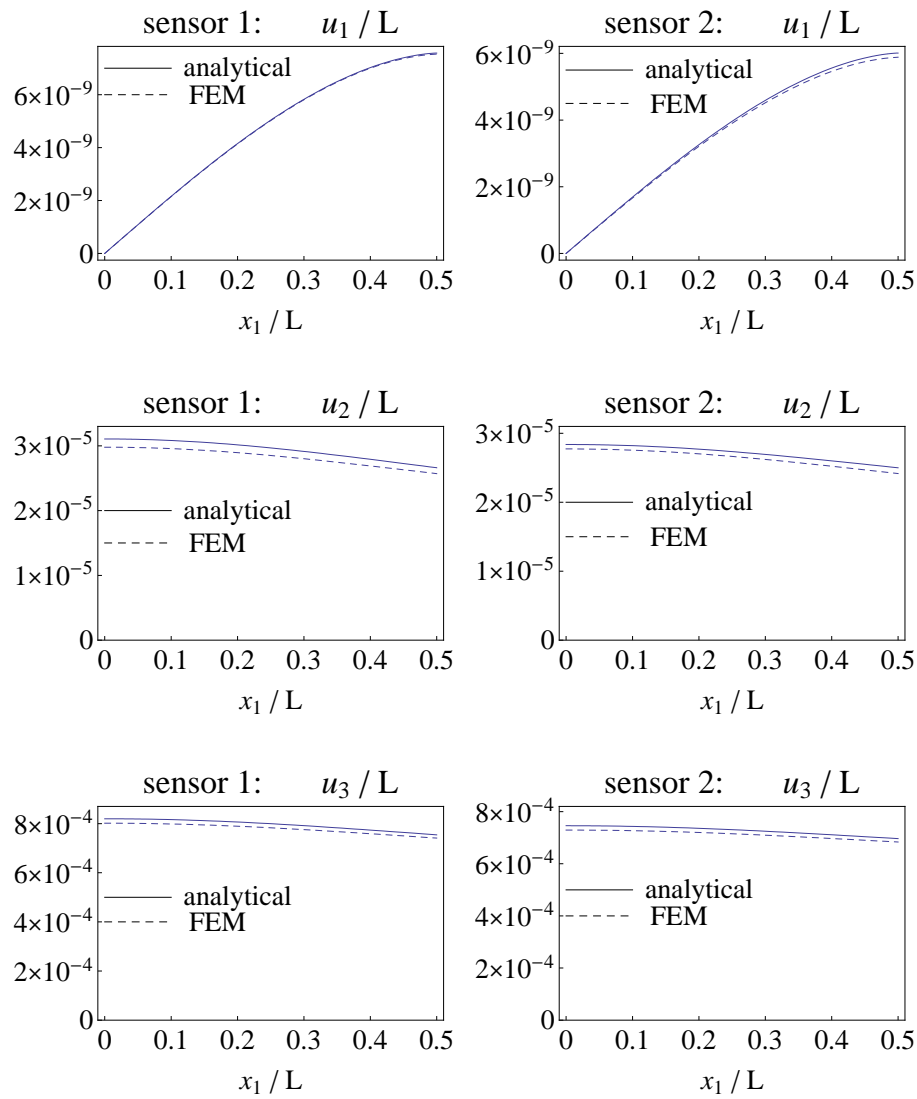


Figure 6.7. Displacements along the fiber/substrate interface: finite element simulation versus semi-analytical result assuming static loading and homogenous substrate ( $\mu = 3$  kPa,  $\nu = 0.48$ ,  $F = 1$  mN)

- for thin fibers (10  $\mu\text{m}$ ) stretching is the predominant mode of deformation;
- for fibers of intermediate thickness (50  $\mu\text{m}$ ) both in- and out-of-plane bending as well as stretching produce comparable strains.

The stated results can at first be surprising for thin fibers having cross-sectional dimensions 10  $\mu\text{m} \times 10 \mu\text{m}$ . We expect very slim sensors to bend more easily than to stretch. This can be easily explained by considering maximal strain resulting from bending moment  $\varepsilon_{\text{bending}}^{\text{max}} = Mh/(2JE)$  and from axial force  $\varepsilon_{\text{stretching}} = P/(EA)$ . For rectangular cross-section with  $h = w$  we obtain

$$\frac{\varepsilon_{\text{bending}}^{\text{max}}}{\varepsilon_{\text{stretching}}} = \frac{6}{h} \frac{M}{P} \quad (6.11)$$

and see that this ratio goes to infinity when  $h$  approaches zero. Thus, thin fibers are expected to bend more easily than to stretch. This reasoning is done with the silent assumption that the bending moment  $M$  and axial force  $P$  are independent of each other and independent from fiber's thickness. In our case, however, the loading is exerted on the sensor by the substrate, which in turn is subjected to a concentrated force. In other words, we do not impose the axial force independently from the bending moment. It is therefore better to write for  $n$ th fiber

$$\frac{\varepsilon_{\text{bending}}^{\text{max}}}{\varepsilon_{\text{stretching}}} = \frac{h}{2} \frac{u_i^{\text{f}(n)''}(x_1)}{u_1^{\text{f}(n)'}(x_1)}, \quad (6.12)$$

where for  $i = 2, 3$  we have either the in-plane displacement  $u_2^{\text{f}(n)}(x_1)$  or out-of-plane displacement  $u_3^{\text{f}(n)}(x_1)$ . When fibers get thinner, their constraining effect becomes smaller and deformation tends to be the same as of the substrate along line segment  $(-\frac{L}{2} \leq x_1 \leq \frac{L}{2}, x_2^{(n)}, 0)$  due to the external excitation in the absence of the fibers. Thus,  $u_1^{\text{f}(n)}(x_1)$ ,  $u_2^{\text{f}(n)}(x_1)$  and  $u_3^{\text{f}(n)}(x_1)$  tend to free fields  $\hat{u}_1^{(n)}$ ,  $\hat{u}_2^{(n)}$ ,  $\hat{u}_3^{(n)}$ , see equation (6.2). For very small fibers we are therefore justified to write the approximation

$$\frac{\varepsilon_{\text{bending}}^{\text{max}}}{\varepsilon_{\text{stretching}}} = \frac{h}{2} \frac{\hat{u}_i^{(n)''}(x_1)}{\hat{u}_1^{(n)'}(x_1)}, \quad i = 2, 3. \quad (6.13)$$

We see that free fields  $\hat{u}_j^{(n)}$ ,  $j = 1, 2, 3$  are independent of  $h$  and as  $h$  goes in the limit to zero, so does the ratio  $\varepsilon_{\text{bending}}^{\text{max}}/\varepsilon_{\text{stretching}}$ . This simple reasoning justifies the statement that for very thin fibers, stretching is the predominant mode of

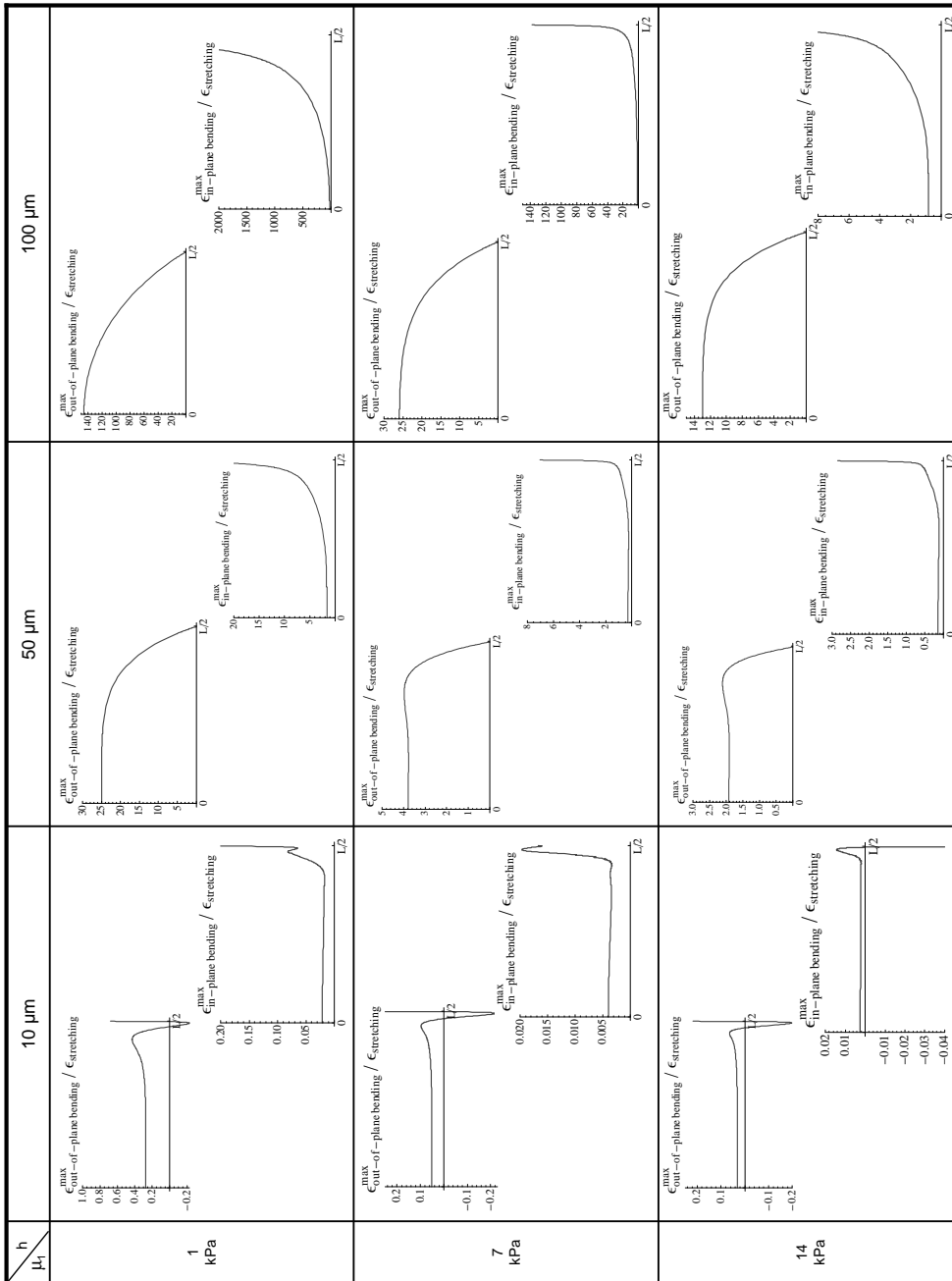


Figure 6.8. Dominant modes of sensor's deformation.

deformation, as presented in Figure 6.8. It simply follows the deformation of the outer surface of the considered half space.

## 6.5. Back-analysis

### 6.5.1. Observations

Assuming that the layered substrate is probed, using time-harmonic source, in a frequency-sweep setting, the experimental (i.e. observed) data set stemming from the PVDF sensor array takes the format

$$V_{\text{obs}}^{(n)}(\omega_k), \quad n = 1, \dots, N, \quad k = 1, \dots, K. \quad (6.14)$$

Here  $n$  denotes the fiber number (position) in the array. The frequency sweep is performed over a discrete set of frequencies  $\omega_k$ , and  $V_{\text{obs}}^{(n)}(\omega_k)$  is the complex-valued voltage quantity synthesizing in- and out-of-phase components of the voltage generated by the  $n$ th sensor under time-harmonic excitation at frequency  $\omega_k$ . In situations when transient excitation is employed to generate the Rayleigh and body waves in the substrate,  $V_{\text{obs}}^{(n)}(\omega_k)$  can be alternatively interpreted as the Fourier transform of its temporal companion,  $\tilde{V}_{\text{obs}}^{(n)}(\omega_k)$ .

In an attempt to mimic the typical Spectral Analysis of Surface Waves (Heisey et al. [90], Ganji et al. [71]) and its MASW successor (Park et al. [157, 158]) one may next be enticed to convert (6.14) into a set of frequency response functions

$$\frac{V^{(m)}(\omega_k)}{V^{(n)}(\omega_k)}, \quad m > n, \quad m, n = 1, \dots, N, \quad k = 1, \dots, K \quad (6.15)$$

and to use (6.15) as experimental input, for the phase of such complex-valued quantities carries information about the phase velocity (and thus dispersion) of surface waves. As a more direct approach to the viscoelastic reconstruction of layered substrate, however, one may retain (6.14) as "raw" experimental input. In such case the computation of (6.10), which simulate  $V_{\text{obs}}^{(n)}$ , necessitates knowledge of the axial force  $F$  used to excite the tissue. This can be accomplished either via a force-sensing vibratory source (a hypothesis used hereon for simplicity), or by including  $F$  into the list of unknown parameters. As shown by Guzina et al. [83], the latter strategy provides an effective means for estimating the source strength in situations where force sensing may not be available.

### 6.5.2. Minimization

With reference to the experimental data set (6.14) representing a collection of voltages generated by the array of  $N$  piezoelectric (PVDF) fibers over  $K$  sampling frequencies, one may introduce the cost functional

$$\mathcal{J} = \sum_{k=1}^K \sum_{n=1}^N \overline{[V^{(n)}(\omega_k) - V_{\text{obs}}^{(n)}(\omega_k)]} [V^{(n)}(\omega_k) - V_{\text{obs}}^{(n)}(\omega_k)], \quad (6.16)$$

where over-bar symbol indicates complex conjugate,  $V_{\text{obs}}^{(n)}(\omega_k)$  denote the experimental measurements, and  $V^{(n)}(\omega_k)$  are their predictions i.e. simulations for a trial layered profile. With reference to (6.1), the idea is to postulate the a priori knowledge of the layers' mass densities  $\rho_s$  and elastic bulk moduli  $K_s$ , ( $s = 1, 2, \dots, S$ ) and to minimize  $\mathcal{J}$  with respect to the vector of viscoelastic parameters

$$\mathbf{p} = \{\eta_1^{(1)}, \eta_2^{(1)}, \dots, \eta_P^{(1)}, \dots, \eta_1^{(S)}, \eta_2^{(S)}, \dots, \eta_P^{(S)}\} \quad (6.17)$$

characterizing the substrate in terms of its shear moduli. Here it is noted that (6.17) implicitly assumes that the layer thicknesses,  $h_s$ , ( $s = 1, 2, \dots, S - 1$ ) are known beforehand, as exposed, for instance, via high-frequency ultrasound (Liu and Ebbini [126]). In situations where such hypothesis does not apply, the problem can be resolved by either (i) including  $h_s$  into the list of unknown parameters  $\mathbf{p}$ , or (ii) taking  $h_s = H/M$  where  $x_3 \in [-H, 0]$  is the depth range of interest, and  $M$  is an integer such that  $h_s$  meets the sought spatial resolution of vertical substrate reconstruction.

To maintain the physical significance of a solution, however, the arguments of  $\mathcal{J}$ , i.e. the components of  $\mathbf{p}$  must be subject to suitable inequality constraints. In the context of isotropic linear viscoelasticity, complex shear modulus (6.1) is typically parameterized such that the thermomechanical stability of a system is maintained when  $\eta_p^s \geq 0$ ,  $p = 1, 2, \dots, P$  (Findley [65]). To facilitate the enforcement of such constraints, one may conveniently supersede  $\mathbf{p}$  by

$$\mathbf{p}^* = \log\{\eta_1^{(1)}, \eta_2^{(1)}, \dots, \eta_P^{(1)}, \dots, \eta_1^{(S)}, \eta_2^{(S)}, \dots, \eta_P^{(S)}\} \quad (6.18)$$

and pose the incipient minimization problem as

$$\min_{\mathbf{p}^*} \mathcal{J}(\mathbf{p}^*). \quad (6.19)$$

In what follows, the function  $\mathcal{J}(\mathbf{p}^*)$  is minimized via gradient-based BFGS quasi-Newton method and an inexact line search algorithm based on the strong

Wolfe condition [147]. The computation of material sensitivities  $\partial\mathcal{J}/\partial\mathbf{p}^*$  is accomplished numerically via the use of finite differences.

Within the framework of the MASW testing, it is noted that the above spectral analysis of surface and body waves is general in the sense that: (i) it requires no a priori assumption about the modal participation of Rayleigh surface waves propagating through the substrate, and (ii) it includes both near- and far-field effects, and thus imposes no restrictions on the source-receiver spacing. The latter feature of the proposed back-analysis is particularly important in the context of meaningful shear-wave attenuation characterizing soft tissues.

## 6.6. Numerical results

For simplicity, the viscoelastic substrate characterization via an array of PVDF fibers is considered for a canonical synthetic configuration where: (i) the fibers are in direct contact with the substrate; (ii) the substrate, i.e. skin, is represented by a three-layer half-space model ( $S = 3$ ) which neglects the presence of very thin layers (namely that of stratum corneum and a soft "interphase" layer between the epidermis and dermis), and (iii) the complex shear modulus (6.1) of each layer is, over a given frequency range, rate-independent so that

$$\mu_s^*(\omega; \eta_1^{(s)}, \eta_2^{(s)}, \dots, \eta_P^{(s)}) = \eta_1^{(s)} + i\eta_2^{(s)} = \text{const}, \quad i = \sqrt{-1}, \quad s = 1, 2, 3. \quad (6.20)$$

Under such hypotheses, the vector of unknown material parameters (6.17) specializes to

$$\mathbf{p} = \{ \eta_1^{(1)}, \eta_2^{(1)}, \eta_1^{(2)}, \eta_2^{(2)}, \eta_1^{(3)}, \eta_2^{(3)} \},$$

where the sought "true" values of  $\eta_p^{(s)}$ , namely  $\eta_p^{(s)\text{true}}$  ( $p = 1, 2, s = 1, 2, 3$ ) are taken following Table 6.1. Consistent with earlier discussion,  $\mathbf{p}^{\text{true}}$  is sought via the minimization of (6.16) with respect to  $\mathbf{p}^* = \log\mathbf{p}$  which assumes prior knowledge of  $\rho_s^{\text{true}} = 1100 \text{ kg/m}^3$  and  $K_s^{\text{true}} = 1.5 \text{ GPa}$ ,  $s = 1, 2, 3$  (see Table 6.1).

The set of excitation frequencies employed to probe the tissue is taken as

$$\omega_k [\text{rad/s}] = 200\pi k, \quad k = 1, 2, \dots, K$$

covering the range of linear frequencies  $f = \omega/(2\pi) \in [100, 100K] \text{ Hz}$ , and shear wavelengths in the uppermost layer  $f^{-1} \sqrt{\frac{\text{Re}(\mu_1^*)}{\rho_1}} \in [3K^{-1}, 3]a$ , hereby the minimum illuminating wavelength equals roughly  $9K^{-1}$  inter-fiber distances.

### 6.6.1. Effect of number of sensors

The convergence of the optimization procedure is illustrated in Figure 6.9 in terms of increasing number of sensors from  $N = 3$  to  $N = 5$ . The array is probed at one frequency only (100 Hz). The distance between sensors is assumed to be 2 mm, the distance between the excitation force and the nearest sensor is 10 mm. Each sensor has a square cross-section  $w \times h = 100 \mu\text{m} \times 100 \mu\text{m}$  and length  $L = 10$  mm. It can be seen that adding sensors in the array does not improve the convergence and obtained complex moduli of all layers are much different from the true ones (with the error up to 55 % in case of  $\mathcal{R}e(\mu_1^*)$  and three sensors). Thus, inverse analysis performed at one frequency only gives a local minimum, which can be much different from the global one. Increasing the number of sensors in the array does not improve the reconstructed result.

### 6.6.2. Effect of frequency sweep

With reference to Figure 6.2, the ensuing examples assume two testing configurations consisting of two and four fibers ( $N = 2$  or  $N = 4$ ), each having length  $L = 10$  mm and the square cross-section  $100 \mu\text{m} \times 100 \mu\text{m}$ , arranged such that the distance from the loading point to the nearest fiber is 10 mm and the spacing between fibers is 2 mm for  $N = 2$  or 3.3 mm for  $N=4$ .

The convergence of the optimization procedure is examined in Figure 6.10 and Figure 6.11 respectively for two and four fibers and for three progressively richer in frequency data sets, namely those assuming  $K = 3$ ,  $K = 4$  and  $K = 5$ . As can be seen from the display, the sweeps with  $K = 3$  and  $K = 4$  are only partially successful in resolving the synthetic skin profile, encountering particular difficulties in resolving its attenuation characteristics synthesized via  $\mathcal{I}m(\mu_s^*)$ ,  $s = 1, 2, 3$ . In contrast, the example with five testing frequencies (100, 200, 300, 400 and 500 Hz) demonstrates that the proposed back-analysis is capable of resolving both real and imaginary parts of all three sublayers with satisfactory accuracy (the maximum relative error between the reconstructed and "true" modulus is less than 1 %). Here it is noted that the shear wavelength in the uppermost layer at 500 Hz is roughly 5 mm — a length scale that may be compared to the inter-fiber distances of 2 and 3.3 mm in both cases, the thickness of epidermis  $h_1 = 0.5$  mm, and the thickness of dermis  $h_2 = 2$  mm. In this regard, one may recall the results in Lai and Rix [118] which demonstrate that the coupling between the wave dispersion and attenuation, taken into account in this study, is pronounced at shear wavelengths as long as ten times the minimum layer thickness, which is the case with the present example. To justify the use

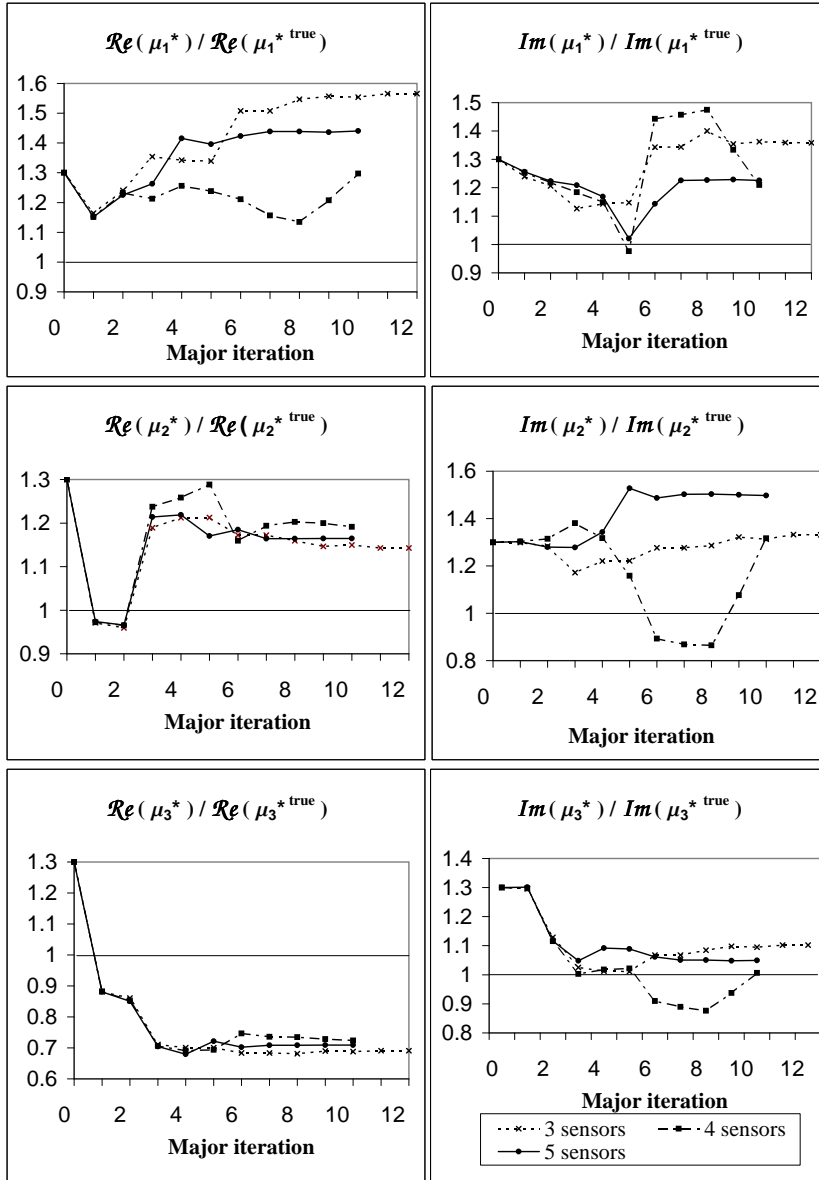


Figure 6.9. Convergence of the reconstructed shear moduli for one frequency  $f = \omega/(2\pi) = 100$  Hz assuming increasing number of sensors with 2 mm spacing. Synthetic skin profile:  $\mu_1^{*true} = (9.4 + 3.4i)$  kPa - epidermis ( $h_1 = 0.5$  mm),  $\mu_2^{*true} = (7 + 0.3i)$  kPa - dermis ( $h_2 = 2$  mm), and  $\mu_3^{*true} = (1.1 + 0.5i)$  kPa - subcutaneous tissue (bottom half-space).

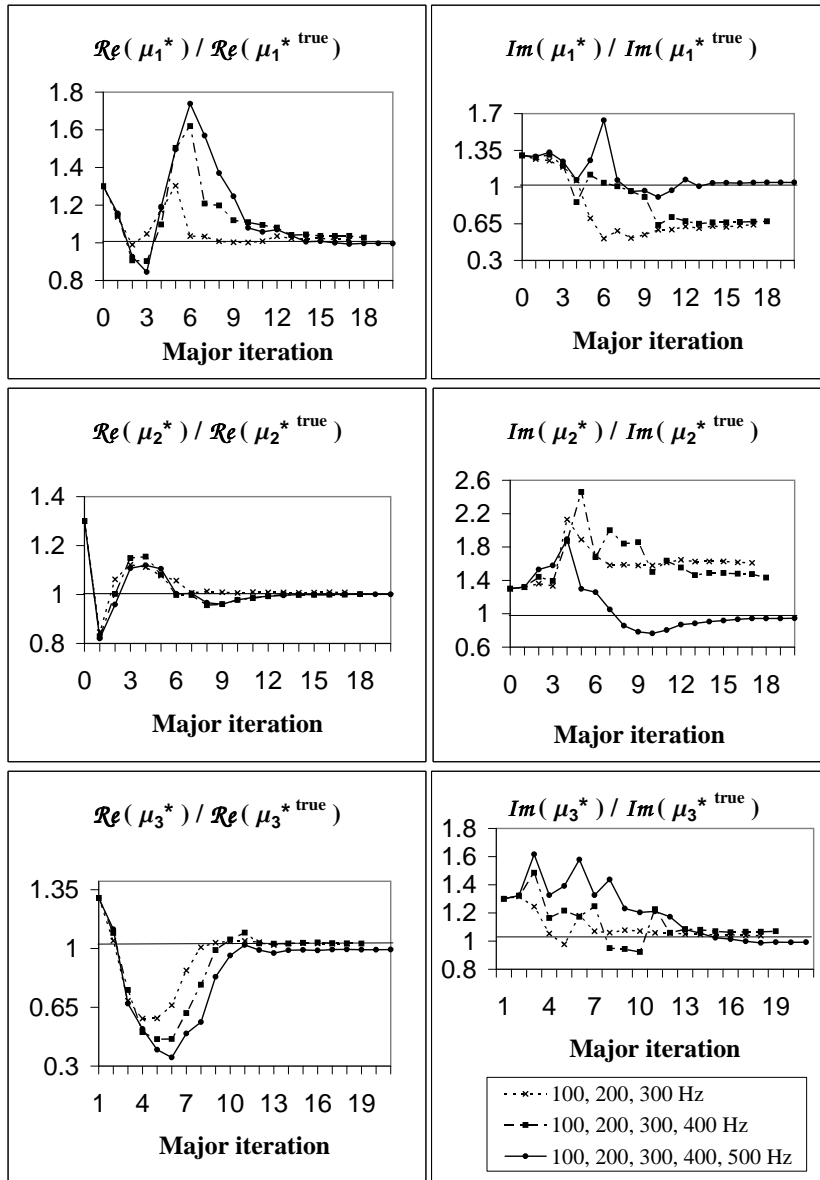


Figure 6.10. Convergence of the reconstructed shear moduli for selected frequency data sets ( $K = 3, 4, 5$ ) assuming two-fiber sensing array and noise-free measurements. Synthetic skin profile:  $\mu_1^{*true} = (9.4 + 3.4i)$  kPa - epidermis ( $h_1 = 0.5$  mm),  $\mu_2^{*true} = (7 + 0.3i)$  kPa - dermis ( $h_2 = 2$  mm), and  $\mu_3^{*true} = (1.1 + 0.5i)$  kPa - subcutaneous tissue (bottom half-space).

of the shear wavelength as the characteristic length scale in the discussion, it is further noted that (i) the skin sublayers exhibit notable contrast in the shear (as opposed to bulk) modulus, see e.g. Geerligs [73], and (ii) the wavelength of the Rayleigh waves, carrying most of the surface motion energy, is much closer to that of shear waves than to that of compressional waves (Achenbach [1]).

It should also be noted that already set up with only 2 sensors in the array, probed at sufficiently reach frequency sweep was enough to provide correct shear moduli. This shows once again that it is the number of "sweeps" and not the number of sensors in the array, which is crucial for a proper reconstruction of skin parameters.

### 6.6.3. Experimental noise

To expose the sensitivity of the proposed scheme to measurement uncertainties, a 5 % uniformly-distributed random noise is added to synthetic observations (6.14). The testing configuration is the same as in Section 6.6.2. for  $N = 4$ . Thus, it consists of four fibers each having length  $L = 10$  mm and square cross section  $w \times h = 100 \mu\text{m} \times 100 \mu\text{m}$  with spacing of 3.3 mm. The associated results of minimization, i.e. substrate reconstruction, are plotted in Figure 6.12 versus the number of testing frequencies, ranging from  $K = 2$  to  $K = 6$ . Despite the presence of measurement errors, the back-analysis with  $K = 5$  and  $K = 6$  still resolves the preponderance of the viscoelastic profile with reasonable accuracy. The only exception to this claim is the imaginary part of the bottom shear modulus,  $\mathcal{I}m(\mu_3^*)$ , which differs from its "true" value by roughly 10 %. The latter error can be attributed to a combined effect of: (i) injected 5 % measurement noise, (ii) deterioration of the model resolution with depth, and (iii) smallness of the bottom viscosity parameter in question (see Table 6.1). In particular, a comparison of the noise-free inversion results in Figure 6.11 (where all parameters are resolved within 1 %) and those in Figure 6.12 reveals that the parameter most affected by measurement inaccuracies is in fact  $\mathcal{I}m(\mu_3^*)$ . This is consistent with observations in the literature that the resolution of Rayleigh-wave inversion may deteriorate with depth — especially when using a limited number of excitation frequencies (Xia et al. [218]), and that the reconstruction of the layers' dissipative characteristics is generally less accurate than that of the corresponding elasticity parameters (Guzina and Madyarov [82], Xia et al. [218]).

In concluding the numerical analysis, it is noted that the foregoing results are inherently dependent on the accuracy of the assumed input parameters, most notably layer thicknesses  $h_s$  ( $s = 1, 2$ ). As examined earlier, the latter

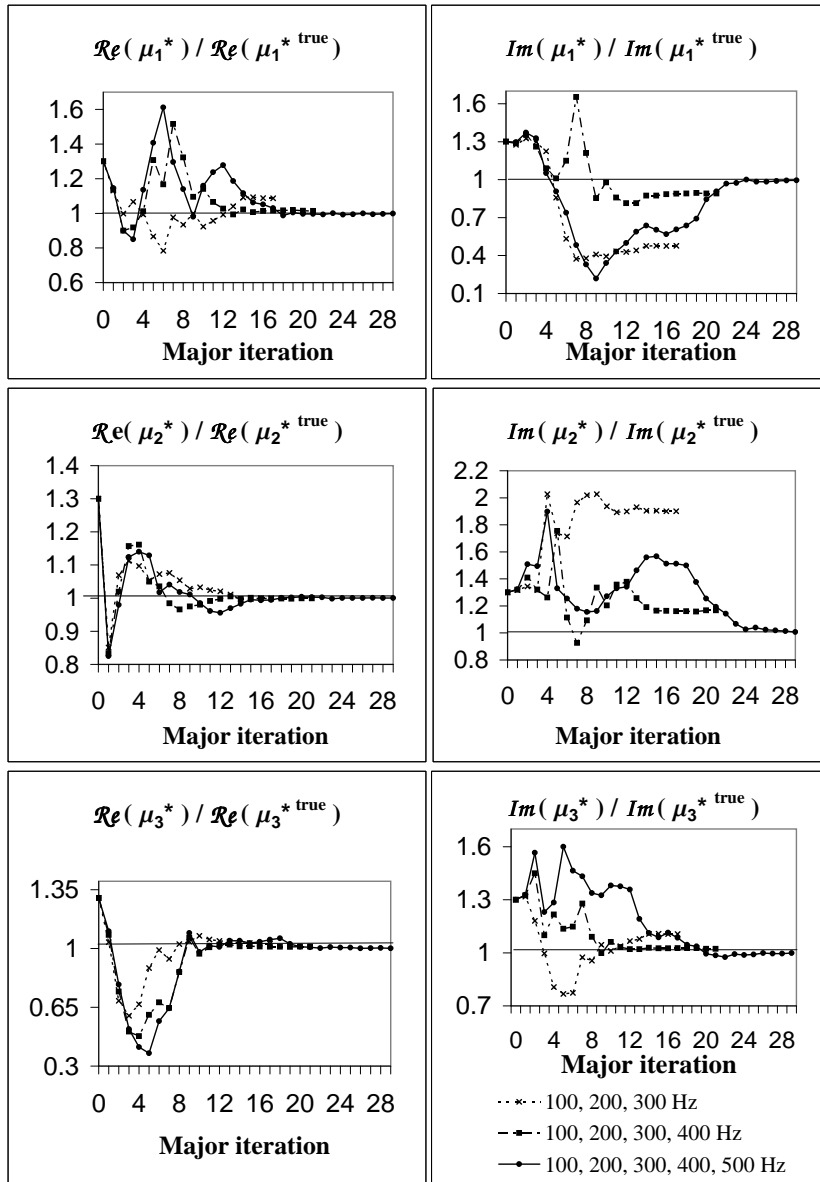


Figure 6.11. Convergence of the reconstructed shear moduli for selected frequency data sets ( $K = 3, 4, 5$ ) assuming four-fiber sensing array and noise-free measurements. Synthetic skin profile:  $\mu_1^{*true} = (9.4 + 3.4i)$  kPa - epidermis ( $h_1 = 0.5$  mm),  $\mu_2^{*true} = (7 + 0.3i)$  kPa - dermis ( $h_2 = 2$  mm), and  $\mu_3^{*true} = (1.1 + 0.5i)$  kPa - subcutaneous tissue (bottom half-space).

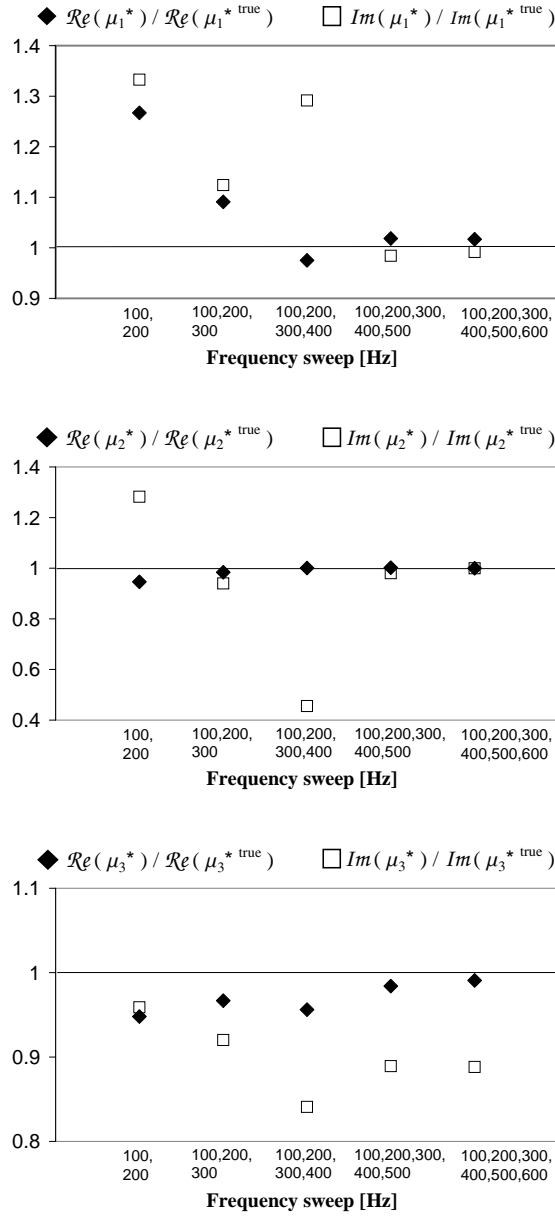


Figure 6.12. Reconstructed shear moduli for selected frequency data sets ( $K = 3, 4, 5$ ) assuming four-fiber sensing array and measurements polluted with 5 % random noise. Synthetic skin profile:  $\mu_1^{*\text{true}} = (9.4 + 3.4i)$  kPa - epidermis ( $h_1 = 0.5$  mm),  $\mu_2^{*\text{true}} = (7 + 0.3i)$  kPa - dermis ( $h_2 = 2$  mm), and  $\mu_3^{*\text{true}} = (1.1 + 0.5i)$  kPa - subcutaneous tissue (bottom half-space).

distances can be measured with high accuracy via high-frequency ultrasound as in Liu and Ebbini [126]. In the absence of such critical information, the most systematic way toward reliably estimating the layered tissue properties may entail the inclusion of  $h_s$  into the list  $\mathbf{p}$  of unknown parameters as in Guzina and Madyarov [82]. While increasing the dimension of the parametric space and thus complicating the inversion, such an approach may inherently guard against blunders caused by the erroneous input values of  $h_s$ .

## 6.7. Conclusions

In this chapter, a piezoelectric motion-sensing array and computational framework are proposed for the non-invasive viscoelastic reconstruction of layered skin properties. This is accomplished by the scale reduction of the so-called Multi-channel Analysis of Surface Waves, a seismic surveying methodology that is routinely used in engineering geophysics for the identification of vertical geological profiles. The utility of the new sensor, containing an array of hair-like piezoelectric (PVDF) sensors that are sensitive to tissue deformation and thus motion, is enhanced through a systematic solid-fiber interaction analysis that furnishes integral information, cumulative over the length of each fiber, about the attenuation and dispersion of surface waves. By virtue of a full waveform back-analysis, featuring the proposed predictive model as a tool to interpret electric charges stemming from the fibers, the methodology allows for an effective reconstruction and viscoelastic characterization of cutaneous and subcutaneous tissue sublayers on a millimetre scale. The performance of the proposed sensor array and data interpretation framework is illustrated through numerical simulations, which point to the feasibility of *in vivo* mechanical characterization of stratified skin structure. It has been shown that crucial for proper parameter reconstruction is the frequency sweep and not the number of sensors in the array.

Potential benefits of the new technology are twofold and include (i) low-cost viscoelastic characterization of skin using disposable motion sensor, and (ii) mechanical differentiation between skin sublayers, not achievable through available techniques presented in Section 1.6.3. Thus obtained information could be used for example toward better understanding of skin aging or exposing the effectiveness of various cosmetic treatments. In the context of elastic wave delineation of skin cancer, the proposed developments may provide a critical preparatory step toward non-iterative three dimensional reconstruction of lesions via e.g. the linear sampling method or the topological sensitivity approach, which both

require the mechanical properties of the lesion-free, background layered medium to be known beforehand.

In the context of skin imaging methodologies described in Section 1.6.3., it should also be mentioned that the proposed technology does not require special equipment and training for data interpretation. Its costs are almost negligible, when compared to expenses required for usage of sophisticated hardware in cases of ultrasound or nuclear magnetic resonance. It makes a competitive alternative both on large scale in practical diagnostic as well as in laboratory measurements of skin properties.

## Summary

In the monograph four different aspects of mechanics of thin films have been addressed. Firstly, it concerns the problem of coating degradation due to through thickness cracking. Analysis focuss on the modelling of the process itself, as well as the description of the saturation stage, when no more cracks are expected to appear.

An energy model of segmentation cracking of a thin film deposited on a stretched substrate is derived in Chapter 3. The model is based on an analytical analysis of film delamination, where a constant shear stress at the film/substrate interface and a presence of residual forces is assumed. The residual stresses can be a result either of a mismatch in thermal expansion coefficients between the film and the substrate or a result of the production process. The system response to the residual loading is a development of delaminated zones at the film/substrate interface at both ends of the composite. Another consequence of the residual stresses is a two-stage delamination process, when the substrate is subsequently stretched. During the first stage the length of a single delamination zone does not increase and remains the same as during the residual state. The increase of the external loading results in a formation of reverse slip regions within the already damaged interface. During the second stage of loading a further development of the failure process at the interface takes place. Characteristic is an existence of a plateau of a constant normal stress acting on the film. Because of that, the formation of cracks within the film is strongly dependent upon random distribution of micro-defects within the material and difficult to model by conventional critical stress approach. Instead of using a critical stress approach, a transition condition is adopted, stating that the segmentation occurs when the energy of the cracked system is lower than the energy of the intact system. By the energy of the system its potential energy and the energy dissipated to create the segmentation cracks and to damage the film/substrate interface is understood. This approach does not account for a loading history and assumes a transformation of the film topology. Crack density at the saturation stage can be uniquely identified in this way.

It has been shown that the analysis can be simplified when the film is much thinner than the substrate and their stiffnesses are in the same range. In such a case, one can focus only upon the energies of the film and the interface and neglect the substrate effect. The obtained results shall be the same as if the whole composite was considered.

There are several segmentation cracking models, where fracture criterion is based on stress redistribution, see for example Białas and Mróz [29, 30], Hsueh [93], Yanaka et al. [223, 224]. In the present model it is the fracture energy which plays the same role as film fracture stress in stress criterion models. The main assumption of the energy model is equal spacing between segmentation cracks in the saturation stage. Experimental results show a variation of crack spacing around a mean value. Using a stress redistribution model Agrawal and Raj [4] showed that the maximum and minimum crack spacing should differ by a factor of two. This effect cannot be captured by the present approach.

There is another phenomenon that is also not included in the present analysis. Since we use a topological transformation from an uncracked to a fully damaged state of the system, we do not consider the loading history. In the framework of this energy approach it is not possible to model a relation between applied load and crack density. This effect can be easily captured by stress redistribution models (see, for instance, Białas and Mróz [29]).

The energy model is formulated for the second stage of loading. With that in mind it should be stated that the residual stresses do not have any effect upon segmentation cracking, since the residual damage zones are erased by reverse slip zones during the second stage of loading. According to the present approach the residual stresses would have effect upon the results when segmentation cracking took place during the first loading stage.

Numerical simulation of through thickness cracking concerns another aspect of the phenomenon without focusing on the saturation stage, though. It reveals that due to decreasing value of  $G_I$  one obtains increasing number of cracks within the coating. Multiple cracking within a coating can reduce the magnitude of critical energy release rate for the interface between the coating and the substrate, suggesting that through thickness cracking can be beneficial for coating life time, as it is observed within EB PVD. Presented quantitative results of the finite element simulations can be used to tailor coating properties.

In order to obtain crack localization during the numerical computations, the loading step has to be small enough to allow for satisfaction of failure criteria in only one integration point per loading step. A standard cohesive zone analysis is used mostly to model delamination processes, that is a development of cracks at a material interface, being a well defined plane of weakness. In such a

case several integration points can be simultaneously subjected to progressive damage leading anyway to failure localization on a single plane and enabling to follow a physical equilibrium path. The presented static analysis, however, tries to simulate development of a number of through thickness cracks for neither of which a formation place can be defined in advance. A way to find it and to overcome convergence problems is to allow for satisfaction of failure condition in only one integration point within a single loading step. This leads to a realistic failure scenario, where one observes a multitude of separated cracks. The obtained numerical results resemble the experiment quantitatively: both provided similar number of TBC through thickness cracks as well as their localization.

Secondly, the monograph concerns the problem of stress development within thin film structures due to mechanical and thermal loadings. This aspect is particularly important in the case of thermal barrier coatings serving as an insulation layer in gas turbines. Due to severe working conditions (high temperature up to 1200°C, chemical oxidation) the stress state in TBC system is very complex, as resulting from creep and relaxation combined with growth of oxide layer. Mechanical analysis adopted in the monograph relies on micro modelling, where phenomena occurring in a unit cell of TBC system are assumed to be generalized for a whole coating. With the stress state within a TBC unit cell at hand, mechanisms leading to coating spallation and degradation can be better understood. The main results can be summarized as:

- during thermal loading the creep of CMSX-4 substrate can be neglected, since it does not play almost any role on the stress redistribution around the asperity;
- the cooling stage is the most crucial for microcrack development within the unit cell;
- for elastic and viscous materials stress distribution after cooling to ambient is basically identical for a single loading cycle with the dwell time of a number of multiple loading cycles;
- crack development at the TGO/BC interface leads to a formation of crucial tensile zones within TBC and, provided the TGO layer is sufficiently thick, also within TGO.

Combined development of the interface crack and of the thickening of the TGO leads to an appearance of a tensional zone within TGO besides the roughness peak and the following hypothesis of damage evolution around an asperity can be formulated. After cooling down to ambient a microcrack at the TGO/BC interface forms. Its appearance influences the stress redistribution within TBC, allowing for a creation of a tensional zone and a formation of TBC microcrack.

Subsequent TGO thickening increases the area under tension within TBC and promotes the development of the TBC crack. With TGO being thick enough, a tensional zone develops within TGO allowing for linking of TBC and the interface crack through TGO.

This hypothesis is in good agreement with the cracking scenario presented by Chang et al. [43] and Freborg et al. [68] and provides some additional quantitative information. Further research would require to model crack development within TBC (using for example cohesive zone elements) and to examine its influence upon stress redistribution within TGO. The next step could be modelling of linking of the TBC and the interface cracks.

An aspect of frictional slip between a coating and a substrate is a third phenomenon addressed in the monograph. A semi-analytical estimation and, in a particular case, a correct analytical solution is provided. This situation corresponds to a frictional slip of a rigid film on a rigid substrate. In that part of the monograph an attempt is made to depart from one dimensional strip models (e.g. Białaś and Mróz [29, 30], Schreyer and Peffer [174], Timm et al. [198]) toward more complex situation of a coating treated as a two dimensional continuum. In this way, effect of material contraction due to Poisson's ratio could be captured. In context of the approximation, it can be stated that the mechanism of delamination is governed solely by the fundamental solution due to a concentrated force — this solution determines the interfacial stresses and the moving boundary. The delamination area is the same as the region of fundamental field, where the horizontal components of the displacement vectors point in the same direction as the loading force.

The presented approach can be used to obtain approximate, closed-form solutions for similar delamination problems, for example when considering a film in the shape of a two dimensional wedge loaded at its vertex by an in-plane point force inducing symmetrical frictional slip. The algorithm providing an approximate solution is:

1. obtain a solution for the fundamental displacement field  $\{u_x^P, u_y^P\}$  resulting from the point force alone;
2. approximate the distribution of interfacial forces using field  $\{u_x^P, u_y^P\}$ ;
3. condition  $\delta P = 0$  provides a function representing the moving boundary;
4. use the superposition principle to calculate the stress field.

With the value of shear stress  $\tau^f$  remaining constant during the slip process a crude assumption regarding the interface constitutive law is made. More realistic relation between the shear stress and relative displacement would require the stress first to reach a peak shear strength  $\tau^{\text{peak}}$  and then to decrease to

a residual value denoted by  $\tau^f$ , where  $\tau^f < \tau^{\text{peak}}$ . Such an analysis was performed for example by Palmer and Rice [154], who considered growth of slip surfaces in over-consolidated clay. In the case discussed in Chapter 5, however, the assumption of plane-stress conditions is crucial and makes the results applicable to an advanced slip situation only, where the characteristic length  $2l_0$  of the damaged zone is big when compared to film thickness  $h$ . In such a case the value of the interface shear stress is likely to be higher than  $\tau^f$  only in the vicinity of the moving boundary and, with a good approximation, within most of the damaged area the ultimate shear stress  $\tau^f$  is reached. It should also be mentioned that simple interface constitutive laws, as that adopted here, are used for film segmentation cracking problems, rendering solutions which can be successfully used in practice when calculating crack densities, see for example Białaś and Mróz [30] or Timm et al. [198].

Fourthly, the monograph aims also at mechanical characterization of thin films using non-invasive methods. A piezoelectric motion-sensing array and computational framework are proposed for the non-invasive viscoelastic reconstruction of layered skin properties. This is accomplished by the scale reduction of the so-called Multi-channel Analysis of Surface Waves, a seismic surveying methodology that is routinely used in engineering geophysics for the identification of vertical geological profiles. The utility of the new sensor, containing an array of hair-like piezoelectric sensors that are sensitive to tissue deformation and thus motion, is enhanced through a systematic solid-fiber interaction analysis that furnishes integral information, cumulative over the length of each fiber, about the attenuation and dispersion of surface waves. By virtue of a full waveform back-analysis, featuring the proposed predictive model as a tool to interpret electric charges stemming from the fibers, the methodology allows for an effective reconstruction and viscoelastic characterization of cutaneous and subcutaneous tissue sublayers on a millimeter scale. The performance of the proposed sensor array and data interpretation framework is illustrated through numerical simulations, which point to the feasibility of *in vivo* mechanical characterization of stratified skin structure. It has been shown that crucial for proper parameter reconstruction is the frequency sweep and not the number of sensors in the array.

Potential benefits of the new technology are twofold and include (i) low-cost viscoelastic characterization of skin using disposable motion sensor, and (ii) mechanical differentiation between skin sublayers, not achievable through available techniques. Thus obtained information could be used for example toward better understanding of skin aging or exposing the effectiveness of various cosmetic treatments. In the context of elastic wave delineation of skin cancer,

the proposed developments may provide a critical preparatory step toward non-iterative three dimensional reconstruction of lesions via e.g. the linear sampling method or the topological sensitivity approach, which both require the mechanical properties of the lesion-free, background layered medium to be known beforehand.

In short, the novel aspects of the reported research are:

- application of energy model of segmentation cracking to description of saturation stage of multiple cracks within silicon oxide coating on polymer substrates;
- description of the effect of residual stresses on segmentation cracking;
- quantitative analysis of thin coating through thickness cracking providing theoretical explanation to the every day engineering experience that multiple cracking in the film can reduce the magnitude of energy release rate for the interface between the coating and the substrate (in other words: through thickness cracking can be beneficial for film's life-time);
- analysis of the significance of loading step during finite element analysis of multiple through thickness cracking; practical suggestions allowing to overcome convergence problems during similar analyses;
- analysis of key aspects governing stress development within thermal barrier coatings and subsequent description of mechanisms leading to coating spallation and delamination;
- formulation of semi-analytical methodology allowing for description of two dimensional frictional slip at coating/substrate interface (in contrast to the already known in literature one dimensional strip models);
- derivation of simple analytical formulas describing process of delamination of a rigid film from a rigid substrate;
- formulation of conceptual piezoelectric sensor setup for measurements of complex elastic moduli of stratified thin film structure during non-destructive in vivo experiments;
- suggestions for the effective applications of the sensors array.

The subsequent research would certainly involve formulation of more sophisticated tools toward better understanding of failure processes within thermal barrier coatings. This would require finite element analysis of crack formation within TBC and TGO layers, and their subsequent linking explaining the delamination phenomenon. To that end, asperities with different dimensions should be considered, and accumulative knowledge stemming from this micro modelling could provide assessment of coatings life time on gas turbine blades.

# A

## Green's function for a one dimensional elastic strip

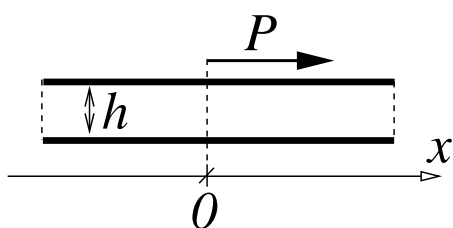


Figure A.1. Strip loaded by a point force.

Infinite elastic strip of thickness  $h$  and width  $w$  loaded at point  $x = 0$  by a concentrated force  $P$  is presented in Figure A.1 The resultant stress is given by

$$\sigma(x) = -\frac{P}{2hw} \text{sign } x. \quad (\text{A.1})$$

Hooke's law  $\sigma = E\varepsilon$  and small strain-displacement relation  $\varepsilon = du/dx$  provide the displacement field

$$u(x) = -\frac{P}{2hwE} (|x| - d), \quad (\text{A.2})$$

where  $d$  is an undefined integration constant. By letting  $P = 1$  and assuming the force to be imposed at an arbitrary location  $X$ , we obtain respectively stress and displacement Green's functions used in Section 5.4.

$$\tilde{\sigma}(x, X) = -\frac{1}{2hw} \text{sign}(x - X), \quad (\text{A.3})$$

$$\tilde{u}(x, X) = -\frac{1}{2hwE} [ |x - X| - d(X) ]. \quad (\text{A.4})$$

In the above formulas, small  $x$  stands for an observation point, whereas capital  $X$  is a source point. Value of  $d$  in equation (A.4) can in general depend on the location of the unit force, resulting in the notation  $d(X)$ .



## B

# Green's functions for an infinite plate loaded by an in-plane point force

The starting point for the derivation of Green's function is the solution for a force at point  $O$  of an infinite plate of thickness  $h$ , as presented in Figure B.1(a). This solution can be found, for example, in Timoshenko and Goodier [199], Article 38. Since only the stresses are given in [199], we will derive here the expressions for the displacement field.

Assuming plane stress conditions, the polar stress components of the problem depicted in Figure B.1(a) have the form (Timoshenko and Goodier [199])

$$\boldsymbol{\sigma} = \begin{bmatrix} \sigma_{rr} & \sigma_{r\varphi} \\ \sigma_{\varphi r} & \sigma_{\varphi\varphi} \end{bmatrix} = P \frac{1-\nu}{4\pi hr} \begin{bmatrix} \frac{3+\nu}{\nu-1} \cos \varphi & \sin \varphi \\ \sin \varphi & \cos \varphi \end{bmatrix}. \quad (\text{B.1})$$

Plane stress Hook's law provides components of the strain tensor

$$\begin{aligned} \epsilon_{rr} &= \frac{\sigma_{rr} - \nu\sigma_{\varphi\varphi}}{E} = P \frac{(\nu^2 - 2\nu - 3) \cos \varphi}{4\pi Eh} \frac{1}{r}, \\ \epsilon_{\varphi\varphi} &= \frac{\sigma_{\varphi\varphi} - \nu\sigma_{rr}}{E} = P \frac{(1+\nu)^2 \cos \varphi}{4\pi Eh} \frac{1}{r}, \\ \epsilon_{r\varphi} &= \frac{1+\nu}{E} \sigma_{r\varphi} = P \frac{(1-\nu^2) \sin \varphi}{4\pi Eh} \frac{1}{r}. \end{aligned} \quad (\text{B.2})$$

Integration of relations

$$\epsilon_{rr} = u_{r,r}, \quad \epsilon_{\varphi\varphi} = \frac{u_{\varphi,\varphi} + u_r}{r}, \quad \epsilon_{r\varphi} = \frac{u_{r,\varphi} + r u_{\varphi,r} - u_\varphi}{2r}, \quad (\text{B.3})$$

with boundary conditions

$$\begin{aligned} u_\varphi(r, \varphi = 0) = 0, \quad u_\varphi(r, \varphi = \pi) = 0 \quad \text{for } r \geq 0, \\ u_r(r = d, \varphi = 0) = 0, \end{aligned} \quad (\text{B.4})$$

provides the displacement field

$$\mathbf{u} = \begin{bmatrix} u_r \\ u_\varphi \end{bmatrix} = P \frac{1+\nu}{4\pi E h} \begin{bmatrix} \frac{3+2\nu-\nu^2}{1+\nu} \cos \varphi \ln \frac{d}{r} \\ (1+\nu + (3-\nu) \ln \frac{r}{d}) \sin \varphi \end{bmatrix}. \quad (\text{B.5})$$

The first two conditions (B.4) simply enforce the symmetry of the displacement field with respect to the axis co-linear with the external force  $P$ . The last one means that the plate does not displace at an arbitrary point on the symmetry axis at the distance  $d$  from the loading force. There are no physical prerequisites to chose any specific value of  $d$  and, as such, it can be treated just like an undefined, superfluous integration constant.

To derive the Green's functions we shall consider two different cartesian coordinate systems, namely  $\{x^I, y^I\}$  and  $\{x^{II}, y^{II}\}$ . In the first one the loading force  $P$  has the direction of axis  $x^I$ , in the second one it is aligned with the axis  $y^{II}$  as presented in Figure B.1(b) and Figure B.1(c). The following formulas relate the polar with the two cartesian coordinate systems

$$\begin{aligned} \sin \varphi &= \frac{y^I}{\sqrt{(x^I)^2 + (y^I)^2}} = \frac{-x^{II}}{\sqrt{(x^{II})^2 + (y^{II})^2}}, \\ \cos \varphi &= \frac{x^I}{\sqrt{(x^I)^2 + (y^I)^2}} = \frac{y^{II}}{\sqrt{(x^{II})^2 + (y^{II})^2}}, \\ r &= \sqrt{(x^I)^2 + (y^I)^2} = \sqrt{(x^{II})^2 + (y^{II})^2}. \end{aligned} \quad (\text{B.6})$$

Additionally, the following relations hold

$$[\vec{e}_r, \vec{e}_\varphi]^T = \mathbf{B}^I [\vec{e}_x^I, \vec{e}_y^I]^T = \mathbf{B}^{II} [\vec{e}_x^{II}, \vec{e}_y^{II}]^T, \quad (\text{B.7})$$

where the matrices  $\mathbf{B}^I$  and  $\mathbf{B}^{II}$  have the form

$$\mathbf{B}^I = \begin{bmatrix} \cos \varphi & \sin \varphi \\ -\sin \varphi & \cos \varphi \end{bmatrix}, \quad \mathbf{B}^{II} = \begin{bmatrix} -\sin \varphi & \cos \varphi \\ -\cos \varphi & -\sin \varphi \end{bmatrix}. \quad (\text{B.8})$$

The transformations  $(\mathbf{B}^I)^T \boldsymbol{\sigma} \mathbf{B}^I$  and  $(\mathbf{B}^{II})^T \boldsymbol{\sigma} \mathbf{B}^{II}$  together with (B.1), (B.6) and (B.8) provide stress components respectively in the first and in the second

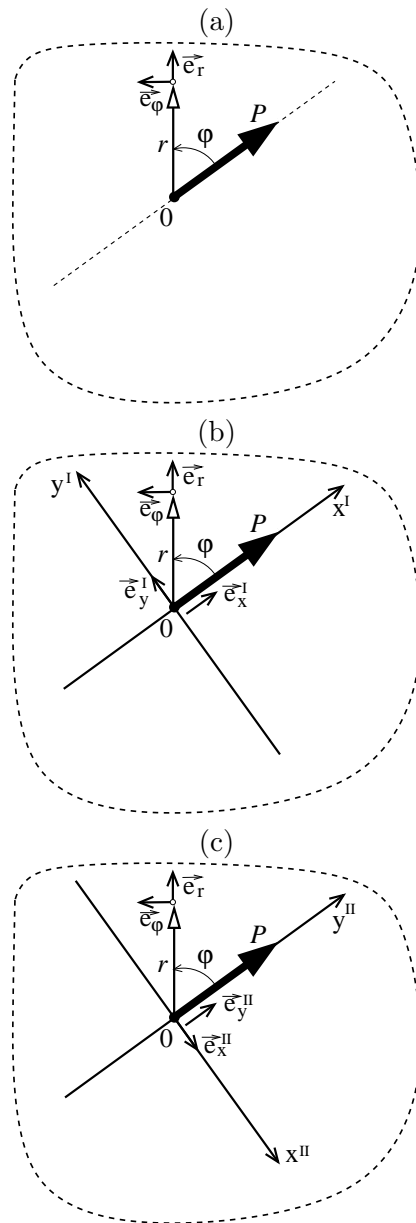


Figure B.1. (a) Infinite film loaded by in-plane point force. (b),(c) Two cartesian coordinate systems  $\{x^I, y^I\}$  and  $\{x^{II}, y^{II}\}$ .

cartesian coordinate system. We obtain

$$\begin{aligned}\sigma_{x^I x^I} &= P \frac{x^I [(\nu - 1)(y^I)^2 - (3 + \nu)(x^I)^2]}{4\pi h [(x^I)^2 + (y^I)^2]^2}, \\ \sigma_{y^I y^I} &= P \frac{x^I [(1 - \nu)(x^I)^2 - (1 + 3\nu)(y^I)^2]}{4\pi h [(x^I)^2 + (y^I)^2]^2}, \\ \sigma_{x^I y^I} &= P \frac{y^I [(\nu - 1)(y^I)^2 - (3 + \nu)(x^I)^2]}{4\pi h [(x^I)^2 + (y^I)^2]^2}\end{aligned}\quad (\text{B.9})$$

in the first cartesian coordinate system and

$$\begin{aligned}\sigma_{x^{II} x^{II}} &= P \frac{y^{II} [(1 - \nu)(y^{II})^2 - (1 + 3\nu)(x^{II})^2]}{4\pi h [(x^{II})^2 + (y^{II})^2]^2}, \\ \sigma_{y^{II} y^{II}} &= P \frac{y^{II} [(\nu - 1)(x^{II})^2 - (3 + \nu)(y^{II})^2]}{4\pi h [(x^{II})^2 + (y^{II})^2]^2}, \\ \sigma_{x^{II} y^{II}} &= P \frac{x^{II} [(\nu - 1)(x^{II})^2 - (3 + \nu)(y^{II})^2]}{4\pi h [(x^{II})^2 + (y^{II})^2]^2}\end{aligned}\quad (\text{B.10})$$

in the second.

The transformations  $(\mathbf{B}^I)^T \mathbf{u}$  and  $(\mathbf{B}^{II})^T \mathbf{u}$  together with formulas (B.5), (B.6) and (B.8) provide displacement components respectively in the first and in the second cartesian coordinate system. We obtain

$$\begin{aligned}u_{x^I} &= P \frac{1 + \nu}{4\pi E h} \left[ (3 - \nu) \ln \frac{d^I}{\sqrt{(x^I)^2 + (y^I)^2}} - (1 + \nu) \frac{(y^I)^2}{(x^I)^2 + (y^I)^2} \right], \\ u_{y^I} &= P \frac{(1 + \nu)^2}{4\pi E h} \frac{x^I y^I}{(x^I)^2 + (y^I)^2}\end{aligned}\quad (\text{B.11})$$

in the first cartesian coordinate system and

$$\begin{aligned}u_{x^{II}} &= P \frac{(1 + \nu)^2}{4\pi E h} \frac{x^{II} y^{II}}{(x^{II})^2 + (y^{II})^2}, \\ u_{y^{II}} &= P \frac{1 + \nu}{4\pi E h} \left[ (3 - \nu) \ln \frac{d^{II}}{\sqrt{(x^{II})^2 + (y^{II})^2}} - (1 + \nu) \frac{(x^{II})^2}{(x^{II})^2 + (y^{II})^2} \right]\end{aligned}\quad (\text{B.12})$$

in the second. The auxiliary parameter  $d$  in (B.5) has been changed to  $d^I$  and  $d^{II}$  respectively in (B.11) and (B.12).

Equations (B.9) and (B.10) can be used to obtain stress Green's functions in a general cartesian coordinate system  $\{x, y\}$ . For a unit force acting in the positive  $x$  direction we have

$$\begin{aligned}\tilde{\sigma}_{xx}^x &= \frac{(x-X)[(\nu-1)(y-Y)^2 - (3+\nu)(x-X)^2]}{4\pi h [(x-X)^2 + (y-Y)^2]^2}, \\ \tilde{\sigma}_{yy}^x &= \frac{(x-X)[(1-\nu)(x-X)^2 - (1+3\nu)(y-Y)^2]}{4\pi h [(x-X)^2 + (y-Y)^2]^2}, \\ \tilde{\sigma}_{xy}^x &= \frac{(y-Y)[(\nu-1)(y-Y)^2 - (3+\nu)(x-X)^2]}{4\pi h [(x-X)^2 + (y-Y)^2]^2}.\end{aligned}\quad (\text{B.13})$$

Unit force aligned with the positive  $y$  direction induces the stresses

$$\begin{aligned}\tilde{\sigma}_{xx}^y &= \frac{(y-Y)[(1-\nu)(y-Y)^2 - (1+3\nu)(x-X)^2]}{4\pi h [(x-X)^2 + (y-Y)^2]^2}, \\ \tilde{\sigma}_{yy}^y &= \frac{(y-Y)[(\nu-1)(x-X)^2 - (3+\nu)(y-Y)^2]}{4\pi h [(x-X)^2 + (y-Y)^2]^2}, \\ \tilde{\sigma}_{xy}^y &= \frac{(x-X)[(\nu-1)(x-X)^2 - (3+\nu)(y-Y)^2]}{4\pi h [(x-X)^2 + (y-Y)^2]^2}.\end{aligned}\quad (\text{B.14})$$

In equations (B.13) and (B.14) small letters ( $x, y$ ) indicate an observation point and capital letters ( $X, Y$ ) stand for a source point.

Equations (B.13) and (B.14) can be re-written in the polar parametrization of space. By substituting

$$x = r \cos \varphi, \quad y = r \sin \varphi, \quad X = R \cos \Phi, \quad Y = R \sin \Phi \quad (\text{B.15})$$

into (B.13) and (B.14) we obtain

$$\begin{aligned}\tilde{\sigma}_{xx}^x &= (R \cos \Phi - r \cos \varphi) \cdot \\ &\cdot \frac{(3+\nu)(R \cos \Phi - r \cos \varphi)^2 + (1-\nu)(R \sin \Phi - r \sin \varphi)^2}{4\pi h [r^2 + R^2 - 2rR \cos(\Phi - \varphi)]^2}, \\ \tilde{\sigma}_{yy}^x &= (R \cos \Phi - r \cos \varphi) \cdot \\ &\cdot \frac{(\nu-1)(R \cos \Phi - r \cos \varphi)^2 + (1+3\nu)(R \sin \Phi - r \sin \varphi)^2}{4\pi h [r^2 + R^2 - 2rR \cos(\Phi - \varphi)]^2}, \\ \tilde{\sigma}_{xy}^x &= (R \sin \Phi - r \sin \varphi) \cdot \\ &\cdot \frac{(3+\nu)(R \cos \Phi - r \cos \varphi)^2 + (1-\nu)(R \sin \Phi - r \sin \varphi)^2}{4\pi h [r^2 + R^2 - 2rR \cos(\Phi - \varphi)]^2},\end{aligned}\quad (\text{B.16})$$

and respectively

$$\begin{aligned}
\tilde{\sigma}_{xx}^y &= (R \sin \Phi - r \sin \varphi) \cdot \\
&\cdot \frac{(1 + 3\nu)(R \cos \Phi - r \cos \varphi)^2 - (1 - \nu)(R \sin \Phi - r \sin \varphi)^2}{4\pi h [r^2 + R^2 - 2rR \cos(\Phi - \varphi)]^2}, \\
\tilde{\sigma}_{yy}^y &= (R \sin \Phi - r \sin \varphi) \cdot \\
&\cdot \frac{(1 - \nu)(R \cos \Phi - r \cos \varphi)^2 + (3 + \nu)(R \sin \Phi - r \sin \varphi)^2}{4\pi h [r^2 + R^2 - 2rR \cos(\Phi - \varphi)]^2}, \quad (\text{B.17}) \\
\tilde{\sigma}_{xy}^y &= (R \cos \Phi - r \cos \varphi) \cdot \\
&\cdot \frac{(1 - \nu)(R \cos \Phi - r \cos \varphi)^2 + (3 + \nu)(R \sin \Phi - r \sin \varphi)^2}{4\pi h [r^2 + R^2 - 2rR \cos(\Phi - \varphi)]^2}.
\end{aligned}$$

Here, again, small letters ( $r, \varphi$ ) indicate an observation point and capital ( $R, \Phi$ ) stand for a source point.

Equations (B.11) and (B.12) can be used to obtain displacement Green's functions in a general cartesian coordinate system  $\{x, y\}$ . For a unit force acting in a positive  $x$  direction we simply have

$$\begin{aligned}
\tilde{u}_x^x &= \frac{1 + \nu}{4\pi Eh} \left[ (3 - \nu) \ln \frac{d^x(X, Y)}{\sqrt{(x - X)^2 + (y - Y)^2}} - \right. \\
&\quad \left. - (1 + \nu) \frac{(y - Y)^2}{(x - X)^2 + (y - Y)^2} \right], \quad (\text{B.18}) \\
\tilde{u}_y^x &= \frac{(1 + \nu)^2}{4\pi Eh} \frac{(x - X)(y - Y)}{(x - X)^2 + (y - Y)^2}.
\end{aligned}$$

Unit force aligned with a positive  $y$  direction results in the displacements

$$\begin{aligned}
\tilde{u}_x^y &= \frac{(1 + \nu)^2}{4\pi Eh} \frac{(x - X)(y - Y)}{(x - X)^2 + (y - Y)^2}, \\
\tilde{u}_y^y &= \frac{1 + \nu}{4\pi Eh} \left[ (3 - \nu) \ln \frac{d^y(X, Y)}{\sqrt{(x - X)^2 + (y - Y)^2}} - \right. \\
&\quad \left. - (1 + \nu) \frac{(x - X)^2}{(x - X)^2 + (y - Y)^2} \right]. \quad (\text{B.19})
\end{aligned}$$

The upper index  $j$  in  $\tilde{u}_i^j$  stands for the source direction, the lower index  $i$  stands for displacement direction. Again, the small letters ( $x, y$ ) in equations (B.18)

and (B.19) indicate an observation point, the capital  $(X, Y)$  a source point. The auxiliary parameters  $d^I$  and  $d^{II}$  have been changed respectively to  $d^x$  and  $d^y$ . In general, the Green's functions can depend on a position of source point and this fact has been indicated in (B.18) and (B.19) by writing respectively  $d^x(X, Y)$  and  $d^y(X, Y)$ . There is of course  $d = d^I = d^x(0, 0)$  and  $d^{II} = d^y(0, 0)$ .

After substituting equations (B.15) into (B.18) and (B.19) we obtain displacement Green's functions in the polar parametrization of space

$$\begin{aligned}\tilde{u}_x^x &= \frac{1 + \nu}{4\pi Eh} \left[ (3 - \nu) \ln \frac{d^x(R, \Phi)}{\sqrt{r^2 + R^2 - 2rR \cos(\Phi - \varphi)}} - \right. \\ &\quad \left. - (1 + \nu) \frac{(R \sin \Phi - r \sin \varphi)^2}{r^2 + R^2 - 2rR \cos(\Phi - \varphi)} \right], \\ \tilde{u}_y^x &= \tilde{u}_x^y = \frac{(1 + \nu)^2}{4\pi Eh} \frac{(R \cos \Phi - r \cos \varphi)(R \sin \Phi - r \sin \varphi)}{r^2 + R^2 - 2rR \cos(\Phi - \varphi)}, \quad (\text{B.20}) \\ \tilde{u}_y^y &= \frac{1 + \nu}{4\pi Eh} \left[ (3 - \nu) \ln \frac{d^y(R, \Phi)}{\sqrt{r^2 + R^2 - 2rR \cos(\Phi - \varphi)}} - \right. \\ &\quad \left. - (1 + \nu) \frac{(R \cos \Phi - r \cos \varphi)^2}{r^2 + R^2 - 2rR \cos(\Phi - \varphi)} \right].\end{aligned}$$

Small letters  $(r, \varphi)$  indicate an observation point and capital  $(R, \Phi)$  stand for a source point. In consistency with previous notation, there is  $d = d^I = d^x(0, 0)$  and  $d^{II} = d^y(0, 0)$ .



## Parameters used in equations (6.4)

For completeness the expressions for parameters  $a_i$ ,  $b_1$  ( $i = 1, 2, 3$ ) and  $c_j$ ,  $d_j$  ( $j = 2, 3$ ) as featured in equations (6.4) can be written as

$$a_1(\zeta) = -\cos(\vartheta\zeta) \mathcal{H} - \cos(\vartheta\zeta) - 2t \sin(\vartheta\zeta),$$

$$b_1(\zeta) = -\sin(\vartheta\zeta) \mathcal{H} + \sin(\vartheta\zeta),$$

$$a_2(\zeta) = \cos(\vartheta\zeta) \mathcal{H} + \frac{1}{M} \left\{ (1 + c \, ch + s \, sh) \cosh(\vartheta\zeta) + \right. \\ \left. + s \, ch [\sin(\vartheta\zeta) - \sinh(\vartheta\zeta)] - sh \left[ c \, \sinh(\vartheta\zeta) + \sin \frac{\vartheta(L - 2\zeta)}{2} \right] \right\},$$

$$b_2(\zeta) = -\sin(\vartheta\zeta) \mathcal{H} - \frac{1}{M} \left\{ \sinh(\vartheta\zeta) + s \left[ \cosh \frac{\vartheta(L - 2\zeta)}{2} - ch \cos(\vartheta\zeta) \right] + \right. \\ \left. + sh \cos \frac{\vartheta(L - 2\zeta)}{2} - c \, \sinh \frac{\vartheta(L - 2\zeta)}{2} \right\},$$

$$c_2(\zeta) = -\cosh(\vartheta\zeta) \mathcal{H} - \frac{1}{M} \left\{ \cos(\vartheta\zeta) + ch \left[ \cos \frac{\vartheta(L - 2\zeta)}{2} - s \, \sinh(\vartheta\zeta) \right] + \right. \\ \left. + sh \left[ s \, \cosh(\vartheta\zeta) - c \, \sinh(\vartheta\zeta) - \sin \frac{\vartheta(L - 2\zeta)}{2} \right] \right\},$$

$$d_2(\zeta) = \sinh(\vartheta\zeta) \mathcal{H} - \left\{ sh \left[ c \, \cosh(\vartheta\zeta) + s \, \sinh(\vartheta\zeta) - \cos \frac{\vartheta(L - 2\zeta)}{2} \right] + \right. \\ \left. + ch \left[ \sin \frac{\vartheta(L - 2\zeta)}{2} - s \, \cosh(\vartheta\zeta) \right] - \sin(\vartheta\zeta) \right\},$$

$$a_3 = \frac{s \operatorname{ch} + c \operatorname{sh}}{2M},$$

$$b_3 = \frac{1}{2} - \frac{s \operatorname{sh}}{2M},$$

$$c_3 = -\frac{s \operatorname{ch} + c \operatorname{sh}}{2M},$$

$$d_3 = \frac{1}{2} + \frac{s \operatorname{sh}}{2M},$$

where

$$s = \sin \frac{\vartheta L}{2}, \quad c = \cos \frac{\vartheta L}{2}, \quad t = \operatorname{tg} \frac{\vartheta L}{2},$$

$$\operatorname{sh} = \sinh \frac{\vartheta L}{2}, \quad \operatorname{ch} = \cosh \frac{\vartheta L}{2},$$

$$M = 1 + \cos \frac{\vartheta L}{2} \cosh \frac{\vartheta L}{2}, \quad \mathcal{H} = H(\zeta - x) - H(x - \zeta)$$

and  $H(x)$  is Heaviside function.

# Bibliography

1. J. D. Achenbach. *Wave propagation in elastic solids*, volume 16 of *Applied Mathematics and Mechanics*. North-Holland Publishing Company, Amsterdam, 1973.
2. P. G. Agache, C. Monneur, J. L. Leveque, and J. Rigal. Mechanical properties and Young's modulus of human skin in vivo. *Archives of Dermatological Research*, 269(3):221–232, 1980.
3. T. Agner. Ultrasound a-mode measurement of skin-thickness. In J. Serup and G. B. E. Jemec, editors, *Handbook of non-invasive methods and the skin*, pages 289–292. CRC Press, Boca Raton FL, 1995.
4. D. Agrawal and R. Raj. Measurement of the ultimate shear strength of a metal-ceramic interface. *Acta Metallurgica*, 37(4):1265–1270, 1989.
5. D. C. Agrawal and R. Raj. Ultimate shear strengths of copper-silica and nickel-silica interfaces. *Materials Science and Engineering: A*, 126(1-2):125–131, 1990.
6. M. Ahrens, R. Vaßen, D. Stöver, and S. Lampenscherf. Sintering and creep processes in plasma-sprayed thermal barrier coatings. *Journal of Thermal Spray Technology*, 13(3):432–442, 2004.
7. B. E. Alaca, M. T. A. Saif, and H. Sehitoglu. On the interface debond at the edge of a thin film on a thick substrate. *Acta Materialia*, 50(5):1197–1209, 2002.
8. C. Alexander and T. Cook. Accounting for the natural tension in the mechanical testing of human skin. *The Journal of Investigative Dermatology*, 69(3):310–314, 1977.
9. T. L. Anderson. *Fracture mechanics. Fundamentals and applications*. Taylor & Francis Group, USA, 2005.
10. M. Andritschky, P. Alpuim, D. Stöver, and C. Funke. Study of the mechanics of the delamination of ceramic functional coatings. *Materials Science and Engineering: A*, 271(1-2):62–69, 1999.
11. R. Anton. *Untersuchungen zu den Versagensmechanismen von Wärmedämmschicht-Systemen im Temperaturbereich von 900° C bis 1050° C bei zyklischer Temperaturbelastung*. Dissertation, RWTH Aachen, Germany, 2002.

12. B. Audoly and A. Boudaoud. Buckling of a thin film bound to a compliant substrate – Part I: Formulation, linear stability of cylindrical patterns, secondary bifurcations. *Journal of the Mechanics and Physics of Solids*, 56(7):2401–2421, 2008.
13. B. Audoly and A. Boudaoud. Buckling of a thin film bound to a compliant substrate – Part II: A global scenario for the formation of herringbone pattern. *Journal of the Mechanics and Physics of Solids*, 56(7):2422–2443, 2008.
14. B. Audoly and A. Boudaoud. Buckling of a thin film bound to a compliant substrate – Part III: Herringbone solutions at large buckling parameter. *Journal of the Mechanics and Physics of Solids*, 56(7):2422–2443, 2008.
15. J. Aveston and A. Kelly. Theory of multiple fracture of fibrous composites. *Journal of Materials Science*, 8(3):352–362, 1973.
16. D. Bader and P. Bowker. Mechanical characteristics of skin and underlying tissues in vivo. *Biomaterials*, 4(4):305–308, 1983.
17. J. Barbanel. *Time dependent mechanical properties of skin*. Dissertation, University of Strathclyde, Glasgow, UK, 1979.
18. A. Barel, W. Courage, and P. Clarys. Suction method for measurement of skin mechanical properties: the cutometer. In J. Serup and G. B. E. Jemec, editors, *Handbook of non-invasive methods and the skin*. CRC Press, Boca Raton, 1995.
19. G. Barenblatt. *The mathematical theory of equilibrium cracks in brittle fracture*, volume 7 of *Advances in Applied Mechanics*. Academic Press, New York, 1962.
20. G. Barenblatt. *Scaling*. Cambridge University Press, UK, 2003.
21. T. Beck, M. Białaś, P. Bednarz, L. Singheiser, K. Bobzin, N. Bagcivan, D. Parkot, T. Kashko, J. Petković, B. Hallstedt, S. Nemna, and J. M. Schneider. Modeling of coating process, phase changes, and damage of plasma sprayed thermal barrier coatings on ni-base superalloys. *Advanced Engineering Materials*, 12(3):110–126, 2010.
22. P. Bednarz. *Finite element simulation of stress evolution in thermal barrier coating systems*, volume 60 of *Schriften des Forschungszentrum Jülich, Reihe Energietechnik*. Forschungszentrum Jülich, Germany, 2007.
23. M. Białaś. *Modelowanie rozwoju uszkodzeń w warstwach kontaktowych materiałów*. Dissertation, Institute of Fundamental Technological Research, Warsaw, 2003.
24. M. Białaś. Finite element analysis of stress distribution in thermal barrier coatings. *Surface and Coatings Technology*, 202(24):6002–6010, 2008.
25. M. Białaś. Progressive frictional delamination of an infinite elastic film on a rigid substrate due to in-plane point loading. *Journal of Elasticity*, Accepted. DOI: 10.1007/s10659-011-9360-3.

26. M. Białaś and B. B. Guzina. On the viscoelastic characterization of thin tissues via surface-wave sensing. *International Journal of Solids and Structures*, 48(14-15):2209–2217, 2011.
27. M. Białaś, P. Majerus, R. Herzog, and Z. Mróz. Numerical simulation of segmentation cracking in thermal barrier coatings by means of cohesive zone elements. *Materials Science and Engineering: A*, 412(1-2):241–251, 2005.
28. M. Białaś and Z. Mróz. Modelling of progressive interface failure under combined normal compression and shear stress. *International Journal of Solids and Structures*, 42(15):4436–4467, 2005.
29. M. Białaś and Z. Mróz. Crack patterns in thin layers under temperature loading. Part I: Monotonic loading. *Engineering Fracture Mechanics*, 73(7):917–938, 2006.
30. M. Białaś and Z. Mróz. Crack patterns in thin layers under temperature loading. Part II: Cyclic loading. *Engineering Fracture Mechanics*, 73(7):939–952, 2006.
31. M. Białaś and Z. Mróz. An energy model of segmentation cracking of thin films. *Mechanics of Materials*, 39(9):845–864, 2007.
32. N. Bowden, S. Brittain, A. Evans, J. W. Hutchinson, and G. M. Whitesides. Spontaneous formation of ordered structures in thin films of metals supported on an elastomeric polymer. *Nature*, 393(6681):146–149, 1998.
33. D. Breid and A. J. Crosby. Surface wrinkling behavior of finite circular plates. *Soft Matter*, 5(2):425–431, 2009.
34. W. J. Brindley and J. D. Whittenberger. Stress relaxation of low pressure plasma-sprayed nickel alloys. *Materials Science and Engineering: A*, 163(1):33–41, 1993.
35. E. P. Busso, J. Lin, and S. Sakurai. A mechanistic study of oxidation-induced degradation in a plasma-sprayed thermal barrier coating system. Part II: Life prediction model. *Acta Materialia*, 49(9):1529–1536, 2001.
36. E. P. Busso, J. Lin, S. Sakurai, and M. Nakayama. A mechanistic study of oxidation-induced degradation in a plasma-sprayed thermal barrier coating system. Part I: Model formulation. *Acta Materialia*, 49(9):1515–1528, 2001.
37. M. Caliez, J.-L. Chaboche, F. Feyel, and S. Kruch. Numerical simulation of EBPVD thermal barrier coatings spallation. *Acta Materialia*, 51(4):1133–1141, 2003.
38. M. Caliez, F. Feyel, S. Kruch, and J.-L. Chaboche. Oxidation induced stress fields in an EB-PVD thermal barrier coating. *Surface and Coatings Technology*, 157(2-3):103–110, 2002.
39. G. T. Camacho and M. Ortiz. Computational modelling of impact damage in brittle materials. *International Journal of Solids and Structures*, 33(20-22):2899–2938, 1996.

40. P. P. Camanho and C. G. Dávila. Mixed-mode decohesion finite elements for the simulation of delamination in composite materials. Report TM-2002-211737, NASA, Langley Research Center, Hampton, Virginia, June 2002.
41. R. Capozucca. Experimental FRP/SRP-historic masonry delamination. *Composite Structures*, 92(4):891–903, 2010.
42. S. Catheline, J.-L. Gennisson, G. Delon, M. Fink, R. Sinkus, S. Abouelkaram, and J. Culioli. Measurement of viscoelastic properties of homogeneous soft solid using transient elastography: An inverse problem approach. *The Journal of the Acoustical Society of America*, 116(6):3734–3741, 2004.
43. G. C. Chang, W. Phucharoen, and R. A. Miller. Behavior of thermal barrier coatings for advanced gas turbine blades. *Surface and Coatings Technology*, 30(1):13–28, 1987.
44. B. F. Chen, J. Hwang, I. F. Chen, G. P. Yu, and J.-H. Huang. A tensile-film-cracking model for evaluating interfacial shear strength of elastic film on ductile substrate. *Surface and Coatings Technology*, 126(2-3):91–95, 2000.
45. X. Chen and J. W. Hutchinson. Herringbone buckling patterns of compressed thin films on compliant substrates. *Journal of Applied Mechanics*, 71(5):597–603, 2004.
46. S. Chi and Y.-L. Chung. Cracking in coating-substrate composites with multi-layered and FGM coatings. *Engineering Fracture Mechanics*, 70(10):1227–1243, 2003.
47. Y.-L. Chung and C.-F. Pon. Boundary element analysis of cracked film-substrate media. *International Journal of Solids and Structures*, 38(1):75–90, 2001.
48. D. Clemens, W. J. Quadackers, F. Schubert, and H. Nickel. Einfluss von Si and Ti auf das Oxidationsverhalten von MCrAlY-Legierungen. Report Jül-3444, Forschungszentrum Jülich, 1997.
49. T. Cook, H. Alexander, and M. Cohen. Experimental method for determining the 2-dimensional mechanical properties of living human skin. *Medical and Biological Engineering and Computing*, 15(4):381–390, 1977.
50. A. Cottone and G. Giambanco. Minimum bond length and size effects in FRP-substrate bonded joints. *Engineering Fracture Mechanics*, 76(13):1957–1976, 2009.
51. H. L. Cox. The elasticity and strength of paper and other fibrous materials. *British Journal of Applied Physics*, 3(3):72–78, 1952.
52. J. T. de Masi, K. D. Sheffler, and M. Oritz. Thermal barrier coating live prediction development, Phase I. Contractor Report 182230, NASA, 1989.
53. Deassault Systèmes. *ABAQUS version 6.7, User documentation*, 2007.

54. P. R. Dhar and J. W. Zu. Design of a resonator device for in vivo measurement of regional tissue viscoelasticity. *Sensors and Actuators A: Physical*, 133(1):45–54, 2007.
55. S. Diridollou, M. Berson, V. Vabre, D. Black, B. Karlsson, F. Auriol, J. Gregoire, C. Yvon, L. Vaillant, Y. Gall, and F. Patat. An in vivo method for measuring the mechanical properties of the skin using ultrasound. *Ultrasound in Medicine & Biology*, 24(2):215–224, 1998.
56. D. M. Dobkin and M. K. Zuraw. *Principles of chemical vapor*. Kluwer Academic Publishers, 2003.
57. G. Döpfer, E. Lugscheider, K. Bobezin, and A. Etzkorn. Thermomechanical behaviour of EB-PVD and thermal sprayed thermal barrier coatings. In A. Strang, W. M. Banks, R. D. Conroy, G. M. McColvin, J. C. Neal, and S. Simpson, editors, *Proceedings of the Fifth International Charles Parsons Turbine Conference*, volume 736, pages 733–740, 2000.
58. D. S. Dugdale. Yielding of steel sheets containing slits. *Journal of the Mechanics and Physics of Solids*, 8(2):100–104, 1960.
59. J. Dundurs. Effect of elastic constants on stress in a composite under plane deformation. *Journal of Composite Materials*, 1(3):310–322, 1967.
60. H. Echsler. *Oxidationsverhalten und mechanische Eigenschaften von Wärmedämmschichten und deren Einfluss auf eine Lebensdauervorhersage*. Dissertation, RWTH Aachen, Germany, 2003.
61. C. Escoffier, J. de Rigal, A. Rochefort, R. Vasselet, J. Lévêque, and P. Agache. Age-related mechanical properties of human skin: An in vivo study. *Journal of Investigative Dermatology*, 93(3), 1989.
62. A. G. Evans, M. Y. He, and J. W. Hutchinson. Mechanics-based scaling laws for the durability of thermal barrier coatings. *Progress in Materials Science*, 46(3-4):249–271, 2001.
63. A. G. Evans, D. R. Mumm, J. W. Hutchinson, G. H. Meier, and F. S. Pettit. Mechanisms controlling the durability of thermal barrier coatings. *Progress in Materials Science*, 46(5):505–553, 2001.
64. M. Fatemi and J. F. Greenleaf. Probing the dynamics of tissue at low frequencies with the radiation force of ultrasound. *Physics in Medicine and Biology*, 45(6):1449–1464, 2000.
65. W. N. Findley, J. S. Lai, and K. Onaran. *Creep and relaxation of nonlinear viscoelastic materials*. Dover, New York, 1989.
66. G. Fleury and F. Schubert. *Anisotrope Stoffgesetze für das viskoplastische Verformungsverhalten der einkristallinen Superlegierung CMSX-4*. Dissertation, RWTH Aachen, Germany, 1997.

67. J. Fraden. *Handbook of modern sensors: physics, designs, and applications*. Springer, 2004.
68. A. M. Freborg, B. Ferguson, W. Brindley, and G. Petrus. Modeling oxidation induced stresses in thermal barrier coatings. *Materials Science and Engineering: A*, 245(2):182–190, 1998.
69. L. B. Freund and S. Suresh. *Thin film materials: stress, defect formation, and surface evolution*. Cambridge University Press, 2003.
70. T. Futatsugi, S. Ogawa, M. Takemoto, M. aki Yanaka, and Y. Tsukahara. Integrity evaluation of SiO<sub>x</sub> film on polyethylene terephthalate by AE characterization and laser microscopy. *NDT & E International*, 29(5):307–316, 1996.
71. V. Ganji, N. Gucunski, and S. Nazarian. Automated inversion procedure for spectral analysis of surface waves. *Journal of Geotechnical & Geoenvironmental Engineering*, 124(8):757–770, 1998.
72. F. Gastaldi and D. Kinderlehrer. The partially supported elastic beam. *Journal of Elasticity*, 13(1):71–82, 1983.
73. M. Geerligs. *In vitro mechanical characterization of human skin layers: stratum corneum, epidermis and hypodermis*. Dissertation, Technische Universiteit Eindhoven, Holland, 2006.
74. M. Gell, E. Jordan, K. Vaidyanathan, K. McCarron, B. Barber, Y.-H. Sohn, and V. K. Tolpygo. Bond strength, bond stress and spallation mechanisms of thermal barrier coatings. *Surface and Coatings Technology*, 120-121:53–60, 1999.
75. G. Gioia and M. Ortiz. Delamination of compressed thin films. volume 33 of *Advances in Applied Mechanics*, pages 119–192. Elsevier, 1997.
76. M. Gniadecka and J. Serup. Suction chamber method for measurement of skin mechanical properties: the dermaflex. In J. Serup, B. E. Jemec, and G. L. Grove, editors, *Handbook of non-invasive methods and the skin*, chapter 66, pages 579–582. CRC/Taylor & Francis, Boca Raton FL, 2 edition, 2006.
77. R. Grahame. A method for measuring human skin elasticity in vivo with observations on the effects of age, sex and pregnancy. *Clinical Science*, 39(2):223–229, 1970.
78. E. Grande, M. Imbimbo, and E. Sacco. Bond behaviour of CFRP laminates glued on clay bricks: Experimental and numerical study. *Composites Part B: Engineering*, 42(2):330–340, 2011.
79. B. Gudmundsson and B. E. Jacobson. Structure formation and interdiffusion in vacuum plasma sprayed CoNiCrAlY coatings on IN738LC. *Materials Science and Engineering*, 100:207–217, 1988.
80. H. Guo, R. Vaßen, and D. Stöver. Thermophysical properties and thermal cycling behavior of plasma sprayed thick thermal barrier coatings. *Surface and Coatings Technology*, 192(1):48–56, 2005.

81. B. B. Guzina and A. Lu. Coupled waveform analysis in dynamic characterization of lossy solids. *Journal of Engineering Mechanics*, 128(4):392–402, 2002.
82. B. B. Guzina and A. I. Madyarov. On the spectral analysis of Love waves. *Bulletin of the Seismological Society of America*, 95(3):1150–1169, 2005.
83. B. B. Guzina, K. Tuleubekov, D. Liu, and E. S. Ebbini. Viscoelastic characterization of thin tissues using acoustic radiation force and model-based inversion. *Physics in Medicine and Biology*, 54(1):4089–4112, 2009.
84. U. A. Handge, Y. Leterrier, G. Rochat, I. M. Sokolov, and A. Blumen. Two scaling domains in multiple cracking phenomena. *Physical Review E*, 62(6):7807–7810, 2000.
85. U. A. Handge, I. M. Sokolov, and A. Blumen. Disorder and plasticity in the fragmentation of coatings. *Physical Review E*, 64(1):106–109, 2001.
86. J. A. Haynes, E. D. Rigney, M. K. Ferber, and W. D. Porter. Oxidation and degradation of a plasma-sprayed thermal barrier coating system. *Surface and Coatings Technology*, 86-87(1):102–108, 1996.
87. M.-Y. He, A. G. Evans, and J. W. Hutchinson. The ratcheting of compressed thermally grown thin films on ductile substrates. *Acta Materialia*, 48(10):2593–2601, 2000.
88. M.-Y. He and J. W. Hutchinson. Kinking of a crack out of an interface. *Journal of Applied Mechanics*, 56(2):270–278, 1989.
89. S. Heckmann, R. Herzog, R. Steinbrech, F. Schubert, and L. Singheiser. Viscoplastic properties of separated thermal barrier coatings under compression loading. In *Proceedings of the 7th Liege Conference 2002, 30 September - 2 October 2002, Liège, Belgium*, volume 21 of *Materials for Advanced Power Engineering*, pages 561–568, 2002.
90. J. S. Heisey, K. Stokoe II, and A. Meyer. Moduli of pavement systems from spectral analysis of surface waves. *Transportation Research Record*, 852:22–31, 1982.
91. S. S. Herman, H. and R. McCune. Thermal spray: current status and future trends. *MRS Bulletin*, 25(7):17–25, 2000.
92. B. Holt, A. Tripathi, and J. Morgan. Viscoelastic response of human skin to low magnitude physiologically relevant shear. *Journal of Biomechanics*, 41(12):2689–2695, 2008.
93. C.-H. Hsueh. Analyses of multiple film cracking in film/substrate systems. *Journal of the American Ceramic Society*, 84(12):2955–2961, 2001.
94. C.-H. Hsueh and E. Fuller Jr. Analytical modeling of oxide thickness effects on residual stresses in thermal barrier coatings. *Scripta Materialia*, 42(8):781–787, 2000.

95. C.-H. Hsueh and E. R. Fuller Jr. Residual stresses in thermal barrier coatings: effects of interface asperity curvature/height and oxide thickness. *Materials Science and Engineering: A*, 283(1-2):46–55, 2000.
96. C.-H. Hsueh and M. Yanaka. Multiple film cracking in film/substrate systems with residual stresses and unidirectional loading. *Journal of Materials Science*, 38(8):1809–1817, 2003.
97. M. S. Hu and A. G. Evans. The cracking and decohesion of thin films on ductile substrates. *Acta Metallurgica*, 37(3):917–925, 1989.
98. W. T. S. Huck, N. Bowden, P. Onck, T. Pardoen, J. W. Hutchinson, and G. M. Whitesides. Ordering of spontaneously formed buckles on planar surfaces. *Langmuir*, 16(7):3497–3501, 2000.
99. J. W. Hutchinson, M. Y. He, and A. G. Evans. The influence of imperfections on the nucleation and propagation of buckling driven delaminations. *Journal of the Mechanics and Physics of Solids*, 48(4):709–734, 2000.
100. J. W. Hutchinson and Z. Suo. Mixed mode cracking in layered materials. volume 29 of *Advances in Applied Mechanics*, pages 63–191. Elsevier, 1991.
101. I. V. Ivanov. Analysis, modelling, and optimization of laminated glasses as plane beam. *International Journal of Solids and Structures*, 43(22-23):6887–6907, 2006.
102. W. D. James, T. Berger, and D. Elston. *Andrews' diseases of the skin: clinical dermatology*. Elsevier-Saunders, 2006.
103. M. Jinnestrand and S. Sjöström. Investigation by 3D FE simulations of delamination crack initiation in TBC caused by alumina growth. *Surface and Coatings Technology*, 135(2-3):188–195, 2001.
104. S. Kärki, J. Lekkala, H. Kuokkanen, and J. Halttunen. Development of a piezoelectric polymer film sensor for plantar normal and shear stress measurements. *Sensors and Actuators A: Physical*, 154(1):57–64, 2009.
105. A. M. Karlsson and A. Evans. A numerical model for the cyclic instability of thermally grown oxides in thermal barrier systems. *Acta Materialia*, 49(10):1793–1804, 2001.
106. A. M. Karlsson, J. W. Hutchinson, and A. G. Evans. A fundamental model of cyclic instabilities in thermal barrier systems. *Journal of the Mechanics and Physics of Solids*, 50(8):1565–1589, 2002.
107. A. Kelly. *Strong Solids*. Clarendon Press, Oxford, 1966.
108. A. Kelly and W. R. Tyson. Tensile properties of fibre-reinforced metals: Copper/tungsten and copper/molybdenum. *Journal of the Mechanics and Physics of Solids*, 13(6):329–350, 1965.
109. S.-R. Kim and J. A. Nairn. Fracture mechanics analysis of coating/substrate systems. Part I: Analysis of tensile and bending experiments. *Engineering Fracture Mechanics*, 65(5):573–593, 2000.

110. S.-R. Kim and J. A. Nairn. Fracture mechanics analysis of coating/substrate systems. Part II: Experiments in bending. *Engineering Fracture Mechanics*, 65(5):595–607, 2000.
111. S. J. Kirkpatrick, D. D. Duncan, and L. Fang. Low-frequency surface wave propagation and the viscoelastic behavior of porcine skin. *Journal of Biomedical Optics*, 9(6):1311–1319, 2004.
112. S. C. Ko, Y. C. Kim, S. S. Lee, S. H. Choi, and S. R. Kim. Micromachined piezoelectric membrane acoustic device. *Sensors and Actuators A: Physical*, 103(1-2):130–134, 2003.
113. K. Kokini and Y. R. Takeuchi. Multiple surface thermal fracture of graded ceramic coatings. *Journal of Thermal Stresses*, 21(7):715–725, 1998.
114. J. Korelc. Automatic generation of finite-element code by simultaneous optimization of expressions. *Theoretical Computer Science*, 187(1-2):231–248, 1997.
115. J. Korelc. Multi-language and multi-environment generation of nonlinear finite element codes. *Engineering with Computers*, 18(4):312–327, 2002.
116. J. Korelc. AceFEM. Mathematica finite element environment, 2009. Available at <http://www.fgg.uni-lj.si/Symech/>.
117. S. A. Kruse, J. A. Smith, A. J. Lawrence, M. A. Dresner, A. Manduca, J. F. Greenleaf, and R. L. Ehman. Tissue characterization using magnetic resonance elastography: preliminary results. *Physics in Medicine and Biology*, 45(6):1579–1590, 2000.
118. C. G. Lai and G. J. Rix. Solution of the Rayleigh eigenproblem in viscoelastic media. *Bulletin of the Seismological Society of America*, 92(6):2297–2309, 2002.
119. K. Langer. Zur Anatomie und Physiologie der haut. i. über der Spaltbarkeit der Cutis. *Sitzungsbericht der Akademie der Wissenschaften in Wien*, 44(19–46), 1861.
120. N. Laws and G. J. Dvorak. Progressive transverse cracking in composite laminates. *Journal of Composite Materials*, 22(10):900–916, 1988.
121. C.-C. Lee, Q. Guo, G. Cao, and I. Shen. Effect of electrode size and silicon residue on piezoelectric thin-film membrane actuators. *Sensors and Actuators A: Physical*, 147(1):279–285, 2008.
122. C. K. Lee. Theory of laminated piezoelectric plates for the design of distributed sensors/actuators. Part I: Governing equations and reciprocal relationships. *The Journal of the Acoustical Society of America*, 87(3):1144–1158, 1990.
123. W. S. Lee and S. S. Lee. Piezoelectric microphone built on circular diaphragm. *Sensors and Actuators A: Physical*, 144(2):367–373, 2008.
124. Y. Leterrier, J. Andersons, Y. Pitton, and J.-A. E. Månson. Adhesion of silicon oxide layers on poly(ethylene terephthalate). II: Effect of coating thickness on

- adhesive and cohesive strengths. *Journal of Polymer Science Part B: Polymer Physics*, 35(9):1463–1472, 1997.
125. Y. Leterrier, L. Boogh, J. Andersons, and J.-A. E. Månson. Adhesion of silicon oxide layers on poly(ethylene terephthalate). I: Effect of substrate properties on coating's fragmentation process. *Journal of Polymer Science Part B: Polymer Physics*, 35(9):1449–1461, 1997.
  126. D. Liu and E. Ebbini. Viscoelastic property measurement in thin tissue constructs using ultrasound. *IEEE Transactions on Ultrasonics, Ferroelectrics and Frequency Control*, 55(2):368–383, 2008.
  127. O. Lokshin and Y. Lanir. Micro and macro rheology of planar tissues. *Biomaterials*, 30(17):3118–3127, 2009.
  128. T. J. Lu, A. G. Evans, and J. W. Hutchinson. The effects of material properties on heat dissipation in high power electronics. *Journal of Electronic Packaging*, 120(3):280–289, 1998.
  129. X. Q. Ma, S. Cho, and M. Takemoto. Acoustic emission source analysis of plasma sprayed thermal barrier coatings during four-point bend tests. *Surface and Coatings Technology*, 139(1):55–62, 2001.
  130. J. E. Mahan. *Physical vapor deposition of thin films*. John Wiley & Sons, New York, 2000.
  131. P. Majerus. Report on thermal barrier coatings. Technical report, Center of Excellence AMAS, Warsaw, 2002.
  132. P. Majerus. *Neue Verfahren zur Analyse des Verformungs- und Schädigungsverhaltens von MCrAlY-Schichten im Wärmedämmschichtsystem*, volume 34 of *Schriften des Forschungszentrum Jülich, Reihe Energietechnik*. Forschungszentrum Jülich, Germany, 2004.
  133. A. K. Mal. Guided waves in layered solids with interface zones. *International Journal of Engineering Science*, 26(8):873–881, 1988.
  134. B. M. Malyshev and R. L. Salganik. The strength of adhesive joints using the theory of cracks. *International Journal of Fracture*, 1(2):114–128, 1965.
  135. J. Manschot. *The mechanical properties of human skin in vivo*. Dissertation, Catholic University of Nijmegen, Holland, 1985.
  136. M. Martena, D. Botto, P. Fino, S. Sabbadini, M. M. Gola, and C. Badini. Modelling of TBC system failure: Stress distribution as a function of tgo thickness and thermal expansion mismatch. *Engineering Failure Analysis*, 13(3):409–426, 2006.
  137. A. P. McGuigan, G. A. D. Briggs, V. Burlakov, M. Yanaka, and Y. Tsukahara. An elastic-plastic shear lag model for fracture of layered coatings. *Thin Solid Films*, 424(2):219–223, 2003.

138. J.-M. Miao and C.-Y. Wu. Numerical approach to hole shape effect on film cooling effectiveness over flat plate including internal impingement cooling chamber. *International Journal of Heat and Mass Transfer*, 49(5-6):919–938, 2006.
139. P. Michlik and C. Berndt. Image-based extended finite element modeling of thermal barrier coatings. *Surface and Coatings Technology*, 201(6):2369–2380, 2006.
140. R. A. Miller and C. E. Lowell. Failure mechanisms of thermal barrier coatings exposed to elevated temperatures. *Thin Solid Films*, 95(3):265–273, 1982.
141. S. Moriya, Y. Kuroda, M. Sato, M. Tadano, A. Moro, and M. Nino. Research on the application of PSZ/Ni FGM thermal barrier coating to the combustion chamber (Damage conditions of TBC and its mechanism). *Materials Science Forum*, 308-311:410–415, 1999.
142. Z. Mróz and M. Białas. A simplified analysis of interface failure under compressive normal stress and monotonic or cyclic shear loading. *International Journal for Numerical and Analytical Methods in Geomechanics*, 29(4):337–368, 2005.
143. S. Muralidhar, A. Jagota, S. J. Bennison, and S. Saigal. Mechanical behaviour in tension of cracked glass bridged by an elastomeric ligament. *Acta Materialia*, 48(18-19):4577–4588, 2000.
144. J. A. Nairn. The strain energy release rate of composite microcracking: a variational approach. *Journal of Composite Materials*, 23(11):1106–1129, 1989.
145. J. A. Nairn and K. Sung-Ryong. A fracture mechanics analysis of multiple cracking in coatings. *Engineering Fracture Mechanics*, 42(1):195–208, 1992.
146. K. R. Nightingale, M. L. Palmeri, R. W. Nightingale, and G. E. Trahey. On the feasibility of remote palpation using acoustic radiation force. *The Journal of the Acoustical Society of America*, 110(1):625–634, 2001.
147. J. Nocedal and S. J. Wright. *Numerical optimization*. Springer, New York, 1999.
148. G. Odland. Structure of the skin. In L. A. Goldsmith, editor, *Physiology, biochemistry and molecular biology of the skin*. Oxford University Press, 1991.
149. M. Ohring. *The materials science of thin films*. Academic Press, San Diego, 1992.
150. J. Ophir, I. Céspedes, H. Ponnekanti, Y. Yazdi, and X. Li. Elastography: A quantitative method for imaging the elasticity of biological tissues. *Ultrasonic Imaging*, 13(2):111–134, 1991.
151. N. S. Ottosen and M. Ristinmaa. *The mechanics of constitutive modeling*. Elsevier, 2005.
152. D. Ouis. Combination of a standard viscoelastic model and fractional derivative calculus to the characterization of polymers. *Materials Research Innovations*, 7(1):42–46, 2003.

153. R. Y. S. Pak and B. B. Guzina. Three-dimensional Green's functions for a multi-layered half-space in displacement potentials. *Journal of Engineering Mechanics*, 128(4):449–461, 2002.
154. A. C. Palmer and J. R. Rice. The growth of slip surfaces in the progressive failure of over-consolidated clay. *Proceedings of the Royal Society of London A*, 332(1591):527–548, 1973.
155. Y. Pan, E. Lankenau, J. Welzel, R. Birngruber, and R. Engelhardt. Optical coherence gated imaging of biological tissues. *IEEE Journal of Selected Topics in Quantum Electronics*, 2(4):1029–1034, 1996.
156. A. Pandolfi, P. R. Guduru, M. Ortiz, and A. J. Rosakis. Three dimensional cohesive-element analysis and experiments of dynamic fracture in C300 steel. *International Journal of Solids and Structures*, 37(27):3733–3760, 2000.
157. C. B. Park, R. D. Miller, and J. Xia. Multichannel analysis of surface waves (MASW). *Geophysics*, 64(3):800–808, 1999.
158. C. B. Park, R. D. Miller, J. Xia, and J. Ivanov. Multichannel analysis of surface waves (MASW)—active and passive methods. *The Leading Edge*, 26(1):60–64, 2007.
159. A. P. Parker. Stability of arrays of multiple edge cracks. *Engineering Fracture Mechanics*, 62(6):577–591, 1999.
160. P. N. Patel, C. K. Smith, and C. W. Patrick. Rheological and recovery properties of poly(ethylene glycol) diacrylate hydrogels and human adipose tissue. *Journal of Biomedical Materials Research Part A*, 73A(3):313–319, 2005.
161. M.-J. Pindera, J. Aboudi, and S. M. Arnold. The effect of interface roughness and oxide film thickness on the inelastic response of thermal barrier coatings to thermal cycling. *Materials Science and Engineering: A*, 284(1-2):158–175, 2000.
162. M.-J. Pindera, J. Aboudi, and S. M. Arnold. Analysis of spallation mechanism in thermal barrier coatings with graded bond coats using the higher-order theory for FGMs. *Engineering Fracture Mechanics*, 69(14-16):1587–1606, 2002.
163. D. B. Plewes, J. Bishop, A. Samani, and J. Sciarretta. Visualization and quantification of breast cancer biomechanical properties with magnetic resonance elastography. *Physics in Medicine and Biology*, 45(6):1591–1610, 2000.
164. A. Preumont. *Mechatronics: dynamics of electromechanical and piezoelectrical systems*. Springer, Dordrecht, 2006.
165. W. J. Quadackers, A. K. Tyagi, D. Clemens, R. Anton, and L. Singheiser. The significance of bond coat oxidation for the life of TBC coatings. In J. M. Hampikian and N. B. Dahorte, editors, *Proceedings of the Symposium on High Temperature Coatings III, TMS Annual Meeting, San Diego, CA, USA, 28 Feb.-4 Mar. 1999*, volume 3 of *Elevated temperature coatings: Science and technology*, pages 119–130, 1999.

166. M. Rajadhyaksha and J. Zavislan. Confocal laser microscope images tissue in vivo. *Laser Focus World*, 3(2):119–128, 1997.
167. S. Rangaraj and K. Kokini. Estimating the fracture resistance of functionally graded thermal barrier coatings from thermal shock tests. *Surface and Coatings Technology*, 173(2-3):201–212, 2003.
168. S. Rangaraj and K. Kokini. Interface thermal fracture in functionally graded zirconia-mullite-bond coat alloy thermal barrier coatings. *Acta Materialia*, 51(1):251–267, 2003.
169. S. Rangaraj and K. Kokini. A study of thermal fracture in functionally graded thermal barrier coatings using a cohesive zone model. *Journal of Engineering Materials and Technology*, 126(1):103–115, 2004.
170. J. R. Rice. Elastic fracture mechanics concepts for interfacial cracks. *Journal of Applied Mechanics*, 55(1):98–103, 1988.
171. D. Rigney, R. Viguie, D. Wortman, and D. Skelly. PVD thermal barrier coating applications and process development for aircraft engines. *Journal of Thermal Spray Technology*, 6(2):167–175, 1997.
172. J. C. J. Schellekens and R. de Borst. On the numerical integration of interface elements. *International Journal for Numerical Methods in Engineering*, 36(1):43–66, 1993.
173. U. T. Schmidt, O. Vöhringer, and D. Löhe. The creep damage behavior of the plasma-sprayed thermal barrier coating system NiCr22Co12Mo9-NiCoCrAlY-ZrO<sub>2</sub>/7%Y<sub>2</sub>O<sub>3</sub>. *Journal of Engineering for Gas Turbines and Power*, 121(4):678–682, 1999.
174. H. L. Schreyer and A. Peffer. Fiber pullout based on a one-dimensional model of decohesion. *Mechanics of Materials*, 32(12):821–836, 2000.
175. F. Schubert, G. Fleuri, and T. Steinhaus. Modelling of the mechanical behaviour of the single-crystal alloy CMSX-4 during thermomechanical loading. *Modelling and Simulation in Materials Science and Engineering*, 8(6):947–957, 2000.
176. U. Schulz, M. Menzbach, C. Leyens, and Y. Yang. Influence of substrate material on oxidation behavior and cyclic lifetime of EB-PVD TBC systems. *Surface and Coatings Technology*, 146-147(0):117–123, 2001.
177. G. W. Schulze and F. Erdogan. Periodic cracking of elastic coatings. *International Journal of Solids and Structures*, 35(28-29):3615–3634, 1998.
178. D. Schwingel, R. Taylor, T. Haubold, J. Wigren, and C. Gualco. Mechanical and thermophysical properties of thick PYSZ thermal barrier coatings: correlation with microstructure and spraying parameters. *Surface and Coatings Technology*, 108-109(0):99–106, 1998.

179. A. Selvadurai and K. Willner. Surface-stiffened elastic halfspace under the action of a horizontally directed Mindlin force. *International Journal of Mechanical Sciences*, 48(10):1072–1079, 2006.
180. A. P. S. Selvadurai, N. Kringos, and A. Scarpas. Bond stress development at a surface coating-substrate interface due to the action of a nucleus of thermo-elastic strain. *Surface and Coatings Technology*, 202(9):1704–1711, 2008.
181. J. Serup, J. Keiding, A. Fullerton, M. Gniadecka, and R. Gniadecki. High-frequency ultrasound examination of the skin: Introduction and guide. In J. Serup, B. E. Jemec, and G. L. Grove, editors, *Handbook of non-invasive methods and the skin*, chapter 56, pages 473–492. CRC/Taylor & Francis, Boca Raton FL, 2 edition, 2006.
182. K. Sfar, J. Aktaa, and D. Munz. Numerical investigation of residual stress fields and crack behavior in TBC systems. *Materials Science and Engineering: A*, 333(1-2):351–360, 2002.
183. C. Sheppard and D. Shotton. *Confocal laser scanning microscopy*. Microscopy handbooks. BIOS Scientific, 1997.
184. F.-S. Shieu, R. Raj, and S. Sass. Control of the mechanical properties of metal-ceramic interfaces through interfacial reactions. *Acta Metallurgica et Materialia*, 38(11):2215–2224, 1990.
185. N. Sridhar, D. J. Srolovitz, and Z. Suo. Kinetics of buckling of a compressed film on a viscous substrate. *Applied Physics Letters*, 78(17):2482–2484, 2001.
186. J. Stockfleth, L. Salamon, and G. Hinrichsen. On the deformation mechanisms of oriented PET and PP films under load. *Colloid & Polymer Science*, 271(5):423–435, 1993. 10.1007/BF00657386.
187. Z. Suo. Singularities, interfaces and cracks in dissimilar anisotropic media. *Proceedings of the Royal Society of London A*, 427(1873):321–358, 1990.
188. A. Suzuki and K. Nakayama. Mechanical impedance of soft living tissue based on the model of an oscillating disc on a semi-infinite viscoelastic medium. *Japanese Journal of Medical Electronics and Biological Engineering*, 37(3):243–249, 1999.
189. M. Taniwaki, T. Hanada, and N. Sakurai. Device for acoustic measurement of food texture using a piezoelectric sensor. *Food Research International*, 39(10):1099–1105, 2006.
190. J.-F. Thimus, Y. Abousleiman, A.-D. Cheng, O. Coussy, and E. Detournay, editors. *Poromechanics - A Tribute to Maurice A. Biot, Proceedings of the Biot Conference on Poromechanics, Louvain-la-Neuve, Belgium, 14-16 September 1998*, Rotterdam, 1998. A. A. Balkema.
191. T. B. Thoe, D. K. Aspinwall, and N. Killey. Combined ultrasonic and electrical discharge machining of ceramic coated nickel alloy. *Journal of Materials Processing Technology*, 92-93(0):323–328, 1999.

192. M. D. Thouless. Crack spacing in brittle films on elastic substrates. *Journal of the American Ceramic Society*, 73(7):2144–2146, 1990.
193. M. D. Thouless and A. G. Evans. Comment on the spalling and edge-cracking of plates. *Scripta Metallurgica et Materialia*, 24(8):1507–1510, 1990.
194. M. D. Thouless, A. G. Evans, M. F. Ashby, and J. W. Hutchinson. The edge cracking and spalling of brittle plates. *Acta Metallurgica*, 35(6):1333–1341, 1987.
195. M. D. Thouless, E. Olsson, and A. Gupta. Cracking of brittle films on elastic substrates. *Acta Metallurgica et Materialia*, 40(6):1287–1292, 1992.
196. G. Thurn, G. A. Schneider, H.-A. Bahr, and F. Aldinger. Toughness anisotropy and damage behavior of plasma sprayed ZrO<sub>2</sub> thermal barrier coatings. *Surface and Coatings Technology*, 123(2-3):147–158, 2000.
197. M. G. A. Tijssens, B. L. J. Sluys, and E. van der Giessen. Numerical simulation of quasi-brittle fracture using damaging cohesive surfaces. *European Journal of Mechanics - A/Solids*, 19(5):761–779, 2000.
198. D. H. Timm, B. B. Guzina, and V. R. Voller. Prediction of thermal crack spacing. *International Journal of Solids and Structures*, 40(1):125–142, 2003.
199. S. P. Timoshenko and J. N. Goodier. *Theory of Elasticity*. Engineering Societies Monographs. McGraw-Hill Inc., 1951.
200. O. Trunova. *Effect of thermal and mechanical loadings on the degradation and failure modes of APS TBCs*. Dissertation, RWTH Aachen, Germany, 2006.
201. O. Trunova, R. Herzog, T. Wakui, R. W. Steinbrech, E. Wessel, and L. Singheiser. Micromechanisms affecting macroscopic deformation of plasma-sprayed TBCs. In *Proceedings of 28th International Conference on Advanced Ceramics and Composites, 21-27 January 2004, Cocoa Beach, USA*, volume 25 of *Ceramic Engineering and Science Proceedings*, pages 411–416, 2004.
202. E. Tzimas, H. Müllejans, S. Peteves, J. Bressers, and W. Stamm. Failure of thermal barrier coating systems under cyclic thermomechanical loading. *Acta Materialia*, 48(18-19):4699–4707, 2000.
203. P. Ueberschlag. PVDF piezoelectric polymer. *Sensor Review*, 21(2):118–126, 2001.
204. M. Ventre, F. Mollica, and P. A. Netti. The effect of composition and microstructure on the viscoelastic properties of dermis. *Journal of Biomechanics*, 42(4):430–435, 2009.
205. A. Vexler, I. Polyansky, and R. Gorodetsky. Evaluation of skin viscoelasticity and anisotropy by measurement of speed of shear wave propagation with viscoelasticity skin analyzer. *Journal of Investigative Dermatology*, 113(5):732–739, 1999.

206. D. Vlasblom. *Skin elasticity*. Dissertation, Catholic University of Utrecht, Holland, 1967.
207. K. T. Voisey and T. Clyne. Laser drilling of cooling holes through plasma sprayed thermal barrier coatings. *Surface and Coatings Technology*, 176(3):296–306, 2004.
208. C. Wagner. Beitrag zur theorie des anlaufsvorganges. *Zeitschrift für Physikalische Chemie B*, 21(1-2):25–41, 1933.
209. S. Wagner, S. P. Lacour, J. Jones, P.-H. I. Hsu, J. C. Sturm, T. Li, and Z. Suo. Electronic skin: architecture and components. *Physica E: Low-dimensional Systems and Nanostructures*, 25(2-3):326–334, 2004.
210. W. A. B. Wan Abas and J. C. Barbenel. Uniaxial tension test of human skin in vivo. *Journal of Biomedical Engineering*, 4(1):65–71, 1982.
211. J. Welzel, E. Lankenau, R. Birngruber, and R. Engelhardt. Optical coherence tomography of the human skin. *Journal of the American Academy of Dermatology*, 37(6):958–963, 1997.
212. M. L. Williams. The stress around a fault or crack in dissimilar media. *Bulletin of the Seismological Society of America*, 49(2):199–204, 1959.
213. S. A. Wissing and R. H. Müller. The influence of solid lipid nanoparticles on skin hydration and viscoelasticity - in vivo study. *European Journal of Pharmaceutics and Biopharmaceutics*, 56(1):67–72, 2003.
214. Wolfram Research, Inc., Champaign, IL. *Mathematica Version 6.0*, 2007.
215. P. K. Wright and A. G. Evans. Mechanisms governing the performance of thermal barrier coatings. *Current Opinion in Solid State and Materials Science*, 4(3):255–265, 1999.
216. J. Z. Wu, R. G. Cutlip, D. Welcome, and R. G. Dong. Estimation of the viscous properties of skin and subcutaneous tissue in uniaxial stress relaxation tests. *Bio-Medical Materials and Engineering*, 16(1):53–66, 2006.
217. J. Xia, R. D. Miller, C. B. Park, and G. Tian. Determining  $q$  of near-surface materials from Rayleigh waves. *Journal of Applied Geophysics*, 51(2-4):121–129, 2002.
218. J. Xia, R. D. Miller, C. B. Park, and G. Tian. Inversion of high frequency surface waves with fundamental and higher modes. *Journal of Applied Geophysics*, 52(1):45–57, 2003.
219. C. Xie and W. Tong. Cracking and decohesion of a thin  $\text{Al}_2\text{O}_3$  film on a ductile Al-5%Mg substrate. *Acta Materialia*, 53(2):477–485, 2005.
220. T. Xu, M. Y. He, and A. G. Evans. A numerical assessment of the durability of thermal barrier systems that fail by ratcheting of the thermally grown oxide. *Acta Materialia*, 51(13):3807–3820, 2003.

221. T. Xydeas, K. Siegmann, R. Sinkus, U. Krainick-Strobel, S. Miller, and C. D. Claussen. Magnetic resonance elastography of the breast : Correlation of signal intensity data with viscoelastic properties. *Investigative Radiology*, 40(7):412–420, 2005.
222. M. Yanaka, Y. Kato, Y. Tsukahara, and N. Takeda. Effects of temperature on the multiple cracking progress of sub-micron thick glass films deposited on a polymer substrate. *Thin Solid Films*, 355-356:337–342, 1999.
223. M. Yanaka, T. Miyamoto, Y. Tsukahara, and N. Takeda. In situ observation and analysis of multiple cracking phenomena in thin glass layers deposited on polymer films. *Composite Interfaces*, 6(5):409–424, 1998.
224. M. Yanaka, Y. Tsukahara, N. Nakaso, and N. Takeda. Cracking phenomena of brittle films in nanostructure composites analysed by a modified shear lag model with residual strain. *Journal of Materials Science*, 33(8):2111–2119, 1998.
225. H. Yuan and J. Chen. Computational analysis of thin coating layer failure using a cohesive model and gradient plasticity. *Engineering Fracture Mechanics*, 70(14):1929–1942, 2003.
226. H. Yuan, J. G. Teng, R. Seracino, Z. S. Wu, and J. Yao. Full-range behavior of FRP-to-concrete bonded joints. *Engineering Structures*, 26(5):553–565, 2004.
227. A. Zemtsov. Nuclear magnetic resonance (NMR) examination of the skin. In J. Serup and G. B. E. Jemec, editors, *Handbook of non-invasive methods and the skin*. CRC Press, Boca Raton FL, 1995.
228. G. Zhang. Evaluating the viscoelastic properties of biological tissues in a new way. *Journal of Musculoskeletal and Neuronal Interactions*, 5(1):85–90, 2005.
229. T.-Y. Zhang and M.-H. Zhao. Equilibrium depth and spacing of cracks in a tensile residual stressed thin film deposited on a brittle substrate. *Engineering Fracture Mechanics*, 69(5):589–596, 2002.
230. X. Zhang, R. R. Kinnick, M. R. Pittelkow, and J. F. Greenleaf. Skin viscoelasticity with surface wave method. In *2008 IEEE International Ultrasonics Symposium*, pages 651–653, 2008.
231. F. Zhou and J. F. Molinari. Dynamic crack propagation with cohesive elements: a methodology to address mesh dependency. *International Journal for Numerical Methods in Engineering*, 59(1):1–24, 2004.
232. F. Zhou and J.-F. Molinari. Stochastic fracture of ceramics under dynamic tensile loading. *International Journal of Solids and Structures*, 41(22-23):6573–6596, 2004.
233. Y. C. Zhou, T. Tonomori, A. Yoshida, L. Liu, G. Bignall, and T. Hashida. Fracture characteristics of thermal barrier coatings after tensile and bending tests. *Surface and Coatings Technology*, 157(2-3):118–127, 2002.



# Mechaniczne modelowanie cienkich warstw

## Streszczenie

Cienkie warstwy znajdują zastosowanie w wielu gałęziach techniki. Odnajdujemy je w układach scalonych, czyli w każdym komputerze. Tutaj przewodzenie ładunków elektrycznych jest w dużej mierze zależne od rodzaju powierzchni kontaktowych na granicy cienkich warstw materiałów o różnych właściwościach elektrycznych i mechanicznych (Freund i Suresh [69], Lu i współpracownicy [128]). Kolejnym przykładem zastosowania cienkich warstw są pokrycia elementów turbin gazowych, na przykład ich łopatki (Evans i współpracownicy [62, 63]). Izolacja, wykonana z bardzo porowatej ceramiki o małej przewodności cieplnej, odgrywa tutaj istotną rolę, chroniąc właściwy materiał łopatki przed temperaturami znacznie przewyższającymi jego temperaturę topnienia oraz zapewniając ochronę przed czynnikami korozyjnymi. Wiąże się z tym istotny aspekt ekonomiczny, zastosowanie warstw izolacji termicznej pozwala bowiem na wydłużenie całkowitego okresu pracy turbiny oraz prowadzi do zwiększenia jej wydajności. Szczególnie materiały o zmieniających się właściwościach mechanicznych i termicznych po grubości pokrycia odgrywają coraz ważniejszą rolę w tego rodzaju zastosowaniach. Należy wymienić tutaj pokrycia wielowarstwowe (po angielsku *multi-layered*), gdzie zmiana cech mechaniczno-termicznych jest skokowa po grubości oraz te, gdzie jest ona ciągła (Pindera i współpracownicy [161, 162]). Te drugie noszą raczej niefortunną w języku polskim nazwę materiałów gradientowych (po angielsku *graded materials*). Cienką warstwą jest także ludzka skóra, dlatego mechanika cienkich warstw znajduje także swoje zastosowanie w tych dziedzinach techniki lub nauki, których nazwa zaczyna się przedrostkiem bio- (Białas i Guzina [26]). W szczególności odgrywa rolę w diagnostyce komórek nowotworowych (w sensie mechanicznym są one sztywniejsze od komórek zdrowych) oraz przy produkcji sztucznej skóry (Wag-

ner i współpracownicy [209]).

Czas użytkowania elementów maszyn lub konstrukcji szczególnie narażonych na ścieranie w wyniku kontaktu z otoczeniem może być znacznie zwiększony właśnie poprzez zastosowanie na nich cienkich pokryć. Należy tutaj wymienić dyski komputerowe wykorzystujące zjawisko magnetyzmu lub sztuczne implanty bioder lub kolan (Freund i Suresh [69]). Niewielka grubość cienkich warstw odgrywa istotne znaczenie w innych gałęziach techniki. Polimerowe filmy wykorzystuje się przy produkcji laminowanych szyb — łączą one ze sobą elementy szklane (Ivanov [101], Muralidhar i współpracownicy [143]). Ten sam materiał, ale dodatkowo zbrojony włóknami, wykorzystuje się w budownictwie do wzmocnienia uszkodzonych elementów konstrukcyjnych (Cottone i Giambanco [50]).

Pierwszym wnioskiem jaki nasuwa się po przejrzaniu powyższej listy jest stwierdzenie, że rolą cienkich warstw nie jest przenoszenie dużych obciążeń, powiedzielibyśmy, że nie pełnią one roli nośnej. W większości przypadków tak rzeczywiście jest, spełniają one jedynie zadanie ochronne. Mimo to, w wielu sytuacjach sam sposób ich produkcji powoduje wytworzenie dużych naprężeń początkowych, które w połączeniu z tymi, które wywołuje obciążona konstrukcja, mogą prowadzić do uszkodzenia warstwy. Najczęściej spotykane rodzaje uszkodzeń to pęknięcia po grubości lub odspajanie warstwy. Ich obecność może oznaczać całkowitą bezużyteczność elementu, który warstwa ma chronić.

Konstrukcja, której rozmiar w jednym kierunku jest znacznie mniejszy niż w dwóch pozostałych to w mechanice konstrukcji płyta lub powłoka. Najważniejsza różnica, która pojawia się jednak, gdy mamy na myśli cienką warstwę polega na tym, że nie możemy tutaj pominąć materiału, który znajduje się pod nią i efektu, który on wywołuje. W wielu przypadkach nie jest nawet możliwe, aby wykonać eksperyment z samą cienką warstwą, a trudności związane są najczęściej z jej znikomą grubością. Chcąc modelować mechaniczne zachowanie się warstwy, wykorzystujemy pojęcie powierzchni kontaktowej, to jest powierzchni łączącej warstwę z podłożem. Dla tego obszaru definiujemy cechy mechaniczne, które oddają specyficzny charakter połączenia dwóch różnych materiałów warstwy i podłoża.

Celem rozprawy jest opracowanie różnych metod mechanicznej analizy cienkich warstw ze szczególnym uwzględnieniem opisu stanu naprężenia, wywołanego nim rozwoju uszkodzeń (pęknięcie po grubości warstwy oraz jej odspajanie) oraz identyfikacji cech mechanicznych warstwy. Przyjęte modelowanie opiera się o mechanikę kontynuálną ciała stałego i nie uwzględnia efektów wywołanych *explicite* analizą ziaren, dyslokacji lub wtrąceń obecnych w cienkim filmie. Typowy rząd grubości warstw omawianych w pracy to  $0.5 \mu\text{m} - 2 \text{ mm}$ . Jedynie proces pęknięcia segmentacyjnego opisany w Rozdziale 3 dotyczy warstw znacznie

cieńszych, o grubości 30–660 nm.

Oryginalne aspekty prezentowanej rozprawy to:

- zastosowanie energetycznego modelu pęknięcia segmentacyjnego do opisu zjawisk zachodzących w warstwie tlenku krzemu na podłożu polimerowym;
- wyjaśnienie wpływu naprężeń wstępnych na proces pęknięcia segmentacyjnego w tym przypadku;
- ilościowa analiza procesu rozwoju spękań po grubości warstwy izolacji termicznej;
- wykazanie istotności wielkości kroku obciążenia w analizie metodą elementów skończonych procesu rozwoju dużej liczby nie połączonych ze sobą spękań; sformułowanie wskazówek praktycznych zezwalających na uniknięcie problemów ze zbieżnością obliczeń;
- analiza głównych czynników decydujących o rozwoju stanu naprężenia w warstwach izolacji termicznej i podanie hipotetycznego scenariusza opisującego proces delaminacji tych warstw;
- sformułowanie metody pozwalającej na pół-analityczne oszacowanie procesu dwuwymiarowego poślizgu ciernej warstwy na sztywnym podłożu;
- wyprowadzenie prostych wzorów opisujących kształt strefy zdelaminowanej oraz proces delaminacji sztywnej warstwy ze sztywnego podłoża;
- koncepcyjne sformułowanie zasad działania czujnika piezoelektrycznego pozwalającego na pomiar sprzężonych modułów sprężystych wielowarstwowego materiału;
- sformułowanie praktycznych wskazówek służących zwiększeniu efektywności działania zaproponowanego czujnika.

## Opis segmentacyjnego pęknięcia po grubości warstwy

Pęknięcie cienkiej warstwy po jej grubości na skutek rozciągania podłoża to jeden z rodzajów uszkodzeń typowych dla tego typu konstrukcji. Szczególnym przypadkiem są sytuacje, gdy spękania mają kształt prostych, równoległych linii. Eksperymentalne badania pokazują, że ich liczba początkowo wzrasta, aby ostatecznie się ustabilizować i nie zwiększać, mimo rozciągania podłoża. Zjawisko to nazywane jest pękaniem segmentacyjnym, a maksymalna gęstość spękań może służyć do określenia cech mechanicznych warstwy lub powierzchni kontaktowej pomiędzy warstwą a podłożem.

Rozdział 3 zawiera mechaniczny model tego zjawiska. Opiera się on na prostym opisie jednowymiarowym, pozwalającym na uzyskanie analitycznych wyników. Mimo swojej prostoty uwzględnia naprężenia początkowe wynikające, na przykład, ze sposobu produkcji cienkiej warstwy, oraz plastyczny poślizg na granicy warstwa/podłoże, przy założeniu stałej wartości naprężenia stycznego na powierzchni kontaktowej. Bezpośrednią konsekwencją powstałych naprężeń resztkowych jest względny poślizg pomiędzy filmem a podłożem, obserwowany na obydwu krańcach rozważanej próbki. Dodatkowo, model analityczny wskazuje na dwuetapowy proces uplastycznienia się powierzchni kontaktowej, zachodzący podczas rozciągania podłoża. Na etapie pierwszym długość obszaru uplastycznionego nie zwiększa się i przyjmuje wartość równą wywołanej jedynie naprężeniami wstępnymi. Monotonicznie wzrastające odkształcenie podłoża na tym etapie skutkuje zmianą kierunków poślizgów względnych pomiędzy warstwą a podłożem w obszarach już uplastycznionych. Na etapie drugim uplastycznieniu ulega poprzednio niezniszczony obszar powierzchni kontaktowej. Charakterystyczne dla obydwu etapów jest wytworzenie obszaru wewnątrz cienkiego filmu, w którym występuje naprężenie rozciągające o stałej wartości, tak jak w przypadku rozciąganego pręta. W takiej sytuacji powstanie pęknięć po grubości warstwy silnie zależy od znajdujących się w niej mikrouszkodzeń, wywołujących koncentrację naprężeń. Aby opisać rozwój uszkodzenia i przejście do stanu z ustabilizowaną i nie wzrastającą liczbą spękań, w Rozdziale 3 użyto model energetyczny, bazujący na topologicznej transformacji pomiędzy stanem początkowym, bez spękań, a stanem końcowym, odpowiadającym maksymalnie popękanej warstwie. Warunek przejścia pomiędzy tymi stanami jest warunkiem energetycznym, zakładającym osiągnięcie minimalnej wartości energii potencjalnej układu oraz energii rozproszonej na utworzenie spękań i uplastycznienie powierzchni kontaktowej. Użyte podejście nie uwzględnia śledzenia całego procesu jako funkcji czasu. Pozwala na jednoznaczne określenie gęstości spękań w stanie ustabilizowanym. Pokazano, że przeprowadzona analiza może zostać znacznie uproszczona, gdy warstwa jest znacznie cieńsza od podłoża, przy założeniu podobnych wartości ich modułów sprężystych. W takim wypadku, w warunku energetycznym transformacji można pominąć człony odpowiadające energii podłoża. W literaturze znanych jest wiele podejść, gdzie pękanie segmentacyjne opisane jest w oparciu o kryteria naprężeniowe (Białas i Mróz [29, 30], Hsueh [93], Yanaka i współpracownicy [223, 224]). Model przedstawiony w monografii korzysta z energii powierzchniowej dla cienkiej warstwy, która odgrywa taką samą rolę, jak naprężenie krytyczne w wymienionych pracach. Jednym z kluczowych założeń jest przyjęcie identycznej odległości pomiędzy spękaniami w warstwie. W rzeczywistości sytuacja jest o wiele bardziej skom-

plikowana. Badania eksperymentalne wykazują rozrzut tej wielkości wokół wartości średniej. Agrawal i Raj [4] pokazali, że odległość maksymalna powinna różnić się od minimalnej co najwyżej dwa razy. Tych efektów nie można opisać stosując zaproponowane podejście. Wykorzystując je nie da się również uwzględnić procesów związanych z historią procesu, na przykład zależności pomiędzy przyłożoną siłą a ilością spękań. Do ich opisu stosuje się modele oparte o kryterium naprężeniowe, tak jak przedstawili to między innymi Białas i Mróz [29].

Zaproponowany model energetyczny został sformułowany dla drugiego etapu obciążenia. Możemy więc stwierdzić, że dla spękań zachodzących na tym etapie naprężenia początkowe nie mają żadnego wpływu na ten proces. Podczas tego etapu początkowe obszary uplastycznienia powierzchni kontaktowej są już zastąpione strefami o przeciwnym kierunku poślizgu względnego między warstwą a podłożem i nie mają żadnego wpływu na energetyczny warunek pęknięcia. Zaproponowane podejście wykazuje jednak, że należy uwzględniać naprężenia początkowe adoptując kryterium energetyczne dla spękań zachodzących na pierwszym etapie obciążenia.

## Mechaniczna analiza warstw izolacji termicznej

Warstwy izolacji termicznej (po angielsku *Thermal Barrier Coating*, w skrócie *TBC*) odgrywają ważną rolę ochronną na elementach turbin gazowych, chroniąc znajdujący się pod nimi materiał przed działaniem agresywnego środowiska zewnętrznego. Ich grubość to zazwyczaj około 300  $\mu\text{m}$ , lecz różnica temperatury na grubości warstwy sięga 200°C. Te doskonałe własności izolacyjne warstwa zawdzięcza swojej porowatej strukturze (Evans i współpracownicy [62, 63]).

Pomiędzy warstwą izolacji termicznej a materiałem podłoża znajduje się dodatkowa warstwa kleju (po angielsku *Bond Coat*, w skrócie *BC*), której głównym zadaniem jest zapewnienie przyczepności izolacji do materiału konstrukcyjnego. W trakcie użytkowania turbiny, pomiędzy warstwą TBC a warstwą BC wytwarza się dodatkowy materiał. Jest to tlenek  $\text{Al}_2\text{O}_3$ , powstający na skutek utlenienia aluminium, będącego jednym ze składników warstwy BC. Tak więc rozpatrując rozwój naprężeń oraz uszkodzeń w warstwach izolacji termicznej musimy w zasadzie uwzględnić warstwy trzech różnych materiałów: TBC, tlenku  $\text{Al}_2\text{O}_3$  (*Thermally Grown Oxide*, *TGO*) oraz BC. Zjawisko przyrostu grubości warstwy TGO oraz efekty reologiczne, które uaktywniają się w wysokich temperaturach, sprawiają, że modelowanie mechaniczne jest tu niezwykle skomplikowane i zadawalające rezultaty jesteśmy w stanie uzyskać w zasadzie jedynie korzystając

z metody elementów skończonych. Należy w tym miejscu zaznaczyć, że wśród warstw TBC wyróżniamy dwa ich rodzaje: warstwy powstałe poprzez fizyczne osadzanie z fazy gazowej (z angielskiego *Physical Vapour Deposition, PVD*) oraz poprzez osadzanie specjalnych proszków roztopionych wcześniej do stanu plazmy (*Air Plasma Sprayed, APS*). Różnią się one strukturą oraz własnościami termiczno-mechanicznymi. Modelowanie przedstawione w Rozdziale 4 dotyczy warstwy APS TBC.

### Numeryczne modelowanie pęknięcia warstwy izolacji termicznej w teście zginania

Pierwsza część Rozdziału 4 dotyczy pęknięcia warstwy izolacji termicznej po jej grubości w testach zginania. Eksperymenty przedstawione przez Majerusa [132] służą jako punkt wyjścia do stworzenia modelu numerycznego omawianego zjawiska. Pozwala on na śledzenie procesu w funkcji czasu, bez uwzględnienia zniszczenia powierzchni kontaktowej oraz bez przeskoku od razu do stanu nasyconego, jak ma to miejsce dla modelu energetycznego opisanego w Rozdziale 3. Podejście pokazuje, że malejąca wartość energii krytycznej  $G_I$  powoduje zwiększenie liczby spękań. Z kolei, pęknięcie warstwy po jej grubości prowadzi do zmniejszenia się wartości energii uwalnianej dla spękań delaminacyjnych pomiędzy warstwą a podłożem. Jest to ważny wniosek w przypadku pokryć elementów turbin gazowych, gdzie spękania po grubości są dopuszczalne, natomiast odpadanie warstwy i narażenie elementu turbiny na działanie wysokiej temperatury jest zjawiskiem niepożądanym. Tym samym, przedstawione wyniki mogą służyć do odpowiedniego projektowania pokryć, tak aby wartość  $G_I$  dla spękań po grubości była jak najniższa, to jest aby chronić warstwę przed delaminacją kosztem spękań po jej grubości. W tej części monografii pokazano, iż aby w trakcie obliczeń MES uzyskać lokalizację uszkodzeń w postaci dużej liczby spękań po grubości warstwy, należy zwracać uwagę na to, aby krok obciążenia podczas obliczeń był dostatecznie mały. Warunkiem na jego długość jest spełnienie kryterium zniszczenia dla wszystkich elementów kohezyjnych jedynie w jednym punkcie całkowania podczas zadanego kroku obciążenia. Standardowo elementy kohezyjne wykorzystuje się do opisu zjawiska delaminacji na z góry zadanej powierzchni. W takim przypadku kryterium zniszczenia może być spełnione od razu w kilku punktach całkowania bez wpływu na zbieżność obliczeń. W przedstawionym modelu elementów skończonych proces spękania nie jest przypisany do z góry założonej powierzchni. Nie znana jest także liczba spękań. W takiej sytuacji spełnienie warunku zniszczenia tylko w jednym punkcie całkowania podczas kroku obciążenia pozwoliło na uzyskanie

wyników zgodnych z uzyskanymi eksperymentalnie, zarówno co do liczby spękań oraz ich lokalizacji.

### Modelowanie stanu naprężenia oraz procesu delaminacji w warstwach izolacji termicznej

Kluczowym dla warstw izolacji termicznej jest problem ich delaminacji oraz odrywania od podłoża. Temu zagadnieniu poświęcona jest druga część Rozdziału 4 monografii. Mechaniczne modelowanie polega na rozpatrzeniu pewnego elementu reprezentatywnego zawierającego warstwy TBC, BC oraz TGO ze znajdującym się pod nimi materiałem podłoża. Rozmiary elementu reprezentatywnego są tak dobrane, aby zawierał on nierówność na granicy wymienionych materiałów, która powstaje na skutek procesu produkcji pokryć APS TBC. Nierówność ta wywołuje koncentracje naprężeń i w rezultacie sprzyja rozwojowi mikropęknięć. Ich kolejne łączenie powoduje powstanie makrorysy i delaminację izolacji. Tak więc analiza reprezentatywnego elementu pozwala na ocenę zachowania się całego pokrycia przy założeniu, że zjawiska jakie w nim zachodzą uogólnimy dla całej warstwy.

Pierwszym krokiem w analizie numerycznej było stworzenie odpowiedniego modelu elementów skończonych, który uwzględni zjawiska relaksacji oraz utleniania w wysokich temperaturach. Obliczenia wykonane z jego pomocą pozwoliły on na sformułowanie następujących wniosków:

- dla obciążeń termicznych efekty lepkie w materiale CMSX-4 z którego wykonuje się łopatki mogą zostać pominięte, ponieważ nie mają one żadnego wpływu na koncentracje naprężeń w miejscach wokół nierówności;
- mikro pęknięcia wokół nierówności mogą formować się głównie podczas chłodzenia łopatki;
- przy założeniu, że modelowane materiały zachowują się w sposób sprężysto-lepki, efekt obciążeń cyklicznych jest pomijalny; nie prowadzi do dużych różnic w stanie naprężenia w porównaniu z obciążeniami monotonicznymi;
- rozwój spękania na powierzchni pomiędzy warstwami TGO oraz BC wywołuje powstanie strefy rozciąganej wewnątrz TBC;
- gdy grubość warstwy tlenku przekracza pewną krytyczną wartość pojawia się w nim naprężenie rozciągające.

Na podstawie wymienionych spostrzeżeń możemy sformułować następującą hipotezę opisującą proces delaminacji izolacji termicznej. Podczas chłodzenia

łopatki powstają mikropęknięcia na granicy warstw TGO oraz BC. Ich obecność ma istotny wpływ na stan naprężenia wewnątrz warstwy TBC, wywołując w niej powstanie naprężeń rozciągających oraz mikro spękań. Przyrost grubości warstwy tlenku na skutek utleniania aluminium w wysokich temperaturach, zwiększa obszar działania naprężeń rozciągających w TBC i sprzyja przyrostowi długości mikro-spękań w tym materiale. Gdy grubość warstwy tlenku przekracza krytyczną wartość, także w nim pojawia się strefa rozciągana i mikropęknięcia powstałe wewnątrz TBC mogą powiększyć się, penetrując warstwę TGO. Łączenie się tak powstałych uszkodzeń generowanych przez pojedyncze nierówności, powoduje powstanie makro rysy i odpadnięcie izolacji.

Sformułowana hipoteza nie odbiega zasadniczo od scenariusza zaproponowanego przez Changa i współpracowników [43] oraz Freborga i współpracowników [68]. Dodatkowo, zwraca uwagę na istotny proces przyrostu grubości warstwy tlenku, jak gdyby katalizujący rozwój makro uszkodzenia.

## Poślizg cierny

Problemowi poślizgu ciernego pomiędzy warstwą a podłożem poświęcony jest Rozdział 5 monografii. Zjawisko to należy traktować jako efekt delaminacji warstwy od podłoża, a sama analiza próbuje odejść od jednowymiarowych modeli paska znanych w literaturze (Białas i Mróz [29, 30], Schreyer i Peffer [174], Timm i współpracownicy [198]) w kierunku zagadnienia dwuwymiarowego. W ten sposób możliwe jest uwzględnienie zjawisk nie opisanych przez podejście jednowymiarowe: dokładnego opisu kształtu strefy zdelaminowanej, wpływu współczynnika Poissona na sam proces. Założenie, że materiał sprężystej warstwy ślizga się w sposób cierny po sztywnym podłożu, pozwoliło na uzyskanie przybliżonych rozwiązań pół-analitycznych. W szczególnym przypadku delaminacji sztywnego filmu na sztywnym podłożu otrzymujemy rozwiązanie ścisłe, które dodatkowo opisane jest w sposób analityczny. W kontekście przyjętych przybliżeń można stwierdzić, że proces poślizgu opisany jest poprzez rozwiązanie fundamentalne dla sprężystej, nieskończonej tarczy obciążonej siłą skupioną działającą w jej płaszczyźnie. To właśnie rozwiązanie pozwala na określenie rozkładu naprężeń ciernych na powierzchni kontaktowej pomiędzy warstwą a podłożem. Dodatkowo, na jego podstawie, wyznaczamy kształt strefy zdelaminowanej. Odpowiada on obszarowi w rozwiązaniu fundamentalnym, gdzie jedna ze składowych wektorów przemieszczeń tarczy pokrywa się z kierunkiem działania siły skupionej.

Zaproponowany sposób rozumowania może zostać wykorzystany w celu uzy-

skania oszacowań dla podobnych zagadnień poślizgu. Wymienić można tutaj półprzestrzeń sprężystą spoczywającą w sposób cierny na sztywnym podłożu i obciążoną na swoim brzegu siłą skupioną, działającą w jej płaszczyźnie. Algorytm postępowania jest następujący:

1. uzyskaj rozwiązanie  $\{u_x^P, u_y^P\}$  dla zagadnienia podstawowego, w którym obciążenie pochodzi jedynie od siły skupionej;
2. przybliż rozkład naprężeń stycznych na powierzchni kontaktowej wykorzystując pole  $\{u_x^P, u_y^P\}$ ;
3. warunek  $\delta P = 0$  pozwala na określenie obszaru zdelaminowanego;
4. skorzystaj z zasady superpozycji, aby otrzymać poszukiwane pole naprężeń.

Założenie, że naprężenie styczne na powierzchni kontaktowej ma wartość stałą  $\tau^f$  jest dość restrykcyjne. Bardziej realistyczne jest przyjęcie, że osiąga ono najpierw wartość maksymalną  $\tau^{\text{peak}}$ , a następnie maleje do  $\tau^f$ . Taka analiza została przeprowadzona przez Palmera i Rice'a [154], którzy rozpatrywali poślizg w zagęszczonych gruntach. Sytuacja rozważana w Rozdziale 5 opisana jest jednak poprzez płaski stan naprężenia, który dyktuje zakres stosowalności rozwiązania. Jest ono słuszne, gdy charakterystyczna długość strefy poślizgu jest znacznie większa od grubości warstwy. W tym przypadku wartość naprężenia stycznego na powierzchni kontaktowej jest większa niż  $\tau^f$  jedynie w pobliżu brzegu tej strefy i z dobrym przybliżeniem można przyjąć, że w większości tego obszaru osiąga wartość rezydualną  $\tau^f$ .

## Charakterystyka cech mechanicznych cienkich warstw

W Rozdziale 6 monografii sformułowane zostały teoretyczne podstawy działania czujnika piezoelektrycznego, służącego określaniu parametrów lepko-sprężystych cienkich warstw. W swoim założeniu ma on służyć do charakterystyki mechanicznej wielowarstwowego układu skóry ludzkiej. Koncepcja opiera się na stosowanej w geotektonice analizie fal powierzchniowych (multi-channel analysis of surface waves, Park i współpracownicy [157, 158]), która pozwala na badanie profili geologicznych. Zaproponowany czujnik składa się z szeregu równoległych, bardzo cienkich pasków wykonanych z piezoelektryku PVDF, przyczepianych do naskórka. Drgająca skóra wywołuje odkształcenia sensora, które z kolei generują ładunki elektryczne. Ich wartości, zmierzone dla każdego z pasków PVDF, niosą w sobie informację o charakterze fal powierzchniowych rozchodzących się w warstwach skóry. Wykonanie analizy odwrotnej pozwala

na obliczenie zespolonych modułów sprężystych dla każdej z warstw tworzących skórę. W Rozdziale 6 zaprezentowano efektywność działania teoretycznego modelu sensora, ze zwróceniem uwagi na wpływ błędów pomiarowych. Wykazano, że dla jakości obliczeń kluczowa jest liczba częstotliwości drgań, z jaką pobudza się tkankę podczas eksperymentu, a nie liczba pasków PVDF, tworzących czujnik.

Należy wymienić dwa istotne aspekty zastosowania zaproponowanego czujnika. Po pierwsze, zezwała on na bezinwazyjne i tanie, w porównaniu do innych metod, określenie lepko-sprężystych parametrów skóry. Po drugie, w trakcie analizy jesteśmy w stanie rozróżnić pomiędzy wieloma warstwami, z których zbudowana jest skóra. Szczególnie cenne wydaje się potencjalne zastosowanie czujnika do diagnostyki komórek nowotworowych.